

# Design of Large Wind Turbines using Fluid-Structure Coupling Technique

**Sessarego, Matias; Shen, Wen Zhong; Sørensen, Jens Nørkær; Ramos García, Néstor**

*Publication date:*
2016

*Document Version*
Publisher's PDF, also known as Version of record

# Design of Large Wind Turbines using Fluid-Structure Coupling Technique

Department of Wind Energy
PhD Report 2016

Matias Sessarego

DTU Wind Energy PhD-0068(EN)

October 2016

DTU Wind Energy
Department of Wind Energy

**Authors:** Matias Sessarego
**Title:** Design of Large Wind Turbines using Fluid-Structure Coupling Technique
**Department:** Fluid Mechanics Section

**Abstract:**
Aerodynamic and structural dynamic performance analysis of modern wind turbines are routinely carried out in the wind energy field using computational tools known as aero-elastic codes. Most aero-elastic codes use the blade element momentum (BEM) technique to model the rotor aerodynamics and a modal, multi-body, or finite-element approach to model the turbine structural dynamics. A novel aero-elastic code has been developed called MIRAS-FLEX. MIRAS-FLEX is an improvement on standard aero-elastic codes because it uses a more advanced aerodynamic model than BEM. MIRAS-FLEX combines the three-dimensional viscous-inviscid interactive method, MIRAS, with the dynamics model used in the aero-elastic code FLEX5.

Following the development of MIRAS-FLEX, a surrogate optimization methodology using MIRAS alone has been developed for the aerodynamic design of wind-turbine rotors. Designing a rotor using a computationally expensive MIRAS instead of an inexpensive BEM code represents a challenge, which is resolved by using the proposed surrogate-based approach. The approach is unique because most aerodynamic wind-turbine rotor design codes use the more common and inexpensive BEM technique. As a verification case, the methodology is applied to design a model wind-turbine rotor and is compared in detail with the one designed with BEM. Results demonstrate the methodology is effective for the aerodynamic design of wind-turbine rotors.

To perform more realistic large wind-turbine rotor designs, a structural design code was needed. Such a structural design code has been developed to minimize the cost of energy (COE) of the NREL 5MW wind-turbine blade. Blade stiffness and mass are computed using the NREL PreComp code based on the classical laminate theory, while blade natural frequencies are obtained from the NREL BModes code. The aero-elastic program FLEX5 computes loads based on design load cases from the IEC standards, which are then used to compute the deflections, strains, and buckling constraints. The minimum COE is found by implementing the procedure with a gradient-based optimizer and using the wind turbine design cost and scaling model of NREL.

Last, a unique framework to design large wind-turbine rotors has been developed by combining MIRAS-FLEX, the surrogate-optimization code, and the structural design code. The optimization framework was used to design large wind turbine blades using both FLEX5 and MIRAS-FLEX with good results obtained.

**DTU Wind Energy PhD-0068(EN)**
**October 2016**

**Education:**
PhD

**Supervisors:**
Wen Zhong Shen
Jens Nørkær Sørensen
Néstor Ramos García

**Technical University of Denmark**
Department of Wind Energy
Nils Koppels Allé
Building 403
2800 Kgs. Lyngby
Denmark
Telephone 46 77 50 85

www.vindenergi.dtu.dk

# Design of Large Wind Turbines using Fluid-Structure Coupling Technique

by

**Matias Sessarego**

B.Sc., University of Calgary, 2011
M.Sc., University of Calgary, 2013

Submitted to the Department of Wind Energy in partial fulfillment of the requirements for the degree of

Doctor of Philosophy

at
The Technical University of Denmark

October 2016

# Abstract

Aerodynamic and structural dynamic performance analysis of modern wind turbines are routinely carried out in the wind energy field using computational tools known as aero-elastic codes. Most aero-elastic codes use the blade element momentum (BEM) technique to model the rotor aerodynamics and a modal, multi-body, or finite-element approach to model the turbine structural dynamics. A novel aero-elastic code has been developed called MIRAS-FLEX. MIRAS-FLEX is an improvement on standard aero-elastic codes because it uses a more advanced aerodynamic model than BEM. MIRAS-FLEX combines the three-dimensional viscous-inviscid interactive method, MIRAS, with the dynamics model used in the aero-elastic code FLEX5.

Following the development of MIRAS-FLEX, a surrogate optimization methodology using MIRAS alone has been developed for the aerodynamic design of wind-turbine rotors. Designing a rotor using a computationally expensive MIRAS instead of an inexpensive BEM code represents a challenge, which is resolved by using the proposed surrogate-based approach. The approach is unique because most aerodynamic wind-turbine rotor design codes use the more common and inexpensive BEM technique. As a verification case, the methodology is applied to design a model wind-turbine rotor and is compared in detail with the one designed with BEM. Results demonstrate the methodology is effective for the aerodynamic design of wind-turbine rotors.

To perform more realistic large wind-turbine rotor designs, a structural design code was needed. Such a structural design code has been developed to minimize the cost of energy (COE) of the NREL 5 MW wind-turbine blade. Blade stiffness and mass are computed using the NREL PreComp code based on the classical laminate theory, while blade natural frequencies are obtained from the NREL BModes code. The aero-elastic program FLEX5 computes loads based on design load cases from the IEC standards, which are then used to compute the deflections, strains, and buckling constraints. The minimum COE is found by implementing the procedure with a gradient-based optimizer and using the wind turbine design cost and scaling model of NREL.

Last, a unique framework to design large wind-turbine rotors has been developed by combining MIRAS-FLEX, the surrogate-optimization code, and the structural design code. The optimization framework was used to design large wind-turbine blades using both FLEX5 and MIRAS-FLEX with good results obtained.

# Dansk Resumé

Aerodynamisk og strukturel analyse af moderne vindmøller udføres rutinemæssigt ved hjælp af aero-elastiske beregningsværktøjer. De fleste aero-elastiske koder er baseret på "blade element momentum" (BEM) teori til at modellere aerodynamikken omkring rotoren samt en modal, multi-body, eller finite-element model for den strukturelle dynamik. En ny aero-elastisk kode (MIRAS-FLEX) er blevet udviklet. MIRAS-FLEX er en forbedring i for hold til standard aero-elastiske koder, da der bruges en mere avanceret aerodynamisk model end BEM. MIRAS-FLEX kombinerer den tredimensionale viskose-inviskose interaktive metode, MIRAS, med den dynamiske model, der anvendes i aero-elastiske kode FLEX5.

En surrogat optimeringsmetode er udviklet omkring MIRAS til aerodynamiske design af vindmølle rotorer. Design af et rotor ved hjælp af den beregningsmæssigt dyre MIRAS i forhold til en billig BEM koden repræsenterer en udfordring, der løses ved at bruge den foreslåede surrogat metode. Den fremgangsmåde er unik, fordi de fleste design koder bruger den mere almindelige og billige BEM teknik. Metoden er benyttet til at designe en model vindmølle rotor, der sammenlignes med en tilsvarende model rotor designet med BEM. Resultaterne demonstrerer at metoden er effektiv til aerodynamisk design af vindturbine rotorer.

Et mere realistisk design af store vindmølle rotorer kræver også en strukturel design kode. Strukturel design koden er udviklet for at minimere prisen på energi ("Cost of Energy" = COE) for NREL 5 MW vind-møllevingen. Stivhed og masse af vingerne er beregnet ved hjælp af NREL PreComp, der er baseret på den klassiske laminat teori, mens vingens egen-frekvenser beregnes med NREL BModes. Belastningerne er beregnet af FLEX5 for design last tilfælde defineret af IEC-standarder, som derefter bruges til at beregne deformationer, belastninger, og "buckling" begrænsninger. COE minimeres ved at gennemføre proceduren med en gradient-baseret optimering og omkostninger til vindmøllens design og skaleringsmodel af NREL.

Endelig er MIRAS-FLEX, surrogat optimeringskoden og den strukturelle designkode koblet i et unikt rammeværktøj til design af store vindmølle rotorer. Dette rammeværktøj benyttes til at designe store vindmøllevinger med forbedrede egenskaber.

# Acknowledgements

I would like to thank my supervisors Wen Zhong Shen and Jens Nørkær Sørensen for providing me the opportunity to do my PhD study in the Fluid Mechanics Section of the Department of Wind Energy, Technical University of Denmark. All that I have learned during my three-year stay at this leading research institution in wind energy has greatly contributed to my career as a research engineer in wind energy.

I also would like to thank my co-supervisor Néstor Ramos-García for the many hours spent on working on our Fortran codes and discussing the scientific details of my PhD project. His skill and expertise were crucial for the realization of the project.

Finally, I give many thanks to my family and all members of the Technical University of Denmark who have helped me throughout my stay in Denmark. I am very grateful to have been able to carry out my PhD studies in an open-minded and multi-cultural working environment.

The PhD project was funded by the Danish Council for Strategic Research under the project name OffWindChina (Sagsnr. 0603-00506B). The support is gratefully acknowledged.

# Preface

This dissertation is submitted in partial fulfillment of the requirements for the degree of Doctor of Philosophy in Wind Energy at the Technical University of Denmark. It is based on the work done during a three year Ph.D. study in the Fluid Mechanics Section of the Department of Wind Energy. The work was funded by the Danish Council for Strategic Research under the project name OffWindChina (Sagsnr. 0603-00506B). This dissertation was submitted in October 2016.

This thesis is an extended version of six multi-authored articles that have been submitted for publication. The publications are as follows:

1. Matias Sessarego, Néstor Ramos-García, and Wen Zhong Shen. "Development of a fast fluid-structure coupling technique for wind turbine computations", Journal of Power and Energy Engineering, (Vol. 3, No. 7, July 2015, pages 1-6, journal) [1];

2. Matias Sessarego, Néstor Ramos-García, Wen Zhong Shen, and Jens Nørkær Sørensen. "Development of an aeroelastic code based on three-dimensional viscous-inviscid method for wind turbine computations", Wind Energy John Wiley and Sons (March 2017, journal) [2];

3. Matias Sessarego, Néstor Ramos-García, Hua Yang, and Wen Zhong Shen. "Aerodynamic wind-turbine rotor design using surrogate modeling and three-dimensional viscous-inviscid interaction technique", Renewable Energy Elsevier (Vol. 93, August 2016, pages 620-635, journal) [3];

4. Matias Sessarego and Wen Zhong Shen. "Development of a simple structural design method for large wind turbine blades", 12th European Academy of Wind Energy PhD Seminar (May 2016, conference proceedings) [4];

5. Matias Sessarego, Néstor Ramos-García, Wen Zhong Shen, and Jens Nørkær Sørensen. "Large wind turbine rotor design using an aero-elastic / free-wake panel coupling code", The Science of Making Torque from Wind 2016 (September 2016, conference proceedings) [5];

6. Zhenye Sun, Matias Sessarego, Jin Chen, and Wen Zhong Shen. "Design of the OffWindChina 5-MW wind turbine rotor", Energies (under review, submitted March 2017, journal).

# Nomenclature

| | |
|---|---|
| $\alpha$ | angle of attack |
| $\bar{u}_1$, $\bar{u}_2$, $\bar{u}_3$ | rigid body translations in three dimensions |
| $\beta_{\mathrm{w}}$ | angle between the external and limiting streamlines |
| $\beta_c$ | structural pitch angle |
| $\boldsymbol{\psi}$ | vector of basis functions, $\psi$ |
| $\delta$ | boundary layer thickness |
| $\delta_1^*$ | stream-wise displacement thickness |
| $\delta_2^*$ | span-wise displacement thickness |
| $\mathbb{R}$ | real number |
| $\mathbf{w}$ | vector of weight coefficients, $w$ |
| $\mathbf{x}$ | vector of design variables, $x$ |
| $\mathbf{y_s}$ | sampled points |
| $\mathbf{y}$ | vector of design variables, $y$ |
| $\mu$ | dynamic viscosity of air |
| $\omega$ | rotational/generator speed |
| $\omega_{\mathrm{rotor}}$ | rotor rotation frequency |
| $\phi_1$, $\phi_2$, $\phi_3$ | rigid body rotations in three dimensions |
| $\rho$ | density of air |
| $\sigma_{Ult}$ | effective single cycle strength of the material |
| $\mathrm{X}_{\mathrm{design}}$ | design point of parameter X |
| $\theta_1$ | stream-wise momentum thickness |
| $\theta_2$, $\delta_3$ | momentum thickness due to cross-flow |
| $\widehat{f}$ | surrogate approximation of $f$ |
| $^L$ | lower boundary constraint |
| $^U$ | upper boundary constraint |
| $B$ | number of blades |
| $c$ | chord length |
| $c_1$, $c_2$, $c_3$ | center-point coordinates in three dimensions of panel in MIRAS blade mesh |
| $C_d$ | drag coefficient |
| $C_f$ | skin friction coefficient |
| $C_l$ | lift coefficient |
| $C_P$ | power coefficient |
| $C_p$ | surface pressure distribution |
| $C_{P,\mathrm{fit}}$ | power coefficient for best-fit baseline shape |
| $E$ | modulus of elasticity |
| $EI$ | bending stiffness of cross-section |
| $f$ | scalar-valued objective function |
| $F_{\mathrm{sys}}$ | foundation coordinate system in FLEX5 |
| $H$ | shape factor parameter |
| $K_{\mathrm{sys}}$ | tower top coordinate system in FLEX5 |
| $l$ | local aspect ratio, $c/r$ |
| $L_{\mathrm{Ult}}$ | ultimate load |
| $n$ | number of variables |
| $N_{\mathrm{sys}}$ | shaft coordinate system in FLEX5 |
| $R$ | rotor radius |
| $r$ | radial position of the rotor or span-wise blade position |
| $R_O$ | rotational number, $\omega r/U_{\mathrm{rel}}$ |
| $r^2_{\mathrm{coe}}$ | correlation coefficient |
| $R_{\mathrm{sys}}$ | rotor coordinate system in FLEX5 |
| $R_{hub}$ | hub radius |
| $Re$ | Reynolds number, $\rho U_{\mathrm{rel}} c/\mu$ |
| $T_{\mathrm{sys}}$ | tower bottom coordinate system in FLEX5 |
| $u_1$, $u_2$, $u_3$ | displacement in three dimensions |
| $U_o$ | design wind speed |
| $U_y$ | edge-wise blade tip deflection |
| $U_z$ | flap-wise blade tip deflection |
| $U_{\mathrm{rel}}$ | relative wind speed |
| $V_o$ | wind speed at hub height |
| $V_{\mathrm{avg}}$ | average wind speed |
| $V_{\mathrm{e1}}$ | wind speed with a 1-year recurrence period |
| $V_{\mathrm{e50}}$ | wind speed with a 50-year recurrence period |
| $V_{\mathrm{ref}}$ | reference wind speed |
| $V_{\mathrm{sys}}$ | blade coordinate system in FLEX5 |
| $V_{b1}, V_{b2}, V_{b3}$ | blade velocity in three dimensions |
| $w_1, w_2, w_3$ | induced velocity in three dimensions |
| $X$ | number of grid points along each variable dimension |
| $x_1$, $x_2$, $x_3$ | nodal coordinates in three dimensions of MIRAS blade mesh |
| 2D | Two-dimensional |
| 3D | Three-dimensional |
| AEP | Annual Energy Production |

AL Actuator Line
AL-FLEX5 EllipSys3D coupled with FLEX5 through actuator-line approach
ANN Artificial Neural Network
AOE Annual Operating Expenses
AR Aspect Ratio
Atip tip-to-tower-center-clearance
BECAS BEam Cross section Analysis Software
BEM Blade Element Momentum
BHawC Bonus Energy Horizontal axis wind turbine Code
BOS Balance Of Station
CFD Computational Fluid Dynamics
COE Cost of Energy
CP Control Point
CPU Central Processing Unit
CSD Computational Structural Dynamics
DB Double Biax
DEL Damage Equivalent Load
DLC Design Load Case
DOF Degrees Of Freedom, same as DOFs
DOFs Degrees Of Freedom, same as DOF
DTU Denmark Technical University
DU Delft University of Technology
FAST Fatigue, Aerodynamics, Structures, and Turbulence
FCR Fixed Charge Rate
FEM Finite Element Method
FSI Fluid-Structure Interaction
HAWC2 Horizontal Axis Wind turbine simulation Code 2nd generation
HAWT Horizontal-Axis Wind Turbine
IEC International Electrotechnical Commission
LHS Latin Hypercube Sampling
MATLAB Matrix Laboratory
MEXICO Model rotor EXperiments In COntrolled conditions
MIRAS Method for Interactive Rotor Aerodynamic Simulations
normal normal to the rotor plane, also known as *out-of-plane*
NREL National Renewable Energy Laboratory
NRMSE Normalized Root Mean Squared Error
NTM Normal Turbulence Model
NWTC National Wind Technology Center
OC3 Offshore Code Comparison Collaboration
PI Proportional-Integral
PreComp Pre-Processor for Computing Composite Blade Properties
$Q^3$UIC Quasi-3D Unsteady viscous-inviscid Interactive Code
RKN Runge-Kutta-Nyström
RPM Revolutions Per Minute
RSM Response Surface Model
SF Safety Factor
SQP Sequential Quadratic Programming
ST Station
tangential rotating direction in the rotor plane, also known as *in-plane*
TC Tension Center
TCC Turbine Capital Cost
TI Turbulence Intensity
TSR Tip-Speed Ratio
UD Uni-Directional
VII Viscous-Inviscid Interaction
YZU Yangzhou University

# Contents

# Chapter 1

# Introduction

## 1.1 Background

### 1.1.1 Role of Wind Energy

Energy use world wide is set to grow by one-third to 2040 [6]. Today, fossil fuels account for approximately 81% of the world's energy supply (31.1% oil, 21.4% natural gas, and 28.9% coal) [7], demonstrating humanity's extensive reliance on this single resource. Although the importance of fossil fuels at this moment in time is clear, two very controversial aspects are related to their use. First, fossil fuels are typically classified as a finite resource because they require millions of years to form. In the year 2009, some academics predicted oil reserves might last for 40 years [8]. Natural gas depletion forecasts were a few years longer than oil, and approximately 100-200 years for coal. However, due to many variables, predictions about the future of fossil fuels are very unlikely to hold. For example, new and improved technologies can emerge, unknown at the time of prediction, that extend the amount of fossil fuel acquisition.

The second aspect about fossil fuels is related to climate change. Climate change, global warming, air pollution and acid rain are now generally accepted by the scientific community to be at least partially caused by humanity's fossil fuel consumption. Fossil fuels emit harmful pollutants, primarily in the form of carbon dioxide gas, a contributor to the greenhouse effect. International agreements such as the Kyoto Protocol in 1997 [9] and the Paris Agreement in 2015 [10] aim to set green house gas (GHG) emission reduction targets.

Meeting the future's need for energy without further damage to the environment involves implementing renewable (non-finite) and cleaner alternative-energy solutions. With the current continuous increase in global demand for power, renewable energy technologies are becoming more important in today's energy mix, and are being deployed more quickly and extensively than ever before [7]. Examples of renewable energy include wind power, solar energy, biofuels, hydro-power, geothermal energy, and ocean tidal and wave energy. Wind power, through the use of wind turbines, is now one of the most cost-effective and environmentally-friendly methods of generating electricity. An economic and rapid reduction in carbon dioxide emissions can be achieved by large-scale deployment of wind energy. Within the first three to six months of operation, a wind turbine has offset all emissions from its construction [11]. For its remaining 20 year lifetime, a wind turbine will run emissions free. According to the Global Wind Energy Council [12], the annual installed wind capacity across the globe has been a growing trend for the past 10-15 years as shown in Figure 1.1.

However, like all other power sources, renewable and non-renewable, wind power does come with its own potential drawbacks. Similarly with solar energy, wind power is an intermittent energy source that can only be used when nature supplies it. If wind is not available when there is a need for energy, electricity must be obtained from a substitute energy source. Conversely, when there is a surplus of wind, the energy must

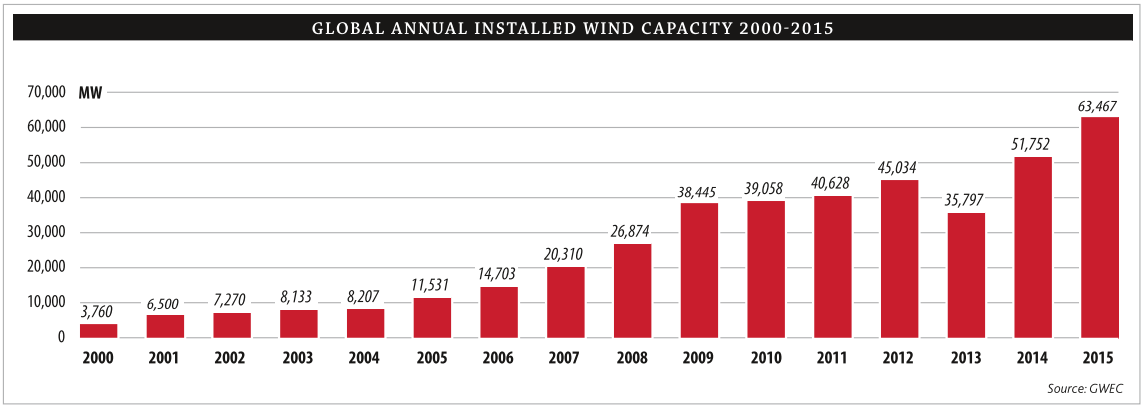


**Figure 1.1:** Annual installed wind capacity across the globe has been a growing trend for the past 10-15 years. Source: Global Wind Energy Council (GWEC) [12].

be stored or exported elsewhere. Conventional power sources such as fossil fuel power plants do not depend on the unpredictability of weather conditions. Other potential drawbacks include visual impact, shadow flickering caused by the sun and rotating blades, noise, collisions with birds and bats, electromagnetic interference, and interference with aviation. Today, offshore wind energy installations have become more attractive than onshore, since communities are far less affected by visual disturbances and noise due to their more remote locations. In addition, the offshore wind resource is superior to that of onshore and there are fewer limitations on rotor size.

### 1.1.2 Wind Power and Increasing Rotor Size

The available power from the wind comes in the form of kinetic energy expressed as:

$$P_{\text{wind}} = \frac{1}{2}\dot{m}V^2 \tag{1.1}$$

where $\dot{m}$ is the mass flow rate and $V$ is the wind speed. The above equation can be rewritten in the following form:

$$P_{\text{wind}} = \frac{1}{2}\rho_{\text{air}}AV^3 \tag{1.2}$$

in terms of the air density, $\rho_{\text{air}}$, and the swept area of the wind-turbine rotor, $A = \pi R^2$. Ideally for power extraction, the kinetic energy from the wind is reduced to zero and converted completely into useful mechanical or electrical energy. This is not achievable realistically, thus the non-dimensional quantity known as the power coefficient, $C_P$, is introduced:

$$P_{\text{turbine}} = C_P\frac{1}{2}\rho_{\text{air}}\pi R^2V^3 \tag{1.3}$$

where $C_P$ is the ratio between the power extracted from the wind, $P_{\text{turbine}}$, to the total available power, $P_{\text{wind}}$. Studying Equation (1.3), the power depends on the wind speed of a site, $V$, the rotor radius, $R$, turbine efficiency $C_P$, and density of air, $\rho_{\text{air}}$. The site has a significant impact because power depends on the cube of the wind speed. Hence, it is most favorable to place turbines where the average wind speed is high. The second most important factor is $R$, where a doubling of $R$ results in four times the power. The increase in power with $R$ is one of the main reasons for the trend of increasing rotor

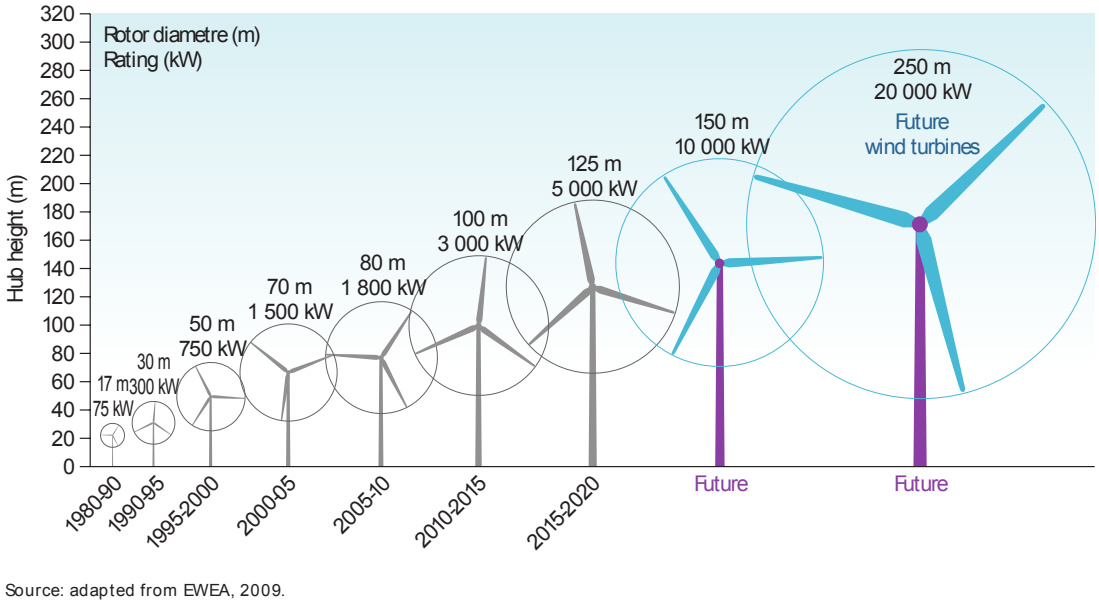


**Figure 1.2:** Increasing turbine size has been effective to lower costs so far, but it is not clear for how long the trend will continue [13].

size throughout the years as shown in Figure 1.2. Figure 1.3 gives a perspective of the immensity of today's turbine blades. Increasing turbine size has been effective to lower costs of wind energy so far, but it is not clear for how long the trend will continue. Research and development is also focused on optimizing $C_P$ using advanced aerodynamic design, control capabilities, and other wind-turbine technology concepts. Not much can be done regarding the density of air, although $\rho_{\text{air}}$ does decrease with higher altitudes thus favoring wind-turbine installations at sea level.

### 1.1.3 Areas of Research

Several areas of research are associated with wind energy, all of which cannot be realistically discussed in detail in this thesis. Research related to wind turbines includes aerodynamics, material science and structural mechanics, aero-elasticity, loads and control, and machine component dynamics. Other areas are wind power economics, management and organization, conversion, integration and planing, and resource assessment, meteorology and remote sensing. The Department of Wind Energy at the Technical University of Denmark (DTU) conducts the majority of these research areas. In the year 2016, DTU Wind Energy is comprised of ten sections:

- Aerodynamic Design (AER)
- Composites and Material Mechanics (COM)
- Fluid Mechanics (FLU)
- Integration and Planning (INP)
- Wind Turbine Loads and Control (LAC)
- Material Science and Characterization (MAC)
- Meteorology and Remote Sensing (MES)
- Resource Assessment Modeling (RAM)
- Test and Measurements (TEM)
- Wind Turbine Structures and Component Design (SAC)

**Figure 1.3:** A wind turbine blade transported on a truck. Photograph was taken from inside a car, giving a perspective of the turbine-blade's immensity. Personal photo from a friend.

Only a subset of the above-mentioned research areas will be investigated in the current thesis. The topics relevant to the thesis consist of the following:

- Fluid-structure interaction (specifically aero-elasticity);
- Optimization techniques (specifically surrogate-modeling);
- Structural design and loads;
- Rotor design.

The above choice of topics was based on the PhD project problem definition:

> "...to develop an integrated design method based on fluid and structure interaction, which can lead to new and higher performance large wind turbine rotors."

In this thesis, a new fluid-structure interaction code is developed and integrated in a rotor design framework. The framework is used to design new and higher performance large wind turbine rotors. The optimization techniques, structural design and loads, and rotor design research areas pertain to the developed framework. But before defining the scope of the thesis in more detail, a thorough literature review in each of the four research topics is presented next.

## 1.2 Literature Review

The current section gives a literature review on each topic studied in the thesis work. There are a total of four topics and each topic is associated with a chapter. The four topics are as follows: fluid-structure interaction (Chapter 2), surrogate-modeling for wind-turbine design (Chapter 3), structural design (Chapter 4), and rotor design (Chapter 5).

### 1.2.1 Fluid-Structure Interaction

Research in computational science and engineering is increasingly confronted with challenging multi-physics problems. Multi-physics problems involve more than one physical domain, often requiring the collaboration of experts from two or more disciplines to solve them. Some of the studied multi-physics problems in the recent years are fluid-structure interaction (FSI) problems. FSI is the mutual action and reaction between a moveable or deformable structure with an internal or surrounding fluid flow [14]. FSI simulations are used to model, e.g. the seismic response of dams [15], ringsail parachute disreefing [16], the hemodynamic and thrombogenic performance of mechanical heart valves [17], and the hydro-elastic response of a pontoon-type very large floating structure [18]. Most importantly for the present thesis, FSI simulations are being used for the analysis of wind turbines as well, see e.g. [19, 20, 21, 22, 23, 24].

Despite the popularity of FSI research, there are still many challenges [14]. A FSI methodology used to simulate one kind of problem successfully is normally not easily applied to another. Fluid-structure interface treatments, mesh configurations, relative time scales, and properties of the fluid and structural parts, which vary from problem to problem, restrict the development of widely-applicable numerical methods. As will be shown later in sections 2.2, 2.3, and 2.4, a custom numerical coupling approach was developed for the novel FSI code developed in this thesis.

First, a brief summary of the different modeling fidelity codes for FSI in wind energy will be provided in subsection 'Modeling Fidelity'. Then, the coupling methods and terminology in FSI will be explained in subsection 'Coupling Methods and Terminology'. A literature review of FSI in wind energy is given in subsection 'Strong- and Loose-Coupling in Wind Energy'. Sections 2.2, 2.3, and 2.4 describes the novel FSI code developed in this thesis.

#### Modeling Fidelity in FSI

Most FSI simulations in modern times are performed using blade element momentum (BEM)-based aero-elastic codes, which rely on simple theoretical equations and empirical data to model the wind-turbine rotor aerodynamics and wake. Such aero-elastic codes are regarded as low-fidelity methods in terms of aerodynamic modeling, but are widely used for engineering design due to their low-computational cost. Examples of BEM-based aero-elastic codes include FLEX5 [25] as discussed in section 1.3.4, FAST [26], HAWC2 [27], BHawC [28], and Bladed [29]. High-fidelity methods refer to computational fluid dynamics (CFD), which model the physics by solving the fundamental equations directly. The equations are evaluated at various points on the fluid domain which have been discretized by using a mesh. Although low-fidelity methods almost always provide less information on the problem solution, they can be highly accurate. From numerical experiments [30], a well-calibrated low-fidelity BEM method was shown to be just as accurate as a CFD solution. Unlike the CFD however, the BEM approach did not provide a complete three-dimensional (3D) description of the flow field around the wind-turbine blade [30]. BEM is disadvantageous to CFD in terms of modeling, because BEM relies on numerous empirical data and engineering models, such as airfoil data, tip and root corrections, as well as yaw, dynamic stall, and dynamic wake models. All the physical effects obtained from the empirical data and engineering models in BEM are intrinsic in CFD. A similar comparison between BEM and CFD is available in subsection 2.4.3 of this thesis.

Researchers and engineers have also applied vortex-based methods to model the wind-turbine rotor performance. Over the last decade, vortex methods have received greater interest in the field of wind energy due to their wide range of available formulations and different levels of complexity. The physical modeling and computational time requirement of vortex codes is viewed as a compromise between BEM and CFD. Therefore, vortex codes can be regarded as medium fidelity compared to BEM and CFD. Examples of FSI using vortex-based methods are found in Kim et al. [21], Riziotis et al. [31], Gebhardt and Roccia [32], and Branlard et al. [33]. Figure 1.4 summarizes the available models for rotor aerodynamics with increasing fidelity.

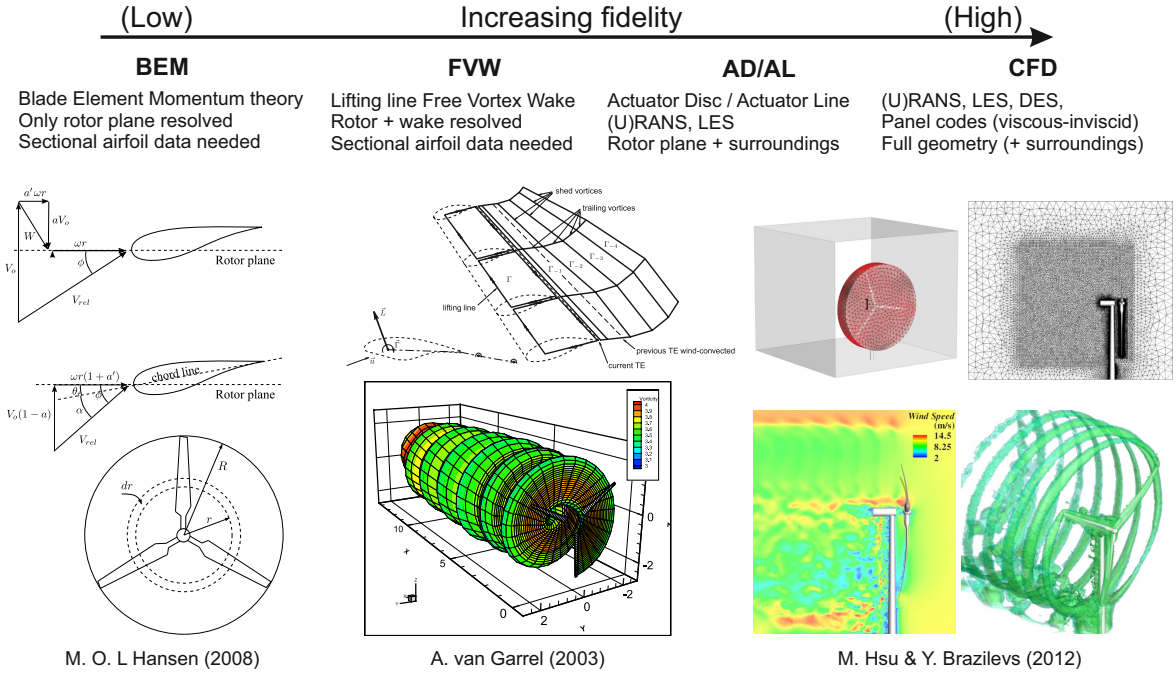


**Figure 1.4:** Rotor aerodynamic modeling with increasing level of fidelity. Reproduced from [20], [34], [35], and [36].

In terms of structural-dynamic modeling in FSI, there is also a wide range from low- to high-fidelity models. The main purpose of a structural model of a wind turbine is to determine the temporal variation of the material loads in the various components [37]. The material loads are found by computing the dynamic response of the wind turbine subject to a time-dependent load from an aerodynamic model, such as BEM, vortex-based codes, or CFD as discussed above. When modeling any mechanical system, the number of degrees of freedom (DOF) is the number of independent parameters used to define the state or configuration of the system. In principle, the higher the number of DOF, the more detail regarding the motions of the system are captured. The increase in detail comes at the expense of the more computational time needed to solve the system. Consequently, the fidelity of a particular structural model can often be assessed by the number of DOF the model uses.

The principle of virtual work, use of modal shape functions, and one-dimensional (1D) linear Euler-Bernoulli beam theory is implemented in FLEX5, while FEM and 1D non-linear beam theory are implemented in BHawC and HAWC2. The entire turbine in FLEX5 is represented as a multi-body, but each blade and tower is represented as a single body only. BHawC and HAWC2 use a co-rotational and multi-body dynamics approach,

respectively, to obtain more detailed dynamics of the blade and turbine. FLEX5 was developed with the principle of using only the most fundamental DOF for efficiency, while BHawC and HAWC2 were developed for more detailed dynamic modeling at the expense of a much larger number of DOF. When viewing the structural model independently, BHawC and HAWC2 can be considered as higher-fidelity codes than FLEX5. The most detailed and computationally demanding approach involves a 2D/3D FEM model, but this has been implemented in very few instances in FSI, such as the work of Brazilevs et al. [19, 20]. Figure 1.5 summarizes the available models for structural-dynamic modeling of a wind-turbine blade only. For details regarding the wide range of aerodynamic and structural-dynamic models for wind turbines, refer to [37]. The methods to couple the aerodynamic and structural parts is described next.

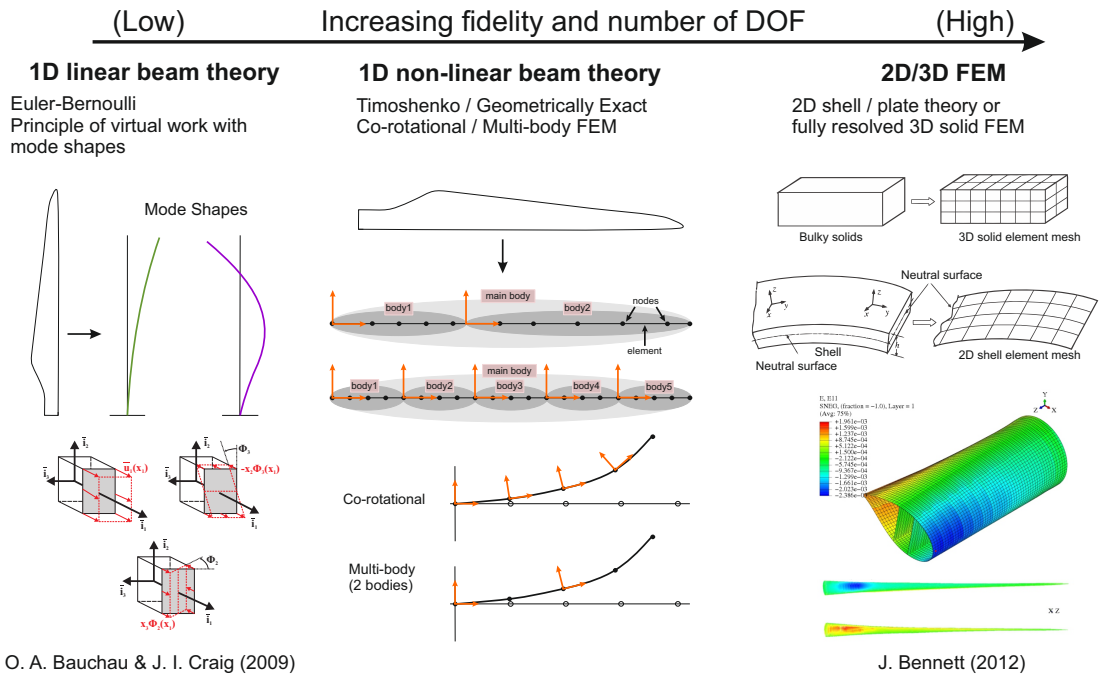


**Figure 1.5:** Structural-dynamic modeling for a wind-turbine blade with increasing level of fidelity. Retrieved from [38], [39] and [40].

### Coupling Methods and Terminology

FSI problems can be solved by the monolithic or partitioned approaches. In the monolithic approach, the equations governing the fluid flow and the structural displacement are solved simultaneously with a single solver. The monolithic approach is advantageous in terms of stability because the mutual influence from the fluid and structural parts are taken into account [41]. Examples of monolithic approaches are found in aero-elastic codes such as FLEX5 (Runge-Kutta-Nyström, see Hansen [35]) and HAWC2 (Newmark algorithm, see Krenk [42]). However, a code needs to be developed incorporating both physical domains to allow a single solver to be used. This limitation can be undesirable for a number of reasons, such as when software modularity needs to be maintained, or the mathematical models and methods within the fluid and structural parts require frequent or occasional updating.

In contrast, the equations governing fluid flow and structural displacement in the partitioned approach are solved separately using two distinct solvers. Solving the equations

from each domain separately means that the flow solution does not change while the solution of the structural part is being updated and vice versa. Each physical domain is kept independent, allowing different and more efficient solvers to be used that have been specifically developed for each physical domain. This advantage allows for existing computational codes to be used for each part of the FSI problem. Partitioned simulations, however, are susceptible to stability and accuracy issues, because their sequentially staggered approach creates artificial energy at the fluid-structure interface. Fortunately, the stability and accuracy issues can be controlled using an appropriate coupling algorithm.

The coupling algorithms in the partitioned case can be either *loosely* (also known as *weakly*) or *strongly coupled*. Loosely coupled schemes require only one evaluation per time step and thus are appealing in terms of computationally efficiency. Strongly-coupled schemes may have the same staggered solution algorithm as loosely-coupled algorithms, but differ in that they perform sub-iterations at each time step. Loosely-coupled algorithms are mostly to blame for numerical instability and inaccuracies in partitioned methods, since they violate energy conservation principles. For this reason, sub-iterations are performed in a strongly-coupled scheme until convergence or a suitable criterion on energy has been met. Nevertheless, numerical instabilities such as the '*added mass effect*' [43] still arise despite the strong coupling. Although a monolithic scheme is considered as a form of strong-coupling [43, 44], important mathematical properties of the fluid and structural subsystems are often ignored to allow a sole solver and achieve the strong coupling.

There also exists multi-rate methods [45] that are designed to solve systems of ordinary differential equations consisting of subsystems with different timescales. The purpose of multi-rate methods are to reduce the integration time by using larger step-sizes for the variables in a system that behave slowly compared to the system with fast variables. Multi-rate methods could be classified in the partitioned approach category, since each of the systems can have their own distinct solver. However, the multi-rate approach differs from loose- and strong-coupling in that an interpolation step is required to transfer information from the system with larger time-step to the system with smaller time-step. When the time-step in a multi-rate approach is set to be the same for all systems, then the multi-rate solver will behave similarly to loose-coupling because the interpolation step is no longer used. Appendix A contains an example application of the multi-rate approach on an analytical test problem.

### Strong- and Loose-Coupling in Wind Energy

Examples of strong coupling are found in [19], [20], [33] and [46]. In Brazilevs et al. [19], air flow is modeled using a residual-based variational multiscale formulation (RB-VMS) [47] and a rotation-free Kirchoff-Love shell formulation together with the bending strip method to model the blade structure made of composite materials. The coupled FSI equations are advanced in time using the Generalized-alpha method and solved in a 'block-iterative' scheme. Within each time-step, the coupled equations are solved using an inexact Newton approach. For every Newton iteration, three steps are performed which update the fluid and structural solutions, as well as the mesh motion in the fluid domain. This three-step iteration is repeated until convergence is achieved. According to the authors, the block iterative approach is suitable for their FSI simulation due to the high structural mass of the National Renewable Energy Laboratory (NREL) 5 MW wind-turbine blades.

Brazilevs et al. [19] only simulated the rotor and managed to extend their work to include the tower and nacelle in [20], thus simulating the "full machine". Hsu and Brazilevs [20] performed a fully coupled, 3D FSI simulation using a low-order-finite-element-based ALE-VMS technique to model the aerodynamics and the same method as in [19] for the structural. The ALE-VMS method is a moving-domain extension of the RBVMS formulation used in [19]. The time integration of the FSI equations and coupling are identical to Brazilevs et al. [19]. The right side of Figure 1.4 depicts the meshing implementation and simulation of the wind turbine from [20].

Branlard et al. [33] coupled a vortex code called Omnivor [48] to the aero-elastic code HAWC2 using strong coupling. Turbulent simulations in [33] were carried out under different shear conditions. Boorsma, Hartvelt, and Orsi [46] coupled the free vortex wake code AWSM [36] to the FOCUS-Phatas simulation software [49], which solves the structural dynamics of a wind turbine using a FEM approach. Both the AVATAR [34] and INNWIND turbine have been modeled for a variety of load cases using the aero-elastic code.

Loose coupling techniques are employed in [21, 22, 23, 50, 51]. Kim et al. [21] analyzed the effect of blade flexibility on the aerodynamic noise using FSI. The FSI code consisted of the Unsteady Vortex Lattice Method for the aerodynamic analysis and the Nonlinear Composite Beam Theory developed by Hodges [52] for the structural. Time integration was performed using a second-order backward Euler method. The authors state that a "loosely coupled analysis is carried out" in their pre-convergence procedure. Further information regarding the coupling technique and time integration were not given. The schematic shown in Figure 1 of their article contains the text "Loosely coupled" between the aerodynamic and structural parts.

Yu and Kwon [23] applied two loose-coupling methodologies using a CFD-CSD approach to predict HAWT rotor performance. The two methodologies consist of a static-coupling approach and the delta-airload loose-coupling methodology. The static approach involved a blade-alone configuration, neglected gravitational loads and rotor-shaft tilt, and is suited for steady axial flows only. These limitations were not present in the delta-airload methodology, thus allowing unsteady time-accurate coupled calculations. In the delta-airload method, the blade aerodynamic loads and the blade elastic deformation are exchanged only once per rotor revolution on a periodic basis. Initially, BEM is used in the computational structural dynamics (CSD) solver to obtain converged deformation data, which is then passed to the CFD solver. At subsequent steps, an iterative coupling procedure is applied until the BEM aerodynamic loads remain unchanged between successive iterations, allowing the blade response to depend only on the CFD loads. The CFD-CSD approach was applied to study axial flows [23], yaw and shear [22], and for rotor design [53].

Reference [50] describes an actuator line (AL) code composed of the finite volume CFD code EllipSys3D and the aero-elastic code FLEX5 using loose coupling (AL-FLEX5). Aero-elastic computations for wake studies in wind farms are described in [54]. Section 2.4.3 contains results from an AL-FLEX5 simulation for a steady wind of 8 m/s.

Saverin et al. [51] applied loose coupling between a lifting line free vortex wake code for the aerodynamic model, with the structural solver BeamDyn [55] based on geometrically exact beam theory. Aero-servo-elastic simulations were carried-out using the DTU 10MW [56] wind turbine. More examples of vortex codes coupled with structural dynamics codes are found in [31, 32, 57], but whether the coupling is loose or strong is not completely clear.

In Chapter 2, a 3D viscous-inviscid interaction (VII) method, MIRAS (Method for Interactive Rotor Aerodynamic Simulations), has been coupled to the structural dynamics model used in FLEX5. FLEX5 was chosen for the structural dynamics because of simplicity, speed, and access to the main developer for guidance. The coupling of MIRAS with HAWC2 is planned for the future. The aerodynamic tool, MIRAS, differs from [21, 31, 32, 33, 46, 50, 51, 57] in that the blade geometry is represented in a 3D manner and the viscous effects on the blade surface are taken into account using an integral boundary layer solver. A variety of test cases are provided to illustrate the versatility of MIRAS-FLEX and how the results compare with other standardized codes. Chapter 2 begins with a description of the geometry in MIRAS and FLEX5 in section 2.2. The two coupling methodologies and corresponding simulation results are shown in sections 2.3 and 2.4. Conclusions are given in section 2.5.

### 1.2.2 Surrogate Modeling in Wind Energy

Wind-turbine blade design involves many disciplines in engineering and several methods have been proposed to determine optimum designs. For blade aerodynamic design, methods range from simplistic methods using analytical expressions, see e.g. [58, 59], to sophisticated optimization problems that incorporate other disciplines in the design process [60, 61]. The majority of blade design problems in the literature implement the BEM method, while others use vortex-based [62, 63] or CFD methods [64].

To mitigate the computational time of wind-turbine design problems, researchers have used surrogate models, e.g. response surface models (RSMs), Kriging and artificial neural networks (ANN). Lee et al. [65] used RSM to reduce the calculation time of a complex two-step multi-objective optimization problem for blade design. RSMs were particularly useful in [66] and [67], where expensive numerical computations of the Navier-Stokes equations were used to design wind-turbine airfoil profiles. Similarly, Han et al. [68] designed wind-turbine airfoils using CFD, but Kriging was the preferred surrogate model. ANN was used as the surrogate model together with CFD in [69] to design wind-turbine airfoils as well.

Chapter 3 describes an initial effort to mitigate the computational time when using surrogate optimization with VII tool for wind-turbine rotor design. The aerodynamic tool used in the present work is the 3D VII method, MIRAS. Only the simplified case of a small model wind-turbine rotor is considered in Chapter 3. In Chapter 5, the optimization method is applied and tested for large wind-turbine blade design with fluid-structure interaction.

Chapter 3 is organized as follows: section 3.2 describes the surrogate-optimization method, section 3.3 describes the basic properties of the model rotor and its design using the inverse-design and surrogate-optimization methodologies, and finally section 3.4 gives the conclusions.

### 1.2.3 Structural Design in Wind Energy

Chapter 4 describes the structural design and loads component of the rotor design framework from Chapter 5. As noted by Ning [70], a blade design based purely on aerodynamic optimization gives multiple solutions that produce the same AEP, but with different masses. To reduce the cost of energy (COE) as much as possible, both the aerodynamic and structural characteristics of the rotor must be considered and should be optimized

simultaneously.

A simple optimization tool to design the internal structure of large wind turbine blades has therefore been developed. The tool uses a combination of classical laminate theory using a shear flow approach to compute blade structural properties (PreComp [71]), a finite-element code to compute the blade coupled mode shapes (BModes [72]), Euler-Bernoulli beam theory to compute blade deflections and strains [35], and the aero-elastic code FLEX5 [25] to compute the design load cases (DLCs). A brief literature review of structural design codes is provided next.

An open-source software in MATLAB, called Co-Blade, was developed by Sale [73] for the structural analysis and design of composite blades for wind and hydro-kinetic turbines. Co-Blade was developed to assist designers in the preliminary design stage to rapidly evaluate different composite layups and to study their effects on composite blade properties as well as material strains and stresses. The methodology used within Co-Blade to compute blade structural properties and to perform structural analysis is similar to the one presented in this chapter (i.e. classical laminate theory with shear-flow and Euler-Bernoulli beam theory). For a given external blade geometry and only one static design load, Co-Blade determines an optimal composite layup which minimizes the blade mass while simultaneously satisfying constraints on maximum strain and stress, buckling, deflection and placement of blade natural frequencies.

Hu, Park, and Choi [74] developed a structural optimization procedure for reducing material cost and weight of a composite 2 MW wind-turbine blade. Constraints on stress ratio, tip deflection, fatigue life and laminate layup requirements are imposed. The stress ratio and tip deflection are evaluated under extreme gust loads, while the fatigue life is evaluated under a stochastic normal wind load. The stress result from the time-varying stochastic wind is converted to histograms of mean and amplitude of maximum stress ratio using the rain-flow counting algorithm. Miner's rule is employed to predict the fatigue life. Structural responses are analyzed by building a finite element model of the blade and using the finite element analysis software package SAMCEF. An evolutionary algorithm is employed as the optimizer to determine the optimal layup using material type, thickness and fibre angle as the design variables.

A structural optimization framework for wind-turbine rotor blades was developed by Bottasso et al. [75] using multi-level sectional/multi-body/3D-FEM analysis. The multi-level design optimization consists of a coarse and a fine level, where the coarse level involves an aero-servo-elastic multi-body code for load calculation and a 2D finite-element-method (FEM) cross-sectional model for stress and strain analysis. The fine level involves a 3D FEM model used for refinement of the coarse-level solution. The merit function of the optimization problem is the total mass of the blade. Structural design variables include the thicknesses of the shear webs, upper and lower spar caps, external blade shell, and skin core. The constrained optimization is performed using the sequential quadratic programming (SQP) method implemented in the *fmincon* routine of the MATLAB software. The methodology is applied to a Class-IIIA 2MW HAWT with a 45 m rotor radius.

Although structural optimization tools have already been developed in the past, e.g. [73], [74] and [75], the motivation for its development is to integrate the tool with a rotor optimization code from [3] (i.e. Chapter 3) using a higher-fidelity aero-elastic model [1] (i.e. Chapter 2). PreComp [71] and BModes [72] were selected for the structural design because both PreComp and BModes run in one or two seconds of CPU time. PreComp and BModes run very quickly and are ideal for optimization problems,

since the structural prediction tools have to run hundreds or even thousands of times to find the optimum structural layup. More accurate structural prediction tools such as BECAS [76], VABS [77], or any other 2D or 3D FEM package requires a mesh and runs significantly slower. Since the structural design tool to be presented in Chapter 4 is used at each iteration of an upper-level optimization of the exterior blade geometry in the rotor design framework, the computational speed of the structural optimization is particularly important.

In Chapter 4, the stand-alone version of the structural design code will be presented. The structural design code combined with MIRAS-FLEX for aero-structural optimization is presented in Chapter 5. The methods, results and conclusions are described in sections 4.2, 4.5, and 4.6, respectively.

### 1.2.4 Rotor Design in Wind Energy

The design of a wind-turbine rotor involves many disciplines including aerodynamics, structural mechanics, control systems, and acoustics. The amount of literature in rotor design found in one and all combinations of the involved disciplines is considerable. The literature review given in this section with respect to wind-turbine rotor design is designed to provide a glimpse of the field and a clearer understanding of where the contributions from this thesis take part. For a more comprehensive literature review, the reader is referred to Chehouri et al. [78]. The following literature review is organized chronologically to some extent by publication date. In the past, blade plan-form design was performed using simple analytical expressions based on wind-turbine rotor aerodynamics only, see e.g. [58] and [59]. The literature review presented herein consists of more recent blade design problems solved using numerical modeling tools and optimization algorithms.

Xudong [79] developed an aero-elastic model using a method identical to the one described in section 1.3.4. However, only 11 DOFs as opposed to 20-28 DOFs available in FLEX5 are used to describe a three-bladed wind turbine. Refer to section 1.3.4 for details. The 11 DOF code was validated with the aero-elastic code FLEX4 [25] and experiments from the MEXICO experiment [80]. The objective of the design optimization was the COE consisting of the AEP and the cost of the rotor only. The variables are the chord, twist and relative thickness distribution, while constraints are boundary limits for the design variables as well as maximum limits on rotor thrust and shaft torque. The MATLAB function *fmincon* was used to perform the optimization on three baseline rotors: MEXICO 25 kW, Tjaereborg 2 MW, and NREL 5 MW.

Yu, Kwon, and Kwon [53] optimized the NREL Phase VI rotor and the NREL 5 MW reference rotor using a 3D coupled CFD and CSD solver. The airfoil shape at various sections of the blade is optimized by using the sectional flow conditions from the CFD-CSD solver and a PARSEC shape function. The authors argue that the improvement in the aerodynamic performance through blade planform optimization alone, e.g. in [79] and [81], is expected to be limited. As a result, they choose the design variables in the PARSEC shape function over a set of blade airfoil sections to design the blade. The objective function is to achieve the maximum lift-over-drag ratio over each one of the sections.

Maki, Sbragio and Vlahopoulos [82] developed a multi-level system design algorithm for wind turbines. The COE comprises the overall system level objective, while performance improvements are made for two technical design disciplines at the same time. The two technical disciplines are the optimal design of the blade geometry for maximum AEP

and the structural design of the blade for minimum root-bending moment. The technical disciplines are computed using the NREL tools HARP_Opt, WT_Perf, PreComp, Modes, IECWind and FAST. A metamodel, specifically Kriging, is used to link the design variables with the performance metrics associated with the blade geometry design. The rotor diameter, rotational speed, maximum rated power, hub height, dimensions of the inner structure, and the geometrical distribution of thickness, twist angle and chord of the blade comprise the overall set of design variables.

Ning, Damiani, and Moriarty [70, 83] performed a study not to demonstrate a specific methodology or to present optimized designs, but rather to understand how different choices in the optimization problem and model choices impact the quality of the solutions. Primarily, the goal was to better understand the appropriateness of various commonly used optimization objectives. Their framework is comprised of five components (details given in parentheses): 1) rotor aerodynamic analysis (BEM method), 2) rotor structural analysis (finite element analysis, classical laminate theory, and simplified buckling and fatigue estimations), 3) cost model (NREL Wind Turbine Design Cost and Scaling Model [84]), 4) reference model (NREL 5 MW), and 5) an optimization strategy (MATLAB's *fmincon*). The design variables are the chord, twist, spar-cap thickness, tip-speed ratio, rotor diameter, and machine rating. Results from using different metrics for the objective, e.g. AEP, mass/AEP, AEP-first-mass-second, and mass-first-AEP-second, are compared in terms of COE. The COE was reasoned as the most appropriate metric from the set. The authors encourage minimization of COE using a high-fidelity cost model and in the presence of uncertainty to create robust turbine designs.

Rotor design using chord, twist, and structural design variables, together with airfoil geometry at five stations along the blade span was performed by Bottasso [85]. Preassumed airfoil shapes are commonly used in industry in a typical blade design, but this approach hinders the full exploration of the design space. By including airfoil shapes as design variables, a truly free-form optimization of rotor blades can be achieved. All variables consist of control points that define a series of Bézier curves, while using constraints on geometry, tip speed, resonance avoidance, and stress to ensure realistic blade solutions. BEM and XFOIL were used for the aerodynamic analyses, while Euler-Bernoulli and anisotropic beam theory were used for the structural design. The objective was to minimize the COE for a 2 MW wind turbine. Significant improvements in COE, AEP, $C_P$ and blade weight were obtained using the proposed framework.

A 3D multi-objective optimization was performed by the author of the present thesis, see [86]. A Pareto surface representing the optimal trade-off between the AEP, blade mass, and flap-wise blade root-bending moment was found using the NREL 5 MW as baseline. The advantages of constructing a Pareto front as opposed to optimizing for a single solution is that the designer can easily study trade-offs in the design objectives. For example, a design with a large AEP will suffer from a larger blade mass and root-bending moment, while another design with smaller AEP will have improvements on the other two objectives. The Pareto front provides this information. Small Wind Turbine Rotor Design Code (SWRDC) was later developed by the author to allow the simultaneous optimization of AEP or $C_P$, blade mass, starting time, and noise [87].

Zahle et al. [88] presented an integrated multi-disciplinary wind turbine optimization framework using state-of-the-art aero-elastic and structural tools: HAWC2, HawcStab2 [89], and BECAS. The optimization framework, called HawtOpt2, uses OpenMDAO [90] to handle the definition of the optimization problem, work flow, data flow, and parallelization of simulation cases. The optimization algorithm used is the open source

gradient-based interior point optimizer IPOPT [91]. HawtOpt2 was used to design an aero-elastically tailored 10 MW wind turbine rotor using the DTU 10MW as the reference.

Today, the advancements in computing capabilities have permitted solution of the most sophisticated numerical optimization problems for blade design [60, 61, 88]. But despite the advances in computing techniques in the recent years, the majority of blade design problems still rely on aero-elastic codes that use BEM approaches to model the rotor aerodynamics. With the exception of section 5.4, Chapter 5 describes an approach to wind-turbine rotor design by incorporating the higher-fidelity free-wake panel aero-elastic coupling code MIRAS-FLEX [1].

The work objectives of Chapter 5 were:

1. To develop an efficient optimization framework for wind-turbine blade design using a high-fidelity aero-elastic model;
2. To create a preliminary design of a 5 MW wind-turbine blade using the developed design framework.

First, section 5.2 describes the methodology of the rotor design framework. The results and conclusions using MIRAS-FLEX is given in section 5.3. Using almost the same methodology but with FLEX5 instead MIRAS-FLEX, the design results for the offshore wind turbine in China (OffWindChina 5 MW) is described in section 5.4.

### 1.2.5 Scope of Thesis

The vast majority of all rotor designs (see detailed literature review in section 1.2.4) have consistently used the BEM technique for the aerodynamic design. In this thesis, instead of BEM, a more advanced viscous-inviscid solver coupled with the elastic model of FLEX5 is utilized. The implications of using a more advanced aerodynamic code such as MIRAS is that the computational cost is much greater compared to the BEM method, making rotor design especially difficult. The considerable computational cost is addressed by using a surrogate-modeling approach, which is applied to design a model wind-turbine rotor and also a large-scale rotor using fluid-structure interaction.

The present thesis develops a fluid-structure coupling technique to couple the unsteady viscous-inviscid solver for horizontal-axis wind turbine aerodynamics, MIRAS, with the aero-elastic code FLEX5 (Chapter 2), and to develop a framework using the new code to design wind-turbine rotors (Chapters 3 and 5). The thesis work is novel in both the development of the new fluid-structure-interaction code and the framework for wind-turbine rotor design.

In the following section of Chapter 1, the codes used in the project will be described to prepare the reader for the remaining chapters. Chapter 2 describes the novel fluid-structure interaction code composed of the 3D viscous-inviscid solver, MIRAS, and the structural dynamics model of FLEX5. Chapter 3 discusses the framework and optimization method for wind-turbine blade design using a model wind-turbine rotor as a validation case. Chapter 4 outlines the structural design code necessary for large-scale wind-turbine rotor design. Chapter 5 describes the application of the combined implementation of the novel fluid-structure interaction code, rotor design framework, and structural design code to the design of a large-scale wind-turbine rotor. Lastly, Chapter 6 provides the conclusions regarding the thesis project.

## 1.3 Participating Codes

### 1.3.1 Overview

This section provides a description of the relevant codes used in the thesis work, which are Q$^3$UIC, MIRAS, FLEX5, surrogate-modeling code, and three codes from NREL. Q$^3$UIC, MIRAS, and FLEX5 are written in the Fortran programming language and have been developed at the Fluid Mechanics Section, Technical University of Denmark. The Q$^3$UIC, MIRAS, and FLEX5 codes are described in sections 1.3.2, 1.3.3, and 1.3.4 respectively. The surrogate-modeling code was developed by Forrester [92] in the MATLAB programming language and modified by the author of the current thesis for wind-turbine rotor design. PreComp, BModes and the wind turbine cost and scaling model are developed by NREL. PreComp and BModes are written in Fortran, while the cost and scaling model is written in Python.

### 1.3.2 Q$^3$UIC

The Q$^3$UIC code is a two-dimensional (2D) and quasi-3D, steady and unsteady, viscous-inviscid interaction (VII) code used for simulating the aerodynamic behavior of airfoils. Q$^3$UIC was developed by Ramos-García et al. [93] and consists of two parts: 1) solving the inviscid part of the solution using 2D panel method, and 2) solving the integral form of the laminar and turbulent boundary layer equations for the viscous part. The viscous part is modeled in the boundary layer region surrounding the airfoil's surface, while the flow outside is assumed inviscid, and can be modeled using potential flow theory. The boundary layer equations are extended to include 3D rotational effects, which gives Q$^3$UIC a quasi-3D capability.

The equations governing the VII technique represent an alternative representation of the Navier-Stokes equations. Instead of solving the Navier-Stokes directly, the simplified VII approach gives comparable accuracy but at a much lower computational cost. Q$^3$UIC is among many codes that are based on VII. The XFOIL code by Drela [94] as well as RFOIL [95] developed at the Delft University of Technology are well-known examples. In Q$^3$UIC, the integral form of the boundary layer $r$– and $\theta$–momentum equations with extension for 3D rotational effects due to Coriolis and centrifugal forces are:

$$\frac{\partial \theta_1}{\partial s} = -\frac{1}{u_\mathrm{e}^2}\frac{\partial}{\partial t}(u_\mathrm{e}\delta_1^*) - \frac{\theta_1}{u_\mathrm{e}}\frac{\partial u_\mathrm{e}}{\partial s}(2+H) + \frac{C_f}{2} + s_\mathrm{w}p_\mathrm{r}\frac{2R_O l}{u_\mathrm{e}c}\delta_2^* \tag{1.4}$$

$$\begin{aligned}\frac{\partial \theta_2}{\partial s} = -\frac{1}{u_e}\frac{\partial \delta_2^*}{\partial t} - \frac{2\theta_2}{u_\mathrm{e}}\frac{\partial u_e}{\partial s} + \tan\beta_\mathrm{w}\frac{C_f}{2} - \frac{1}{u_\mathrm{e}}\frac{\partial u_\mathrm{e}}{\partial r}(2\delta_3+\delta) + \\ \frac{l}{c}\left(\theta_1 + \delta_1^* - \delta - \delta_3 + s_\mathrm{w}p_\mathrm{r}\frac{2R_O}{u_\mathrm{e}}(\delta-\delta_1^*)\right)\end{aligned} \tag{1.5}$$

where the $r$– and $\theta$–integral momentum boundary layer equations have been written in terms of the boundary layer edge velocity, $u_\mathrm{e}$, and the integral boundary layer parameters $\theta_1$, $\theta_2$, $\delta_1^*$, $\delta_2^*$, $\delta$, $\delta_3$, $H$, $C_f$, and $\beta_\mathrm{w}$. $C_f$ is the skin friction coefficient and $c$ is the local airfoil chord.

Thwaites' method is used to solve the boundary layer equations in the laminar flow region, while for the turbulent region the solution of Equations (1.4) and (1.5) is obtained using 3D turbulent closure relations for the streamwise and spanwise boundary layer

variables ($\delta_1^*$, $\delta_2^*$, $\delta_3$, $\theta_1$, $\theta_2$, and $C_f$). The reader is referred to [93] for the list of closure equations. Q$^3$UIC computations are performed for a given local airfoil geometry and the following non-dimensional parameters: Reynolds number, $Re$, rotation number $R_O$, local aspect ratio, $l$, and local angle of attack, $\alpha$. Therefore, the non-dimensional parameters $l$, ratio between chord length and radial position, and $R_O$, ratio between the rotational speed and relative velocity, are given inputs. The sign change of the Coriolis force in reverse flow regions is included through the sign function, $s_\mathrm{w}$. The variation in the shape factor parameter, $H$, is found from the kinetic energy shape parameter equation with a set of closure relations in the total system of equations.

The viscous and inviscid parts are strongly coupled through the *transpiration velocity* concept, see Figure 1.6. In the coupling, the transpiration velocity changes the boundary condition on the solid surface of the body by forcing a normal velocity at the wall. The transpiration velocity can be regarded as an outflow due to boundary layer growth, taking into account the viscous effect in the potential flow solver by pushing the streamlines outwards. A source distribution creating an outward flow equal to the transpiration velocity is introduced in the panel method for this purpose. Integrating the continuity equation across the boundary layer gives the following equation for the transpiration velocity [96]:

$$w_T = \frac{1}{\rho}\frac{\partial}{\partial s}(\rho u_\mathrm{e}\delta_1^*) \tag{1.6}$$

The solution to Equations (1.4) and (1.5) is determined by computing the Jacobian matrix of all the governing equations, which includes the integral momentum equations, the closure relations, the inviscid velocity equations, and the viscous-inviscid transpiration velocity function. As a result, a strong coupling between the viscous and inviscid parts is achieved and the flow around an airfoil up to and after stall can be obtained.

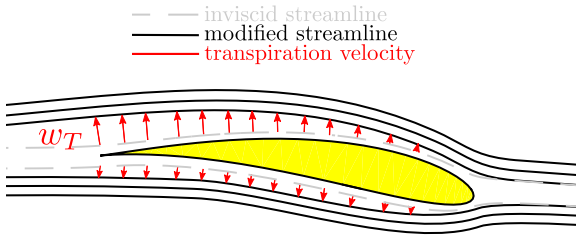


**Figure 1.6:** Transpiration velocity concept shown for an airfoil in Q$^3$UIC.

### 1.3.3 MIRAS

Method for Interactive Rotor Aerodynamic Simulations, MIRAS, is a 3D viscous-inviscid solver for horizontal-axis wind-turbine (HAWT) rotor computations. MIRAS was also developed by Ramos-García et al. [97] after Q$^3$UIC at DTU. The solver predicts the aerodynamic behavior of wind-turbine wakes and blades for steady and unsteady conditions, with or without viscous effects. Similarly as in Q$^3$UIC, the MIRAS code consists of inviscid and viscous parts. In contrast, the inviscid solver is not a 2D panel method but a 3D method using a surface distribution of quadrilateral sources and doublets. The inviscid part is coupled to the viscous part through a viscous boundary layer solver, namely the one used in Q$^3$UIC.

The inviscid solution given by the 3D panel method is modified using the transpiration velocity concept and strip-theory to take into account the viscous and rotational effects,

see Figure 1.7. The cross-sectional angle of attack is used as the coupling parameter between the inviscid and viscous parts. A free-wake model simulates the wake behind the wind-turbine rotor using vortex filaments that carry the vorticity shed by the blades trailing edges. Figure 1.8 depicts the free wake behind a wind-turbine rotor. These features give MIRAS a more detailed aerodynamic description than the BEM technique and at much lower computational cost than Navier-Stokes solvers. MIRAS was validated against experimental data from MEXICO under axial and yawed flow conditions as well as the CFD code EllipSys3D [97, 98, 99]. The governing equations for the inviscid solver as well as the inviscid-viscous coupling are briefly described next. Further details are available in [97].

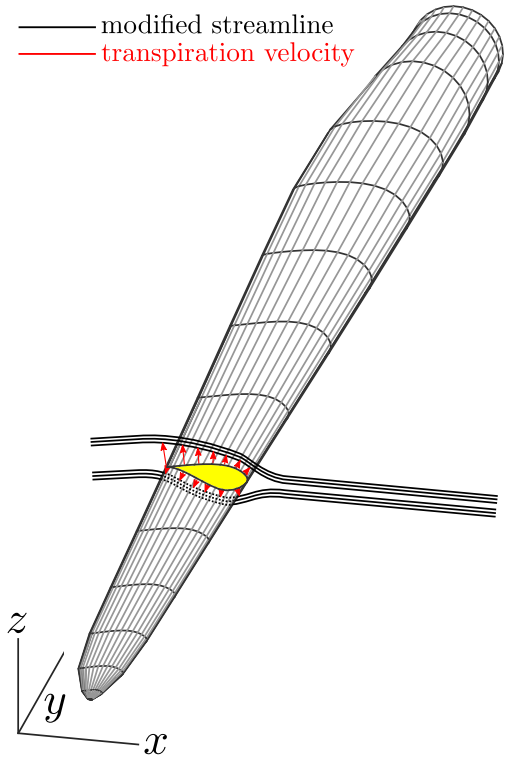


**Figure 1.7:** Three-dimensional panel method shown for a wind-turbine blade in MIRAS where the inviscid streamlines for one station is modified using the transpiration velocity from Q$^3$UIC.

### Governing Equations

For potential flow around a solid body with surface $S$, the velocity at a point $p$ in the flow domain can be expressed as a superposition of the undisturbed velocity, $U_\infty$, and the disturbed velocity created by the solid body, $U_p$:

$$U_I = U_\infty + U_p. \tag{1.7}$$

If the flow is incompressible, inviscid and irrotational, $U_p$ is:

$$U_p = -\nabla\phi \tag{1.8}$$

where $\phi$ is a potential function that satisfies the Laplace equation:

$$\nabla^2\phi = 0. \tag{1.9}$$

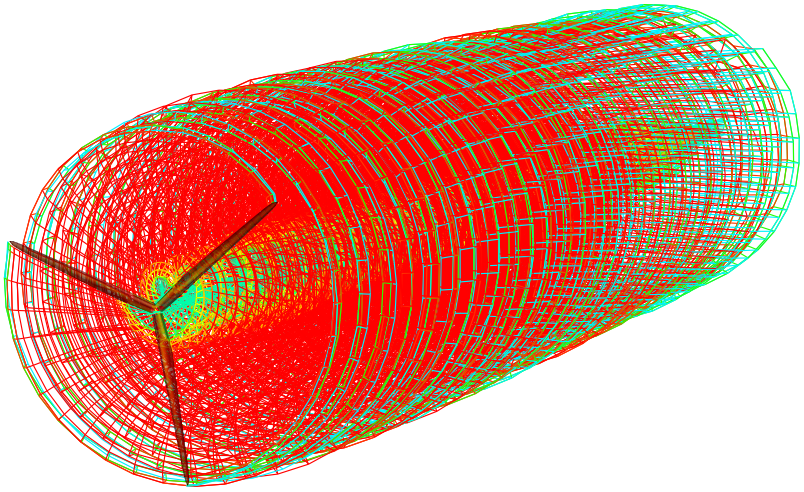

**Figure 1.8:** MIRAS simulation depicting the rotor and free wake under steady and uniform wind inflow conditions.

When the solid body with surface $S$ is impermeable, the normal component of the velocity is zero at the wall giving a Neumann condition of no penetration across the body:

$$\frac{\partial \phi}{\partial n} = \nabla \phi \cdot n = U_\infty \cdot n = 0 \tag{1.10}$$

where $n$ is the unit vector normal to the surface.

The problem is divided into two regions: the solid body and the downstream wake. The body is simulated by a distribution of quadrilateral surface dipoles, $\mu$, and quadrilateral sources, $\sigma$. The viscous effects inside the boundary layer are modeled using the transpiration velocity concept through the additional source distribution $\sigma_{wT}$. The transpiration velocity is computed by the boundary layer solver in Q$^3$UIC, see Equation (1.6). The first row of elements in the wake is simulated using quadrilateral panel dipoles, while further downstream the panels are converted into wake elements formed by straight line vortex filaments of strength $\Gamma$. The influences of the different singularities used to model the inviscid part of the problem are added giving a final expression for the induced velocity:

$$\begin{aligned} \nabla \Phi = -\frac{1}{4\pi} \int_{body} (\sigma + \sigma_{wT}) \nabla \left( \frac{1}{r} \right) + \frac{1}{4\pi} \int_{body} \mu \nabla \left[ \frac{\partial}{\partial n} \left( \frac{1}{r} \right) \right] \\ + \frac{1}{4\pi} \int_{wake} \Gamma \nabla \left[ \frac{\partial}{\partial n} \left( \frac{1}{r} \right) \right] - \nabla \Phi_\infty \end{aligned} \tag{1.11}$$

To meet the Kutta condition of zero loading at the trailing edge, at each time step a quadrilateral panel with a doublet distribution is created as the first wake panel for each of the span-wise stations. The strength of these panels, $\Gamma_{fst}$, is the difference between the upper and lower trailing edge quadrilateral doublets:

$$\Gamma_{fst} = \mu_{upper} - \mu_{lower} \tag{1.12}$$

The first wake panel is convected downstream from the trailing edge with a velocity equal to 30% of the local undisturbed velocity [100]. Downstream of the first row of wake panels

the quadrilateral doublets are transformed into vortex filaments and clustered into vortex elements. The strength of the vortex filaments remain constant in time with their motion in 3-D space represented by Lagrangian fluid markers placed at the end points, which are convected downstream with the velocity **u**:

$$\mathbf{u} = \mathbf{u}_{\infty} + \mathbf{u}_{body} + \mathbf{u}_{wake} \tag{1.13}$$

where $\mathbf{u}_{\infty}$ is the freestream velocity, $\mathbf{u}_{body}$ is the influence of the solid body and $\mathbf{u}_{wake}$ is the induction created by the other wake elements. The velocity induced by the wake vortex filaments is determined by applying Biot-Savart's law. Following Leishman et al. [101], Biot-Savart's law is modified to remove the singularity when $r$ approaches zero by applying a viscous core to all the released vortex filaments during the time-updating procedure. An approximation to the viscous diffusion, vortex core growth and vortex straining is included by modifying Biot-Savart's law as:

$$\mathbf{u}_{wake} = K\frac{\Gamma}{4\pi}\frac{\mathbf{dl}\times\mathbf{r}}{|\mathbf{r}|^3} \tag{1.14}$$

where **dl** is a vector whose magnitude is the length of the differential element of the vortex filament and $K$ is the kernel parameter, which uses the Scully profile for the vortex filament viscous core [102]. The core growth rate is included using the Squire model and the turbulent eddy viscosity parameter [103]. Lastly, the vortex straining model is implemented to include the change in vortex filament radius due to its variations in length, stretching or squeezing [104].

### Hybrid Wake Model

MIRAS contains a hybrid wake feature [105, 106] that splits the wake into a near and a far wake. The near wake is formed by a vortex sheet released at the blade trailing edges. Further downstream, the wake can be modeled using tip and root vortices [105] or using a particle mesh [106]. The transition point between the near and the far wake is determined using a user-specified number of wake revolutions.

As described at the beginning of section 1.3.3, the wake behind a wind-turbine rotor is simulated using vortex filaments. The vortex filaments are constructed using discrete vortices where the trajectory of the discrete vortices is governed by Biot-Savart's interaction law. A direct calculation of the interaction between all the discrete vortices of the flow have a computational scaling of $N^2$, where $N$ is the number of discrete vortex elements. The computational scaling of $N^2$ is considerable and must be reduced to make the interaction calculation more efficient. The first strategy to reduce the number of vortex elements, $N$, by grouping the elements into fewer data points. A second strategy uses a particle-mesh approach, where the vortex elements are translated into particles and projected onto a uniform mesh. Fast recursive algorithms such as the Fast Fourier Transform (FFT) are then used to efficiently compute the particle interactions, which in this case consists of solving the Poisson equation for free-space boundary conditions [107, 108]. The tip and root vortex model uses the first strategy, while the particle mesh evidently uses the second. The hybrid wake enables a significant reduction in computational cost for both the tip/root vortex and particle-mesh models, while at the same time maintain the correct wake induction in the rotor plane.

For the tip/root vortex model, the filaments that make up the vortex sheet in the near wake become clustered into tip and root vortices in the far wake. Figure 1.9 depicts

the hybrid wake where the near wake is a vortex sheet and the far wake is a tip vortex. Equation (1.13), which represents the motion of the filaments with velocity $\underline{\mathbf{u}}$, is modified as follows:

$$\mathbf{u} = \mathbf{u}_\infty + \mathbf{u}_{body} + \mathbf{u}_{vortex-sheet} + \mathbf{u}_{vortex-root-tip} \tag{1.15}$$

where $\mathbf{u}_{vortex-sheet}$ is the induction created by the near wake elements and $\mathbf{u}_{vortex-root-tip}$ is the induction created by the far wake root-tip vortex elements. The near and far wake elements form $\mathbf{u}_{wake}$ in Equation (1.13).

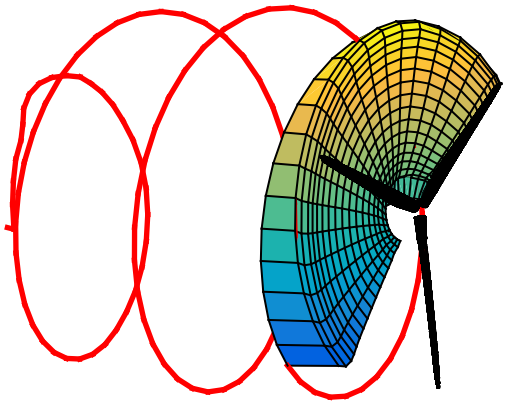

**Figure 1.9:** Illustration of the hybrid wake model. Near wake is a vortex sheet while the far wake is a tip vortex (red line). Root vortex not included in figure.

The alternative is to model the far wake using a particle mesh. Figure 1.10 depicts the flow past the NREL 5 MW rotor simulated with the hybrid filament-mesh method. The vortex sheet is depicted by a wire-frame and is composed of filaments whose interactions are calculated by a direct filament-filament calculation. The particle mesh is depicted by the iso-surface of the vorticity magnitude. The reader is referred to [106] for details on the approach.

### Aerodynamic Forces

The total velocity vector, $\underline{\mathbf{v}}$, is the sum of the kinematic velocity of the local reference system ($\mathbf{V_0} + \mathbf{\Omega} \times \mathbf{r}$) and the induced velocity $(u, v, w)$:

$$\mathbf{v} = [\mathbf{V_0} + \mathbf{\Omega} \times \mathbf{r}] + [u, v, w] \tag{1.16}$$

where $[u, v, w]$ is the inviscid perturbation velocity in panel coordinates calculated using a nodal interpolation of the quadrilateral doublets of strength, $\mu$:

$$u = -\frac{\partial \mu}{\partial l}, \tag{1.17}$$

$$v = -\frac{\partial \mu}{\partial m}, \tag{1.18}$$

$$w = \sigma = -(\mathbf{V_0} + \mathbf{\Omega} \times \mathbf{r}) \cdot \mathbf{n} \tag{1.19}$$

where $l$ and $m$ are the chord-wise and span-wise directions along the body surface, respectively, $\sigma$ is the normal inviscid non-disturbed velocity at the center of each quadrilateral

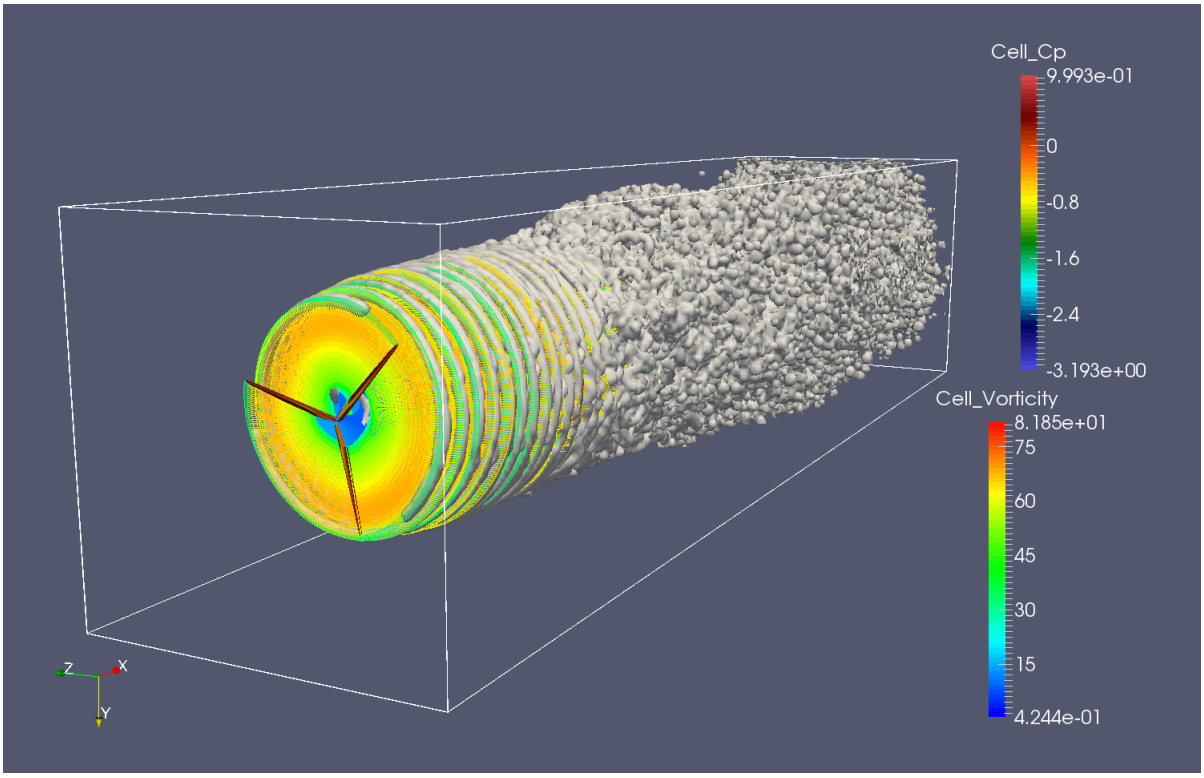


**Figure 1.10:** Illustration of the hybrid wake using the particle mesh model. Near wake is a vortex sheet depicted by a wire-frame, while the far wake is a composed of thousands of particles depicted by the iso-surface of the vorticity magnitude.

panel, and $\mathbf{n}$ is the normal unitary vector pointing out of the specific panel. The pressure on the body surface is obtained through the unsteady Bernoulli equation:

$$\frac{\partial \phi}{\partial t} + \frac{1}{2}|\mathbf{v}|^2 + \frac{1}{\rho}p = \frac{1}{\rho}p_{ref} + \frac{1}{2}|\mathbf{v}_{ref}|^2 \tag{1.20}$$

where $p_{ref}$ is the far-field reference pressure, $\mathbf{v}_{ref}$ is the reference velocity, which for the rotating case is:

$$\mathbf{v}_{ref} = -[\mathbf{V_0} + \mathbf{\Omega} \times \mathbf{r}] \tag{1.21}$$

and the variation of the potential in time, $\partial\phi/\partial t$ is assumed to be equal to the local time variation of the doublet distribution at each panel, $\partial\mu/\partial t$. The dimensionless surface pressure distribution, $C_p$, is then:

$$C_p = \frac{2(p - p_{ref})}{\rho|\mathbf{v}_{ref}^2|} = 1 - \frac{|\mathbf{v}|^2}{|\mathbf{v}_{ref}|^2} - \frac{2}{|\mathbf{v}_{ref}|^2}\frac{\partial \mu}{\partial t} \tag{1.22}$$

where $p$ is the local fluid pressure. The local force, $\mathbf{\Delta F}$, exerted on a panel with area $\mathbf{\Delta S}$ is:

$$\mathbf{\Delta F} = -C_p \left(\frac{1}{2}\rho|\mathbf{v}_{ref}|^2\right)\mathbf{\Delta S} \times \mathbf{n} \tag{1.23}$$

Total body normal and tangential forces are calculated by adding the values of the local panel force vector contributions, $\mathbf{\Delta F}$, in the global coordinate system.

### 1.3.4 FLEX5

FLEX5 is a computer program developed by Øye [25] to model the dynamic behavior of HAWTs operating in specified wind conditions such as simulated turbulent wind. The program runs in the time-domain producing time-series of loads and deflections. Aerodynamics are calculated using the BEM method with additional models important for unsteady and yaw and/or tilt conditions. Such models include the dynamic wake and dynamic stall models, see [109, 110, 111].

The structural behavior of the wind turbine is modeled using the principle of virtual work and carefully selected DOFs. Modal shape functions are used for the deflections of the blades and tower, while stiff bodies connected by flexible hinges model the nacelle, rotor shaft, and hub. FLEX was originally developed with 17-20 DOFs and a few years later upgraded to 28 DOFs. The version of FLEX with 17-20 DOFs is known as FLEX4, while the one with 28 DOFs is FLEX5. Six of the eight additional DOFs in FLEX5 describe the deformations of a flexible foundation, while the remaining two are used to include the second order bending mode of the tower in two directions.

#### Dynamic Model

The principle of virtual work is a method to build the mass matrix $\underline{\underline{M}}$, damping matrix, $\underline{\underline{C}}$, and stiffness matrix, $\underline{\underline{K}}$, for a discretized mechanical system:

$$\underline{\underline{M}}\underline{\ddot{x}} + \underline{\underline{C}}\underline{\dot{x}} + \underline{\underline{K}}\underline{x} = \underline{F}_g \tag{1.24}$$

where $\underline{F}_g$ is the generalized force vector associated with the external loads, e.g. aerodynamic loads. The mass, damping, and stiffness matrices are square and have the dimension $N_{dof} \times N_{dof}$, where $N_{dof}$ is the number of DOFs. The values in the vector $\underline{x}$, i.e. $x_i$, describe the deformation of the mechanical system and are known as the generalized coordinates. Each generalized coordinate is associated with a deflection shape that describes the deformation of the system. When the deflections, $\underline{x}$, and velocities, $\underline{\dot{x}}$, are known, (1.24) can be rewritten as:

$$\underline{\underline{M}}\underline{\ddot{x}} = \underline{F}_g - \underline{\underline{C}}\underline{\dot{x}} - \underline{\underline{K}}\underline{x} = \underline{f}(\dot{x}, \underline{x}, t) \tag{1.25}$$

where $\underline{f}(\dot{x}, \underline{x}, t)$ is usually non-linear arising from non-linear loads or from aerodynamic damping. The non-linear system can be solved for the acceleration, $\underline{\ddot{x}}$, at time $t^n = n\Delta t$, in the time-domain approach using Equation (1.25):

$$\underline{\ddot{x}} = \underline{\underline{M}}^{-1}\underline{f}(\dot{x}, \underline{x}, t) \tag{1.26}$$

A Runge-Kutta-Nyström (RKN) scheme estimates the velocities and positions at the next time-step and new loads are computed using the unsteady BEM method. Equation (1.26) is updated and a new time step can be performed. This process is repeated for a given time period. See [35] for details about the dynamic model in FLEX5. The FLEX5 coordinate system is provided in Figure 2.3 and the 28 DOFs are listed below:

DOF 1-6: Foundation top in $T_{sys}$

1. Translation $x$
2. Translation $z$
3. Rotation $y$
4. Translation $y$
5. Rotation $z$
6. Rotation $x$ (torsion)

DOF 7-10: Tower bending, top deflection in $T_{sys}$

7. 1st mode, translation $z$ + rotation $y$
8. 2nd mode, rotation $y$
9. 1st mode, translation $y$ + rotation $z$
10. 2nd mode, rotation $z$

DOF 11: Yaw, rotation $x$ in $K_{sys}$
DOF 12: Tilt, rotation $y$ in $K_{sys}$ and $N_{sys}$
DOF 13: Shaft rotation, rotation $z$ in $R_{1,sys}$
DOF 14-15: Shaft bending at $R_{1,sys}$

14. 1st mode, rotation $x$
15. 2nd mode, rotation $y$

DOF 16-20: Blade 1 deflection in $V_{1,sys}$

16. 1st flap mode $z$
17. 2nd flap mode $z$
18. 1st edge mode $y$
19. 2nd edge mode $y$

DOF 20-23: Blade 2 deflection in $V_{2,sys}$

20. 1st flap mode $z$
21. 2nd flap mode $z$
22. 1st edge mode $y$
23. 2nd edge mode $y$

DOF 24-27: Blade 3 deflection in $V_{3,sys}$

24. 1st flap mode $z$
25. 2nd flap mode $z$
26. 1st edge mode $y$
27. 2nd edge mode $y$

DOF 28: Shaft torsion, rotation $z$ in $R_{1,sys}$

### 1.3.5 Surrogate Modeling

The surrogate modeling code used in the PhD thesis is taken from [92]. For details how surrogate modeling is implemented in the wind-turbine rotor design framework, refer to Chapter 3. In the present section, only a brief explanation of surrogate modeling is given for the reader's comprehension.

What is surrogate modeling? Consider a photograph of a person's face, which is pixelated, and you had to determine his or her identity. Figure 1.11 illustrates the example, where a face is depicted with increasing quality from left to right. If you guessed the Mona Lisa based on a rough approximation of the full photograph (left of Fig. 1.11), your brain likely went through the process of 1) identifying key features of the photograph, and 2) constructing subconsciously a surrogate model of the full photograph to determine the identity of the person. In other words, the surrogate model substitutes all the small details of the person's face with information that is already known to us. For example, it is not necessary to resolve the threads of the person's hair to determine the person's identity. The hair threads are more easily seen on the second picture (right-side) of Figure 1.11 than on the first picture (left-side). The surrogate model in the human brain fills-in the hair threads subconsciously.

Surrogate models in engineering are educated guesses as to what an engineering func-

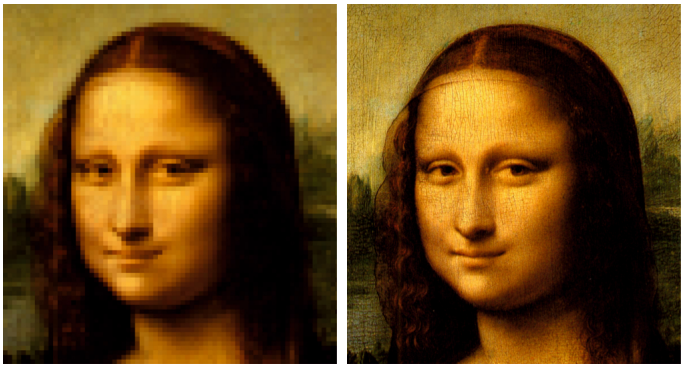

**Figure 1.11:** The face of Mona Lisa with increasing quality from left to right. It is not necessary to resolve every detail of the person's facial photograph (left) to determine his or her identity, since the human brain subconsciously constructs a surrogate model of the full photograph (right).

tion might look like based on a few key points in the design space. While the few points alone are not too informative, they become very useful if a surrogate model with an assumed shape is fitted onto the points. Additional assumptions such as derivatives and continuity at the points can be included so that the surrogate model provides a very good guess of what the entire design space looks like. Using surrogate modeling can therefore be a valuable method for optimization problems where the function is particularly expensive to evaluate. An expensive function in engineering can be a finite-element model to simulate how a product will perform under a given loading. For example, such a model of a car crash together with a surrogate model can be used to study which design parameters can be adjusted to improve the safety of the passengers. In the present PhD thesis, surrogate models are used to design large wind turbine blades using the computationally expensive MIRAS-FLEX code.

### 1.3.6 NREL PreComp and BModes

PreComp (Pre-processor for computing Composite blade structural properties) [71] is a Fortran code developed by NREL to provide span-wise structural properties for composite wind turbine blades, tower and drive-train shaft. PreComp computes these properties using classical laminate theory combined with a shear-flow approach. The structural properties include cross-sectional stiffness, inertia, and offsets of tension center, shear center, and center of mass. Cross-sectional stiffness properties include flap-torsion, lag-torsion, flap-lag, axial-torsion, flap-axial, and lag-axial stiffness. Some or all of these structural properties are used as inputs to modern aero-elastic codes to take into account the elastic behavior of the turbine components. PreComp is not finite-element based and therefore contains more limitations and assumptions. However, it computes the span-wise structural properties in a fraction of a second, making it ideal for optimization work. The analytical methodology of PreComp is possible due to the following assumptions: thin-walled sections and free warping. Other assumptions include straight blades (no curvature or sweep), negligible transverse shearing, no distortion within the plane of the cross-section, webs are normal to the chord, and the composite layup of a web is a single stack of laminas. Furthermore, the shear center computation in PreComp is approximate. To compute the shear center accurately, blades should be modeled as Timoshenko beams and the full 6-by-6 section stiffness matrix must be computed.

BModes [72] is a finite-element and Euler-Bernoulli beam theory based tool to compute the natural frequencies and coupled mode shapes of rotating and non-rotating beams, such as a turbine blade or tower. A coupled mode means that the natural mode of vibration of a beam contains coupled flexural, axial, and torsion motions. The finite-element method in BModes is based on 15 degree of freedom elements with three internal and two boundary nodes, see Figure 1.12. The 15 DOFs comprise 3 DOFs for torsion deflection and 4 DOFs each for axial, flap, and lag deflections. Both the blade and tower can have a tip attachment, such as an aerodynamic brake for the blade and nacelle-rotor subassemblies for the tower. BModes requires specification of rotor speed, blade geometry, and the blade span-wise structural properties as inputs. The structural properties are readily obtained from PreComp.

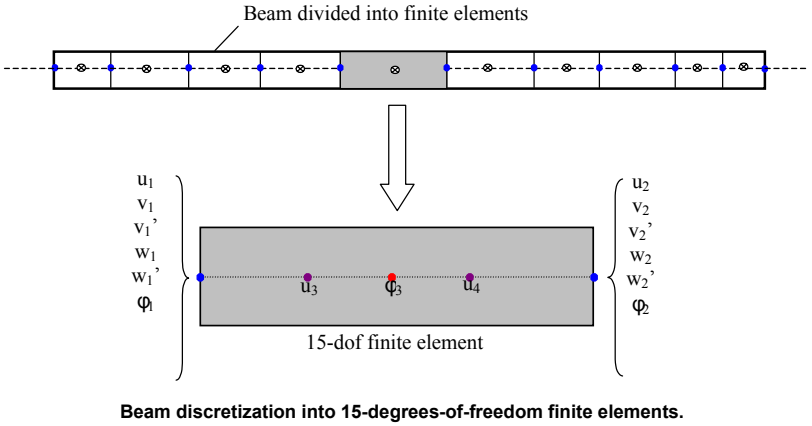


**Figure 1.12:** BModes element taken from [72].

Although there are other more accurate structural prediction tools available, such as BECAS [76], VABS [77], or any other 2D or 3D finite-element-method (FEM) package, PreComp and BModes were selected for the structural design component of the rotor design framework, see Chapters 4 and 5, because both PreComp and BModes run in one or two seconds. Structural prediction tools that run very quickly are ideal for optimization problems, since the prediction tools have to run hundreds or even thousands of times to find the optimum structural layup.

### 1.3.7 NREL Wind Turbine Cost and Scaling Model

NREL's National Wind Technology Center (NWTC) has developed a model for estimating the cost of wind-generated electricity from both land-based and offshore wind turbines. The model is referred to as the NREL Wind Turbine Design Cost and Scaling Model [84]. The cost estimates are projected based on turbine rating, rotor diameter, hub height, and other key turbine descriptors. Cost scaling functions have been developed for major components and subsystems. Figure 1.13 depicts such scaling functions for estimating blade cost. The purpose of the model is to evaluate the impact of a design change of a wind turbine on the system cost and performance. The system cost and performance is quantified using the levelized cost of energy (COE), which is calculated using a simplified formula:

$$\mathrm{COE} = \frac{\mathrm{FCR} \cdot (\mathrm{TCC} + \mathrm{BOS})}{\mathrm{AEP}} + \mathrm{AOE} \tag{1.27}$$

where FCR is fixed charge rate, TCC is turbine capital cost, BOS is balance of station, AOE is annual operating expenses, and AEP is annual energy production. The AOE includes operations and maintenance (O&M), land lease (LLC), and levelized replacement (LRC) costs.

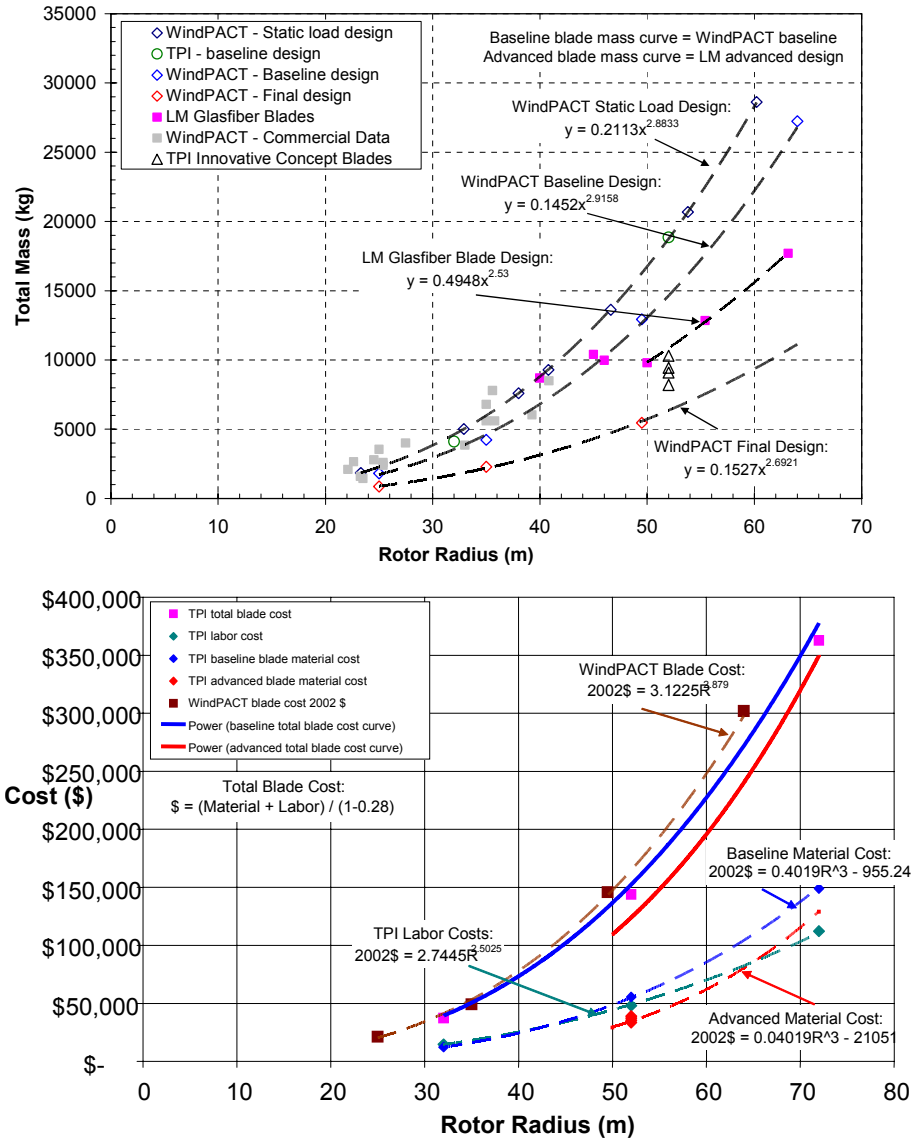


**Figure 1.13:** Blade mass (top) and cost (bottom) scaling relationships taken from [84].

As wind turbines are becoming more sophisticated and larger in size, it is not always evident whether such design changes have a positive overall impact on the COE. COE models, such as the one developed by the NWTC, have therefore become critical tools to designers and forecasters when projecting wind-turbine technology pathways. The NREL Wind Turbine Design Cost and Scaling Model has therefore been implemented in the rotor design framework, to determine the optimal wind-turbine design parameters that minimizes the COE as much as possible. All the underlying scaling functions and cost estimates in the model will not be described here, but are readily available from [84].

# Chapter 2

# Fluid-Structure Interaction

## 2.1 Introduction

This chapter is based on the work: 'Development of a fast fluid-structure coupling technique for wind turbine computations' [1] and 'Development of an aeroelastic code based on three-dimensional viscous-inviscid method for wind turbine computations' [2]. Chapter 2 begins with a description of the geometry in MIRAS and FLEX5 in section 2.2. The two coupling methodologies and corresponding simulation results are shown in sections 2.3 and 2.4. Conclusions are given in section 2.5.

## 2.2 Methodology: Coupling MIRAS and FLEX5

Coupling the panel-method free-wake MIRAS code with the elastic model in FLEX5 requires careful consideration of the distinct coordinate systems, blade numbering, and time-integration schemes. This section will describe the various steps followed to couple MIRAS with FLEX5. The first subsection will describe the MIRAS geometry, followed by the FLEX5 geometry in section 2.2.2. The coupled MIRAS and FLEX5 code will be hereafter referred to as *MIRAS-FLEX*.

### 2.2.1 MIRAS Geometry

MIRAS has a fixed, inertial, and Cartesian coordinate system centered at the rotor hub where the $x$-axis is aligned with the rotor shaft. Positive rotation is defined clockwise when viewing the rotor from the front. At time zero, the first blade, Blade 1, is aligned with the $y$-axis. The remaining blades, e.g. Blade 2 and Blade 3, are situated ahead of Blade 1. As shown on the left of Figure 2.1, Blade 3 leads Blade 2 and Blade 2 leads Blade 1. The blade numbering applies to any number of blades.

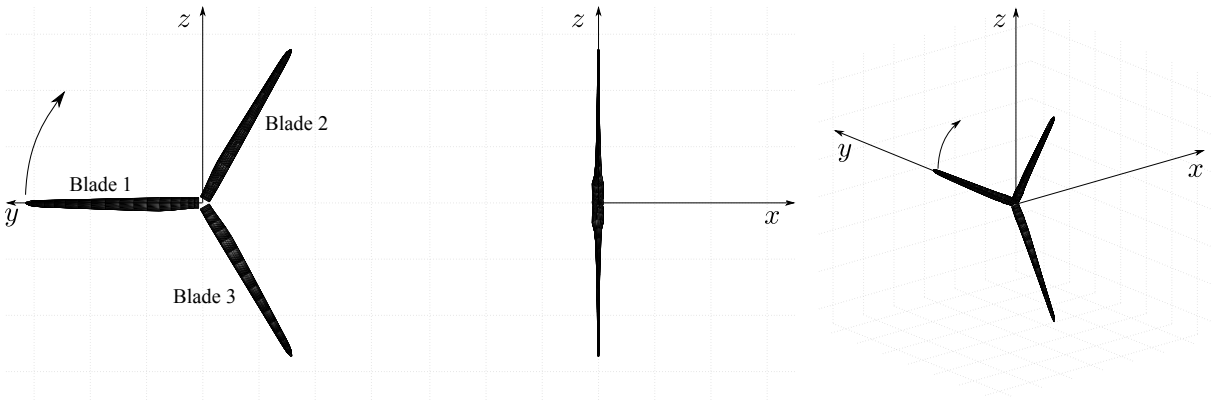


**Figure 2.1:** MIRAS global coordinate system aligned with the rotor's rotational axis. The front (left), side (middle), and three-dimensional (right) views are displayed.

MIRAS also has a coordinate system aligned with blade, see Figure 2.2. The origin is placed at the rotor center, identical to the global coordinate system mentioned above. The $y$-axis is aligned with the blade's pitch axis, and the $x$- and $z$-axes point towards the upper-airfoil surface and leading edge, respectively. The coordinate system does not follow the blade when pitching. On the top right of Figure 2.2, the cross-sectional view of a station selected near the tip of the blade is shown. The blade coordinate system is used as a starting point to modify the blade geometry with the rotations and deflections predicted by FLEX5.

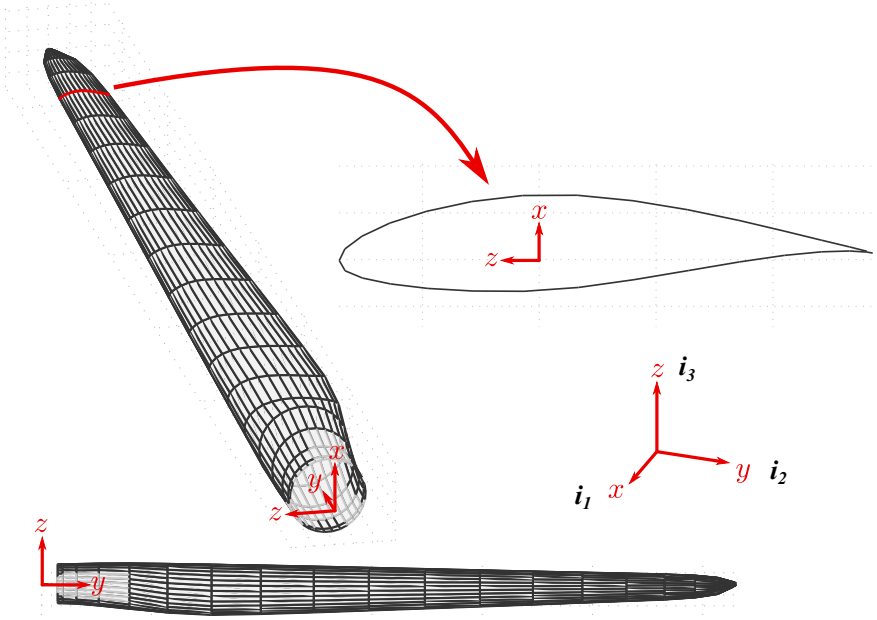


**Figure 2.2:** MIRAS blade coordinate system aligned with the blade pitch axis. Three-dimensional (top left), cross-sectional (top right), and top (bottom) views are shown.

### 2.2.2 FLEX5 Geometry

As shown in Figure 2.3, the geometric layout of FLEX5 is more complicated than MIRAS. In contrast with the MIRAS geometry, which models the rotor only, FLEX5 models the complete turbine and foundation. FLEX5 holds six primary coordinate systems to describe the deflected state of a wind turbine installation. The coordinate systems are named $F_{\text{sys}}$, $T_{\text{sys}}$, $K_{\text{sys}}$, $N_{\text{sys}}$, $R_{\text{sys}}$, and $V_{\text{sys}}$ with their origins located at points $F$, $T$, $K$, $N$, $R$, and $V$, respectively. The remaining quantities shown in Figure 2.3 such as $z_{\text{nav}}$, $z_{\text{RN}}$, $X_{\text{KK2}}$, $H_{\text{i}}$, etc., describe the relative distances of the various components of the turbine installation.

$F_{\text{sys}}$ is the primary reference system and is a fixed and inertial system. Point $F$ is situated at the connecting point between the foundation and the tower when the foundation is undeformed. $T_{\text{sys}}$ is fixed to the tower bottom and moves relative to $F_{\text{sys}}$ when the foundation deflects. $K_{\text{sys}}$ is placed where the extended tower centerline intersects the rotor shaft and is fixed to the nacelle. $N_{\text{sys}}$ is identical to $K_{\text{sys}}$ but is moved forward along the rotor shaft to the front bearing. Both $K_{\text{sys}}$ and $N_{\text{sys}}$ are non-rotating coordinate systems. $R_{\text{sys}}$ is fixed at the hub center where the extended blade centerlines (with no

coning) intersect the rotor shaft and rotates around the $z$-axis. Lastly, $V_{\text{sys}}$ is a coordinate system that exists for each blade and is also placed at the rotor center.

$V_{\text{sys}}$ for Blade 1 coincides with $R_{\text{sys}}$ if there is no coning and if the blade is pitched to have its flat structural beam parallel to the rotor plane, see Figure 2.4. $V_{\text{sys}}$ follows the blade when pitching and rotates around the $z$-axis of $R_{\text{sys}}$. $V_{\text{sys}}$ for other blades, e.g. Blade 2 and Blade 3, are rotated such that Blade 2 lags Blade 1 and Blade 3 lags Blade 2 during normal rotation. A closer view of $V_{\text{sys}}$ is shown in Figure 2.4, where the red rectangle is the structural beam, $\beta$ is the twist, and $\beta_c$ is the structural pitch.

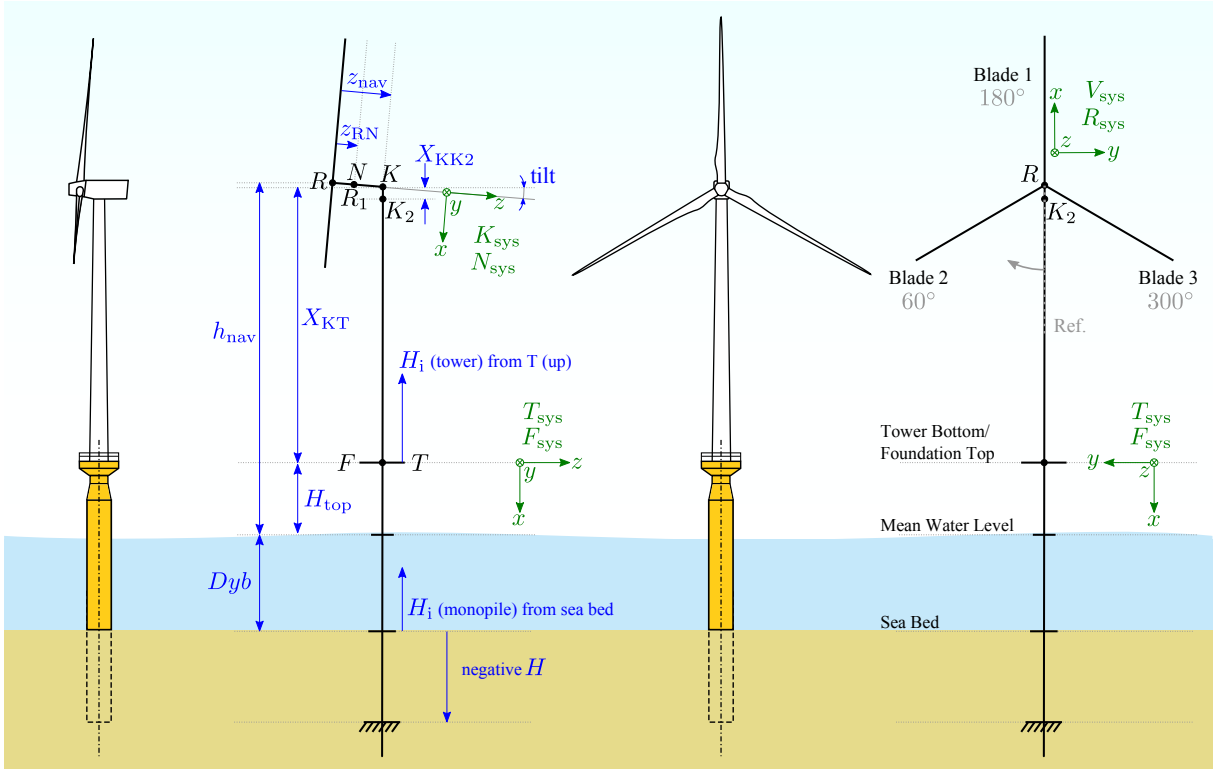


**Figure 2.3:** FLEX5 geometry and coordinate systems. Wind-turbine and mono-pile illustrations modified from [112].

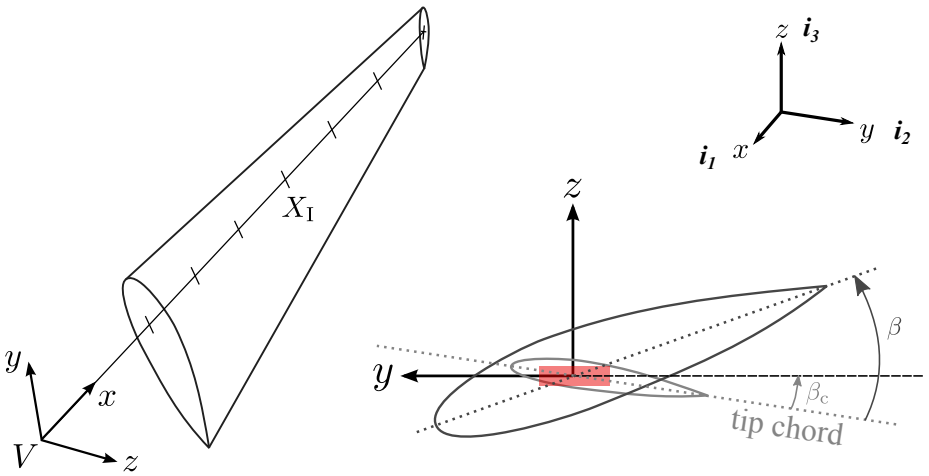


**Figure 2.4:** FLEX5 blade coordinate system.

### 2.2.3 Shape Functions and Deflections

A wind-turbine structure in FLEX5 is modeled dynamically by considering the blades and tower to be flexible cantilevered beams with distributed mass and stiffness properties. In theory, the blades and tower can be modeled using an infinite number of DOFs, since the blades and tower consist of an infinite number of points describing its position in space. Using an infinite number of DOFs however, will be computationally expensive and unnecessary. A wiser choice would be to reduce the number of DOFs to the number of vibration modes considered as dominant, $N$, and subsequently use a linear sum of the dominant modes to model each body in time, e.g. blade and tower. This technique is known as the *normal mode summation method* [113] and is used in FLEX5. The deflection of a beam, which is the distance perpendicular to the undeformed beam, anywhere along the axis of the beam at any time, $U(r,t)$, is given as the summation of the products of each mode shape, $\phi_i(r)$, and their corresponding generalized coordinate, $q_i(t)$:

$$U(r,t) = \sum_{i=1}^{N} \phi_i(r) q_i(t) \tag{2.1}$$

The blade edge-wise and flap-wise deflections, $U_y(r,t)$ and $U_z(r,t)$ respectively, from FLEX5 are referenced to the structural axes, where $r$ is the radial location along the blade and $t$ is time:

$$U_{\mathrm{y}}(r,t) = q_1\phi_1(r) + q_2\phi_2(r) \tag{2.2}$$

$$U_{\mathrm{z}}(r,t) = q_3\phi_3(r) + q_4\phi_4(r) \tag{2.3}$$

where $N = 2$ and $q$ is the generalized coordinate. Indices 1 and 2 represent the DOFs for the first two flap-wise natural mode shapes of a blade. Similarly, 3, and 4 are for the edge-wise mode shapes.

The shape functions used to define the lateral deflections, $U_y(r,t)$ and $U_z(r,t)$, are calculated with the assumption that the points on the blade deflect perpendicular to the undeflected blade length axis ($x$-axis in Figure 2.4). In reality, the points on the blade will move slightly towards the root when the blade deflects to keep the length constant. To calculate more accurately the local force on each panel with a specified area, see subsection 2.2.4, the mesh should take into account the axial deflection. An approach in the FAST_AD code [113, 114] is implemented to calculate the axial deflection of the blades. The axial deflection, $w(r,t)$, in this case is directly related to the lateral deflections:

$$w(r,t) = -\frac{1}{2}\int_0^r \left\{ \left[\frac{\partial U_{\mathrm{z}}(r,t)}{\partial r}\right]^2 + \left[\frac{\partial U_{\mathrm{y}}(r,t)}{\partial r}\right]^2 \right\} \mathrm{d}r \tag{2.4}$$

where $r$ represents the radial location of the undeformed blade and is independent of deflection. The blade root is represented as $r = 0$ in Equation (2.4). For a derivation of Equation (2.4), refer to [113].

The lateral and axial deflections of the beam can be grouped together using the displacement vector $\mathbf{P}(r,t)$:

$$\mathbf{P}(r,t) = U_{\mathrm{z}}(r,t)\boldsymbol{i_1} + w(r,t)\boldsymbol{i_2} + U_{\mathrm{y}}(r,t)\boldsymbol{i_3} \tag{2.5}$$

where $\boldsymbol{i_1}$, $\boldsymbol{i_2}$, and $\boldsymbol{i_3}$ are unit vectors as shown on the top-right of Figure 2.4. Let the three components describing the displacements of the beam to be expressed in matrix

form:

$$\mathbf{P}(r,t) = P_1\boldsymbol{i_1} + P_2\boldsymbol{i_2} + P_3\boldsymbol{i_3} = \begin{bmatrix} P_1 \\ P_2 \\ P_3 \end{bmatrix} \tag{2.6}$$

In Euler-Bernoulli beam theory, the displacement field of a cross-section anywhere along the axis of the beam consists solely of rigid body translations and rigid body rotations [38]. The 3D displacement field at a point in time is then:

$$u_1(x,y,z) = P_1 \tag{2.7}$$

$$u_2(x,y,z) = P_2 - x\frac{\mathrm{d}P_1}{\mathrm{d}y} - z\frac{\mathrm{d}P_3}{\mathrm{d}y} \tag{2.8}$$

$$u_3(x,y,z) = P_3 \tag{2.9}$$

where axial coordinate $r$ is replaced temporarily by $y$.

Let a point of a cross-section in the MIRAS blade system without any pitch be described using the vector $\mathbf{P}_{\text{miras}}$:

$$\mathbf{P}_{\text{miras}} = P_{m,1}\boldsymbol{i_1} + P_{m,2}\boldsymbol{i_2} + P_{m,3}\boldsymbol{i_3} = \begin{bmatrix} P_{m,1} \\ P_{m,2} \\ P_{m,3} \end{bmatrix} \tag{2.10}$$

In Euler-Bernoulli beam theory, the displacements in Equation (2.5) are computed using cross-sectional stiffnesses that are defined about the principal axes, and have their origins located at the tension center (TC). Figure 2.5 depicts the cross-sectional stiffness about the principal axes $EI_1$ and $EI_2$, as well as the tension center.

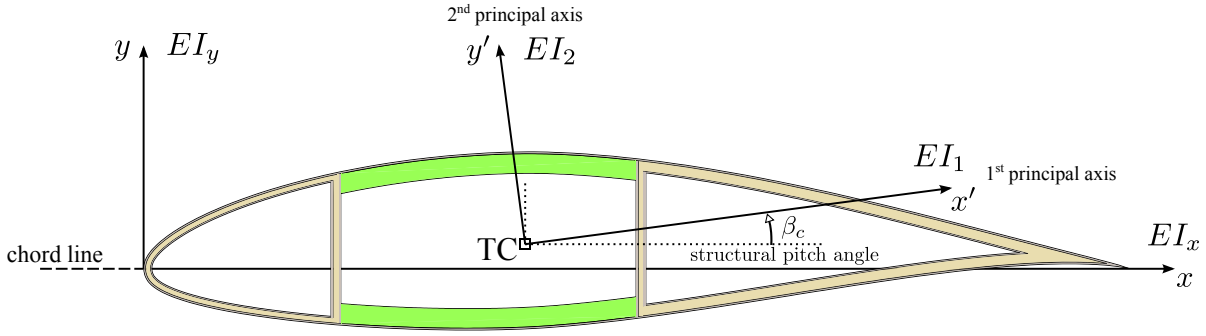


**Figure 2.5:** Cross-section showing structural properties. Modified from [115].

The displacement field should be applied when the cross-section of each blade station along the axis of the beam is defined about the tension center and rotated about the principal bending axes. Each cross-section on the $x$-$z$ plane in the MIRAS blade system is defined in its own coordinate system about the pitch-axis and thus a translation and rotation is recommended:

$$\mathbf{P}_{\text{cross}}(r,t) = \begin{bmatrix} \cos\beta_c & 0 & \sin\beta_c \\ 0 & 1 & 0 \\ -\sin\beta_c & 0 & \cos\beta_c \end{bmatrix} \begin{bmatrix} P_{m,1} - \mathrm{TC}_1 \\ P_{m,2} - (r + R_H) \\ P_{m,3} - \mathrm{TC}_3 \end{bmatrix} = \begin{bmatrix} P_{c,1} \\ P_{c,2} \\ P_{c,3} \end{bmatrix} = \begin{bmatrix} x \\ y \\ z \end{bmatrix} \tag{2.11}$$

where $\mathrm{TC}_1$ and $\mathrm{TC}_3$ are the coordinates of the tension center of the cross-section relative to the pitch-axis and $x$, $y$, and $z$ correspond to the values used in Equations (2.7) to (2.9). The hub radius, $R_H$, and $r$ are subtracted to obtain the MIRAS cross-section at $y = 0$.

The displacement field in Equations (2.7) to (2.9) is added to each MIRAS cross-section defined by Equation (2.11). Then, each cross-section is translated back to the blade coordinate system (see third term in Equation (2.12)):

$$\mathbf{P}_{\text{update}}(r,t) = \begin{bmatrix} P_{c,1} \\ P_{c,2} \\ P_{c,3} \end{bmatrix} + \begin{bmatrix} u_1 \\ u_2 \\ u_3 \end{bmatrix} + \begin{bmatrix} 0 \\ r + R_H \\ 0 \end{bmatrix} \tag{2.12}$$

In the last two steps, $\mathbf{P}_{\text{update}}(r,t)$ is rotated using the FLEX5 $V_{\text{sys}}$-to-$F_{\text{sys}}$ transformation matrix to include the structural pitch, pitch, coning, tilt, and yaw angles, as well as the angular position of each blade. The coordinates in the $F_{\text{sys}}$ are then converted to coordinates compatible with the MIRAS global system. Figures 2.6 and 2.7 depict the undeformed and deflected blade and rotor in the MIRAS blade and global coordinate systems, respectively.

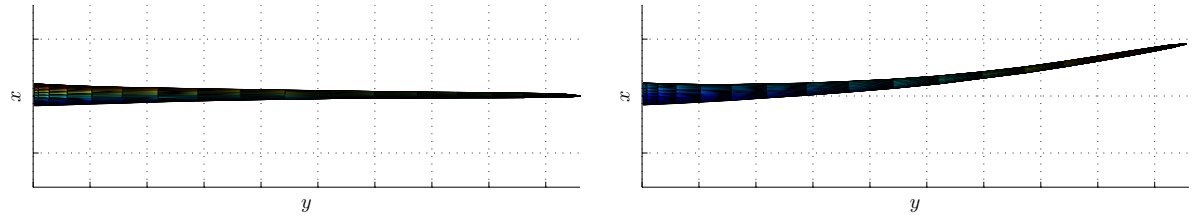


**Figure 2.6:** Undeformed (left) and deflected (right) blade in MIRAS. Flap-wise deflection shown.

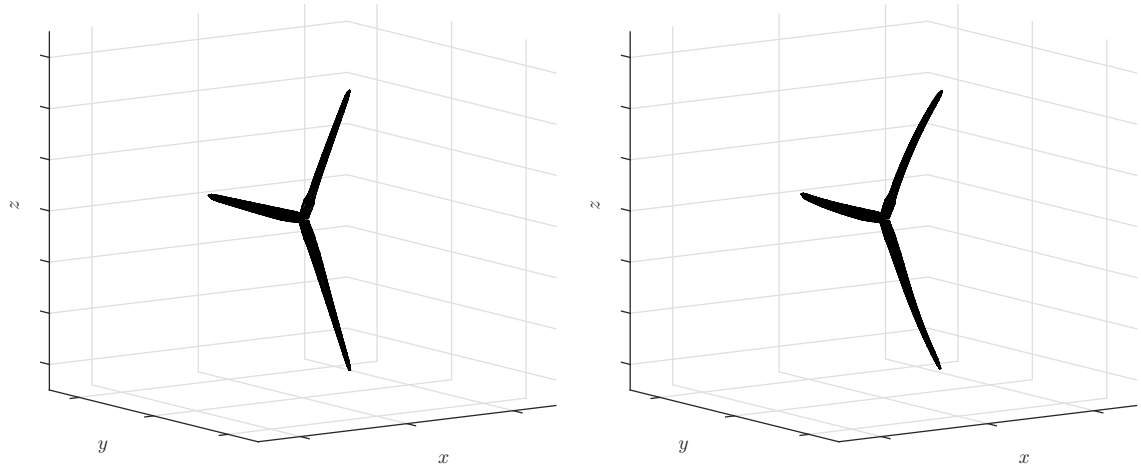


**Figure 2.7:** Undeformed (left) and deflected (right) rotor in the MIRAS global coordinate system.

Euler-Bernoulli beam theory along with the deflections and rotations from FLEX5 are used to modify the mesh in MIRAS. Prior to using the equations however, the non-matching meshes between MIRAS and FLEX5 have to be interpolated. Specifically, the data on the $V_{\text{sys}}$ grid must be interpolated onto the MIRAS blade grid. This interpolation is performed linearly. In MIRAS, the deflections and rotations are applied on the blade stations shown by the airfoil sections with the solid line in Figure 2.8. The airfoil sections have the coordinates $x_{\text{node}}$, $y_{\text{node}}$, and $z_{\text{node}}$, which are the values substituted into

Equations (2.7) to (2.9). The deflections and rotations from FLEX5 are defined on the diamonds that lie on top of the thick red line (beam axis) shown in Figure 2.8. The beam axis is aligned with the pitch axis in MIRAS. The TC is assumed to be equal to the pitch axis, i.e. $\mathrm{TC}_1 = \mathrm{TC}_3 = 0$.

### 2.2.4 Aerodynamic Load Transfer

Using the unsteady Bernoulli equation in MIRAS, the non-dimensional surface pressure distribution $C_p$ is obtained as:

$$C_p = \frac{p - p_{\text{ref}}}{1/2\rho|\mathbf{v}_{\text{ref}}|^2} = 1 - \frac{|\mathbf{v}|^2}{|\mathbf{v}_{\text{ref}}|^2} - \frac{2}{|\mathbf{v}_{\text{ref}}|^2}\frac{\partial\phi}{\partial t} \tag{2.13}$$

where $p$ is the local fluid pressure, $p_{\text{ref}}$ is the far-field reference pressure, $\rho$ is the fluid density, $\mathbf{v}_{\text{ref}}$ is the reference velocity and $\partial\phi/\partial t$ is the variation of the potential function in time. The total velocity vector, $\mathbf{v}$, is the sum of the kinematic velocity of the local reference system ($\mathbf{V_0} + \mathbf{\Omega} \times \mathbf{r}$), the induced velocity, $w_1$, $w_2$, and $w_3$, and the blade velocity, $V_{b1}$, $V_{b2}$, $V_{b3}$:

$$\mathbf{v} = \mathbf{V_0} + \mathbf{\Omega} \times \mathbf{r} + [w_1, w_2, w_3] - [V_{b1}, V_{b2}, V_{b3}] \tag{2.14}$$

The local force, $\mathbf{\Delta F}$, exerted on a panel with area, $\Delta S$, is computed as:

$$\mathbf{\Delta F} = -C_p \left(\frac{1}{2}\rho|\mathbf{v}_{\text{ref}}|^2\right) \Delta S \mathbf{n} \tag{2.15}$$

where $\mathbf{n}$ is the normal unitary vector pointing out of the specific panel. The blade normal, tangential and axial forces are computed by adding the contributions from each panel in the global coordinate system and adding the influence of the sectional friction drag. The forces are then transferred to FLEX5.

The angle of attack at each span-wise station, $i$, is computed as:

$$\alpha_i = \psi_i - \beta_0 - \beta_i \tag{2.16}$$

where $\beta_0$ is the blade pitch angle, $\beta_i$ is the local section twist angle and $\psi_i$ is the flow angle calculated as:

$$\psi_i = \tan^{-1}\left(\frac{v_{1,i} - V_{b1,i}}{(v_{3,i} - V_{b3,i})\cos\theta - (v_{2,i} - V_{b2,i})\sin\theta}\right) \tag{2.17}$$

with $\theta$ being the angular position of the blade and $v_{1,i}$, $v_{2,i}$, $v_{3,i}$ the local velocities computed at the control points. The local velocities include induced velocities and blade rotation, but excludes the influence of the blade itself. Note that the local velocities are still defined in the same local reference system as in Equation (2.14). Including the motions of the blade in the angle of attack calculation is an on/off flag in the MIRAS-FLEX code. The option has been disabled for all simulations in the present thesis, since they are sensitive to small fluctuations and the angle of attack tends to diverge. A strong-coupling approach may be required. The coupling methodologies are described later in sections 2.3 and 2.4.

Load transfer from MIRAS to FLEX5 is performed through interpolation between the 3D mesh of MIRAS (i.e. $x_1$, $x_2$ and $x_3$) and the one-dimensional beam of FLEX5.

Figure 2.8 illustrates the concept, where the loads defined at the center-points of each panel with coordinates $c_1$, $c_2$ and $c_3$ from the MIRAS mesh are converted into equivalent loads in FLEX5 (diamonds). The loads are interpolated from the MIRAS blade grid onto the FLEX5 $V_{\text{sys}}$ grid. The loads in MIRAS are determined using a non-dimensional surface pressure distribution, $C_p$, which is calculated at the center point with the coordinates, $c_x$, $c_y$, and $c_z$, of each panel on the blade surface. The resulting load is then linearly interpolated onto the points on the $V_{\text{sys}}$ grid shown by the diamonds in Figure 2.8. The interpolation is carried out in $B_{\text{sys}}$ and $V_{\text{sys}}$ in MIRAS and FLEX5, respectively, based on the undeformed blade state. To decrease numerical discrepancies in the interpolation, the input stations in MIRAS are set equal to the input stations in FLEX5. In other words, data transfer is performed on a blade station-by-station basis, which does not depend on the bended blade shape. Both the $x_1$-axis in $B_{\text{sys}}$ and the beam in $V_{\text{sys}}$ coincide with the blade pitch-axis.

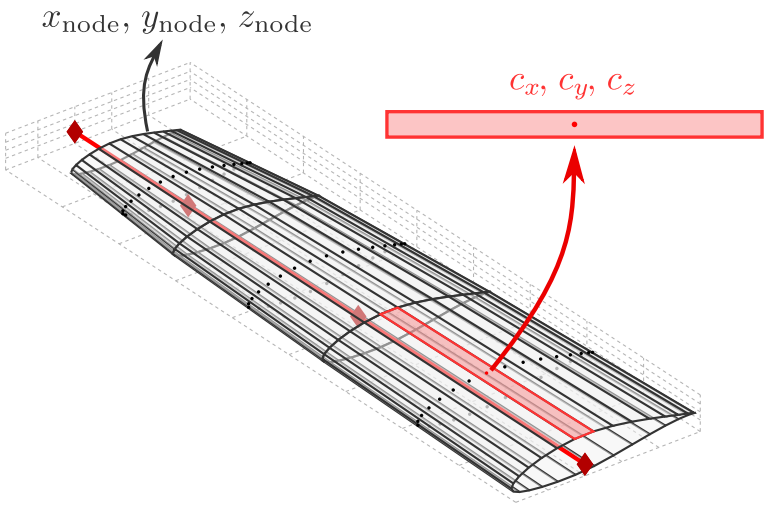


**Figure 2.8:** Non-matching meshes between MIRAS (mesh) and FLEX5 (thick line with diamonds).

### 2.2.5 Time Integration Schemes in MIRAS and FLEX5

Understanding the time integration schemes used in MIRAS and FLEX5 is important for the coupling of the two codes, since they influence at which time step the aerodynamic and structural-dynamic information must be exchanged. They are described in this subsection for completeness, however the coupling methods are described sections 2.3 and 2.4. The time integration schemes for MIRAS and FLEX5 are described next.

There are a number options in MIRAS for selecting the time-integration method, which consists of a first order Euler method, an explicit trapezoidal scheme, and linear multistep methods. The linear multistep methods included are Adams-Bashforth methods up to the fourth order and a fourth-order Adams-Bashforth-Moulton predictor-corrector method. In FLEX5, time integration is performed using a fourth-order Runge-Kutta-Nyström (RKN) technique.

There are similarities and differences between both approaches for time integration worth mentioning. The time integration methods in MIRAS and the RKN in FLEX5 are explicit. Explicit methods calculate the state of the system at a later time from the state

of the system at the current and possibly previous timesteps. In contrast, an implicit method requires both the current state of the system and the later one in the solution process. Examples of implicit methods include the backward Euler, and the Generalized-$\alpha$ and Newmark methods. With the exception of the explicit trapezoidal scheme, all MIRAS time integration methods are multi-step. The RKN in FLEX5 is a single-step method because it discards all information from previous timesteps. To obtain higher-order accuracy, RKN evaluates intermediate steps at $t^{n+1/2}$, where $n$ is the number of the time step. The intermediate steps in the RKN is taken into account in section 2.4.

## 2.3 Coupling Methodology - First Attempt

### 2.3.1 Loosely-Coupled Structural Predictor

There are two main approaches to couple MIRAS and FLEX5, namely the monolithic and partitioned coupling as described in section 1.2.1. The monolithic approach would require to replace the existing time integration schemes in MIRAS and FLEX5 with a single scheme, which would solve the governing equations in both MIRAS and FLEX5 simultaneously. A significant amount of code restructuring is needed in both MIRAS and FLEX5 for this approach since each code was designed to work with a particular scheme. The alternative approach is the partitioned case, where MIRAS and FLEX5 are combined in either a strongly- or loosely-coupled manner. The MIRAS and FLEX5 codes are left intact, but a coupling algorithm is used to transfer the information on loads and deflections between the two codes.

A loosely-coupled methodology is implemented using a structural predictor from the work of Farhat [44] as the first attempt. The method in Farhat [44] has been applied for coupling CFD with the aero-elastic code HAWC2 in Joachim [24]. The loosely-coupled approach was selected to minimize the number of calls to the computationally intensive MIRAS in the MIRAS-FLEX code. The computational cost for a strongly-coupled MIRAS-FLEX code would be considerable. The loose-coupling is displayed in Figure 2.9. In Figure 2.9, the blade at each timestep is represented by a black line. The first two timesteps, i.e. timestep 0 to 1 and 1 to 2, are the initialization steps. The loose coupling starts at the beginning of timestep 2, which consists of a structural predictor step, a call for loads from MIRAS, and a call for deflections from FLEX5.

The structural predictor step is needed to give an estimate of the blade deformations at a future timestep. The predictor in the present loose-coupling method is:

$$U^{n+1} = U^n + \alpha_0 \Delta t \dot{U}^n + \alpha_1 \Delta t (\dot{U}^n - \dot{U}^{n-1}) \tag{2.18}$$

where $U$ are the deflections from FLEX5 at the current $(n)$, previous $(n-1)$, and subsequent $(n+1)$ timesteps. The velocity, $\dot{U}$, is given by the derivative of $U$ and $\Delta t$ is the size of the time step in seconds. The prediction in Equation (2.18) is first-order accurate if $\alpha_0 = 1$ and second-order accurate under the additional condition that $\alpha_1 = 1/2$ [44]. Second-order accuracy is implemented in MIRAS-FLEX. By providing a prediction of the deformation in MIRAS at the following timestep, a more accurate load calculation is obtained. The load is then transfered to FLEX5 to calculate the actual deflection at each timestep. The coupling steps repeat after timestep 3.

Blade motion is fed back into MIRAS by introducing $\dot{U}$ in the governing equations, see section 2.2.4. Blade velocities are obtained in a similar way as for the blade deflections,

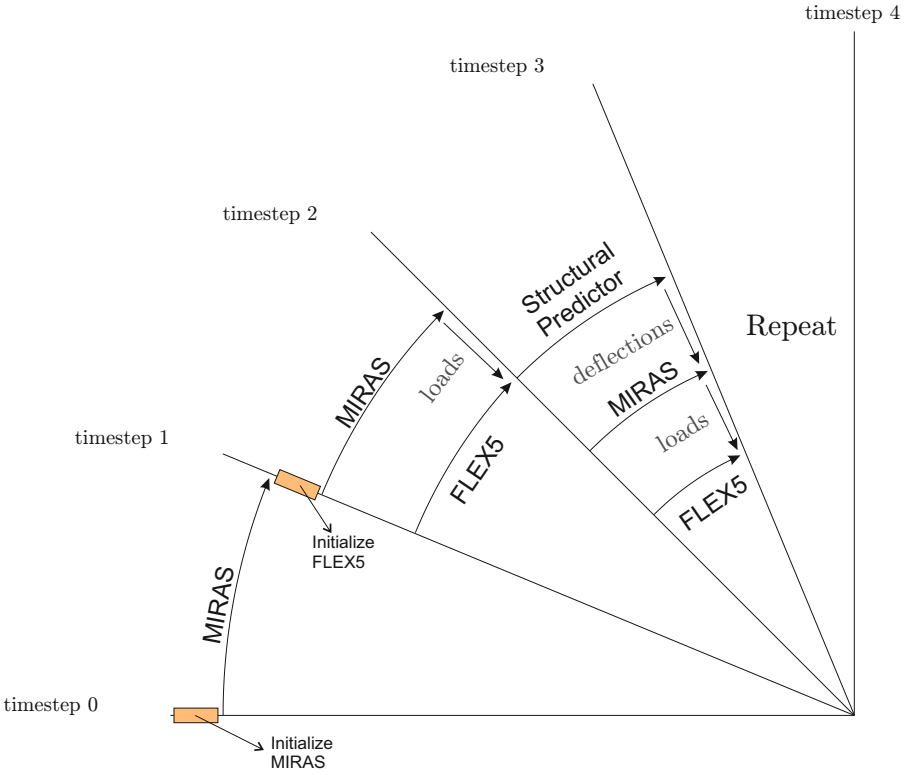


**Figure 2.9:** Loose-coupling methodology in MIRAS-FLEX.

i.e. a predictor for $\dot{U}$ is used:

$$\dot{U}^{n+1} = \dot{U}^n + \alpha_0 \Delta t \ddot{U}^n + \alpha_1 \Delta t (\ddot{U}^n - \ddot{U}^{n-1}) \tag{2.19}$$

### 2.3.2 Description of Comparison Tests

This subsection describes the baseline wind-turbine rotor as well as how the blade mesh and airfoil data are generated for the comparison tests in subsections 2.3.3 and 2.4.3.

The wind turbine chosen for the comparison is the land-based version of the NREL 5 MW Offshore Baseline Wind Turbine [116] with a rotor diameter of 126 m. Table 2.1 summarizes the gross properties of the NREL 5 MW turbine. The NREL 5 MW turbine consists of Delft University of Technology (DU) airfoils between 40% and 21% relative thickness and a 18% NACA airfoil in the blade tip region. Recall from subsection 1.3.3 that instead of traditional airfoil lift and drag coefficients used in BEM-based codes, MIRAS requires transpiration velocity data from Q$^3$UIC. In Figure 2.10, the NREL 5 MW blade mesh consists of 20 span-wise and 150 chord-wise stations, i.e. a total of 3000 points, distributed using cosine spacing. Profile coordinates midway between the span-wise stations, thus 19 profiles in total, are then sent to Q$^3$UIC to create the transpiration velocity data as well as the lift and drag coefficients if desired. As an approximation, the profiles sent to Q$^3$UIC near the root section were replaced with the 40% relative thickness DU airfoil, since Q$^3$UIC computations for airfoils thicker than 40% can be inaccurate. Figure 2.11 depicts the equivalent lift and drag coefficients for the blade shown in Figure 2.10. Note that Q$^3$UIC computations are performed with the

Reynolds number, local aspect ratio, and rotational effects included. Therefore, Q$^3$UIC data varies depending on the wind inflow, $V_o$, and rotor speed conditions.

**Table 2.1:** Gross properties of the NREL 5 MW baseline wind turbine [116].

| | |
|---|---|
| Rated Power | 5 MW |
| Rotor Orientation, Configuration | Upwind, 3 Blades |
| Control | Variable Speed, Collective Pitch |
| Drivetrain | High Speed, Multiple-Stage Gearbox |
| Rotor, Hub Diameter | 126 m, 3 m |
| Hub Height | 90 m |
| Cut-In, Rated, Cut-Out Wind Speed | 3 m/s, 11.4 m/s, 25 m/s |
| Cut-In, Rated Rotor Speed | 6.9 RPM, 12.1 RPM |
| Rated Tip Speed | 80 m/s |
| Overhang, Shaft Tilt, Precone | 5 m, 5°, 2.5° |
| Rotor Mass | 110,000 kg |
| Nacelle Mass | 240,000 kg |
| Tower Mass | 347,460 kg |

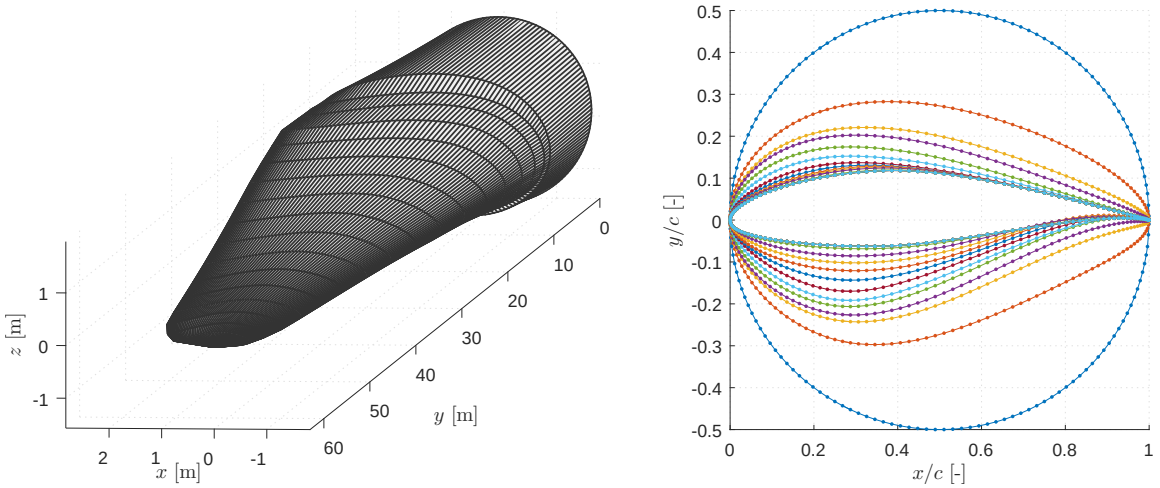


**Figure 2.10:** Blade mesh generation in MIRAS using cosine distributions of 20 and 150 stations in the span-wise and chord-wise directions, respectively. The cross-sectional profiles (right) are extracted from the blade mesh (left) for Q$^3$UIC computations.

### 2.3.3 Simulation Results

Simulations with steady and uniform wind conditions from 5 to 16 m/s were carried out using FAST, FLEX5, MIRAS and MIRAS-FLEX to validate the MIRAS-FLEX code and the loosely-coupled structural-predictor approach. To allow a simpler and closer comparison between all aero-elastic codes, gravity was set to zero and only the 1$^{st}$ and 2$^{nd}$ flap, and 1$^{st}$ edge mode DOFs were enabled in FAST, FLEX5, and MIRAS-FLEX. Loads are compared on an aerodynamic basis, i.e. inertial and gravitational loads are excluded, to allow the addition of MIRAS in the comparison. HAWC2 simulations were also carried out but have been omitted from the figures to reduce cluttering. HAWC2

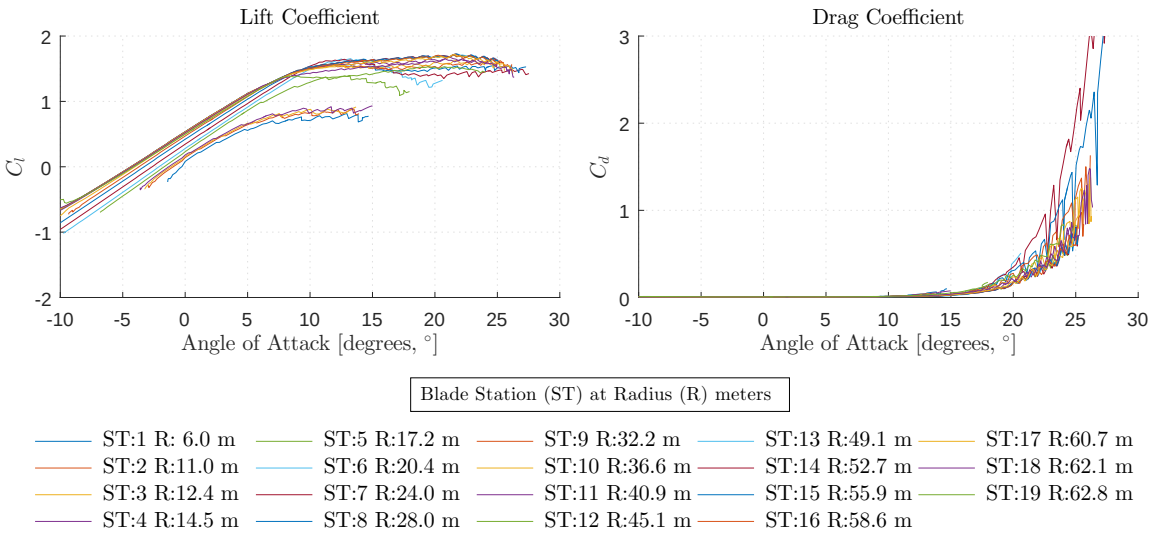


**Figure 2.11:** Lift and drag coefficient data generated using Q$^3$UIC according to a user-specified selection of blade stations in MIRAS. Free-transition and turbulence intensity of 0.001 used in computations.

results were removed since they were nearly identical to FAST. The bended blades are clearly seen in the MIRAS-FLEX simulations when compared with MIRAS alone, see Figure 2.12. Figure 2.13 depicts the aerodynamic power (top) and thrust (bottom) from FAST, FLEX5, MIRAS and MIRAS-FLEX. Tip-speed ratio = 8 is maintained up to the maximum generator speed, and decreases thereafter. Pitch angle is set to 0 degrees, thus pitch regulation was not implemented.

Results for normal and tangential aerodynamic loads are shown in Figures 2.14 and 2.15, respectively. Deflections in both directions are shown in Figures 2.16 and 2.17, respectively, as well. Edge-wise deflections for MIRAS-FLEX and FLEX5 differ from FAST due to the difference in structural pitch (see $\beta_c$ in Figure 2.4) inputs between FLEX5 and FAST. In FLEX5, a single averaged value for structural pitch is entered for the entire blade. Due to the asymmetry of the blade cross-sections in the span-wise direction however, structural pitch varies from the blade root to tip. The variation in structural pitch can be modeled in FAST, but not FLEX5. The structural pitch in FLEX5 was set to zero for the present simulations, but can be adjusted to fit more closely with the results from FAST. The adjustment was made for the second-attempt coupling methodology, see Figure 2.38 in section 2.4.3.

Differences in loads are partly due to different airfoil data, see Figures 2.19, 2.20, 2.21, and 2.22. By using the Q$^3$UIC airfoil data from the MIRAS and MIRAS-FLEX simulations into the FAST and FLEX5 simulations (as opposed to the airfoil data from reference [116]) and adjusting the structural pitch angle, a closer agreement between all codes is obtained. The results from using Q$^3$UIC airfoil data in FAST and FLEX5 is shown in section 2.4.3.

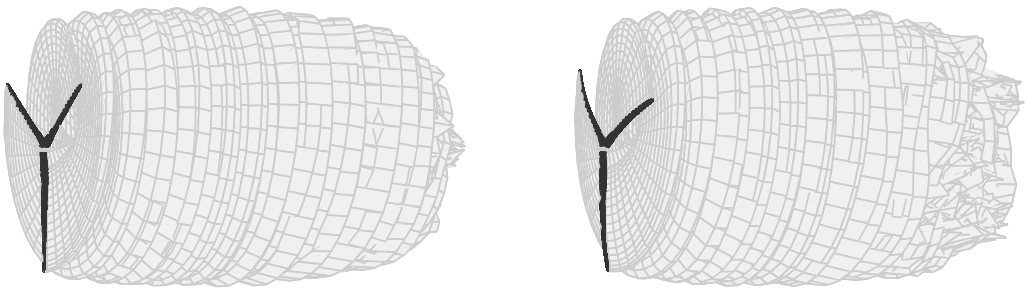

**Figure 2.12:** Fluid only (left) and fluid-structure-interaction (right) simulations of the NREL 5 MW wind-turbine rotor.

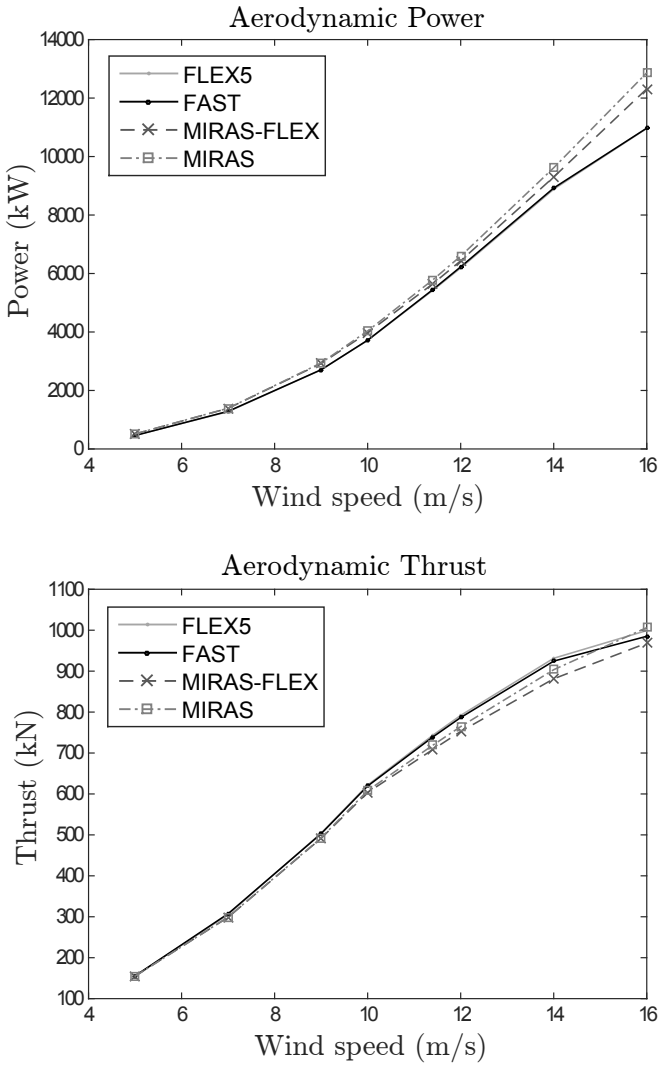


**Figure 2.13:** Aerodynamic power (top) and thrust (bottom) from FLEX5, FAST, MIRAS-FLEX and MIRAS. Tip-speed ratio = 8 is maintained up to the maximum generator speed, and decreases thereafter. Pitch regulation not implemented.

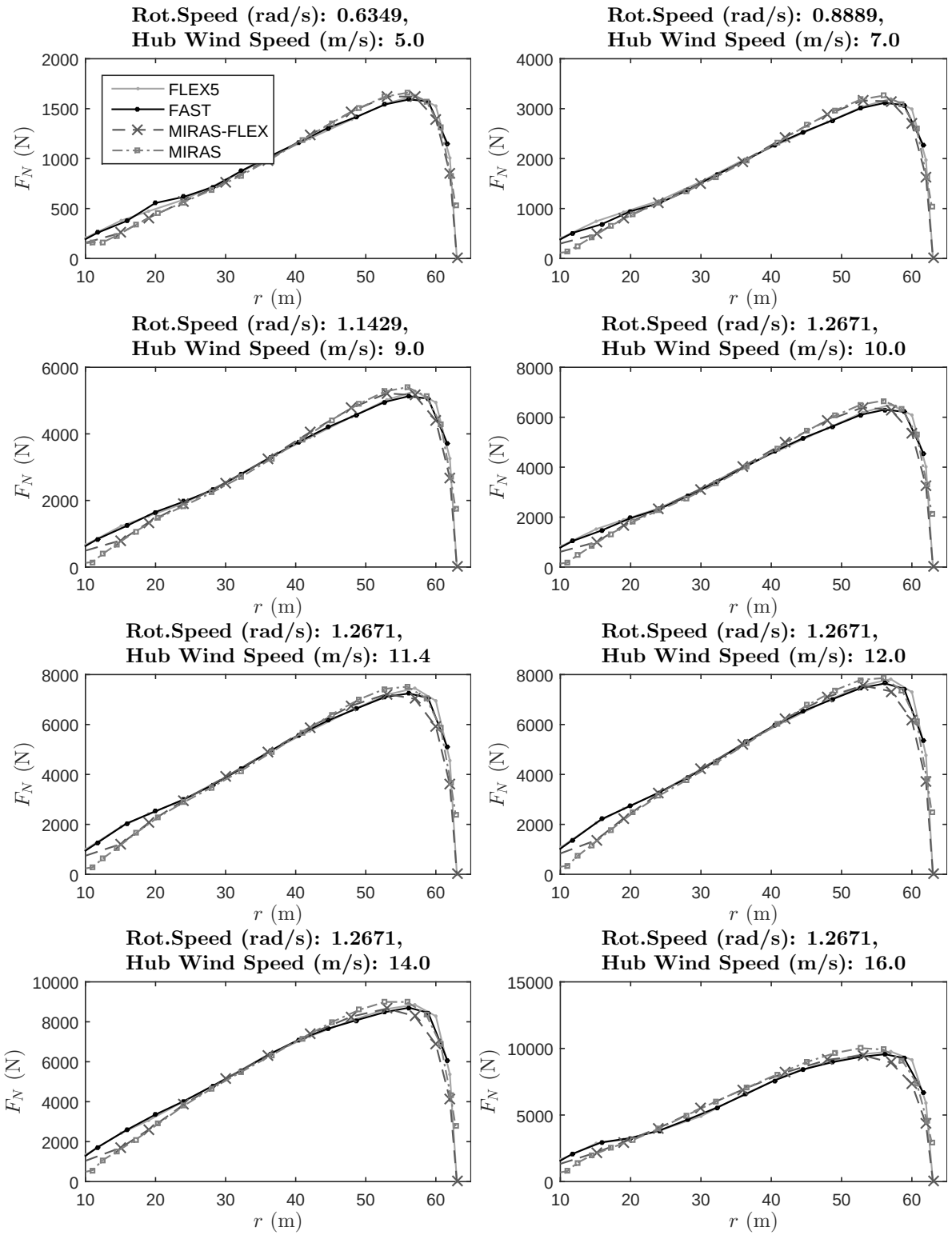


**Figure 2.14:** Aerodynamic load normal to the rotor plane from FLEX5, FAST, MIRAS-FLEX and MIRAS.

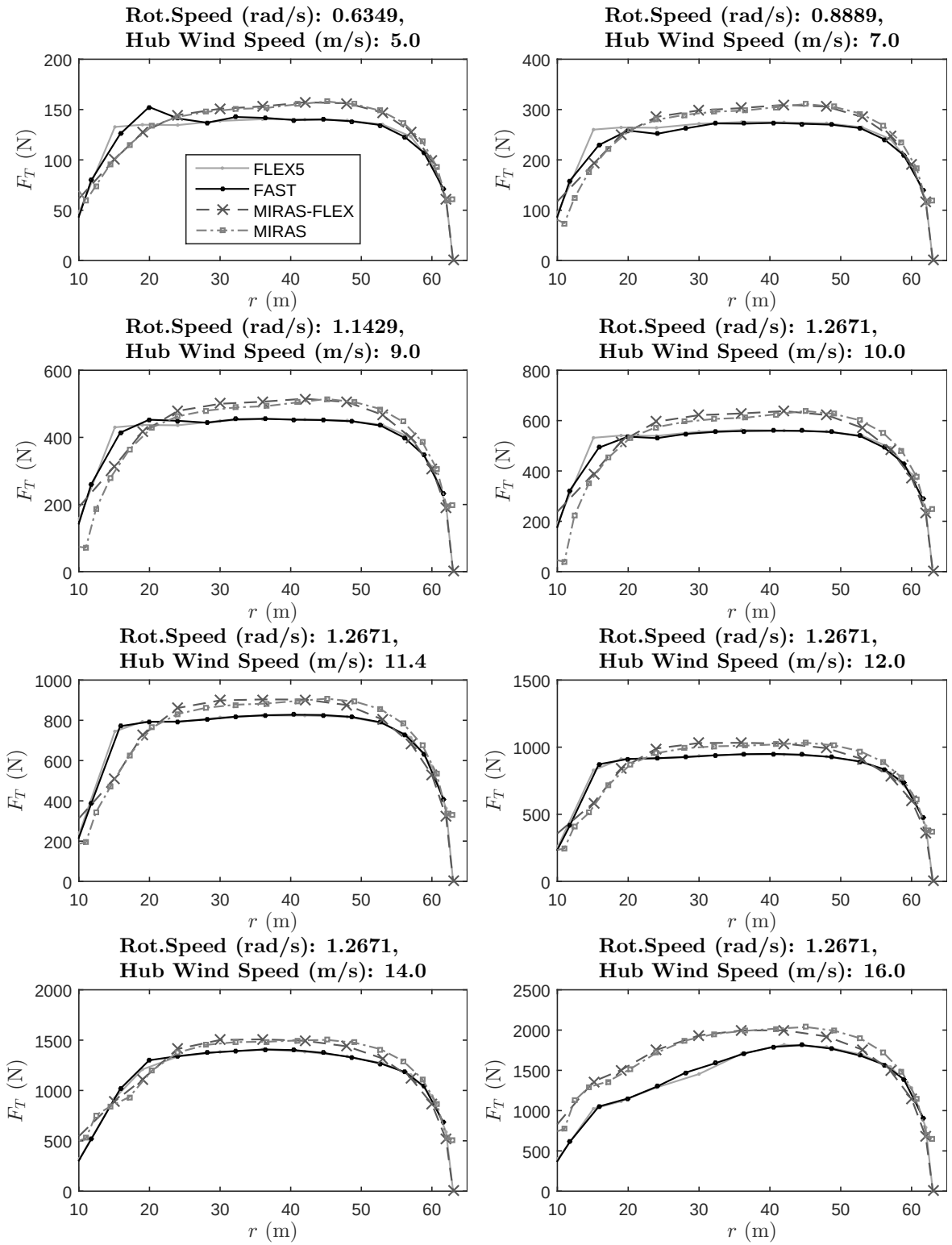


**Figure 2.15:** Aerodynamic load tangential to the rotor plane from FLEX5, FAST, MIRAS-FLEX and MIRAS.

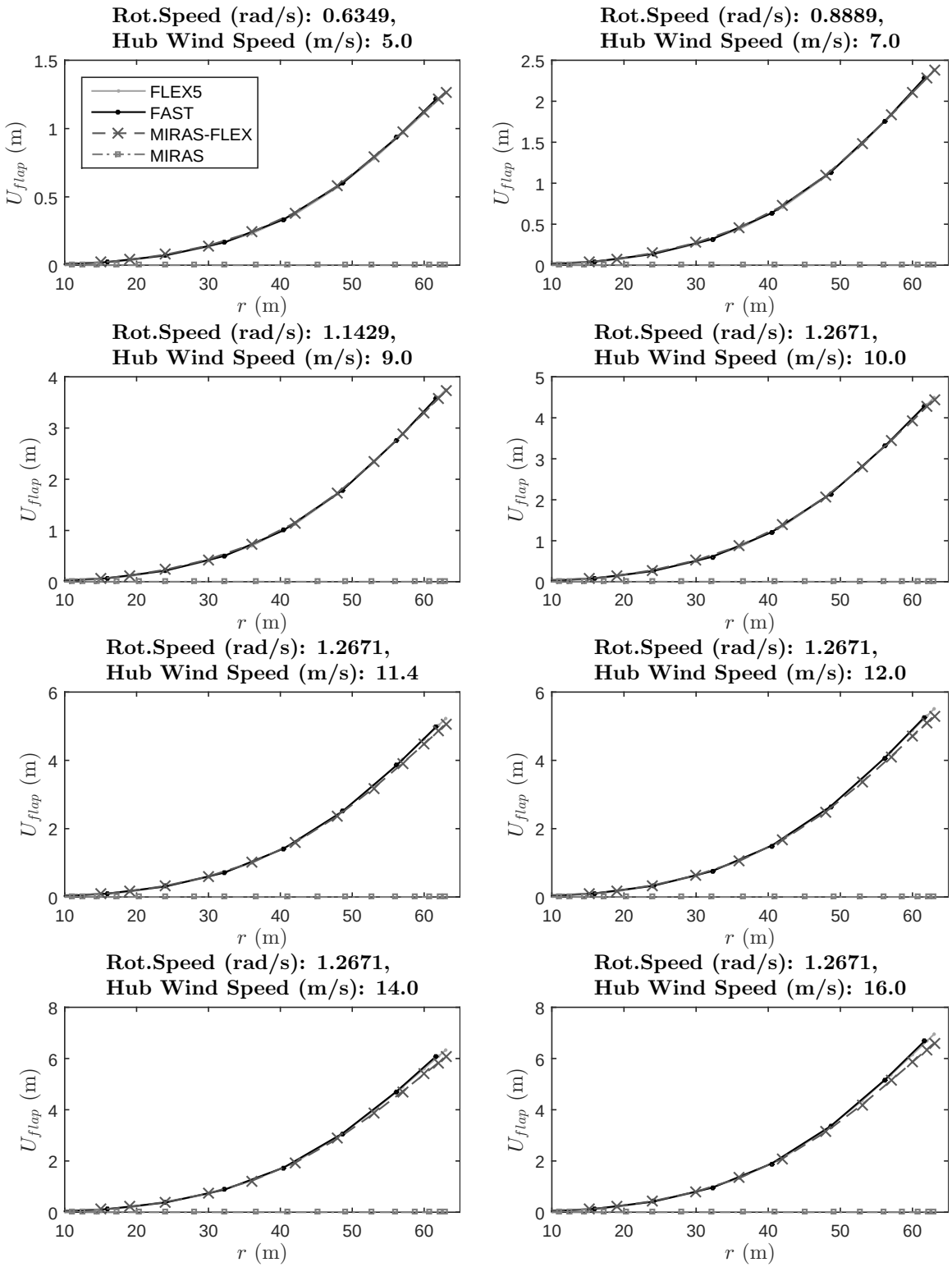


**Figure 2.16:** Flap-wise deflection from FLEX5, FAST, MIRAS-FLEX and MIRAS.

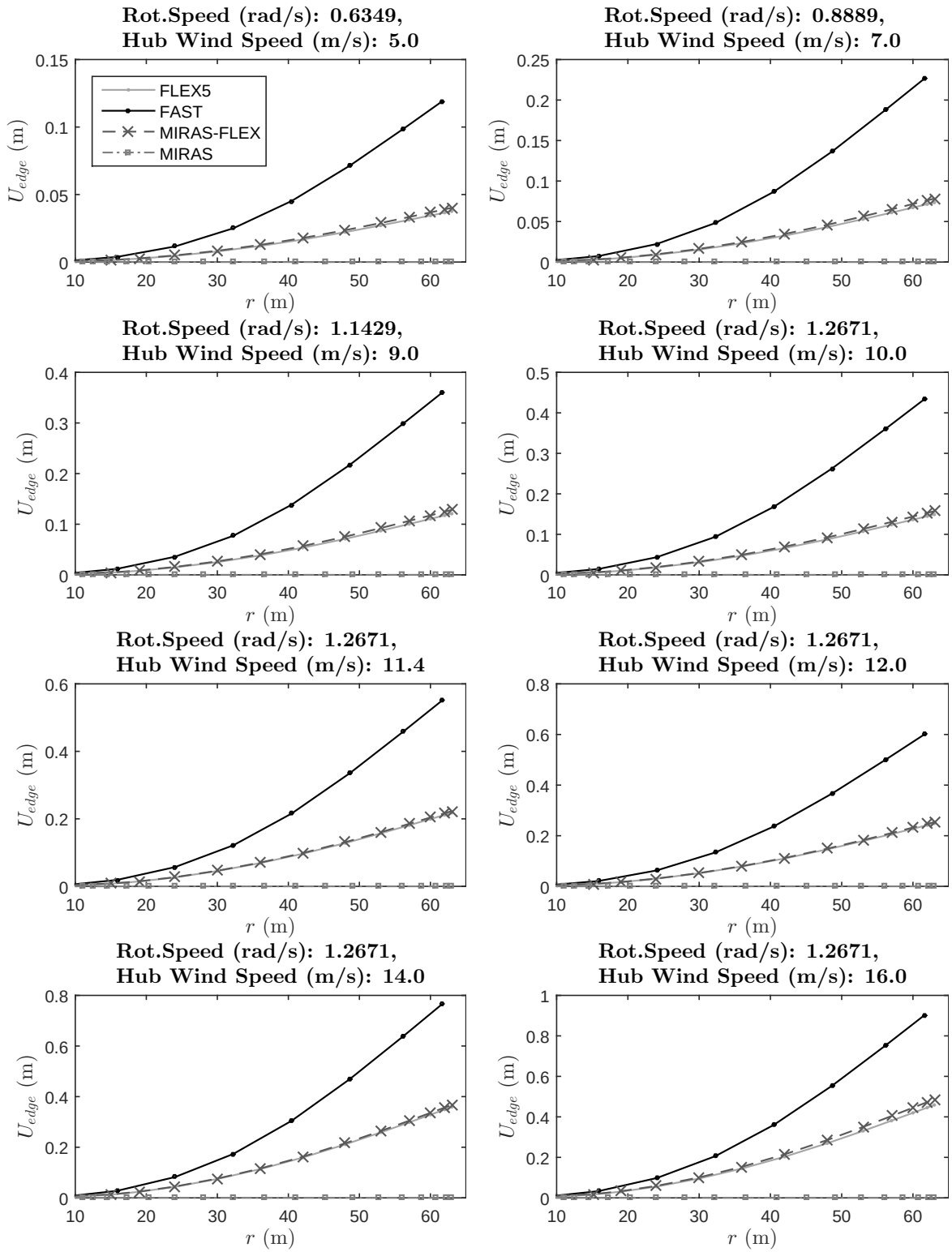


**Figure 2.17:** Edge-wise deflection from FLEX5, FAST, MIRAS-FLEX and MIRAS.

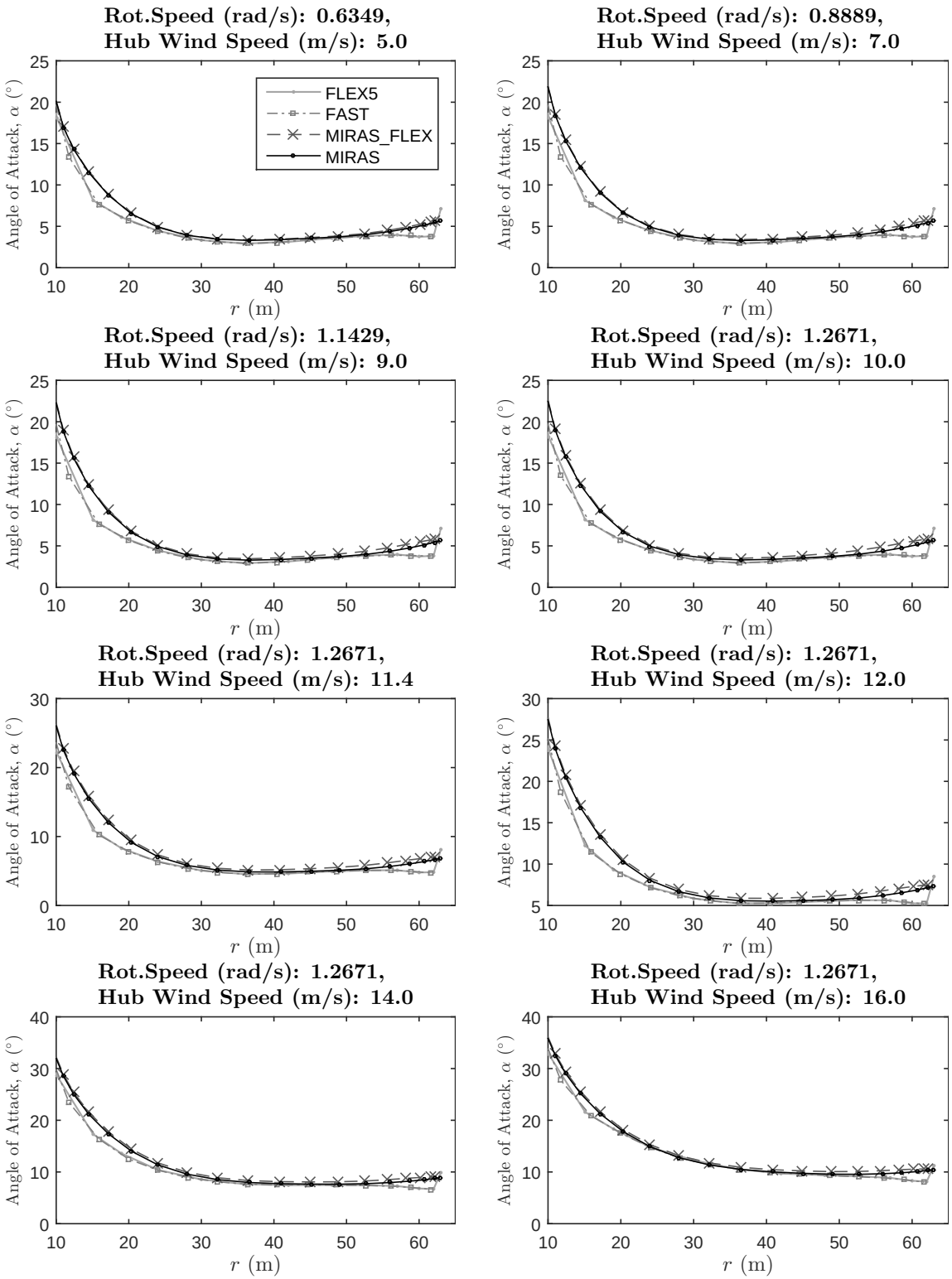


**Figure 2.18:** Angle of attack from FLEX5, FAST, MIRAS-FLEX and MIRAS.

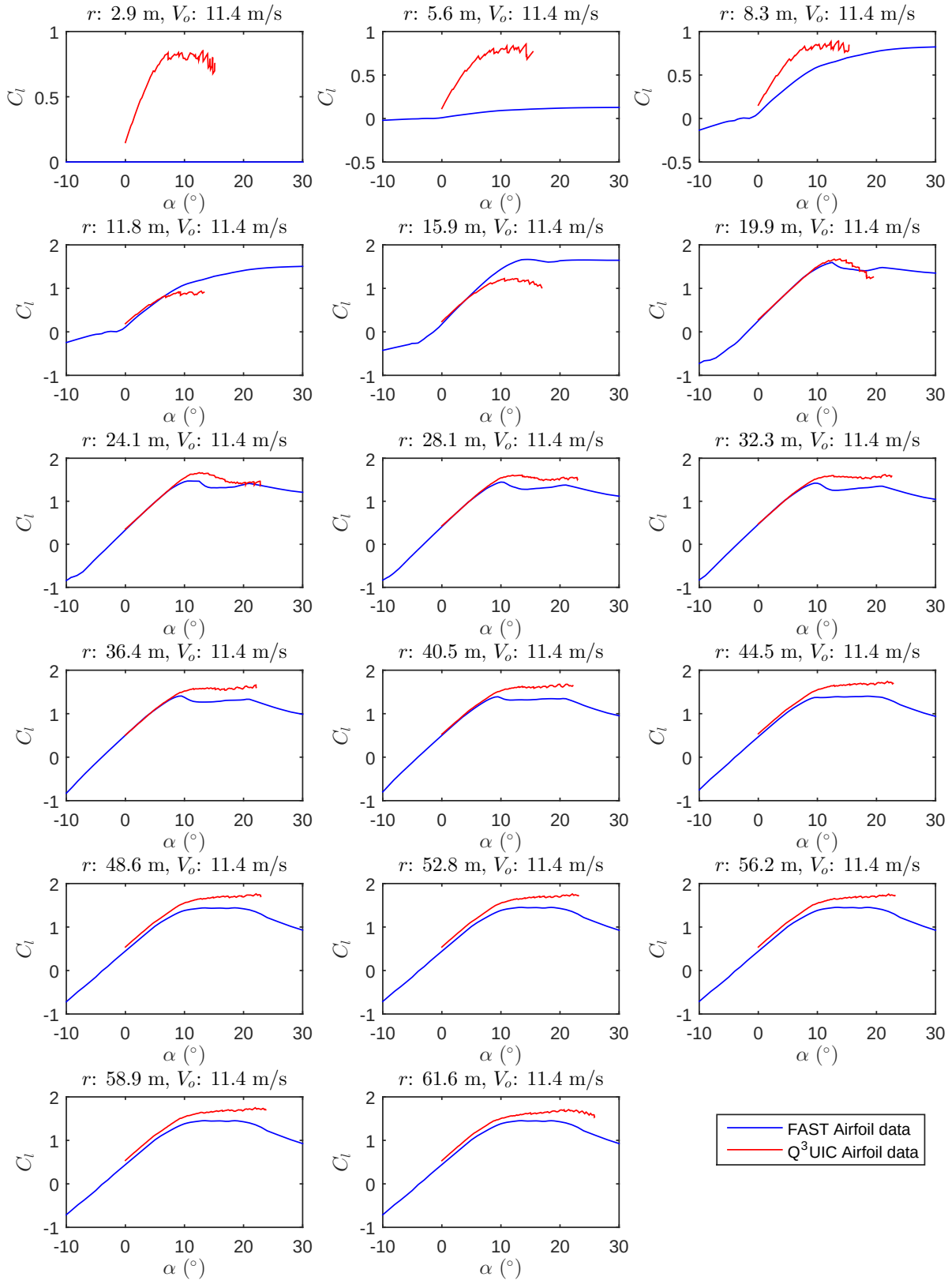


**Figure 2.19:** Airfoil lift data for 11.4 m/s and 12.1 rpm used in FAST, MIRAS-FLEX and MIRAS.

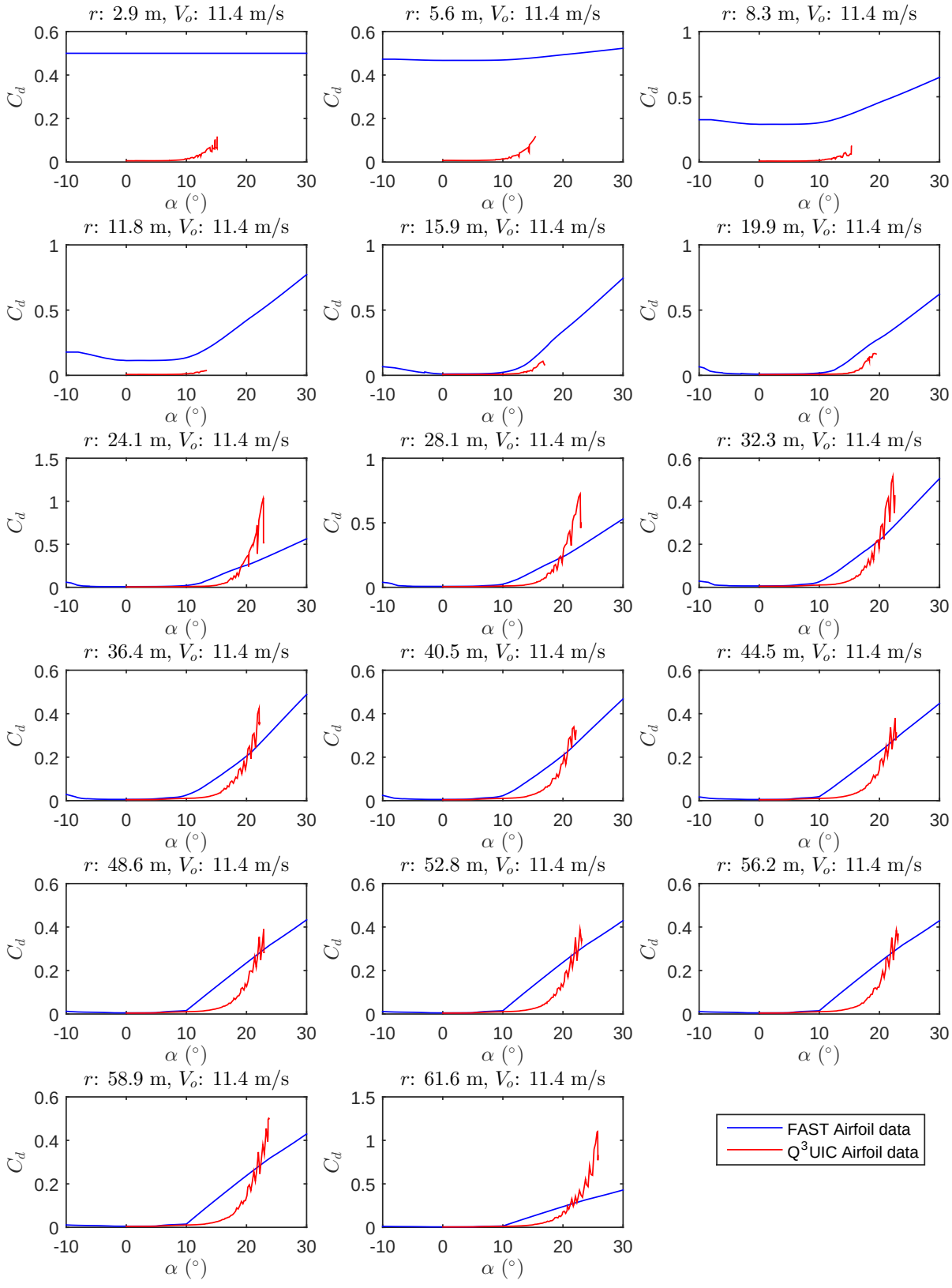


**Figure 2.20:** Airfoil drag data for 11.4 m/s and 12.1 rpm used in FAST, MIRAS-FLEX and MIRAS.

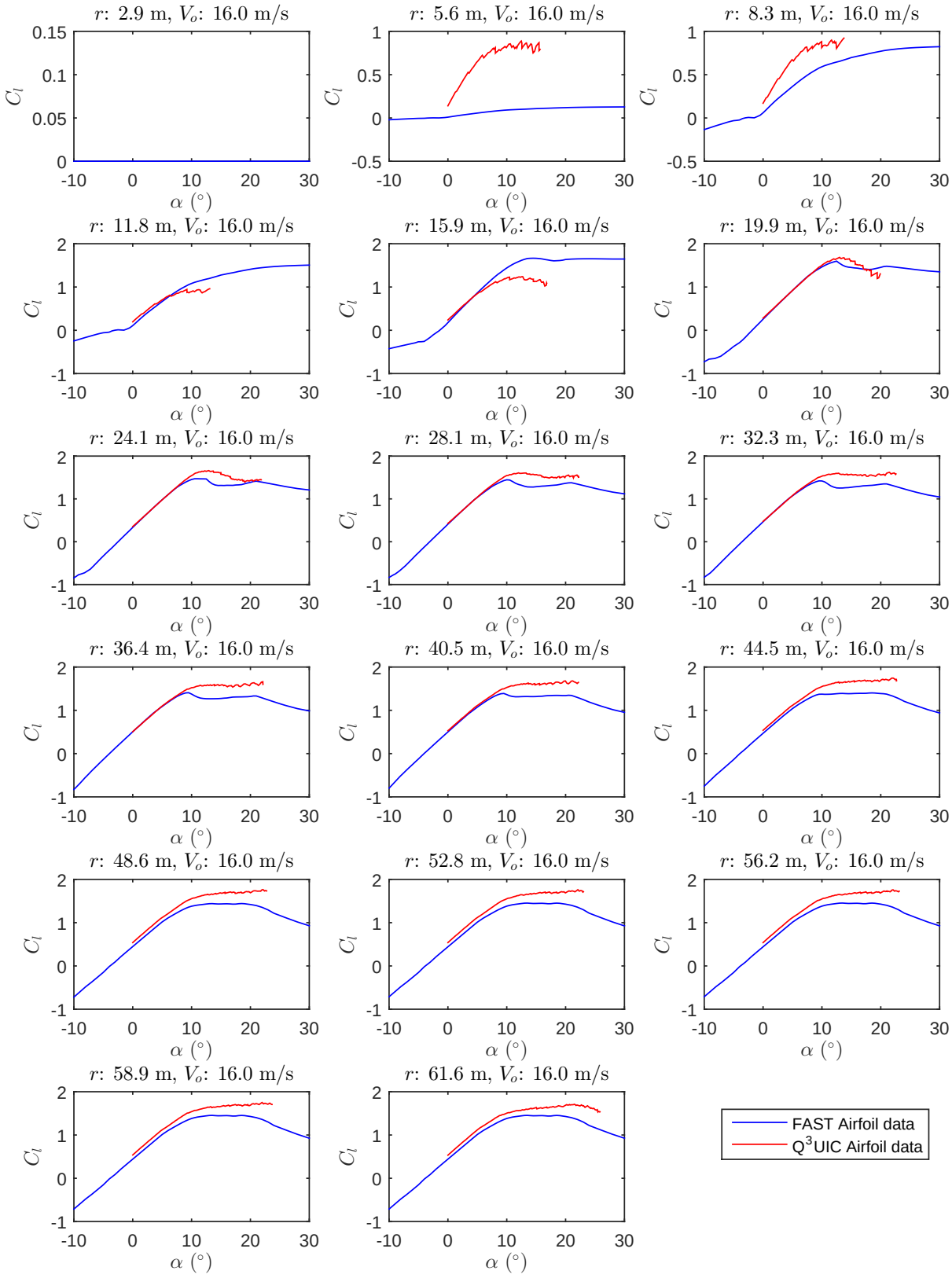


**Figure 2.21:** Airfoil lift data for 16.0 m/s and 12.1 rpm used in FAST, MIRAS-FLEX and MIRAS.

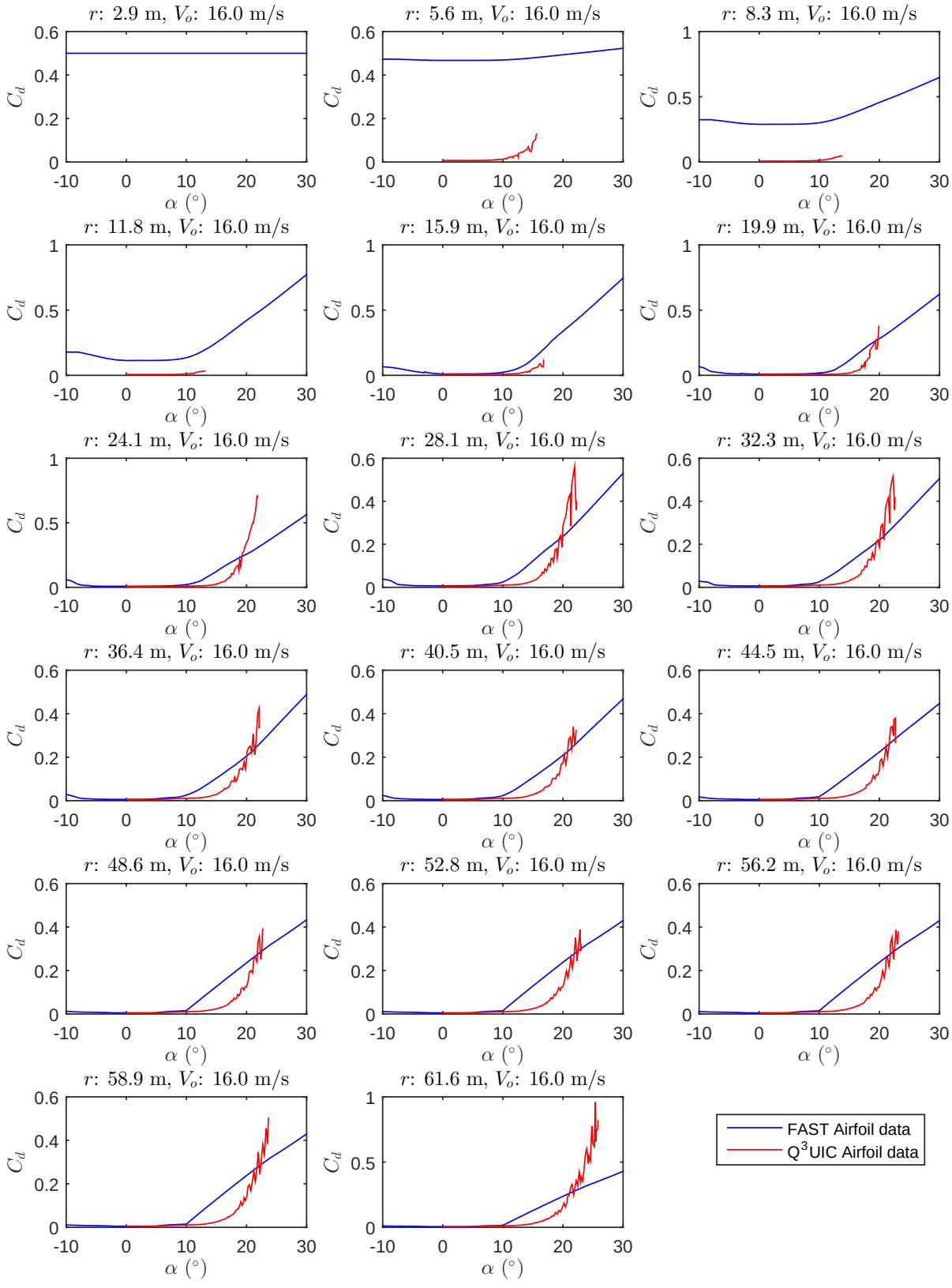


**Figure 2.22:** Airfoil drag data for 16.0 m/s and 12.1 rpm used in FAST, MIRAS-FLEX and MIRAS.

### 2.3.4 Extending the Degrees of Freedom in MIRAS-FLEX

To realistically model the elastic behavior of the entire wind turbine, the DOFs in MIRAS-FLEX was extended beyond the DOFs that describe the blade deformations in time. The additional DOFs include tower, yaw, angular displacement, shaft torsion, etc. For example, Figures 2.23 and 2.24 depict the longitudinal and transverse tower-top displacement/rotation DOFs, respectively, in MIRAS-FLEX. Yaw and tilt DOFs are depicted in Figures 2.25 and 2.26, respectively. Equation (2.18) was reformulated in terms of the values of the DOFs, $X$, for all DOFs in FLEX5 (not only the blade) as shown in Equation (2.20):

$$X^{n+1} = X^n + \alpha_0 \Delta t \dot{X}^n + \alpha_1 \Delta t (\dot{X}^n - \dot{X}^{n-1}) \tag{2.20}$$

The loosely-coupled approach using the structural predictor step of Equation (2.20) was not able to produce stable results when DOFs were enabled for multiple turbine components simultaneously, e.g. blades, tower and shaft. It was necessary to improve the coupling methodology in order to resolve the instability issues in MIRAS-FLEX. Section 2.4 will describe the improved coupling methodology.

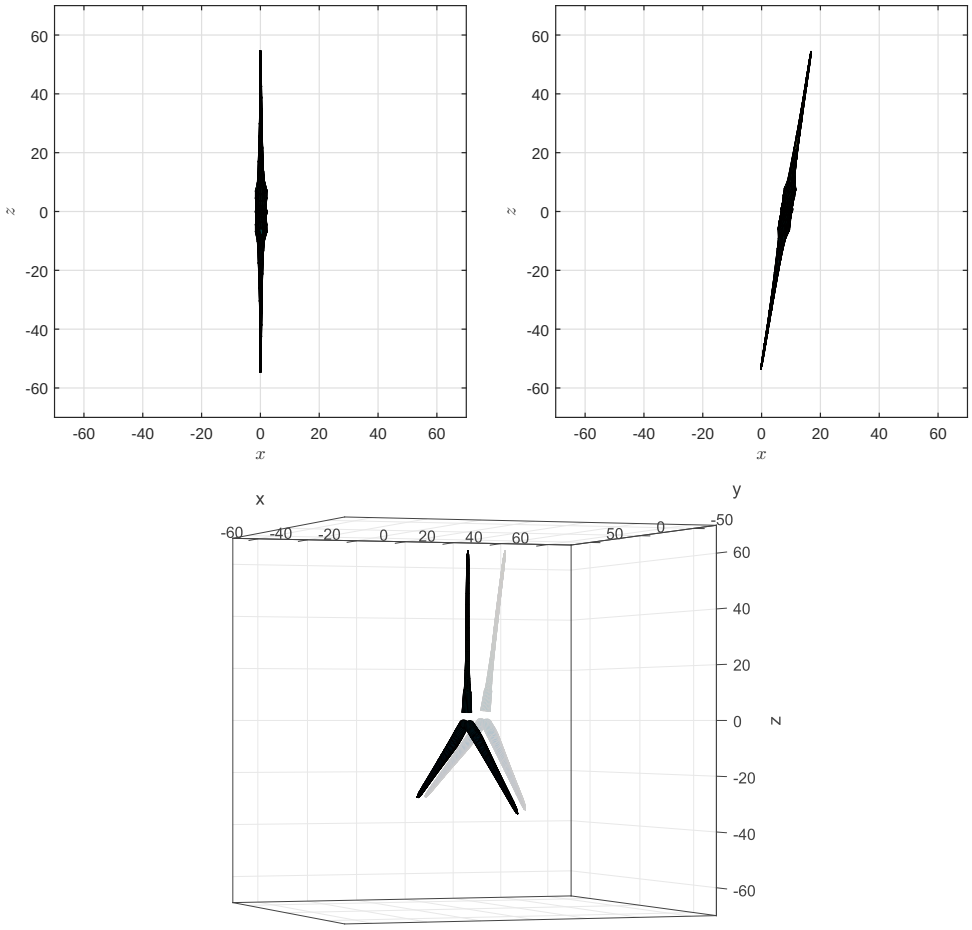


**Figure 2.23:** First longitudinal tower degree of freedom (translation+rotation) in MIRAS-FLEX. Top: Side view of wind turbine rotor where undeflected and deflected tower states are shown on the left and right respectively. Bottom: Perspective view.

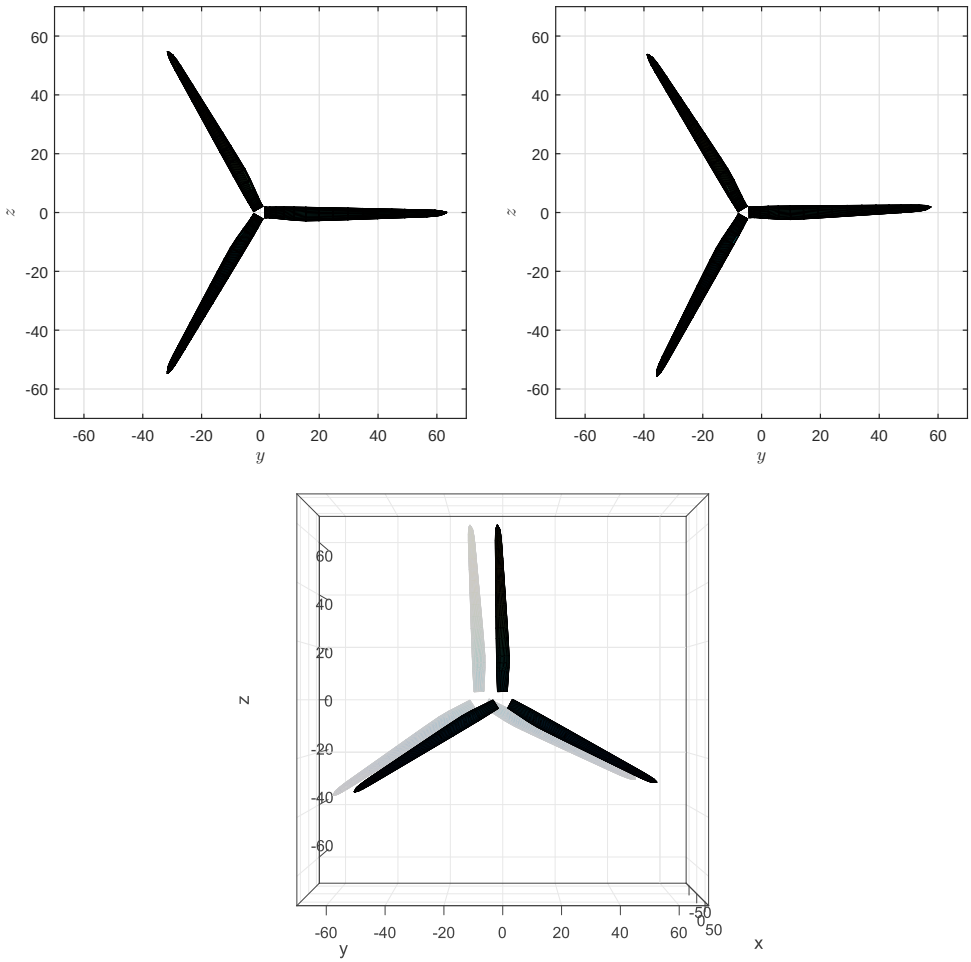


**Figure 2.24:** First transverse tower degree of freedom (translation+rotation) in MIRAS-FLEX. Top: Front view of wind turbine rotor where undeflected and deflected tower states are shown on the left and right respectively. Bottom: Perspective view.

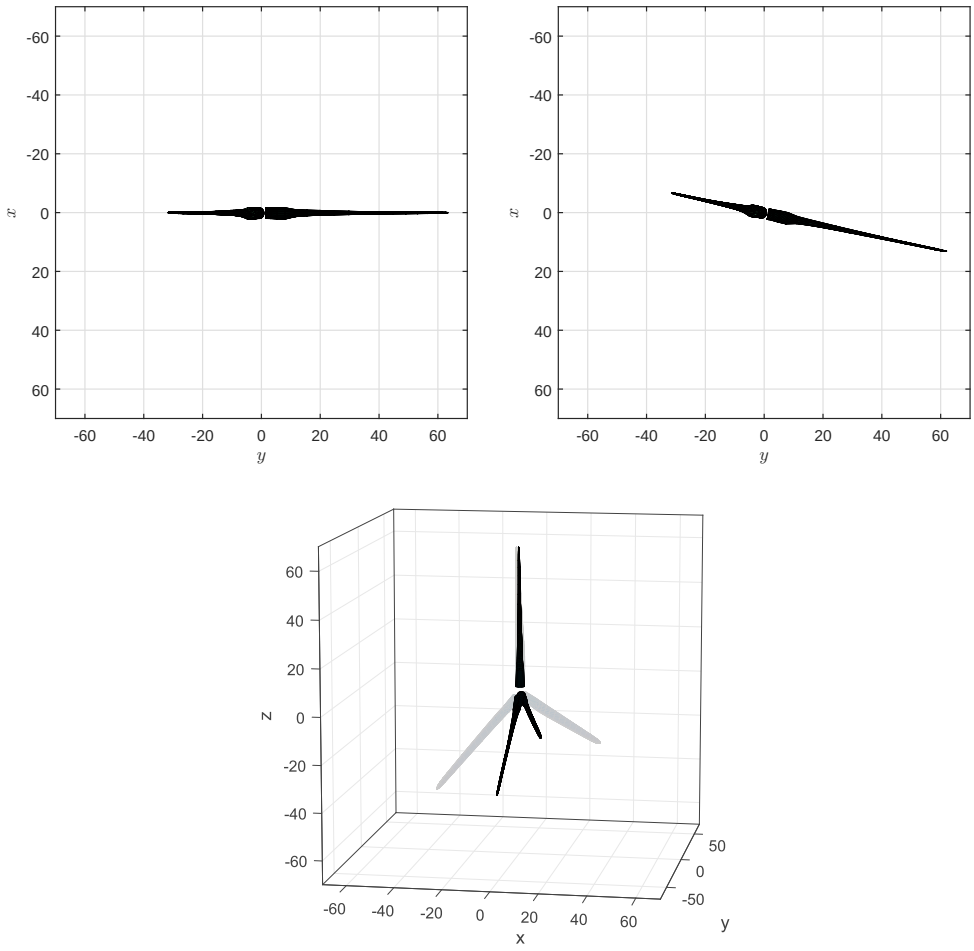


**Figure 2.25:** Yaw degree of freedom (rotation) in MIRAS-FLEX. Top: Top view of wind turbine rotor where normal and yawed states are shown on the left and right respectively. Bottom: perspective view.

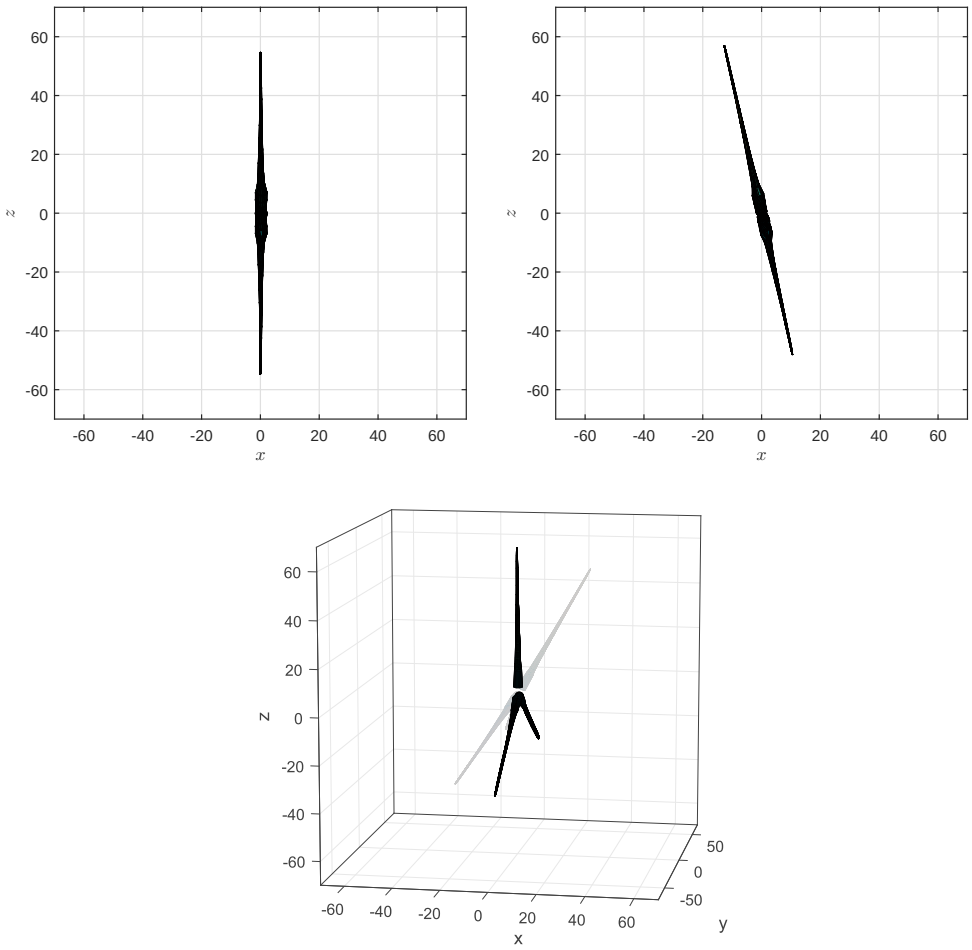


**Figure 2.26:** Tilt degree of freedom (rotation) in MIRAS-FLEX. Top: Side view of wind turbine rotor where normal and tilted states are shown on the left and right respectively. Bottom: perspective view.

## 2.4 Coupling Methodology - Second Attempt

This section will describe the more advanced coupling methodology implemented. First, the predictor-corrector approach will be described in subsection 2.4.1. An outline of the comparison tests is presented in subsection 2.4.2. Then, the results using the predictor-corrector approach will be shown in subsection 2.4.3.

### 2.4.1 Predictor-Corrector, Loosely-Coupled, Multi-Rate Methodology

A predictor-corrector, loosely-coupled, and multi-rate methodology was chosen to transfer the aerodynamic loads as well as the deformations and velocities between MIRAS and FLEX5. The methodology is depicted in Figure 2.27, where MIRAS was selected as the slower subsystem in the multi-rate approach due to its higher computing cost. Loose coupling has been shown to be effective for aero-elastic problems in [44, 117] and the multi-rate approach provides the user the choice to use a more time-efficient solver depending

on the simulation. For example, multi-rate will be more efficient for steady cases with few excitations in the aerodynamic forces, see e.g. subsection 2.4.3. Multi-rate will particularly be useful in optimization studies consisting of steady simulations and the computational time per call to MIRAS-FLEX must be kept to a minimum (see e.g. Chapter 5). For problems where aerodynamic forces vary in small time-steps, one-to-one loose-coupling is performed by setting the time-step in MIRAS equal to the smaller time-step of FLEX5, see e.g. subsections 2.4.3, and 2.4.3. For the case when one-to-one coupling is not used, the smaller time steps of FLEX5 are represented by the tick marks on the FLEX5 arrows in Figure 2.27. The instance when MIRAS is called more times than FLEX5 per time-step has not been considered in the coupling due to the higher computational cost of MIRAS compared to BEM. Strong coupling was not implemented for the same reason. Even though, the benefits from using strong coupling in place of loose coupling for aero-elastic problems are also not entirely evident [44, 117]. If instabilities occur in simulations, the instabilities might be mitigated by reducing the time-step instead of adding sub-iterations as used in strong coupling.

The predictor consists of an aerodynamic predictor step using a first- or second-order Euler and a call to FLEX5. The deflections obtained from FLEX5 based on the predicted aerodynamic load is then transfered to MIRAS to calculate the "correct" aerodynamic load. The correct deflections are obtained by calling FLEX5 for a second time. When MIRAS is called, the aerodynamic predictor step is called soon after and stored for the next time-step. The second call to FLEX5 spans two MIRAS time steps. The predictor-corrector procedure is repeated for each MIRAS time-step, see steps 1 to 4 in Figure 2.27. The aerodynamic load used for the sub-timesteps within the Runge-Kutta-Nyström in FLEX5 is linearly interpolated. Steps 'a' to 'e' are initialization steps carried out only at the beginning of a simulation. Steps 'a' to 'e' and 1 to 4 depicted in Figure 2.27 are summarized below:

a. Initialize MIRAS: Read blade geometry file and user-defined inputs such as wind speed, shear, etc.;
b. Run one time-step of MIRAS to get a load ready for FLEX5 initialization;
c. Initialize FLEX5: Read stiffness data and enabled DOFs, as well as compute initial conditions;
d. Run the aerodynamic predictor using 1st order Euler and store interpolated loads based on FLEX5 time step;
e. Call FLEX5 to obtain deflections and velocities based on predicted aerodynamic load. Send deflections and velocities for the call to MIRAS;
1. Run MIRAS to determine the correct aerodynamic load;
2. Run the aerodynamic predictor and store it for the next time step;
3. Call FLEX5 to calculate the corrected deflections and velocities;
4. Call FLEX5 to obtain deflections and velocities based on predicted aerodynamic load. Repeat steps 1 to 4.

### 2.4.2 Description of Comparison Tests

This subsection gives an outline of the comparison tests performed in subsection 2.4.3. The baseline wind turbine rotor as well as how the blade mesh and airfoil data are generated is the same as described in section 2.3.2. The wind-turbine performance codes used for the MIRAS-FLEX comparison shown in subsection 2.4.3 are as follows:

1. MIRAS standalone developed at the Fluid Mechanics Section, Technical University

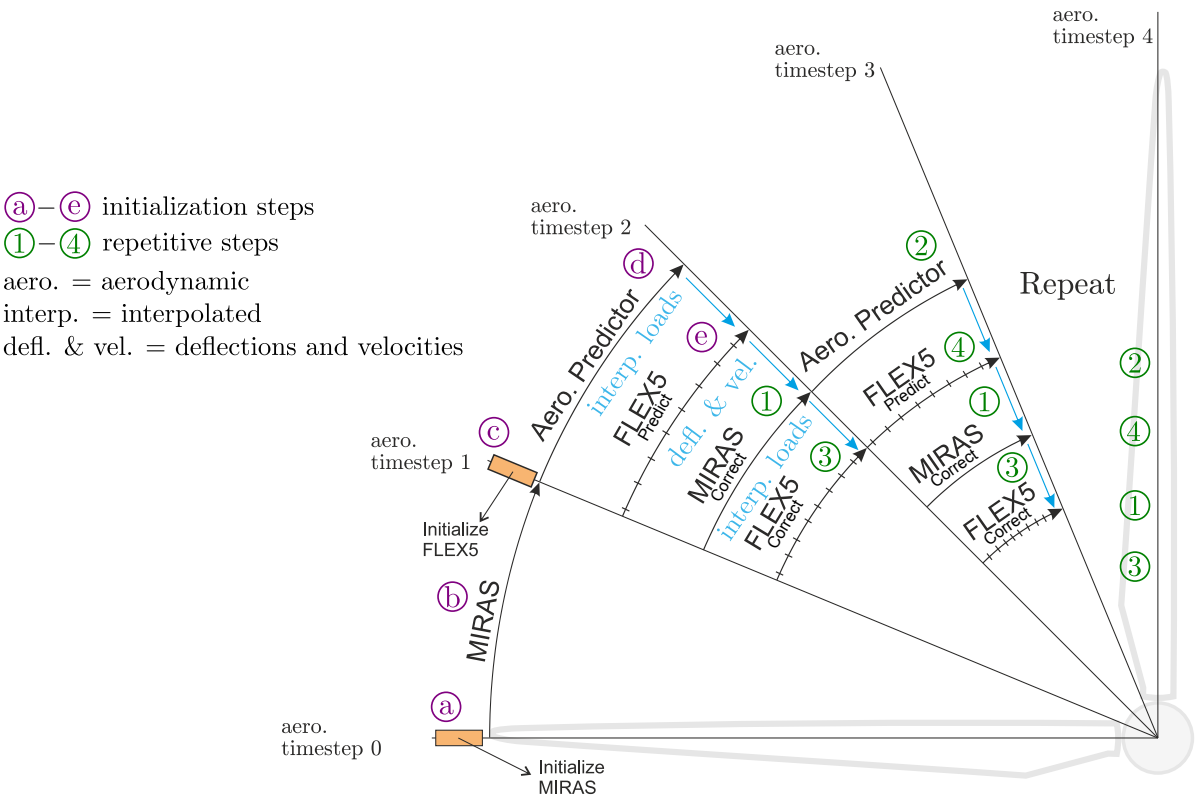


**Figure 2.27:** Azimuthal flow diagram of the predictor-corrector, loosely-coupled, and multi-rate methodology in MIRAS-FLEX. Interpolated loads (interp. loads) from MIRAS are passed onto FLEX5, while deflections and velocities (defl. & vel.) from FLEX5 are passed onto MIRAS. The black lines represent a clockwise rotating blade starting from an azimuthal position of 180° and ending at 90°.

of Denmark, see subsection 1.3.3.

2. FLEX5 developed at the Fluid Mechanics Section, Technical University of Denmark, see subsection 1.3.4. Preprocessing of the eigen-frequencies and mode shapes are computed internally in FLEX5 assuming non-rotating components with a tip mass for the tower, see [35].
3. FLEX5-Q$^3$UIC is identical to FLEX5 above, however airfoil data from reference [116] is not used. Airfoil data from Q$^3$UIC is used instead, see Figure 2.11. Comparisons of FLEX5-Q$^3$UIC with MIRAS and MIRAS-FLEX will reduce discrepancies in the results due to distinct airfoil data inputs.
4. AL-FLEX5 developed at the Fluid Mechanics Section, Technical University of Denmark. AL-FLEX5 is a 3D Navier-Stokes CFD code (EllipSys3D) coupled with FLEX5 via the actuator line (AL) approach.
5. FAST developed by NREL, United States. FAST uses a modal approach as the built-in default, however a multi-body formulation of the turbine dynamics is possible by integrating FAST with ADAMS [118]. There is also the option to use a finite-element approach using geometrically exact beam theory to model the turbine blades [55, 119]. In this work the built-in modal approach in FAST is used to model the turbine structural dynamics. Although much effort was placed in producing correct results from FAST, values presented herein are for reference only (i.e. an experienced FAST user may obtain different results). In the present work, eigen-frequencies and mode shapes are computed externally using the simple mode-shape

generator tool, Modes [120], and given as input to FAST.
For FLEX5 and FAST computations, the airfoil data from [116] is used for all wind and rotor speed conditions. Table 2.2 summarizes the modeling capabilities for the codes used in the test cases. Definition of terms in Table 2.2 will not be given in this article, but can be found in references adjacent to the term. As can be seen in Table 2.2, BEM requires engineering (Eng.) models for many aerodynamic situations, which are intrinsic in the 3D panel free wake vortex particle method (3D-PFWVP) of MIRAS.

**Table 2.2:** Comparison of modeling capabilities for codes used in comparison tests. BEM requires engineering (Eng.) models for many aerodynamic situations, which are intrinsic in the 3D panel free wake vortex particle method (3D-PFWVP).

| Model/Situation | MIRAS-FLEX | MIRAS | FLEX5 | FLEX5-Q$^3$UIC | FAST |
|---|---|---|---|---|---|
| Aerodynamic model | 3D-PFWVP | 3D-PFWVP | BEM | BEM | BEM |
| Axial induction | Intrinsic | Intrinsic | Intrinsic | Intrinsic | Intrinsic |
| Tangential induction | Intrinsic | Intrinsic | Intrinsic | Intrinsic | Intrinsic |
| Radial induction | Intrinsic | Intrinsic | None | None | None |
| Finite number of blades [35] | Intrinsic | Intrinsic | Eng. model | Eng. model | Eng. model |
| Oblique inflow [109] | Intrinsic | Intrinsic | Eng. model | Eng. model | Eng. model |
| Turbulent wake state [35] | Intrinsic | Intrinsic | Eng. model | Eng. model | Eng. model |
| Dynamic inflow [110] | Intrinsic | Intrinsic | Eng. model | Eng. model | Eng. model |
| Stall delay [121] | Intrinsic[1] | Intrinsic[1] | Eng. model | Eng. model | Eng. model |
| Dynamic stall [111] | Eng. model | Eng. model | Eng. model | Eng. model | Eng. model |
| Pressure coefficients[2] | 3D | 3D | None | 2D | None |
| Wake characteristics[3] | 3D | 3D | None | None | None |
| Structural dynamic model | Modal | None | Modal | Modal | Modal |

[1] By using Q$^3$UIC and strip theory [97, 93].
[2] See Figs. 2.30 and 2.40.
[3] See Figs. 2.35, 2.41, and 2.45.

The list of test cases for the MIRAS-FLEX comparison are as follows:

**Test case 1:** Steady and uniform wind inflow of 10 and 15 m/s wind speeds with a rotor RPM of 424.5 from the MEXICO [80] project (Model rotor EXperiments In COntrolled conditions). Although the methodology used to create the blade mesh is identical to the one described for the NREL 5 MW, the MEXICO rotor has a diameter of 4.5 m and uses cylindrical, DU 91-W2-250, RISØ A1-21, and NACA 64-418 airfoils instead. The MEXICO experiment allows measurements to be compared with FAST, FLEX5, and MIRAS, since measurements for the NREL

5 MW do not exist. Since the MEXICO rotor is small and stiff, structural dynamics are neglected and only an aerodynamic comparison is performed here.

**Test case 2:** Comparison with AL-FLEX5. Steady and uniform wind inflow of 8 m/s without tower shadow or wind shear. Tip-speed ratio of 7.55.

**Test case 3:** Steady and uniform wind inflow at speeds ranging from 4 m/s to 14 m/s. Tip-speed ratio of 7.55 is maintained up to the maximum rotor speed of 12.1 RPM which occurs at 10.6 m/s. For wind speeds from 10.6 m/s to 14 m/s rotor speed is maintained at 12.1 RPM, decreasing the tip-speed-ratio for increasing wind speeds. Pitch angle is set to a fixed value of zero for all wind speeds. Pitch regulation at rated power has been omitted, since the stall behavior of MIRAS/MIRAS-FLEX and how it compares with FLEX5 and FAST is more interesting to observe. DOFs considered are 1st flap and 1st edge blade modes only. FLEX5 and FAST are used to compare with MIRAS-FLEX. Tower shadow, tilt angle and gravity were set to zero to obtain non-oscillating loads.

**Test case 4:** Steady wind inflow of 8 m/s with 15° yaw, prescribed power-law wind shear of 0.3, and tip-speed ratio of 7.55. A 15° yaw simulation with wind shear was performed to experiment MIRAS-FLEX for non-axisymmetric conditions. DOFs considered include 1st flap and edge blade modes, 1st for-aft and side-side tower modes, and shaft torsion. Tower shadow is neglected. Due to slightly different eigen-frequency and mode-shape calculations, second-order blade modes are not considered to obtain better agreement between FLEX5 and FAST, which are used to compare with MIRAS-FLEX. Second-order tower modes in FLEX5 supply rotations, but in FAST they supply displacements instead. Therefore, second-order tower modes are also disabled for fair comparison.

**Test case 5:** Comparison to Phase I of the OC3 project [122]. Computations for three load cases were performed and are compared with the publicly available data from project participants. The three load cases are described in Table 2.3. Load case 2.1a consists of a steady and uniform wind speed at 8 m/s with no shear, where the rotor speed is held constant with a fixed blade pitch. There are no wave conditions and structural dynamic modeling is absent. Load case 2.1a is a purely aerodynamic analysis and was designed to quantify differences in aerodynamic modeling from the OC3 participant codes. Similarly as in load case 2.1a, load case 3.1 consists of a steady and uniform wind speed at 8 m/s with no shear and no wave conditions. However, tower, drivetrain and blade DOFs are enabled. In addition, rotational speed and pitch control are active. Only FLEX5 and MIRAS-FLEX computations are added to the comparisons. FAST computations performed by NREL staff are among the OC3 participants. Other participant codes include NREL Adams, GH Bladed, and DTU-Risø HAWC2. Load case 3.2 is the same as load case 3.1 except a turbulent wind inflow with a 11.4 m/s hub wind speed is specified. The publicly available Mann turbulent wind input files used in OC3 were used in the computations.

**Table 2.3:** Load cases from Phase I of the Offshore Code Comparison Collaboration project for MIRAS-FLEX computations.

| Load case | Enabled DOF | Wind conditions | Wave conditions | Analysis type |
|---|---|---|---|---|
| 2.1a | None (constant rotor speed and fixed blade pitch) | Steady, uniform, no shear: $V_o = 8\,\mathrm{m/s}$ | None | Periodic time series solution |
| 3.1 | Tower, drivetrain, blades | Steady, uniform, no shear: $V_o = 8\,\mathrm{m/s}$ | None | Periodic time series solution |
| 3.2 | Tower, drivetrain, blades | Turbulent: $V_o = 11.4\,\mathrm{m/s}$, $\sigma_1 = 1.981\,\mathrm{m/s}$, Mann model | None | Power spectra |

### 2.4.3 Simulation Results

#### Computational cost results

Table 2.4 illustrates the approximate computational cost of the codes used in the comparison tests on a Linux cluster with 2.8 GHz processors. FLEX5 and MIRAS-FLEX were compiled using Fortran 90, while the Windows executable of FAST was run through Wine [123]. FLEX5 and FAST computations were performed using a fourth-order Runge-Kutta time integrator and a time-step of 0.02 seconds for consistency. Time ratios (simulated time/computational time) for FLEX5 and FAST are based on the mean of twenty simulations: Ten simulations from test case 3 and ten simulations from test case 4. Time-steps for MIRAS-FLEX using the multi-rate approach and one-to-one coupling are approximately 0.14 and exactly 0.02 seconds, respectively. In the multi-rate approach, the larger time-step is scaled according to the rotational speed and is rounded to the nearest multiple of the smaller FLEX5 time-step. At 12.1 RPM, for example, MIRAS runs at the larger time-step of 0.14 seconds, while the time-step of FLEX5 is maintained at 0.02 seconds. For reasons explained in subsection 2.4.1, the time ratio for the multi-rate approach is valid only for simple simulations such as test cases 1, 2, and 3, otherwise loads do not convergence and results become erroneous. Lastly, the time ratio for MIRAS-FLEX with one-to-one coupling is approximately 0.0015 for all test cases except test case 1 and 2. MPI with forty cores for MIRAS-FLEX gave a fair compromise between speed and CPU consumption. FLEX5 and FAST run only on one core.

Note the time ratios in Table 2.4 are shown to provide a relative idea of the computational cost of each code only. Time ratios can vary from one computer system to another, and they depend on the number of blade elements/stations, enabled DOFs, and other inputs that affect the number of calculations per time-step, see e.g. subsection 2.3.2. In particular, MIRAS contains several parameters to control the computational speed and accuracy of the wake [106, 97], which has not been investigated in the current study. Figure 2.28 depicts the percent difference (left) and time ratios (right) versus the time-step size for 12 m/s wind speed and 12.1 RPM from test case 3. Selecting a larger time-step size in the multi-rate approach increases the time ratio, but also increases the difference in torque and thrust relative to the one-to-one coupling (time-step size = 0.02 s). In Figure 2.28, one-to-one coupling is the most accurate because the smallest time-step size is used. The smaller the time step, the more data points describing the wake per second

**Table 2.4:** Approximate computational cost for codes used in comparison tests.

| | FLEX5 (fastest) | FAST | MIRAS-FLEX multi-rate | MIRAS-FLEX one-to-one (slowest) |
|---|---|---|---|---|
| Time ratio (simulated time/computational time) | 58.945[1] | 5.034[1] | ≈ 0.024[2] | ≈ 0.0015 |
| Number of cores | 1 | 1 | 40 | 40 |

[1] The mean of twenty simulations using the 4$^{\text{th}}$ order Runge-Kutta time integrator and a time-step of 0.02 seconds.
[2] Recommended for simple simulations such as test cases 1, 2, and 3 only.

of simulation time is generated. The accuracy of the loads computed on the rotor is dependent on the wake resolution, see [97] and [106] for details.

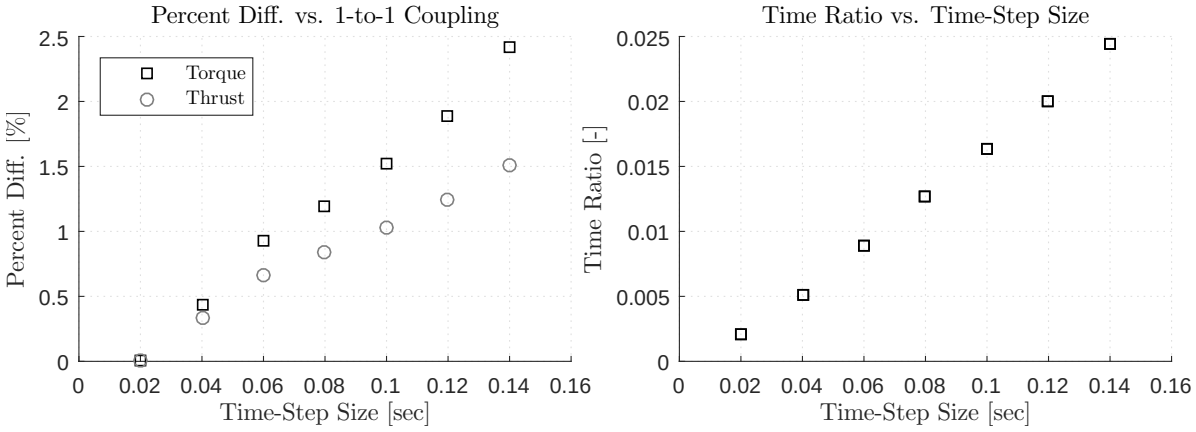


**Figure 2.28:** Percent difference in torque and thrust (left) as well as time ratios (right) versus the time-step size for 12 m/s wind speed and 12.1 RPM from test case 2.

### Test case 1: Comparison with measurements

The comparison of FAST, FLEX5, and MIRAS with measurements from MEXICO are shown in Figures 2.29 and 2.30. MIRAS results are from reference [97]. Figure 2.29 depicts the aerodynamic loads tangential (PYr) and normal (PZr) to the rotor plane for 10 (left) and 15 m/s (right) wind speeds. Tangential loads have a magnitude of 0-50 N/m, while normal loads have a magnitude of 0-500 N/m. Results for all codes generally agree with the measurements. Note that the airfoil data used in FLEX5 and FAST are based on 2D polar measurements [80], while the airfoil data for MIRAS are based on Q$^3$UIC simulations. Figure 2.30 depicts the surface pressure coefficients on the MEXICO blade at the normalized span-wise position of 0.60 for wind speeds 10 (left) and 15 m/s (right). In general, surface pressure coefficients from MIRAS are in agreement with measured values. More detailed MIRAS computations and discussions for the MEXICO rotor are available in [97, 99] and will not be repeated in the current article.

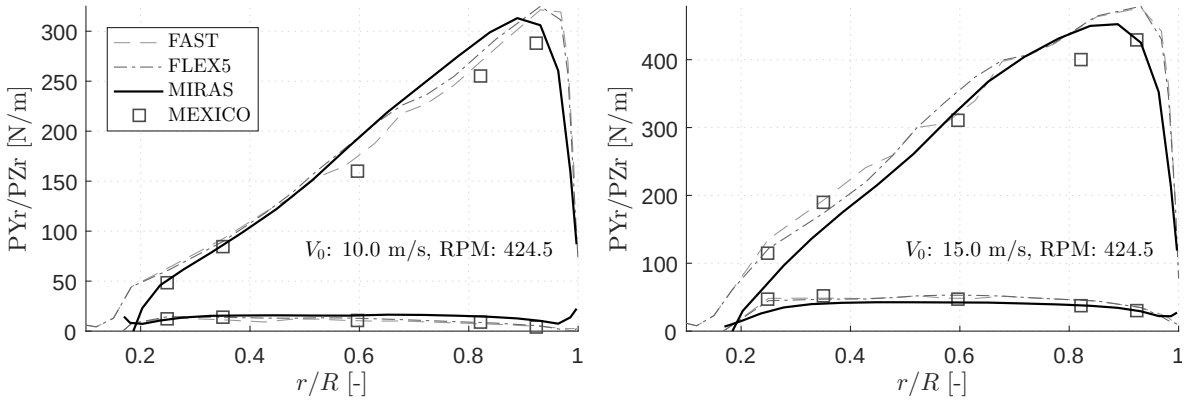


**Figure 2.29:** Aerodynamic loads tangential (PYr) and normal (PZr) to the rotor plane from FAST, FLEX5, MIRAS, and MEXICO measurements for 10 (left) and 15 m/s (right) wind speeds. Tangential loads have a magnitude of 0-50 N/m, while normal loads have a magnitude of 0-500 N/m.

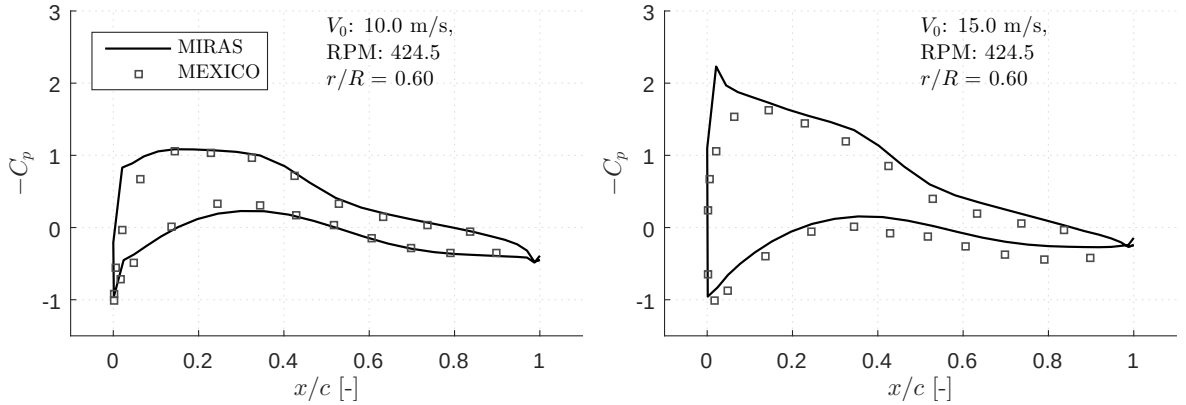


**Figure 2.30:** Pressure coefficient from MIRAS at the normalized span-wise position of 0.60 on the MEXICO blade at wind speeds 10 (left) and 15 m/s (right).

### Test case 2: Comparison with AL-FLEX5

Actuator line computations using EllipSys3D coupled with FLEX5 (AL-FLEX5) were performed to validate MIRAS-FLEX. The computational mesh in the AL-FLEX5 simulation is described in a Cartesian coordinate system containing $3 \times 3 \times 12 = 108$ super-blocks. Three super-blocks in the horizontal ($x$) and vertical ($y$) directions, and twelve in the stream-wise ($z$) direction. Each super-block contains $48^3$ cells giving a total of $108 \times 48^3 = 11.94 * 10^6$ cells in the computational domain. Each cell has a size of $dx$, $dy$, and $dz$, which varies throughout the domain except in the steam-wise direction ($dz$ = constant). The horizontal ($dx$) and vertical ($dy$) lengths of the cells encompassing the rotor at the center of the domain is equidistant ($dx = dy$ = constant), while stretching is used away from the rotor. Stretching is used to reduce unnecessary computations in areas of little interest where minimal variations in the flow-field occur. In dimensional terms, the computational domain is $20R \times 20R \times 28R$ where $R$ is the rotor radius. The equidistant region at the center of the domain where the rotor and wake lie is $6R \times 6R \times 28R$. The number of cells that capture the aerodynamic characteristics of the rotor is 19 per $R$. Figure 2.31 depicts the super-blocks as well as the iso-surface of vorticity from an AL-FLEX5 simulation. In Figure 2.31, a higher number of super-blocks and thus a higher number of cells were used to depict the iso-surface of vorticity with

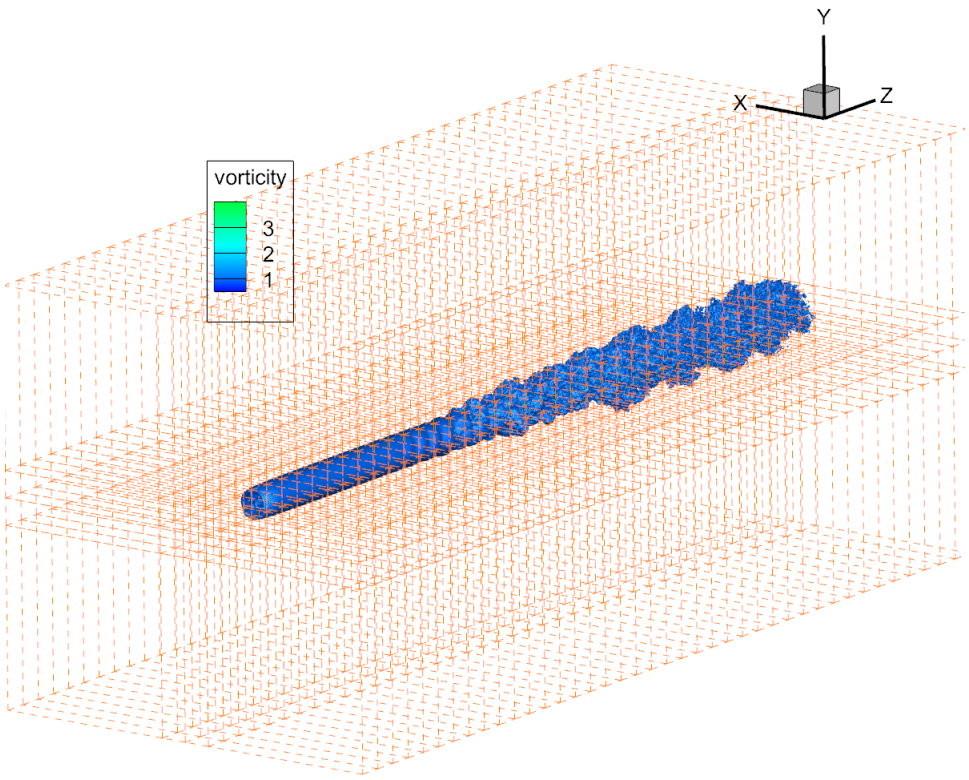


**Figure 2.31:** Computational grid and the iso-surface of vorticity from an EllipSys3D-FLEX5 actuator line simulation.

great detail.

Figure 2.32 depicts the iso-surface of vorticity of an actuator line simulation with a uniform and steady wind speed of 8.0 m/s. Figure 2.33 depicts the time averaged velocity in the stream-wise direction where a velocity deficit upstream and downstream from the rotor is clearly seen. To achieve a better agreement between all codes, the wind speed far upstream (i.e. as far away as possible from the upstream velocity deficit) in the AL-FLEX5 simulation was specified as the free-stream wind speed in FLEX5 and MIRAS-FLEX, which is 8 m/s.

Figure 2.34 shows a comparison of MIRAS-FLEX, FLEX5, and AL-FLEX5 for the NREL 5 MW wind turbine. In general, good agreement is obtained for all quantities. Minor discrepancies between 0 and 5% difference relative to FLEX5, occur for the flap-wise root-bending moment (Flap M R= 1.5m), rotor shaft thrust (Shaft (R1-sys), Thrust), and axial nacelle displacement (Nacelle Z). Larger discrepancies between 5 and 10%, appear for the tower torsion (Tower torsion), flap-wise deflection (Flapwise defl.), rotor shaft torque (Shaft (R1-sys), Torque), and tangential nacelle displacement (Nacelle Y). Discrepancies relating to MIRAS-FLEX are largely due to distinct airfoil data usage. MIRAS-FLEX airfoil data are based on $Q^3$UIC computations, while airfoil data from [116] were used for FLEX5 and AL-FLEX5. Discrepancies with respect to AL-FLEX5 are likely due to the distinct modeling of the flow physics, since MIRAS-FLEX and FLEX5 do not capture the three-dimensional flow field upstream of the rotor. Increasing the resolution of the mesh near the rotor in the AL-FLEX5 calculation might reduce discrepancies. A thorough investigation for such discrepancies has not been conducted.

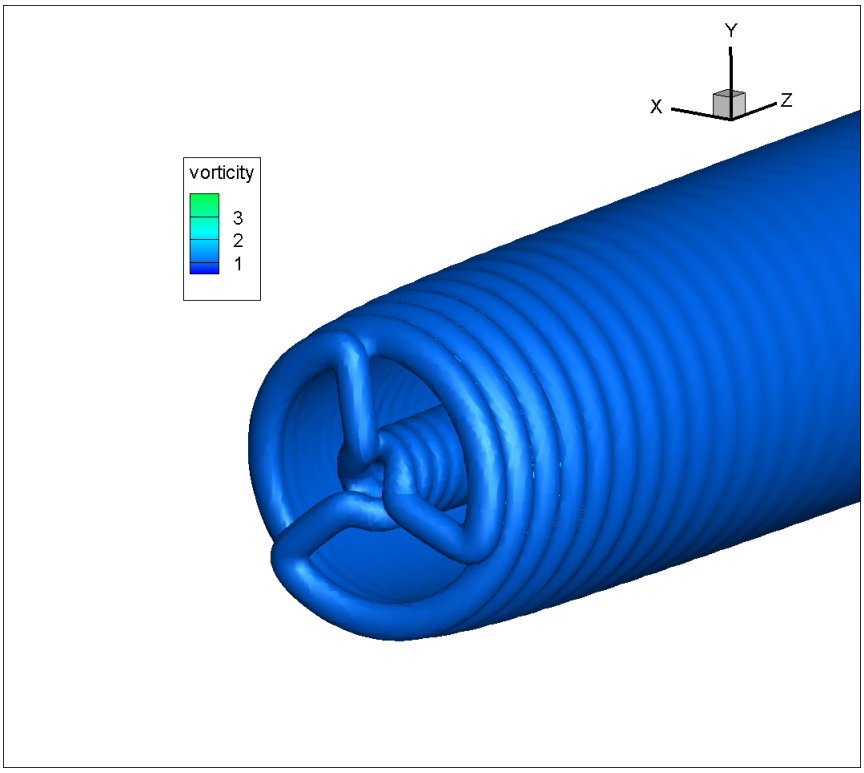


**Figure 2.32:** Iso-surface of vorticity from an EllipSys3D-FLEX5 actuator line simulation.

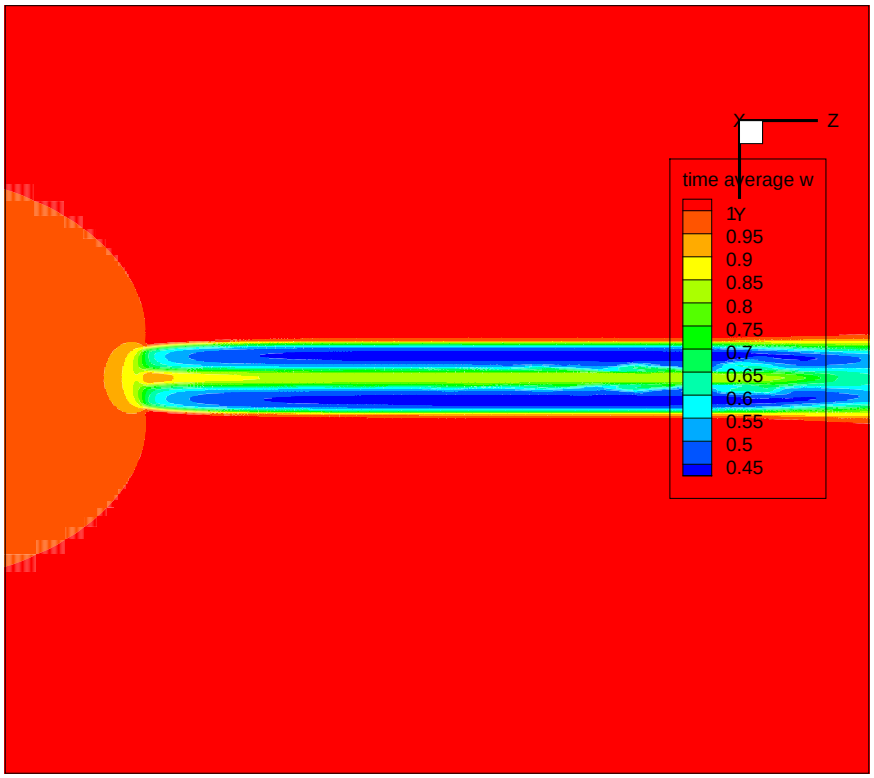


**Figure 2.33:** Time averaged velocity in the stream-wise direction (normal to the rotor plane).

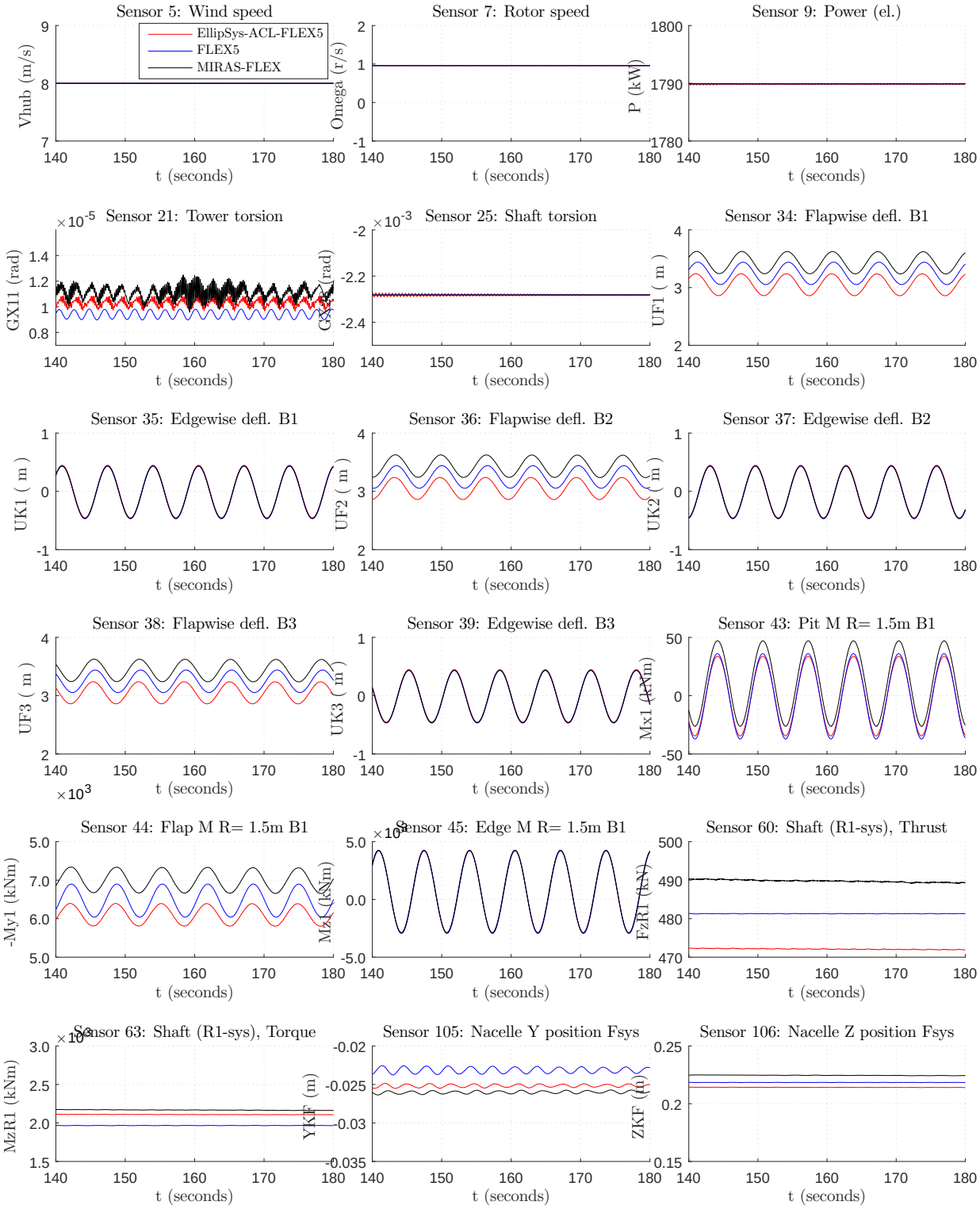


**Figure 2.34:** Comparison of MIRAS-FLEX, FLEX5 and AL-FLEX5 for the NREL 5 MW wind turbine.

### Test case 3: Steady and uniform wind inflow

The wake development in MIRAS and MIRAS-FLEX is illustrated in Figure 2.35. Figure 2.36 depicts the aerodynamic power (top left), thrust (top right), and torque (bottom left), as well as rotor RPM (bottom-right) versus wind speed, $V_o$, for comparison between

FAST, FLEX5, FLEX5-Q$^3$UIC, MIRAS-FLEX and MIRAS. FLEX5 results are almost identical to FAST since both codes use BEM and the modal approach for the aerodynamic and structural dynamics, respectively. MIRAS-FLEX and MIRAS agree well with FLEX5 and FAST, except for the aerodynamic power. MIRAS and MIRAS-FLEX predict higher aerodynamic power, particularly at high wind speeds, than FLEX5 and FAST. The higher aerodynamic power is the result of the higher tangential load predicted by MIRAS and thus a higher aerodynamic torque, see Figure 2.37. In Figure 2.36, the blade deflections present in MIRAS-FLEX is shown to reduce the aerodynamic torque and power slightly compared to MIRAS alone.

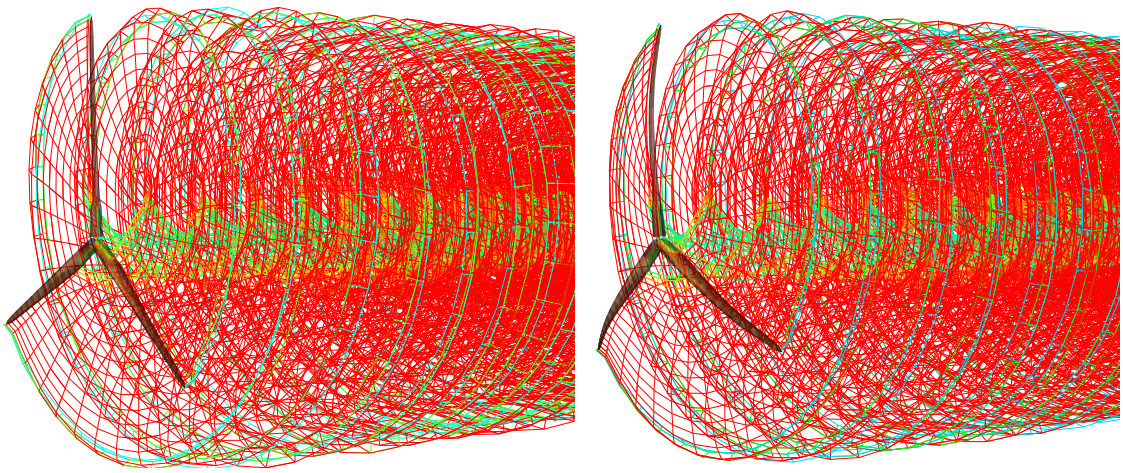

**Figure 2.35:** Wake computed with MIRAS alone (left) and MIRAS-FLEX (right) for a steady uniform wind speed of 14 m/s and a rotor speed of 12.1 RPM.

Figure 2.37 depicts the aerodynamic loads tangential (PYr) and normal (PZr) to the rotor plane, as well as the angle of attack (AoA) from all codes for increasing wind speeds and rotor RPM. Similarly, Figure 2.38 depicts the in-plane (IPDefl) and out-of-plane (OoPDefl) deflections, and angle of attack (AoA) from all codes. In general, the loads from MIRAS and MIRAS-FLEX are similar to FLEX5 and FAST. Observing the results from MIRAS and MIRAS-FLEX as compared to FLEX5 and FAST, the tangential load is higher from the blade root to tip, and deviations occur near the root and tip for the normal load and angle of attack results. The deviations in the normal load are primarily due to different airfoil data as shown by FLEX5-Q$^3$UIC in Figure 2.37 and the airfoil lift coefficient comparison in Figure 2.39. In addition to differences in rotational-effect corrections, the airfoil data from [116] are based on Reynolds numbers of 6 and 7 million, and do not represent the actual Reynolds number on the blade as computed by the Q$^3$UIC and MIRAS codes, see Figure 2.39. FLEX5-Q$^3$UIC in Figures 2.36 and 2.37 demonstrates that using the Q$^3$UIC lift and drag coefficients in place of the reference data from [116] produces results in better agreement with MIRAS and MIRAS-FLEX. Compared to FLEX5-Q$^3$UIC, differences are due to the 3D computation of the pressure coefficient in MIRAS and MIRAS-FLEX giving a higher pressure coefficient and thus higher lift than 2D values, described later.

Particularly at higher wind speeds, blade deflection in MIRAS-FLEX is shown to reduce the load at the tip, but also increase the load at the midspan when compared to MIRAS alone. The increase in load at the midspan is due to the straightening of blade, neutralizing the effect of the precone and exposing the blade more to the wind inflow. The opposite effect is seen at the tip where deflections are very large, causing the blade

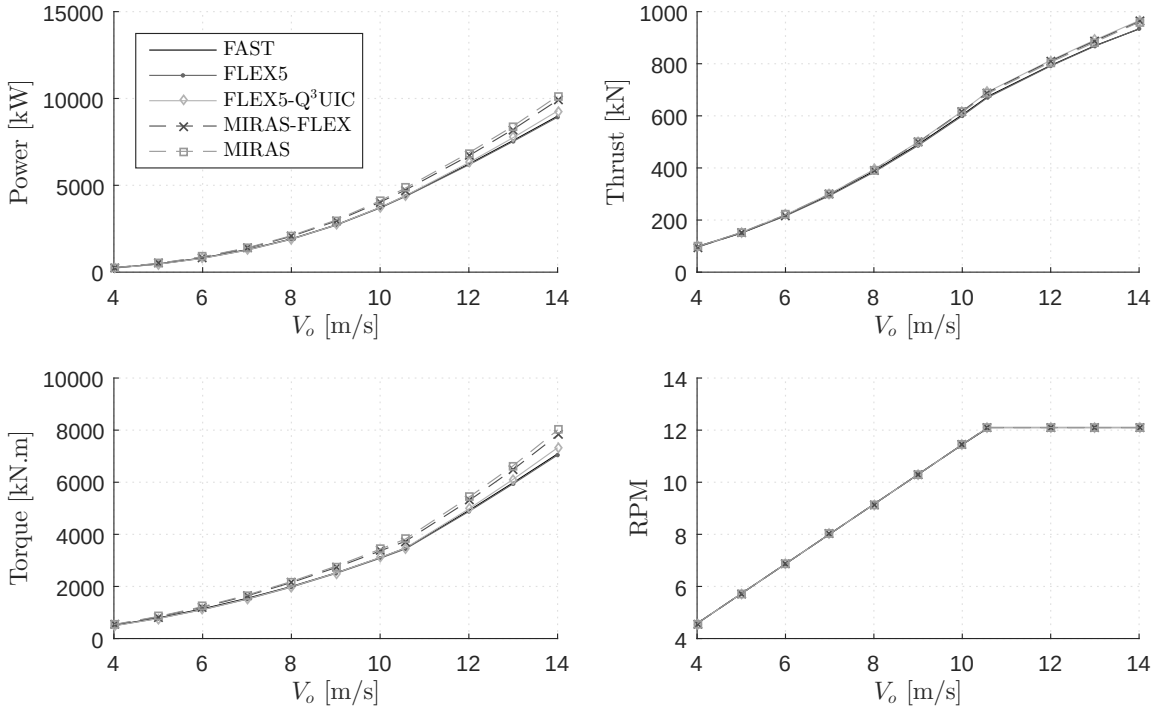


**Figure 2.36:** Aerodynamic power (top left), thrust (top right), and torque (bottom left), as well as rotor RPM (bottom-right) versus wind speed, $V_o$, for comparison between FAST, FLEX5, FLEX5-Q$^3$UIC, MIRAS-FLEX and MIRAS.

to be less exposed to the wind. Since the torque calculation is influenced more by the loads in the tip region, the torque and power for MIRAS-FLEX is less than MIRAS as illustrated in Figure 2.36.

The pressure coefficient, $C_p$, for stations located at the normalized span-wise positions of $r/R = 0.23$, 0.58 and 0.97 of the undeflected blade are shown in Figure 2.40 for FLEX5-Q$^3$UIC, MIRAS-FLEX and MIRAS. Note $r/R$ will be slightly smaller for MIRAS-FLEX results due to axial deflection. For $r/R = 0.23$, the large pressure gradient between $x/c = 0$ and 0.4 indicates the likelihood of flow transition and separation, while the inverted $C_p$ at $x/c = 0.4$, particularly at low wind speeds, indicates a negative contribution to the sectional lift force. These results are expected because the section at $r/R = 0.23$ is near the root with a large thickness-to-chord airfoil profile, and is also experiencing very large angles of attack. For $r/R = 0.58$ and 0.97, normal behavior of attached flow is observed. Particularly at higher wind speeds, slightly larger $C_p$ values on the suction and pressure sides are seen from MIRAS-FLEX compared to MIRAS for $r/R = 0.23$ and 0.58, but slightly smaller $C_p$ for $r/R = 0.97$. The changes in $C_p$ are due to the same reasons as discussed previously for the changes in the load distribution in Figure 2.37. Although FLEX5-Q$^3$UIC computations were performed using lift and drag coefficients, see Figure 2.11, $C_p$ curves used to compute the corresponding coefficients are available from Q$^3$UIC. $C_p$ curves from FLEX5-Q$^3$UIC in Figure 2.40 show reduced values particularly at $r/R = 0.23$ and 0.58 in comparison with MIRAS and MIRAS-FLEX. Tangential force coefficient calculations at $r/R = 0.58$ yielded higher values for MIRAS and MIRAS-FLEX in comparison with FLEX5-Q$^3$UIC, which explains the higher tangential force, torque and power seen in Figures 2.36 and 2.37. Good agreement was found for $C_p$ curves on the blade surface from MIRAS when compared with measurements from MEXICO in test case 1 and [97]. For verification purposes, however, the $C_p$ curves

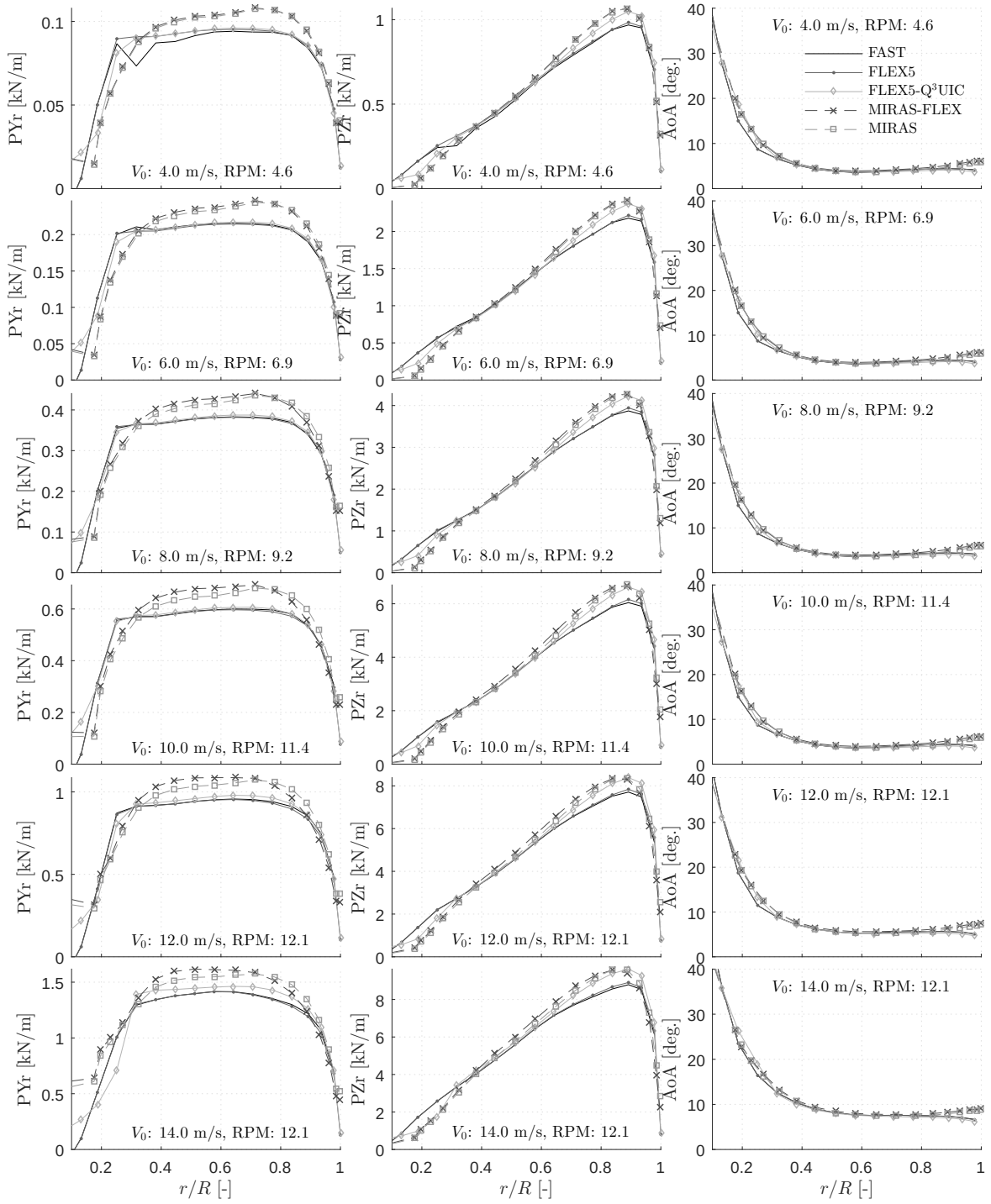


**Figure 2.37:** Aerodynamic loads tangential (PYr) and normal (PZr) to the rotor plane, and angle of attack (AoA) comparison between FAST, FLEX5, FLEX5-Q$^3$UIC, MIRAS-FLEX and MIRAS for increasing wind speeds and rotor RPM.

for the NREL 5 MW in Figure 2.40 should be compared with another tool such as CFD, since measurements do not exist. The $C_p$ curves are presented herein to demonstrate that MIRAS-FLEX is able to output this information, unlike BEM-based aero-elastic codes. They are shown for qualitative purposes, so that the influence of blade deformations on the $C_p$ curves as well as how the $C_p$ curves compare with FLEX5-Q$^3$UIC can be studied.

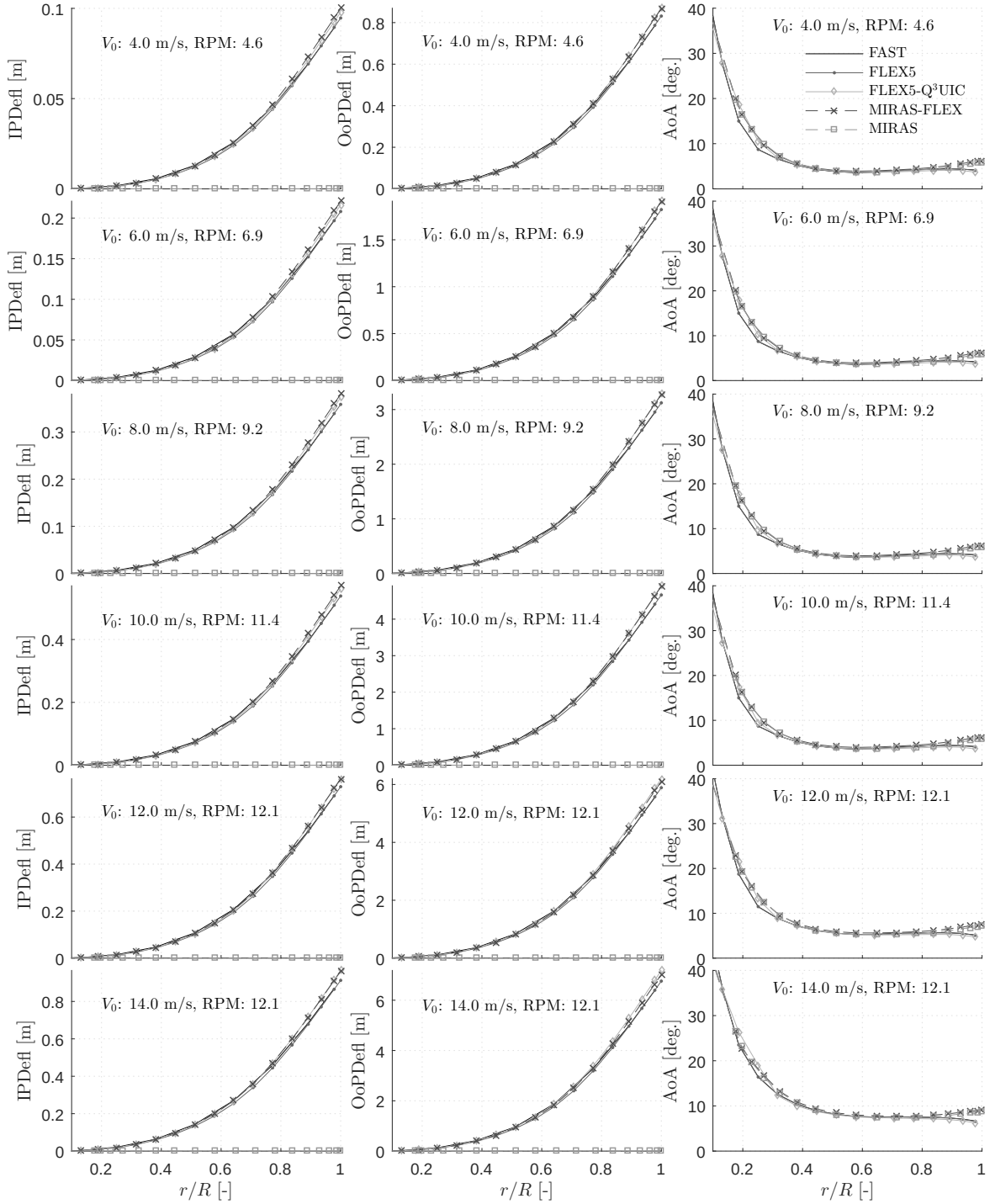


**Figure 2.38:** In-plane (IPDefl) and out-of-plane (OoPDefl) deflections, and angle of attack (AoA) comparison between FAST, FLEX5, FLEX5-Q$^3$UIC, MIRAS-FLEX and MIRAS for increasing wind speeds and rotor RPM.

### Test case 4: Steady wind inflow with yaw and shear

Figure 2.41 gives a visual representation of the 15 degree yaw and prescribed power-law wind shear of 0.3 simulation, while Figure 2.42 displays the time series. In the order from left to right and top to bottom, starting at the top-left and ending at the bottom-right, are the values of rotor torque and thrust, out-of-plane and in-plane root bending moments,

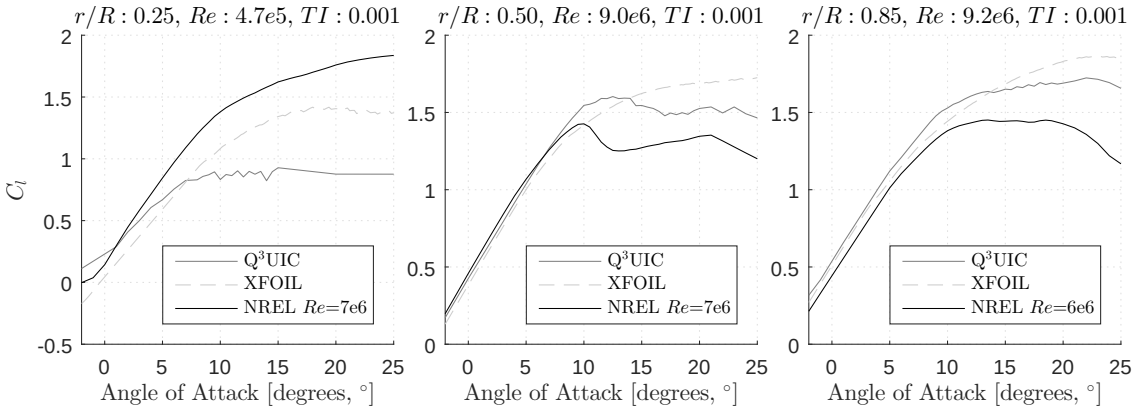


**Figure 2.39:** Lift coefficient comparison for 10.0 m/s and 11.4 RPM between Q$^3$UIC, XFOIL and airfoil data from reference [116] (NREL). Only stations $r/R = 0.25$, $r/R = 0.50$ and $r/R = 0.85$ are shown. Deviations in the normal aerodynamic load in Figure 2.37 are primarily due to differences in lift coefficient between AoA=0° and 9° for $r/R = 0.25$ and $r/R = 0.85$. TI is the turbulence intensity.

out-of-plane and in-plane tip deflections, for-aft and side-side tower-top deflections, as well as nacelle yaw and rotor speed. In general, results for all three codes show good agreement. Discrepancies between FLEX5 and FAST for blade and tower deflections are caused by differences in the eigen-frequency and mode-shape calculations, despite using identical inputs to both codes. Differences in rotor torque and thrust between FAST and FLEX5, which do not occur in test case 1, indicates that yaw in both codes may not be modeled in the same manner[1]. The higher prediction of rotor torque for MIRAS-FLEX than FLEX5 is expected from the test case 3 study. Differences are found in the out-of-plane root-bending moment and tip deflection as well. Recall from Table 2.2 that MIRAS and MIRAS-FLEX do not need a special model for treating wind turbine in yaw and tilt, e.g. [110].

### Test case 5: Comparison to OC3 Phase I

Figure 2.43 depicts the time series of rotor torque (top-left) and thrust (top-right), as well as out-of-plane root-bending moment (bottom left) and shear force (bottom right), FLEX5 and MIRAS-FLEX results for load case 2.1a of OC3 Phase I. Note the results from the OC3 participants in Figure 2.43 are shown with the same color, while FLEX5 and MIRAS-FLEX are shown as thicker lines with different colors. The BEM-based computations of FLEX5 and MIRAS-FLEX are in range of the OC3 participants, however the MIRAS-FLEX torque results deviate slightly. Given that MIRAS uses a different aerodynamic model and different input airfoil data than all codes from the participants, which are BEM-based and use airfoil data from reference [116], the slight deviations in MIRAS-FLEX are justified. For MIRAS-FLEX the rotor torque is higher than those from the participants. Rotor thrust for MIRAS-FLEX is nearly identical to FLEX5. The effect of the tower is shown by the rapid decrease and increase in loads at the blade-tower passing frequency, which is modeled in FLEX5 and MIRAS-FLEX by using a potential flow model of the tower, see [35]. The larger out-of-plane root-bending moment for MIRAS-FLEX is due to the larger normal load occurring near the tip region as compared

[1]Nearly identical torque and thrust between FAST and FLEX5 were found from running the same case with 0° yaw and with wind shear.

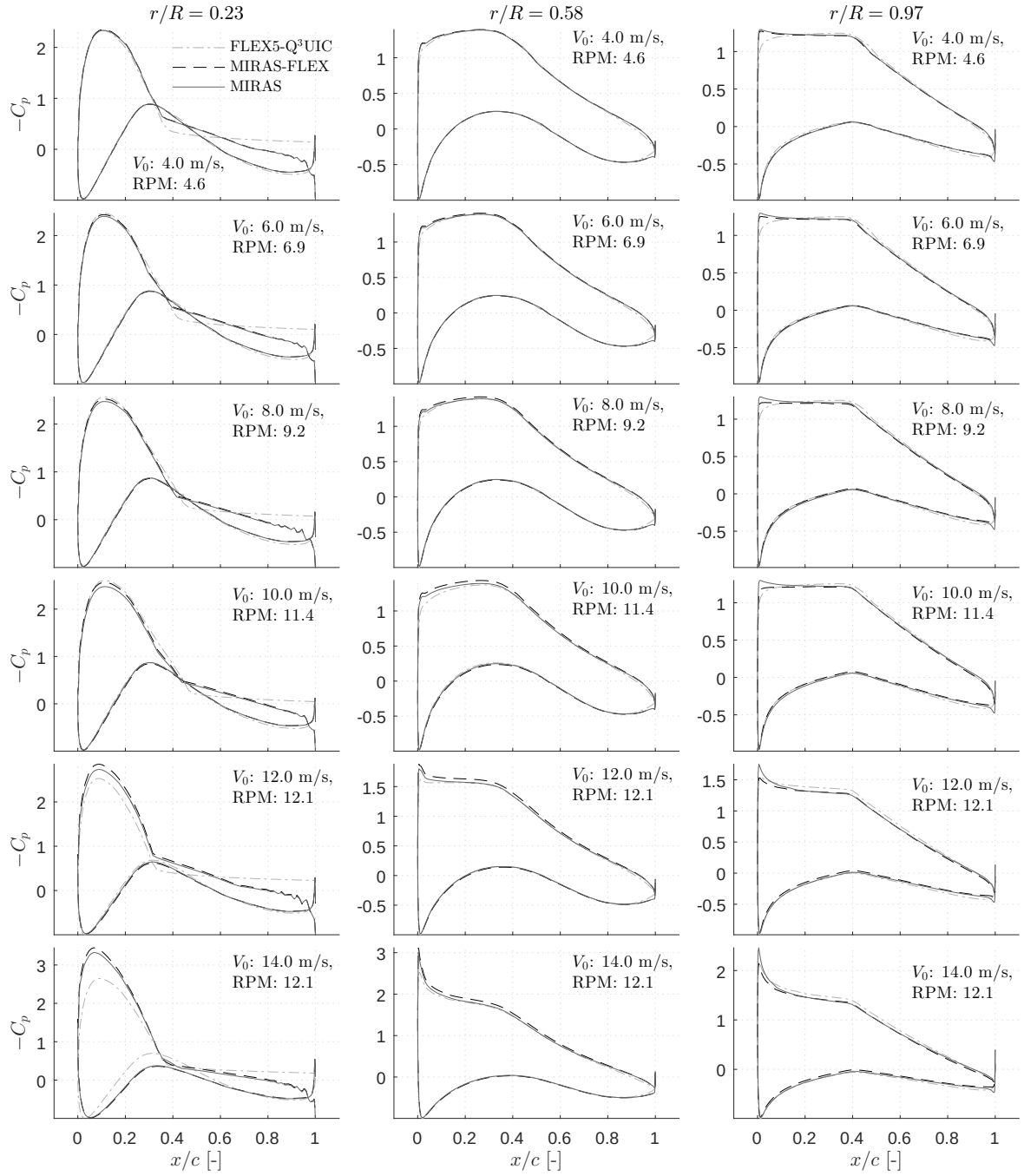


**Figure 2.40:** Pressure coefficient on the NREL 5 MW blade for FLEX5-Q$^3$UIC, MIRAS-FLEX and MIRAS at wind speeds of 4-14 m/s and 4.6-12.1 RPM. Stations located at the normalized span-wise positions of 0.23 (left column), 0.58 (middle column), and 0.97 (right column) of the undeflected blade are shown. Note $r/R$ will be slightly smaller for MIRAS-FLEX results due to axial deflection. $C_p$ curves are not available from FAST and FLEX5 computations.

to FLEX5 and the OC3 participant codes, see Figure 2.37.

In the order from left to right and top to bottom, starting at the top-left and ending at the bottom right, Figure 2.44 depicts the time series of rotor torque and thrust, generator power, rotor speed, out-of-plane and in-plane tip deflections, as well as for-aft and side-side tower-top deflections for load case 3.1. Once again, results from FLEX5 and MIRAS-

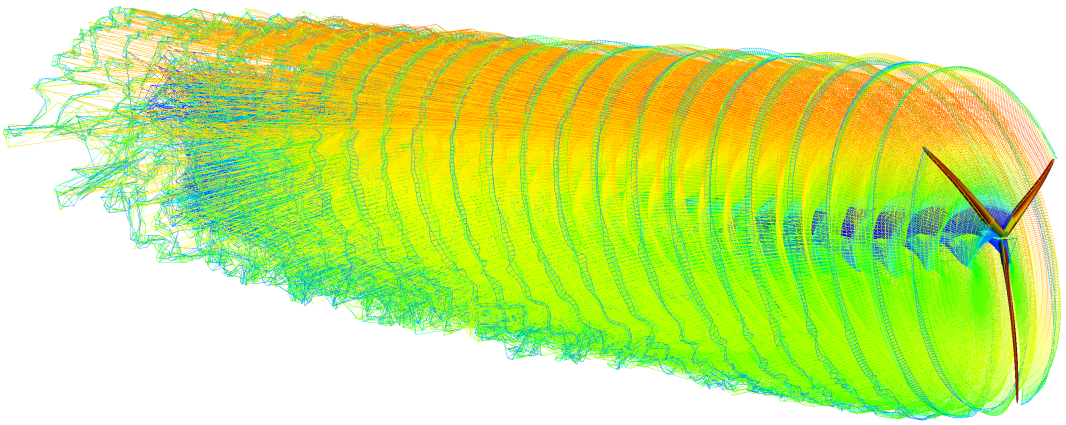

**Figure 2.41:** MIRAS-FLEX simulation for a steady wind inflow of 8 m/s, tip-speed-ratio of 7.55, 15° yaw, and prescribed power-law wind shear of 0.3 for the first 2700 time steps.

FLEX are in range of the OC3 participants, but the MIRAS-FLEX torque and generator power are slightly different for the same reasons as stated previously. Note that the results between all codes are not in phase due to varying rotor speeds, see rotor speed plot in Figure 2.44.

The MIRAS-FLEX simulation for load case 3.2 of the OC3 is shown in Figure 2.45. Figure 2.46 depicts the power spectral density of the tip deflection and root-bending moment in the out-of-plane and in-plane directions from the OC3 participant codes, FLEX5, and MIRAS-FLEX. MIRAS-FLEX results are in good agreement with the participant codes and FLEX5. However, the structural damping for the second flap-wise mode in MIRAS-FLEX had to be increased to achieve better agreement for frequencies greater than 1.5 Hz. Without the increase in damping, frequency peaks appear at approximately 2 Hz as shown in Figure 2.47, see 'MIRAS-FLEX 2$^{nd}$ Flap On'. Results labeled 'MIRAS-FLEX 2$^{nd}$ Flap Damped' are those shown in Figure 2.46 and 'MIRAS-FLEX 2$^{nd}$ Flap Off' are results with the second flap-wise mode DOF switched off. Figure 2.48 compares the time series for the second flap-wise mode DOF between MIRAS-FLEX and FLEX5. The increase in noise from 'MIRAS-FLEX 2$^{nd}$ Flap On' in Figure 2.48 (left side) causes the frequency peak shown in Figure 2.47. A possible explanation for the noise is that the second flap-wise blade modes do not completely converge, particularly for load case 3.2 due to the very rapid changes in wind inflow and blade loading occurring at each time step. MIRAS-FLEX with a strong-coupling approach may resolve the higher frequencies accurately, but has not been implemented due to the high computational expense. Figure 2.49 shows how the pitch controller in MIRAS-FLEX prevents the generator power from exceeding rated.

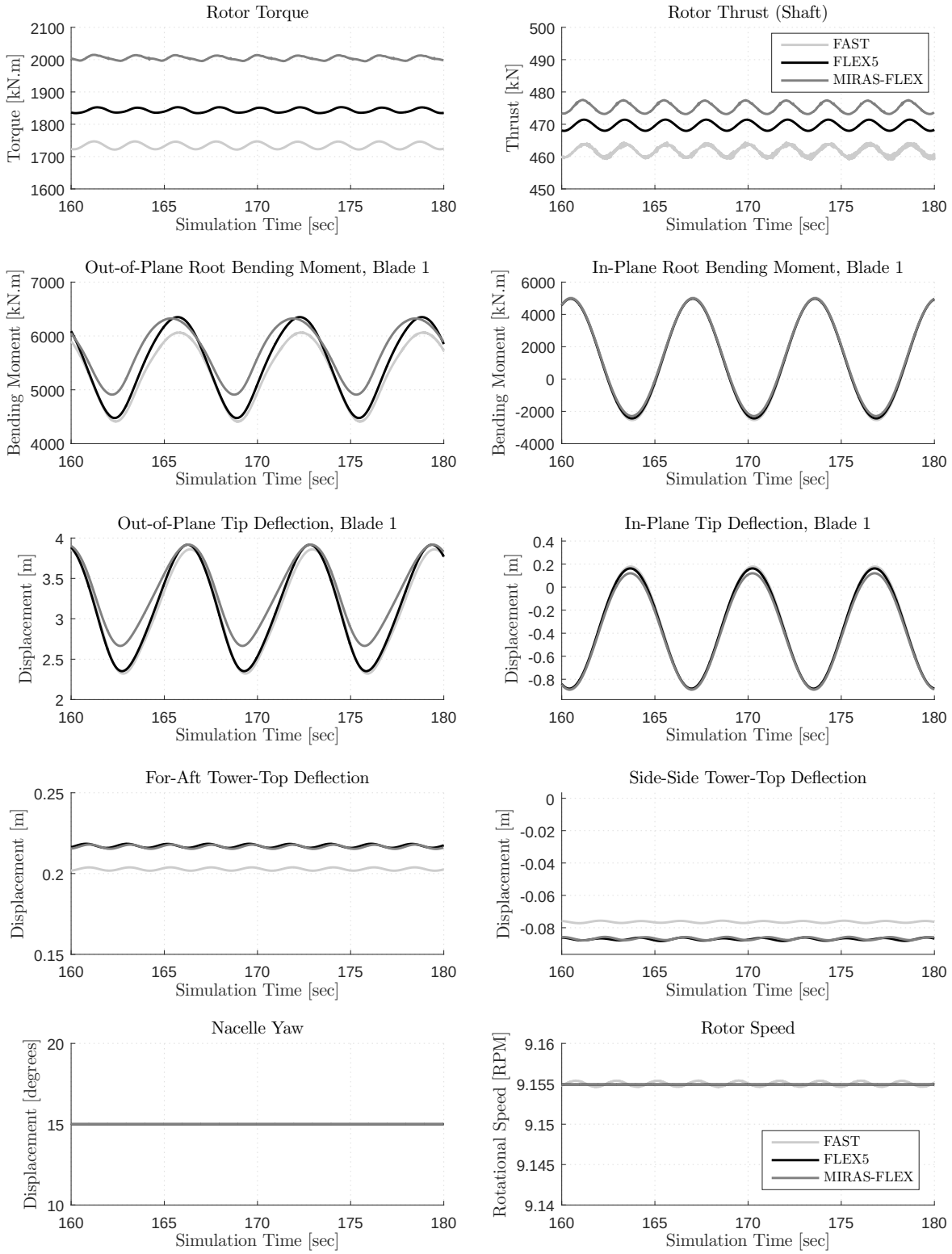


**Figure 2.42:** Simulations of FAST, FLEX5 and MIRAS-FLEX for a steady wind inflow of 8 m/s, tip-speed-ratio of 7.55, 15° yaw, and power law wind shear of 0.3. In the order from left to right and top to bottom, starting at the top-left and ending at the bottom-right: rotor torque and thrust, out-of-plane and in-plane root bending moments, out-of-plane and in-plane tip deflections, for-aft and side-side tower-top deflections, as well as nacelle yaw and rotor speed are shown.

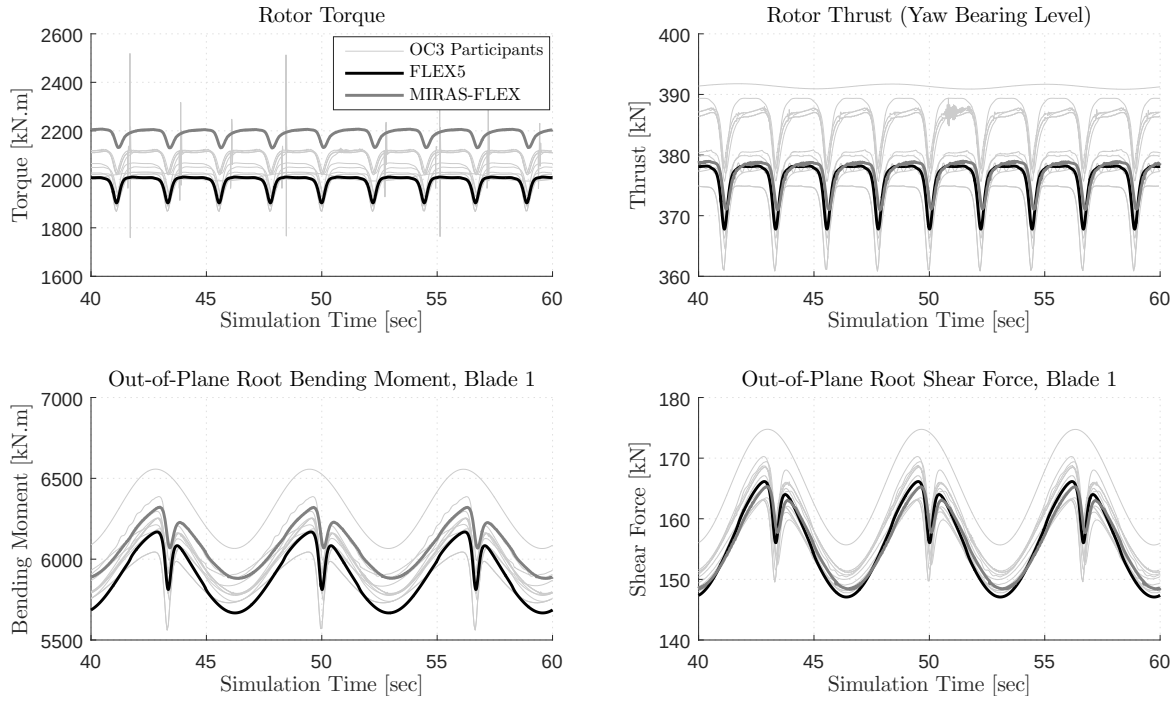


**Figure 2.43:** FLEX5 and MIRAS-FLEX results for load case 2.1a of the OC3 project. Rotor torque (top-left), rotor thrust (top-right), out-of-plane root bending moment (bottom-left) and out-of-plane root shear force (bottom-right) are shown.

## 2.5 Conclusions

A three-dimensional viscous-inviscid interactive solver, MIRAS, has been coupled with the structural dynamic model of FLEX5 using a partitioned, loosely-coupled, and multi-rate methodology to predict the aero-elastic response of wind turbines. The novel code is called MIRAS-FLEX. In general, MIRAS-FLEX results are in good agreement with the standard BEM-based aero-elastic codes FLEX5 and FAST for steady and unsteady conditions. Unsteady conditions consisted of a combination of yaw and wind shear as well as the load cases from the OC3 project. The distinct airfoil data and aerodynamic models used in MIRAS and MIRAS-FLEX result in higher tangential loads in comparison with FLEX5 and FAST. Furthermore, MIRAS-FLEX is shown to produce slightly lower loads near the tip, where deflections are the highest, in comparison with MIRAS alone. The lower load near the tip is due to the inclusion of structural dynamic modeling. Comparisons of MIRAS-FLEX with results from the OC3 project are also in good agreement. Future work consists of investigating strong coupling and the coupling of MIRAS with the multi-body finite element code in HAWC2. MIRAS-FLEX is an accurate and fast alternative aero-elastic tool, which does not rely on the blade element momentum method, for aero-elastic wind-turbine computations.

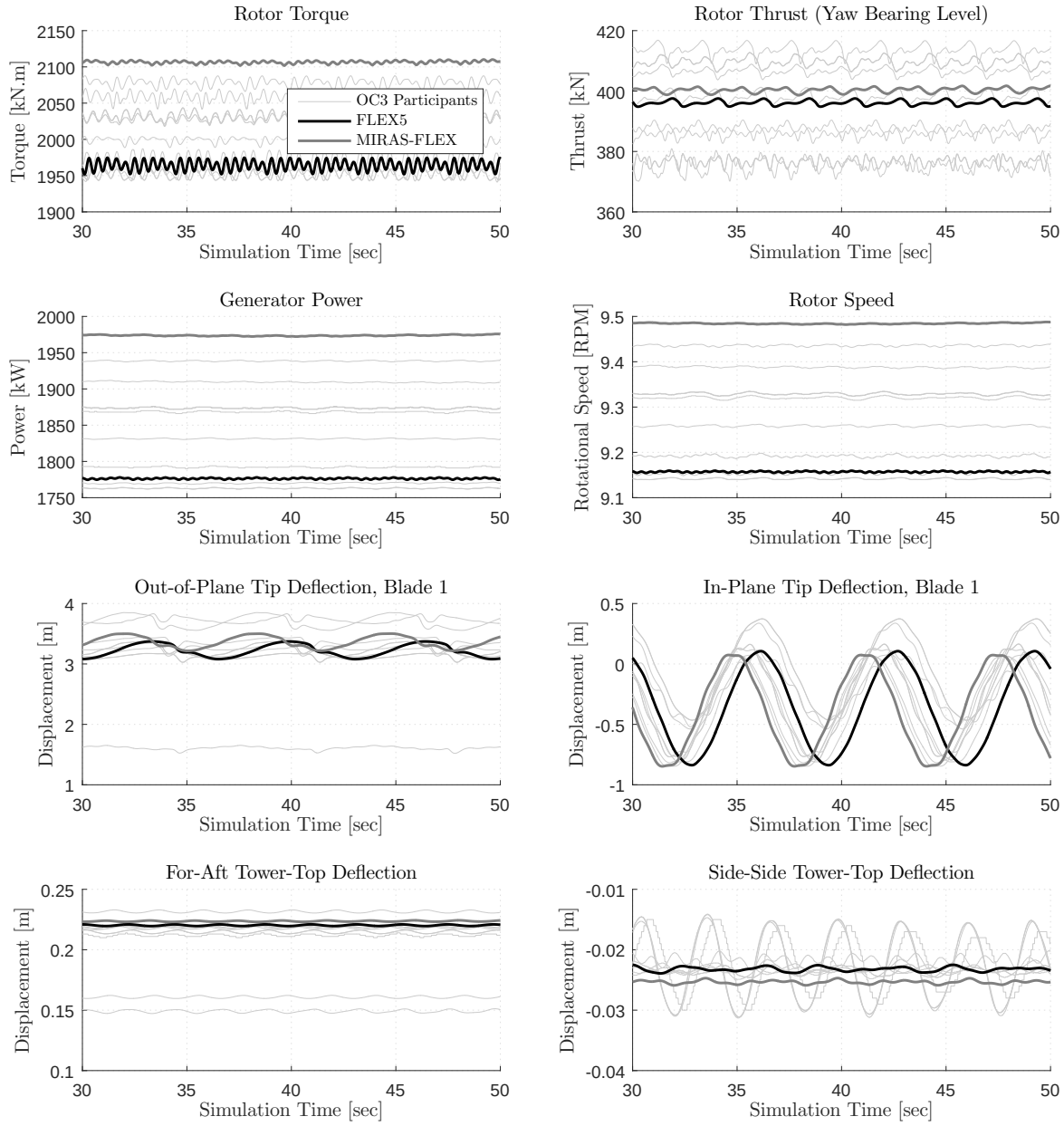


**Figure 2.44:** FLEX5 and MIRAS-FLEX results for load case 3.1 of the OC3 project. In the order from left to right and top to bottom: Rotor torque and thrust, generator power, rotor rotation, out-of-plane and in-plane tip deflections, and for-aft and side-side tower-top deflections.

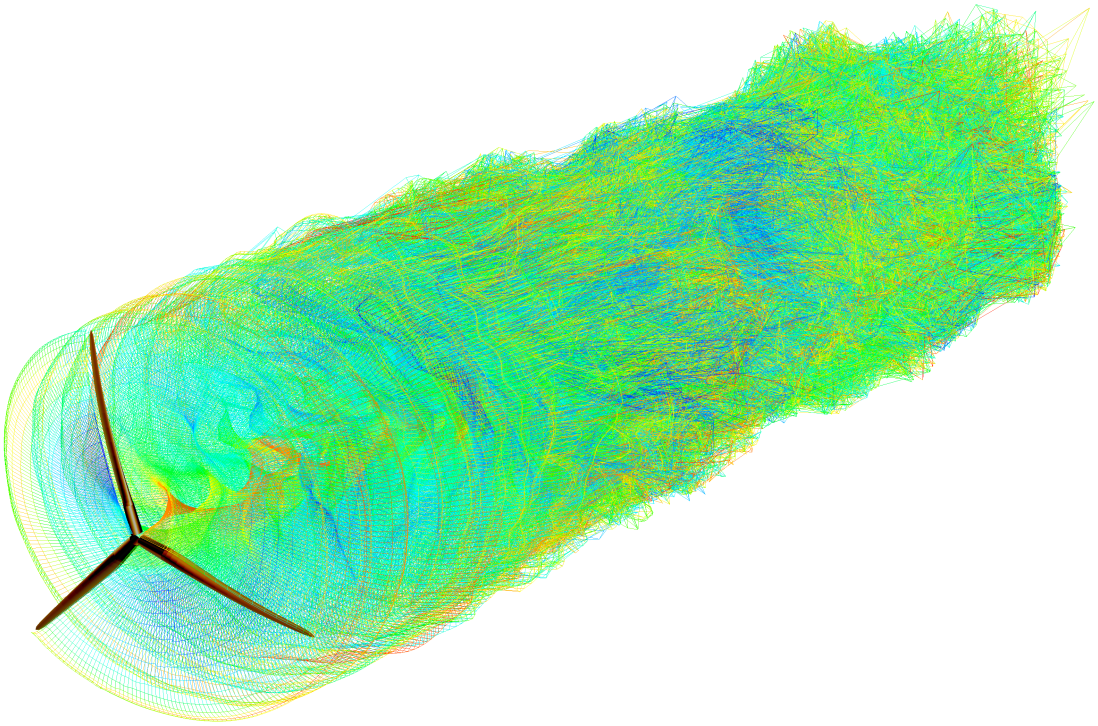

**Figure 2.45:** MIRAS-FLEX simulation with a turbulent inflow for load case 3.2 of the OC3 project.

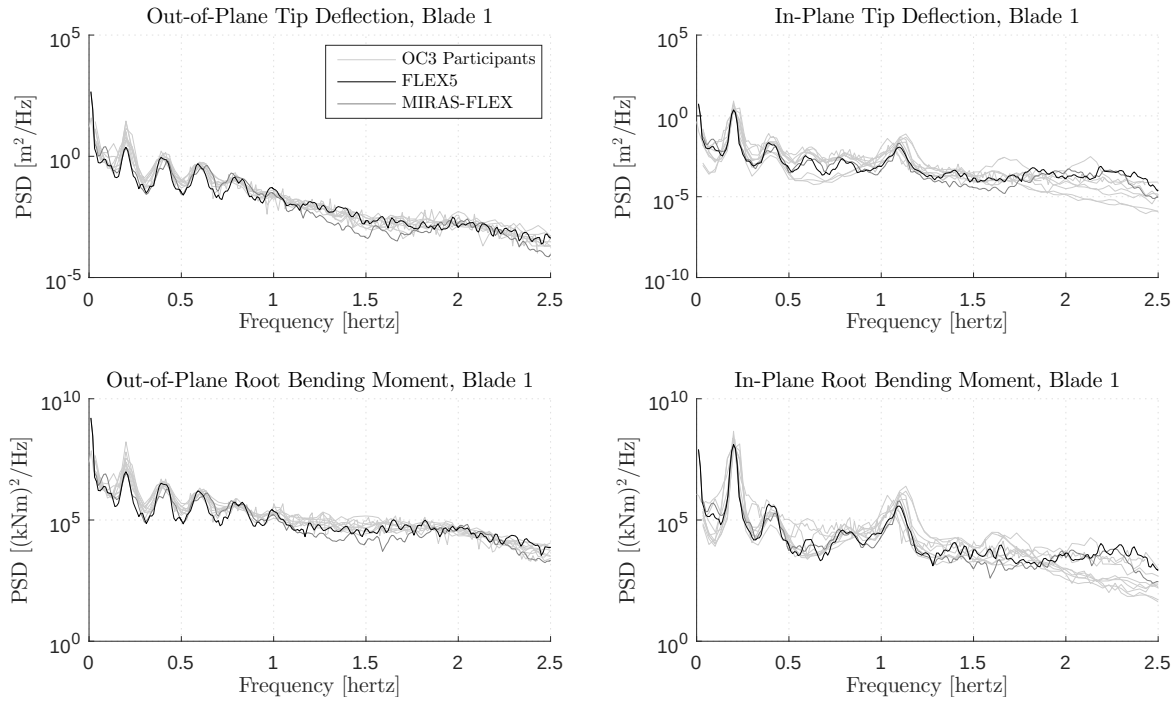


**Figure 2.46:** FLEX5 and MIRAS-FLEX results for load case 3.2 of the OC3 project. Out-of-plane (top-left) and in-plane (top-right) tip deflections, as well as out-of-plane (bottom-left) and in-plane (bottom-right) root-bending moments in the frequency domain are shown.

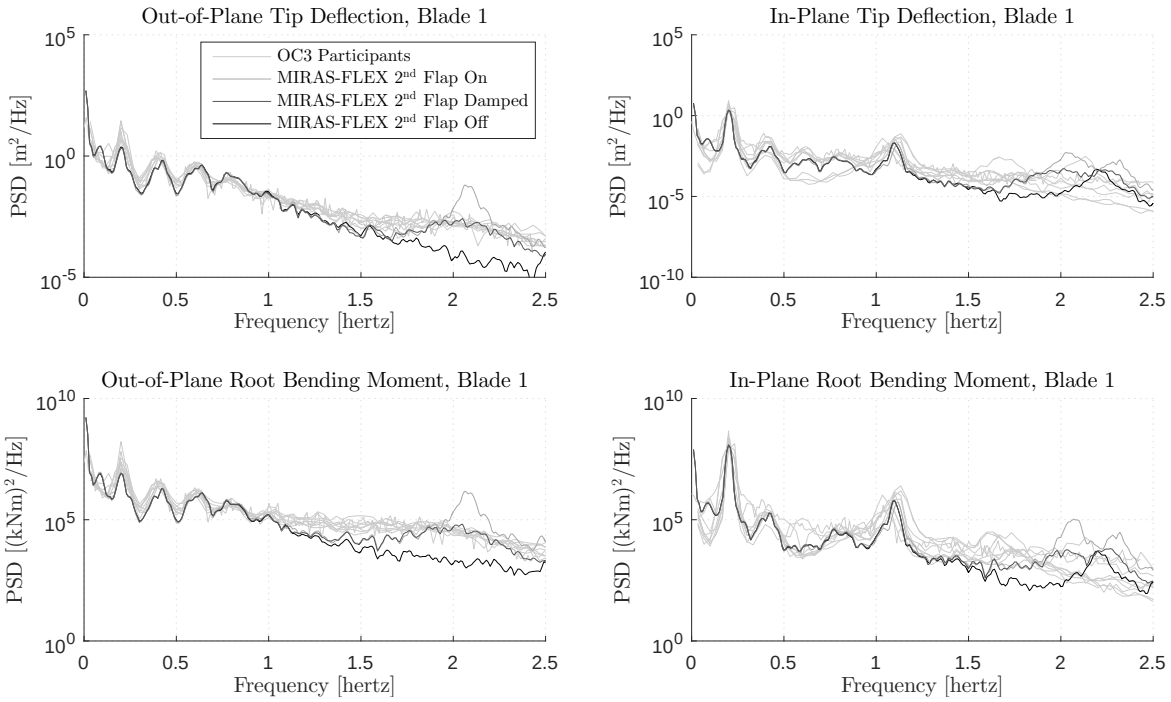


**Figure 2.47:** MIRAS-FLEX results for load case 3.2 of the OC3 project using different options for the second flap-wise mode degree of freedom. Out-of-plane (top-left) and in-plane (top-right) tip deflections, as well as out-of-plane (bottom-left) and in-plane (bottom-right) root-bending moments in the frequency domain are shown.

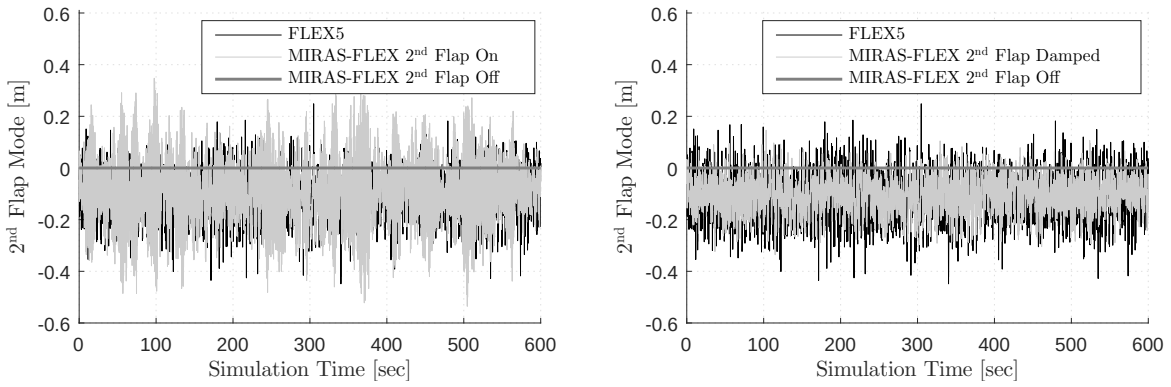


**Figure 2.48:** Time series comparison of the second flap-wise mode degree of freedom between FLEX5, MIRAS-FLEX 2nd Flap On, MIRAS-FLEX 2nd Flap Damped, and MIRAS-FLEX 2nd Flap Off.

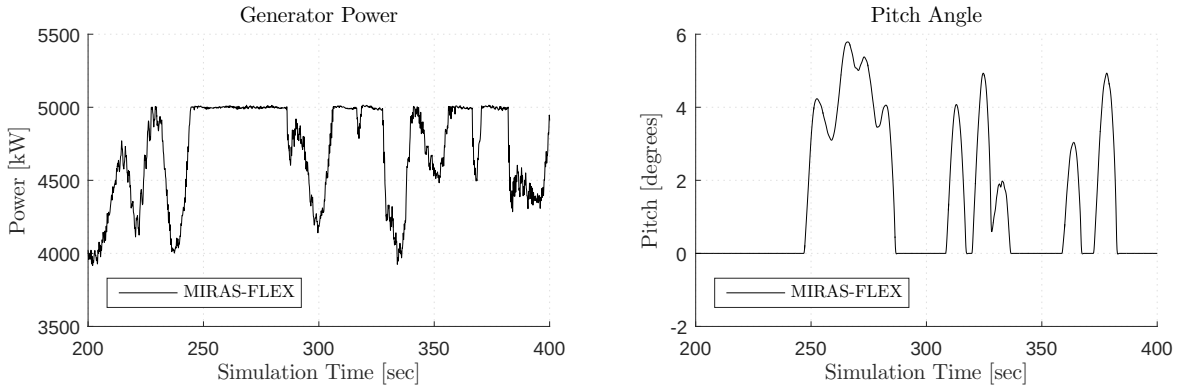


**Figure 2.49:** Generator power (left) and pitch (right) from MIRAS-FLEX for load case 3.2 of the OC3 project. Pitch controller prevents generator power from exceeding rated.

# Chapter 3

# Surrogate Modeling for Wind-Turbine Blade Design

## 3.1 Introduction

This chapter is based on the work: 'Aerodynamic wind-turbine rotor design using surrogate modeling and three-dimensional viscous-inviscid interaction technique' [3]. Chapter 3 is organized as follows: section 3.2 describes the surrogate-optimization method, section 3.3 describes the basic properties of the model rotor and its design using the inverse-design and surrogate-optimization methodologies, and finally section 3.4 gives the conclusions.

## 3.2 Methodology

In this section, we describe the methodology used for the design of the model wind-turbine rotor. It comprises the subsections of *MIRAS simulations in the optimization framework* and *surrogate modeling for optimization.*

### 3.2.1 MIRAS Simulations in the Optimization Framework

MIRAS simulations require transpiration velocity data from Q$^3$UIC as input. To take into account $Re$ and $l$ effects, Q$^3$UIC data must be created each time the blade chord changes. Generating Q$^3$UIC data for each MIRAS call in an optimization process is heavy. Alternatively, the viscous solver in MIRAS has to be fully integrated, resolving the boundary layer equations at each time-step. The later option will also add significant computational overhead, which would be critical in an optimization process. Instead, a Q$^3$UIC database containing transpiration velocity data as a function of $Re$, $R_O$ and $l$ for each airfoil is generated prior to the optimization. Trilinear interpolation is carried out to obtain the data needed for each MIRAS call. For a given airfoil that is a blend of two distinct airfoils, the interpolation is comprised of a trilinear interpolation in each of the two airfoil databases and one linear interpolation to obtain the final Q$^3$UIC data input for MIRAS. A code was developed to generate a Q$^3$UIC database on the Jess cluster. For example, the code together with 80 cores on Jess can generate $18^3 = 5832$ airfoil data files in less 24 hours. Figure 3.1 illustrates the concept.

Despite the savings in computational time by using a Q$^3$UIC database, MIRAS simulations are still computationally heavy. To obtain steady-state results, each unsteady MIRAS simulation starts at time = zero and runs for 360 iterations using an azimuthal discretization of 20° (360*20°*(1 wake rev/360°)=20 wake revolutions). Timestep is calculated as 20°*($\pi$/180°)*(1/RPM)*(30/$\pi$). Figure 3.2 displays the aerodynamic power versus the number of wake revolutions. The initial transient from 0 kW to 5.5 kW represents a slow start function used to prevent a strong starting vortex from affecting the

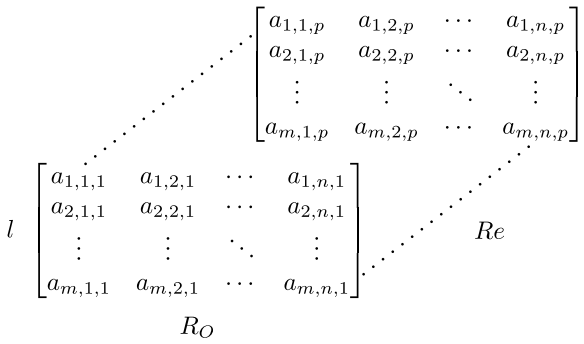


**Figure 3.1:** A Q$^3$UIC database is generated for each airfoil used in a wind-turbine blade, where $a_{1,1,1}, \ldots, a_{m,n,p}$ represent airfoil data files containing the transpiration velocity vs. angle of attack.

final wake solution. During the slow start, both the wind speed as well as the rotational speed follow a hyperbolic increase until its nominal value is reached. The subsequent decay in the aerodynamic power represents the wake approaching steady state.

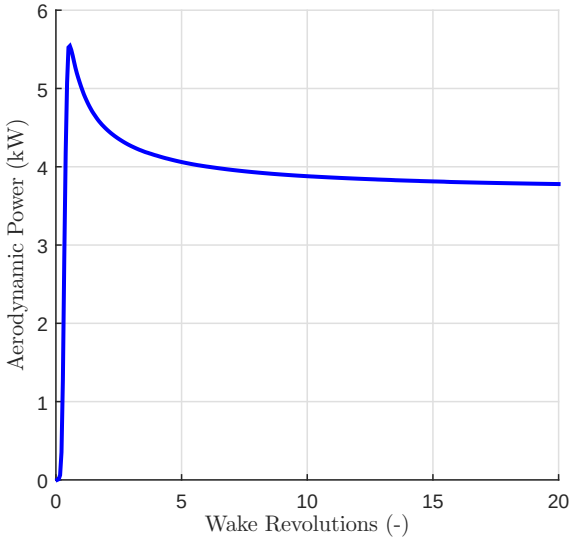


**Figure 3.2:** Plot of rotor aerodynamic power versus number of wake revolutions. As the number of wake revolutions increase, the wake and thus the aerodynamic torque approach the steady-state value.

To further reduce the overall computational time, the sampling plan procedure, see subsection 3.2.2, in the surrogate-optimization scheme using MIRAS is parallelized on the Jess cluster. The sampling plan is performed by submitting jobs in parallel, where each job runs one design. Each design uses $X$ number of nodes with 20 cores each. Each node is a MIRAS call for a specific wind speed. Therefore, a total of $X$ wind speeds are used to sample the power curve. To build a sample in parallel requires: total number of cores = sample size * $X$ * 20 (e.g. 8 * 1 * 20 = 160 cores). After the sample is finished, the number of cores needed for surrogate optimization becomes $X$ * 20 (e.g. 1 * 20 = 20 cores). Figure 3.3 illustrates the surrogate optimization concept using MIRAS on the Jess cluster.

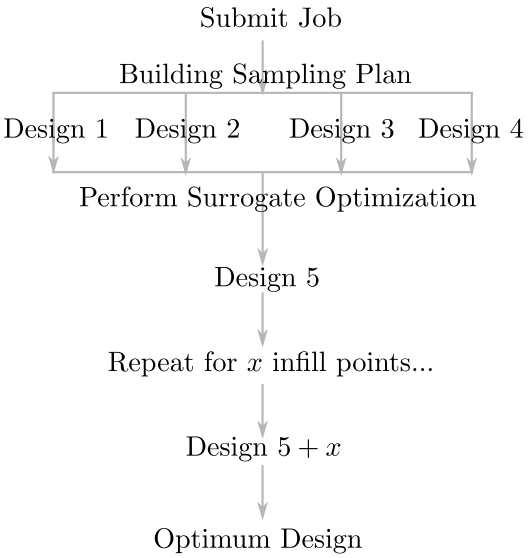


**Figure 3.3:** Diagram depicting the parallel and serial processes on the Jess cluster for surrogate optimization using MIRAS. Example sampling plan size of four shown.

### 3.2.2 Surrogate Modeling for Optimization

MIRAS requires much more computational time than the BEM method. Therefore, the number of calls to MIRAS in a design optimization problem must be kept to a minimum. Surrogate optimization uses a mathematical model for searching local or global optima rather than a black-box function directly [92]. When a black-box function is computational expensive, e.g. MIRAS, surrogate optimization can achieve significant savings in computational time compared to conventional optimization methods. Note, however, that choosing a good surrogate model for the problem at hand is vital to achieve good results. This is a difficult task if the shape of the design space is not known a priori. Surrogate optimization has several other advantages as well. For example, surrogates can be modified to handle noise from numerical discretization errors, local minima, and missing data issues. Missing data occurs when, for example, simulations fail to converge or crash for unknown reasons. Furthermore, surrogates can be easily used to study the entire design space. Studying the entire design space requires evaluating the objective on a $X^n$ grid, where $X$ is the number of points for sampling and $n$ is the number of variables, which makes using a heavy black-box function a computationally infeasible option. Section 3.3.3 explains how the design space can be studied using surrogates.

A brief summary of surrogate optimization implemented in the framework will be described in this subsection. In general, surrogate optimization consists of three steps to find the minimum of a function:

1. creating a sampling plan;
2. constructing a surrogate, and;
3. searching and exploiting the surrogate.

The three steps will be discussed in the subsections of *Creating a Sampling Plan*, *Constructing a Surrogate*, and *Searching and Exploiting the Surrogate*, respectively. Figure 3.4 gives a flowchart of the surrogate optimization scheme used in the current study. Note that MIRAS and BEM are being called only in the *Sampling Plan* and *Infill Point &*

*Rebuild Surrogate* steps in Figure 3.4. Appendix B contains an example of the surrogate optimization method to find the minimum of an analytical test problem.

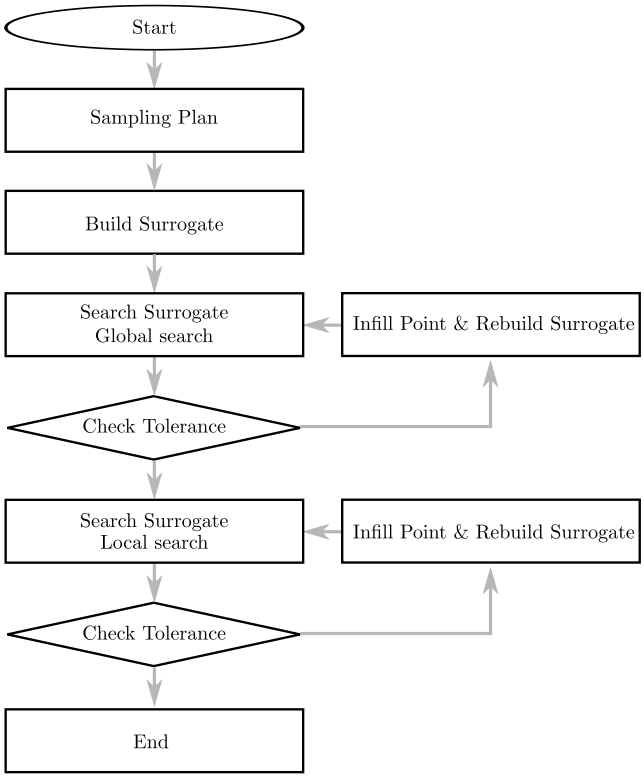


**Figure 3.4:** Flowchart of the surrogate optimization scheme. Sampling plan procedure is parallelized on the Jess cluster.

### Creating a Sampling Plan

A sampling plan involves the process of calling the function, e.g. MIRAS or BEM, at various points in the design space. To create a sampling plan, a uniform level of model accuracy throughout the design space is desired. A uniform level requires a uniform distribution of points and a sampling plan possessing this feature is called *space filling*. One of the simplest ways of sampling the design space in a uniform manner is the *full-factorial* sampling technique. A full-factorial sampling of a three-variable problem is shown in Figure 3.5. The full-factorial sampling plan creates a uniform distribution of points in the design space, however it contains two important flaws.

The first flaw is that full-factorial sampling works only for a total number of points equal to the product of sampling points in each dimension. In Figure 3.5, the total number of points is 3*3*3 = 27, where the number of sampling points in dimensions $x_1$, $x_2$ and $x_3$ are 3, 3 and 3 respectively. Full-factorial sampling does not work if, for example, a total of 28 points are desired. The second flaw is that when projected on to the axes, the points overlap. A sampling technique would be more space filling if points are uniformly distributed when projected on the axes. Another simple sampling plan is a random sampling plan. A random sampling plan can be created for any number of points in the design space (e.g. 28), but is not necessarily uniform. Especially for a small number of points, the spread of points in a random sampling plan can be uneven and thus not space-filling.

A sampling plan that aims to be uniform both in the entire design space and on the projected axes, and can also be generated for any number of points, is the *Latin hypercube sampling* (LHS) technique [92]. Latin hypercube sampling for a three-variable problem is shown in Figure 3.6 and is used in the present optimization framework. All surrogate optimizations performed in this thesis implement Latin hypercube sampling. LHS (Figure 3.6) is more space filling than the full-factorial/grid-based approach (Figure 3.5). Recall that the sampling plan procedure when using MIRAS is parallelized on the Jess cluster to reduce the overall computational time.

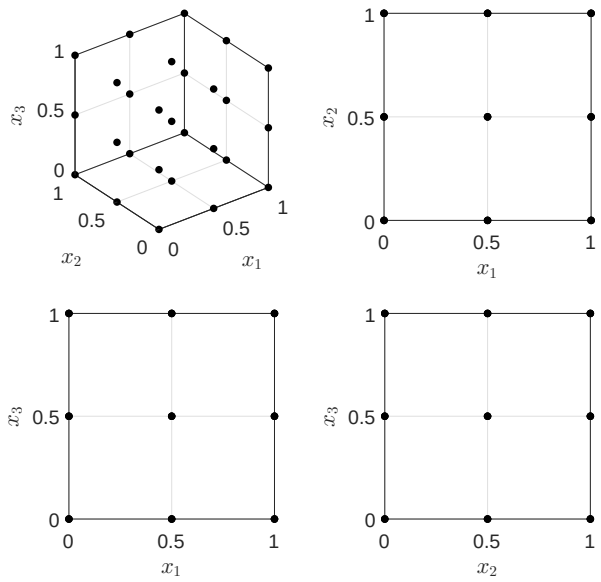


**Figure 3.5:** Illustration in three dimensions of grid-based sampling using 27 points for a three-variable problem. Grid-based approach is less space-filling as shown by the fewer points on the projected axes due to overlap.

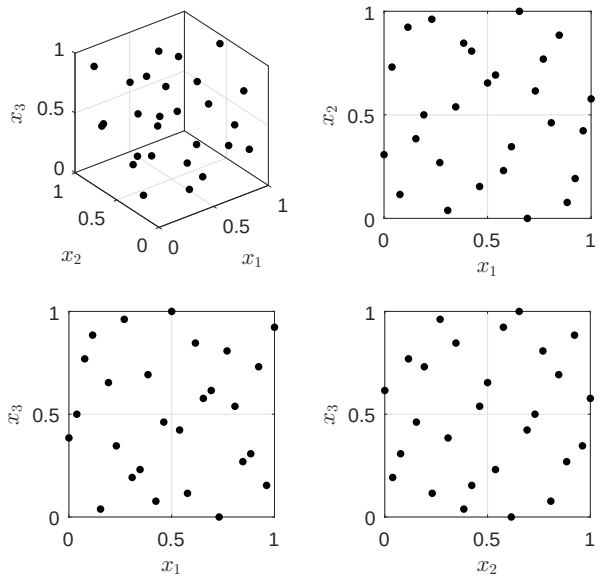


**Figure 3.6:** Illustration in three dimensions of the Latin hypercube sampling (LHS) technique using 27 points for a three-variable problem [92]. LHS aims to be uniform both in the entire design space and on the projected axes.

### Constructing a Surrogate

The following step is to construct a surrogate. Available surrogate models include RSM, radial basis functions as well as Kriging. Kriging represents a special case of the Gaussian radial basis function. Radial basis functions were chosen for the framework because of their simpler implementation and good results obtained for the present model wind-turbine rotor design. A radial basis function is expressed as:

$$\widehat{f}(\mathbf{x}) = \mathbf{w}^{\mathrm{T}}\boldsymbol{\psi} = \sum_{i=1}^{n_c} w_i \psi(\|\mathbf{x} - \mathbf{c}^{(i)}\|) \tag{3.1}$$

where $\widehat{f}$ is the surrogate approximation to the scalar-valued objective function, $f$, $\mathbf{x}$ is the design variable vector, $\mathbf{w}$ is a vector containing the values of the weight coefficients $w_i$ from $i = 1, \ldots, n_c$, and $\boldsymbol{\psi}$ is the $n_c$-vector containing the values of the basis functions $\psi$. The values of the basis functions are evaluated at the Euclidean distances between the prediction site $\mathbf{x}$ and the centers $\mathbf{c}^{(i)}$ of the basis functions. A unique solution for $\mathbf{w}$ in the above equation can be determined when $n_c$ is equal to the number of sampled points and using the so-called *Gram matrix* [92].

The Gram matrix, $\boldsymbol{\Psi}$, can determined when the basis function centers coincide with the sampled points, i.e. $\mathbf{c}^{(i)} = \mathbf{x}^{(i)}$, for all $i = 1 \ldots, n_c$. This simplification leads to the matrix equation:

$$\boldsymbol{\Psi}\mathbf{w} = \mathbf{y_s} \tag{3.2}$$

where $\mathbf{y_s}$ are the sampled points and the Gram matrix is defined as $\boldsymbol{\Psi}_{i,j} = \psi(\|\mathbf{x}^{(i)} - \mathbf{x}^{(j)}\|)$, $i, j = 1, \ldots, n_c$. A unique solution for $\mathbf{w}$ is found from the computation of $\mathbf{w} = \boldsymbol{\Psi}^{-1}\mathbf{y}$.

Examples of basis functions are:

1. linear $\psi(r_b) = r_b$
2. cubic $\psi(r_b) = r_b^3$
3. thin plate spline $\psi(r_b) = r_b^2 \ln r_b$
4. Gaussian $\psi(r_b) = e^{-r_b^2/(2\sigma^2)}$
5. multi-quadratic $\psi(r_b) = (r_b^2 + \sigma^2)^{1/2}$
6. inverse multi-quadratic $\psi(r_b) = (r_b^2 + \sigma^2)^{-1/2}$

Note the substitution $r_b = \|\mathbf{x} - \mathbf{c}^{(i)}\|$ from Equation (3.1). All six basis functions were tested for the model wind-turbine rotor design study. The cubic basis function was found to be the most appropriate in terms of two metrics, see in subsection 3.3.3, and is therefore used in the framework.

### Searching and Exploiting the Surrogate

A custom optimization scheme was developed to explore and exploit the surrogate. The exploration consists of global and local search techniques. Prediction-based exploitation [92] is used to enhance the accuracy of the surrogate model. In other words, infill points at the optimum predicted by the surrogate will eventually converge to a local or global optimum value of the true function for a given number of iterations. Figure 3.7 depicts an example of prediction-based exploitation for a one-variable optimization problem. In this example, a three-point sampling plan is created first, then a Gaussian radial basis function is fit through the points (top-left). One infill point is added at the minimum of the prediction, which is then used to improve and update the radial basis function

model (top-right). The infill strategy converges to the optimum after five updates at the minimum of the prediction (bottom). The custom optimization scheme used for the model rotor design is described in more detail next.

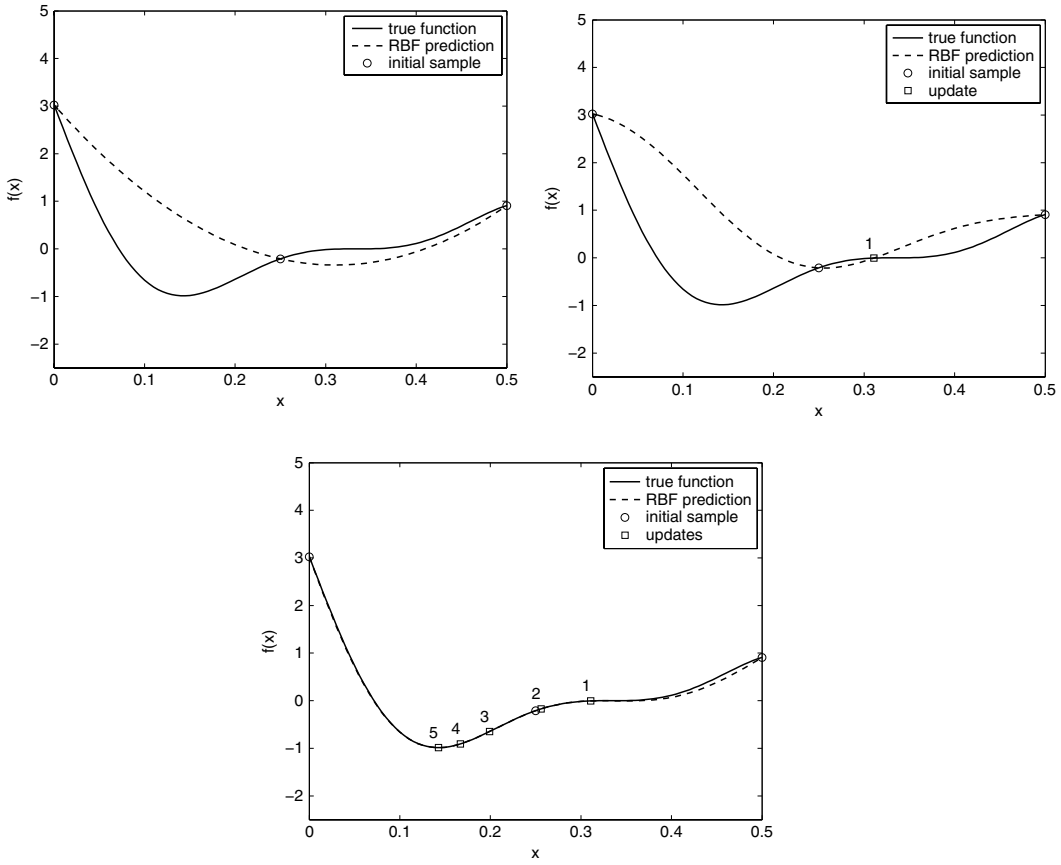


**Figure 3.7:** A Gaussian RBF is fit through a three-point sampling plan (top-left), which is then improved with one update at the minimum of the prediction (top-right). The infill strategy converges to the optimum after five updates at the minimum of the prediction (bottom). Figures from Forrester [92].

The first step is to search the surrogate, $\widehat{f}$, thoroughly on a $X^n$ grid to find the minimum, where $X$ is the number of grid points along each variable dimension and $n$ is the number of variables, see Figure 3.5. The method is called by the authors as the *brute force* approach and is considered as a global search method. Once the minimum of surrogate is found, the true function, $f$, is evaluated at the same point. An infill strategy is used where the true function is evaluated at the minimum of the surrogate and then added to the surrogate model to increase its accuracy. More often than not, the minimum of the surrogate is not the same as the minimum of the true function. The infill strategy should be repeated for a maximum number of iterations or until the minimum of the surrogate is equal to the minimum of the true function. Given that the true function is expensive to evaluate, the maximum number of iterations in this work has been set to eight.

If the minimum of the surrogate (or $f$ evaluated at the minimum of $\widehat{f}$) does not change within the eight iterations, the exploration scheme changes from brute force to local search. A tolerance criterion is used to determine whether successive values of the minimum are sufficiently close to each other. If the tolerance criterion is not satisfied

after the eight brute force iterations, the exploration scheme changes from brute force to local search. The purpose of local search is to refine the final solution from the global search process, which is limited to a resolution of $X^n$.

In the local search, the minimum found from the previous iteration is used as the starting point. The gradient-based *fmincon* function in MATLAB [124] is then used to search the surrogate near the starting point. If the minimum found from the local search differs sufficiently from the previous iteration, the process is repeated up to a maximum of five iterations. Otherwise, the local search is terminated and the optimization is finished. Refer to Figure 3.4 for a flowchart of the scheme.

## 3.3 Model Rotor Design

### 3.3.1 Description of the Model Wind-Turbine Rotor

The blade design framework was applied to design a model wind-turbine rotor for wind-tunnel experiments at a collaborating academic institution, Yangzhou University (YZU). The current PhD project was part of an international collaboration in wind energy between DTU and the Chinese research institutions YZU and Chong Qing University (CQU) funded by the Danish Council for Strategic Research (DSF). As part of the collaboration, the design of a scaled-rotor model for wind tunnel experiments at YZU was needed. The experimental data are collected by YZU and are used to validate simulation tools such as MIRAS.

The model blade was chosen to contain only one airfoil and a pitch-axis that lies at the quarter chord. A three-bladed rotor was chosen to be operated at a tip-speed ratio (TSR) of 5.71 and zero-degree pitch. The TSR of 5.71 was found from an iterative process using BEM by maximizing the power coefficient and varying the design wind speed. The rotor radius $R = 0.75\,\mathrm{m}$ was selected to comply with the size constraints of the wind tunnel as well as prevent flow blockage. The design wind speed is 19.3 m/s and the generator was assumed to have a fixed rotational speed of $\omega$ =146.6 rad/s (1400 RPM). Air density and dynamic viscosity of air were assumed to be $1.205\,\mathrm{kg/m^3}$ and 1.821e-5 ($\mathrm{N\,s/m^2}$), respectively. Air properties have been estimated based on $T = 20°C$ and 1 atm. Lastly, the airfoil chosen is the DTU-LN221 with an airfoil thickness relative to chord of 21%. Figure 3.8 depicts the $x$ and $y$ profile coordinates normalized with the chord length, $c$, of the DTU-LN221 airfoil. The basic data used for the design are summarized in Table 3.1.

Two distinct methods will be used to design the rotor, specifically the chord and twist of the blade planform. The first method is based on an inverse design approach, while the second will use surrogate optimization. The surrogate optimization technique will be tested using a BEM code and MIRAS to evaluate the objective function. The results from both methods are compared in subsection 3.3.3.

### 3.3.2 Inverse Design using BEM Theory

In the inverse design approach, the blade planform is determined using a set of desired parameters and a theoretical model. Usually iterations are carried out until a fully converged solution is obtained. Examples of given desired parameters include lift coefficient and axial induction factor versus the blade span. Details on inverse design can be found in [125, 126] and [127]. In the current study, the given desired parameters are maximum

**Table 3.1:** Basic data chosen for wind-turbine rotor model

| Property | Value |
|---|---|
| Density of air | $1.205\,\mathrm{kg/m^3}$ |
| Dynamic viscosity of air | $1.821\text{e-}5\,\mathrm{N\,s/m^2}$ |
| Design wind speed, $V_o$ | $19.3\,\mathrm{m/s}$ |
| Generator speed, $\omega$ | $146.6\,\mathrm{rad/s}$ (1400 RPM) |
| Pitch | 0 degrees |
| Design tip speed ratio, $\omega R/V_o$ | 5.71 |
| Airfoil name | DTU-LN221 |
| Airfoil thickness relative to chord | 21% |
| Rotor radius, $R$ | $0.75\,\mathrm{m}$ |
| Hub radius, $R_{\mathrm{hub}}$ | $0.1\,\mathrm{m}$ |
| Number of blades, $B$ | 3 |

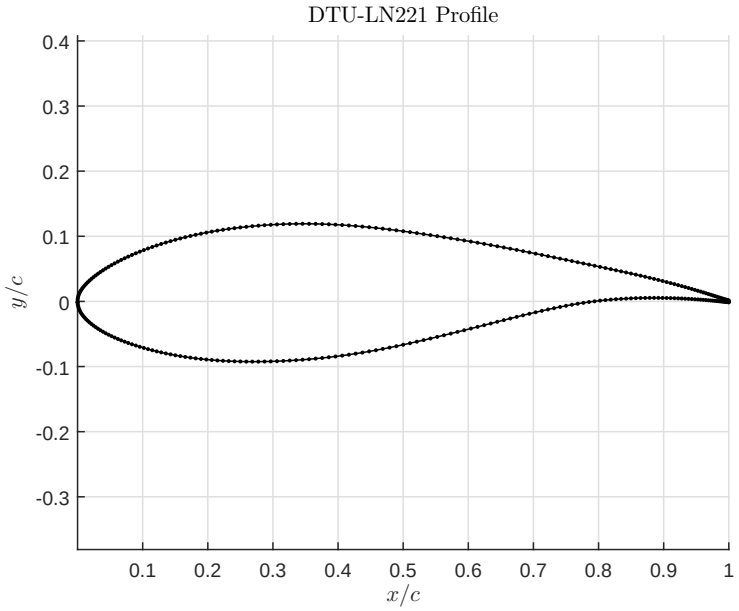


**Figure 3.8:** Profile coordinates of the DTU-LN221 airfoil.

lift-to-drag ratio and the Betz-Joukowski condition, $a = 1/3$. The desired parameters together with BEM theory are used to obtain the blade planform. The implemented inverse-design technique is described in [126], which is based on BEM theory. The following two equations are solved in an iterative loop for each blade element to obtain the normalized chord, $c/R$, and twist, $\theta$, respectively:

$$\frac{c}{R} = 4\pi \frac{r}{R} \sin^2\phi \frac{F}{B} \frac{1}{C_{l,\mathrm{design}} \cos\phi + C_{d,\mathrm{design}} \sin\phi} \tag{3.3}$$

$$\theta = \phi - \alpha_{\mathrm{design}} \tag{3.4}$$

where $r/R$ is the normalized radial position of the rotor or span-wise blade position, $F$ is the Prandtl correction for a finite number of blades, $B$ is the number of blades, and $\phi$ is the flow angle. The design lift coefficient, $C_{l,\mathrm{design}}$, drag coefficient, $C_{d,\mathrm{design}}$, and angle of attack, $\alpha_{\mathrm{design}}$, are extracted from the airfoil data based on the maximum lift-to-drag

ratio design point shown later. Prandtl's correction is obtained as:

$$F = \frac{2}{\pi}\arccos(e^{-f}), \quad f = \frac{B}{2}\frac{R-r}{r\sin\phi} \tag{3.5}$$

while the flow angle is derived from the velocity triangle seen by a rotor blade element, see Figure 3.9:

$$\phi = \arctan\left(\frac{1-a}{1+a'}\frac{V_o}{r\omega}\right) \tag{3.6}$$

where $a'$ is the tangential induction factor obtained from:

$$a' = \frac{1}{(4F\sin\phi\cos\phi/\sigma c_x) - 1}, \quad c_x = C_{l,\text{design}}\sin\phi - C_{d,\text{design}}\cos\phi \tag{3.7}$$

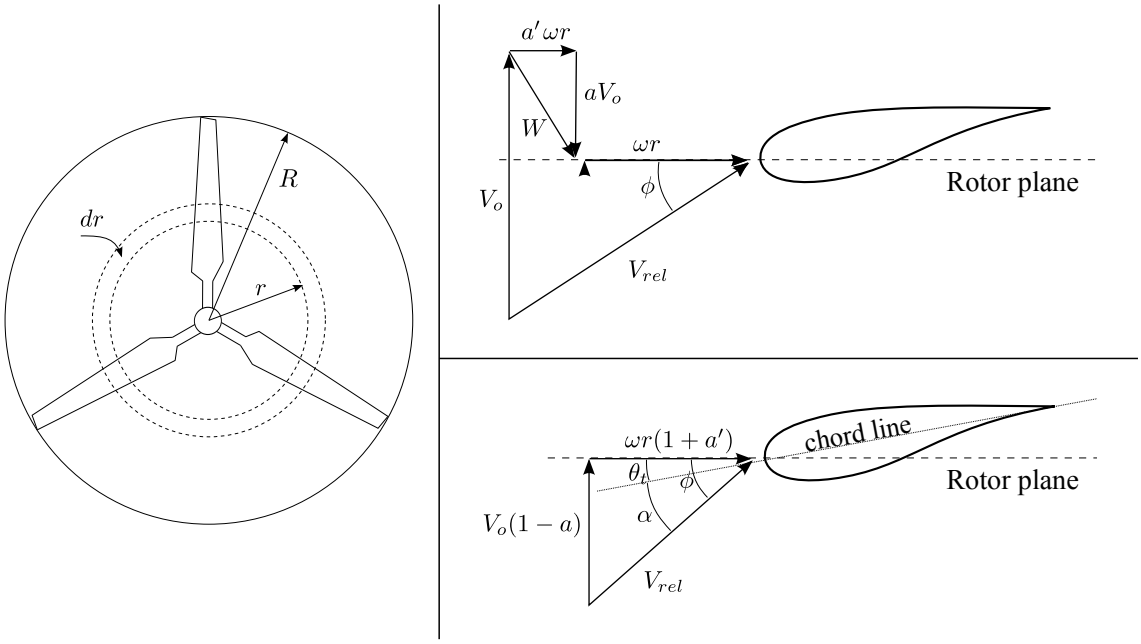


**Figure 3.9:** Blade element discretization (left) and velocity triangle seen by a blade element (right). Reproduced from [35].

Since the size of the model rotor is very small ($R < 1\,\text{m}$), Reynolds numbers are much lower compared to large wind turbines. Viscous effects as a function of Reynolds number should be taken into account in the blade design process. To accomplish this task, the viscous-inviscid interactive solver Q$^3$UIC was used to compute the lift and drag of the DTU-LN221 airfoil for a range of Reynolds numbers between 195,000 and 500,000, see Figure 3.10. Free transition and turbulence intensity of 0.0011 were set for the Q$^3$UIC computations. Note that rotational effects and aspect ratio were not taken into account. The lift and drag were then extrapolated between $\pm 180°$ using the Viterna method [128]. Following [126], the design points chosen were maximum lift-to-drag ratio versus Reynolds number. Figure 3.11 depicts the design points, which are shown as large hollow circles on top of the lift, drag, and lift-to-drag ratio data. The effect of Reynolds number on the design point is shown in Figure 3.12.

Given the design points and the basic data from Table 3.1, it is possible to use the inverse design approach to obtain the ideal chord and twist distributions. Figure 3.13 displays the results from the inverse design. In Figure 3.13, most of the blade operates at

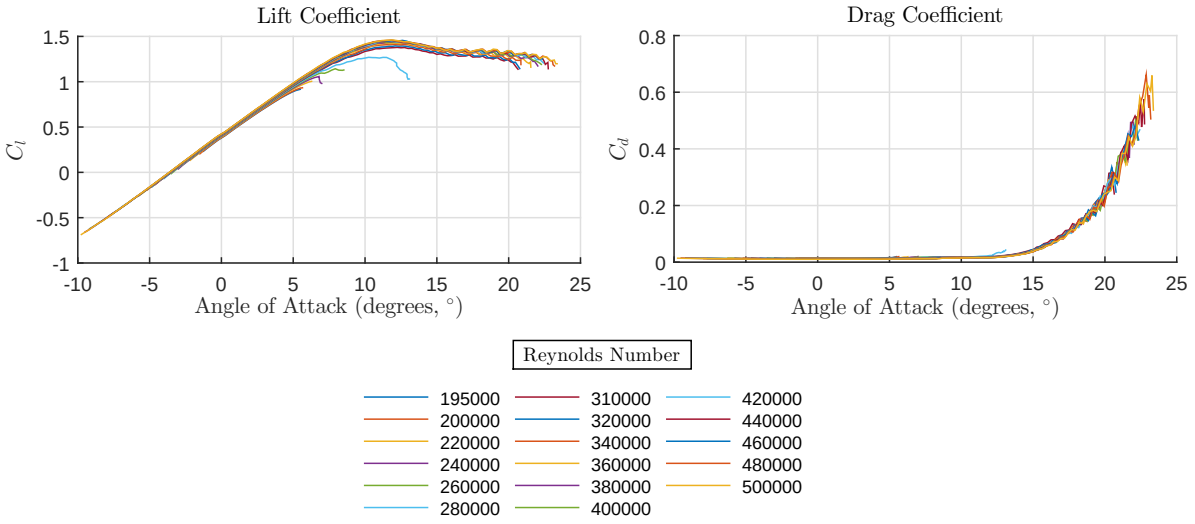


**Figure 3.10:** Airfoil lift and drag data generated using Q$^3$UIC for a range of Reynolds numbers between 195,000 and 500,000.

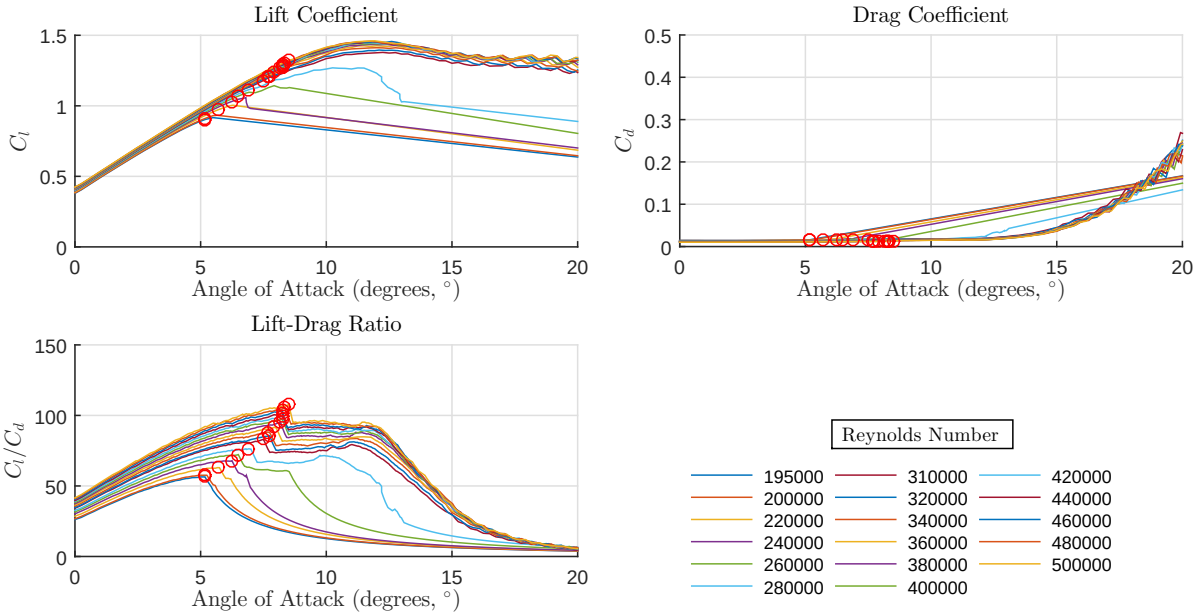


**Figure 3.11:** Lift, drag, and lift-to-drag ratio of the DTU-LN221 airfoil. Maximum lift-to-drag ratio chosen as the design point (hollow circle). Straight lines represent missing data linearly interpolated from Viterna extrapolation.

a Reynolds number of 280,000 and a lift-to-drag ratio of 75, while both quantities drop significantly near the root and tip. The drop is due to the small radius near the root resulting in a low tangential velocity and the tip-loss effect near the tip. The blade from the inverse design procedure can now be used as a baseline for surrogate optimization.

### 3.3.3 Design using Surrogate Optimization

In this subsection, the model rotor design using surrogate optimization with BEM and MIRAS is presented. Results are compared with that designed with the inverse-BEM approach.

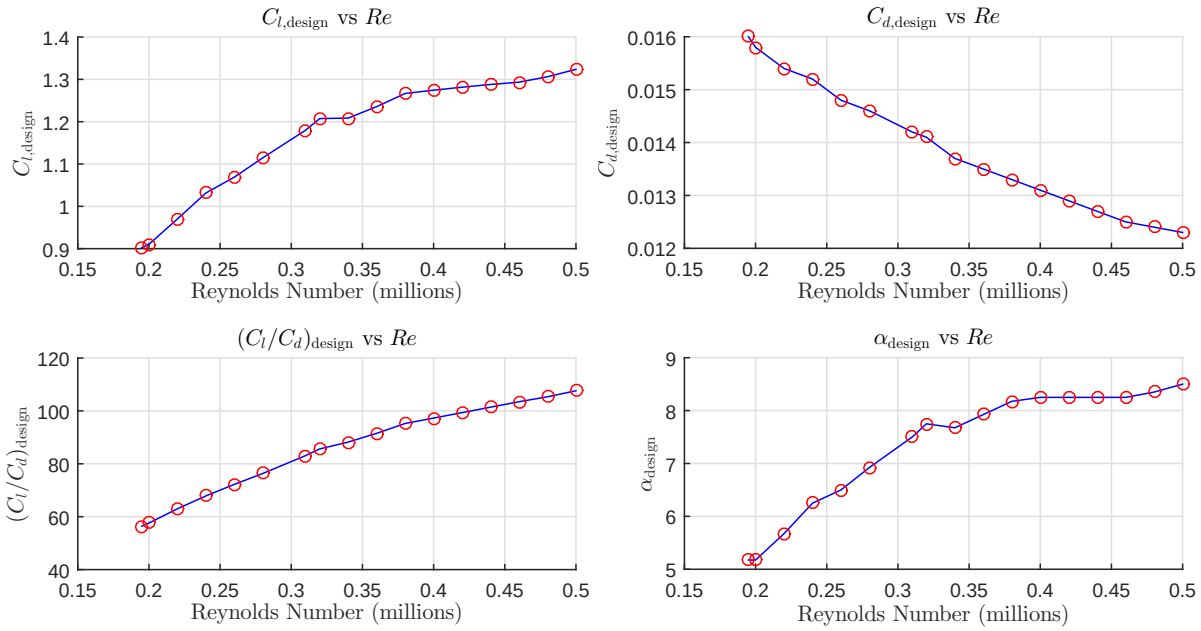


**Figure 3.12:** Lift, drag, lift-to-drag ratio, and angle of attack values versus Reynolds number. Maximum lift-to-drag ratio chosen as the design point.

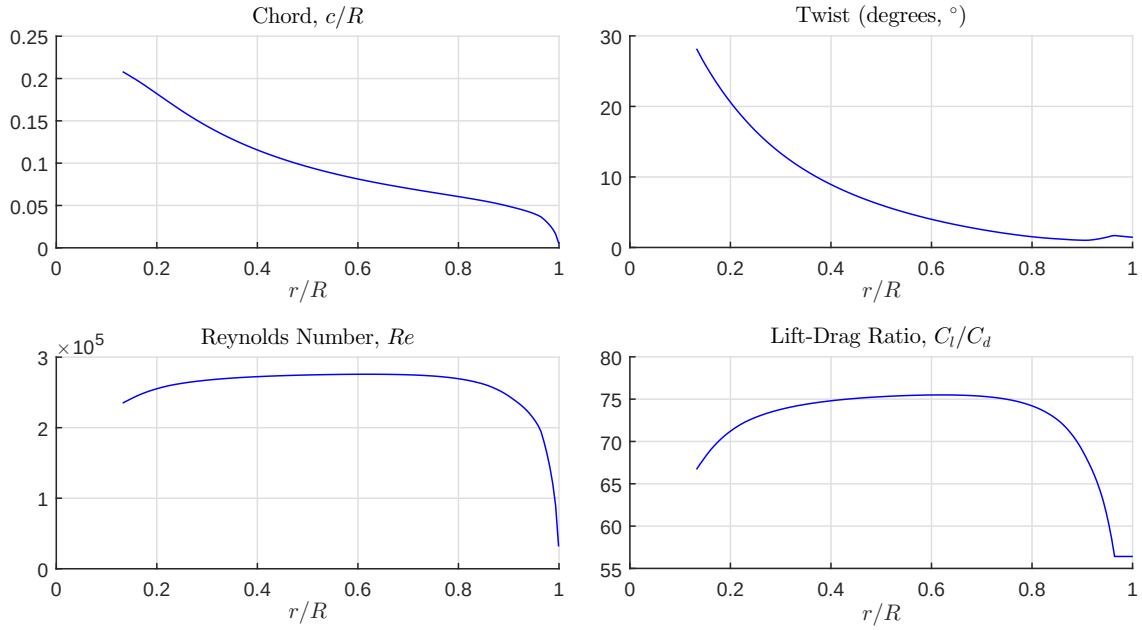


**Figure 3.13:** Design results for a 0.75 m long blade operating at a tip-speed ratio of 5.71 using the inverse-design methodology from [126]. Small abnormal deviations occur on the tip, particularly for the twist and the lift-drag ratio, due to the very low Reynolds number, which cannot be simulated with Q$^3$UIC.

### Description of optimization problem

The optimization problem for the model rotor design is:

$$\begin{aligned} \underset{x}{\text{minimize}} \quad & -C_P(\mathbf{x})/C_{P,\text{fit}} \\ \text{subject to} \quad & \mathbf{x} \in \mathbb{R}^n, \\ & g_c(\mathbf{x}) \leq 0, \\ & x_k^L \leq x_k \leq x_k^U, k = 1, \ldots, n. \end{aligned} \tag{3.8}$$

where the objective function is to maximize the power coefficient $C_P$ (or minimize $-C_P$). The power coefficient is normalized with a fit of the baseline rotor ($C_{P,\text{fit}}$) from section 3.3.2. The vector of design variables, $\mathbf{x}$, are the control points (CPs) of B-splines [129] that define the chord and twist distributions, see e.g. Figure 3.14. Details on B-splines are available in Appendix C. The vector $\mathbf{x}$ contains a total of $n$ variables that are real numbers, $\mathbb{R}$. The non-linear constraint function, $g_c$, guarantees that the chord is monotonically decreasing from root to tip. The upper ($U$) and lower ($L$) boundary constraints, $x_k^L \leq x_k \leq x_k^U$, are bounds on the CPs. There are four CPs each for chord and twist, but only two CPs, i.e. $\text{CP}_2$ and $\text{CP}_3$, used as design variables. $\text{CP}_1$ and $\text{CP}_4$ are fixed to baseline values, see Figure 3.14. Figure 3.14 displays the best fit shape for the implemented blade parameterization method and represents $C_{P,\text{fit}}$ in Equation 3.8. Variables have been normalized with the upper and lower bounds to prevent bias and improve optimizer performance. Table 3.2 lists the parameters used in the optimization of the model rotor design.

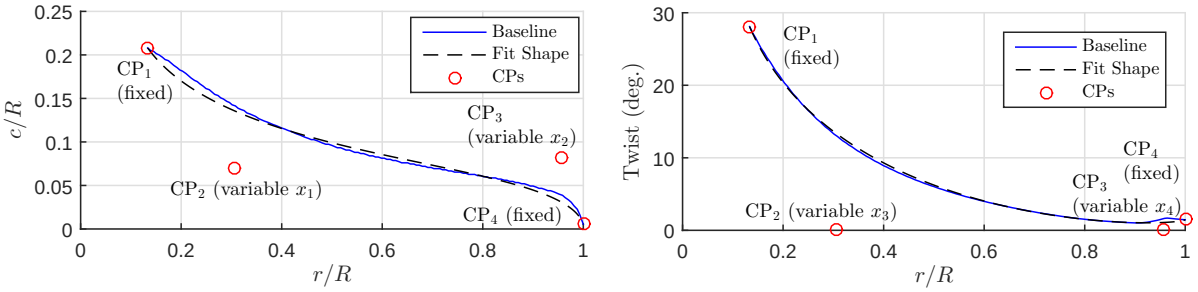


**Figure 3.14:** Fitted shape is based on curve fitting the CPs with the blade from the inverse design approach (baseline).

The optimization problem of Equation 3.8 was performed using an in-house BEM code as described by Hansen [35] and MIRAS. The BEM code runs assuming Reynolds number effects are negligible. In other words, only one table of lift and drag data at $Re = 280,000$ was used in the BEM algorithm. The purpose of using BEM is to evaluate the quality of the surrogate model compared to the true design space using metrics, see later in subsection *Design Space Shape*. Furthermore, the optimum blade design from the surrogate optimization technique should be compared with the optimum from the true design space to test the effectiveness of the optimization method. These quality tests cannot be performed using MIRAS due to its large computational expense. The BEM and MIRAS codes in the current study run for approximately 5 (1 CPU core) and 18,000 seconds (20 CPU cores), respectively. For the number of function calls shown in Table 3.2, including parallelization of the sampling plan, approximately 1 minute and 3 days are required for the surrogate optimization to finish for the BEM and MIRAS cases, respectively.

**Table 3.2:** Parameters used in the optimization of the model-rotor design problem.

| Description | Symbol(s) | Value |
|---|---|---|
| Number of variables | $n$ | 4 |
| Upper chord (m) | $x_1^U$, $x_2^U$ | 0.1 |
| Lower chord (m) | $x_1^L$, $x_2^L$ | 0.0001 |
| Upper twist (deg.) | $x_3^U$, $x_4^U$ | 45.0 |
| Lower twist (deg.) | $x_3^L$, $x_4^L$ | 0.0 |
| $r/R$ location of $CP_1$ | - | 0.13 |
| $r/R$ location of $CP_2$ | - | 0.31 |
| $r/R$ location of $CP_3$ | - | 0.96 |
| $r/R$ location of $CP_4$ | - | 1.00 |
| Number of grid points in each dim. | $X$ | 12 |
| Sampling plan size | - | 8 |
| Global search iterations | - | 8 |
| Local search iterations | - | 5 |
| Total number of function calls | - | 21 |

### Blade Shape

The blades from the surrogate optimizations using BEM and MIRAS shown in three dimensions are given in Figure 3.15. Blades generated from the sampling plan described in subsection 3.2.2 are shown in Figures 3.16 and 3.17. The blade shapes are significantly different from each other because they represent distinct regions of a large design space bounded by the upper and lower values of chord and twist in Table 3.2.

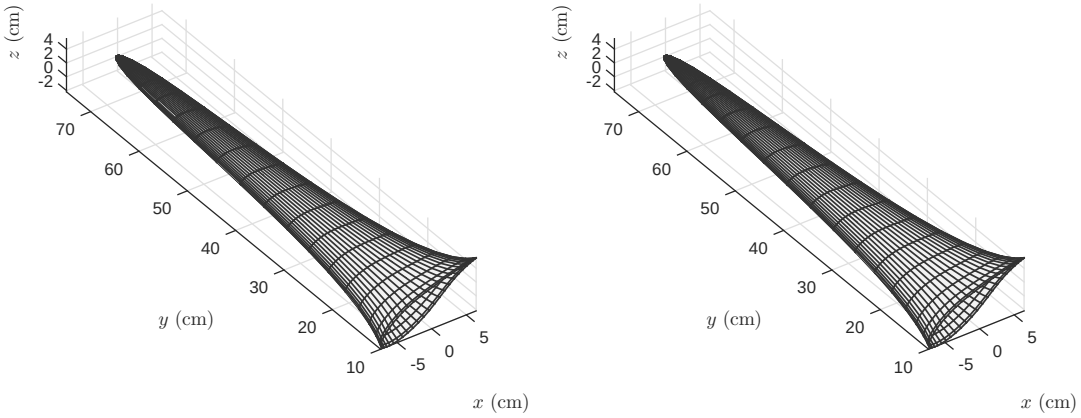


**Figure 3.15:** Final blade shapes obtained from surrogate optimization using BEM (left) and MIRAS (right).

The results for the optimum blade shapes are summarized in Table 3.3 and compared to the baseline of section 3.3.2 in Figures 3.18, 3.19, and 3.20. Recall from the *Description of optimization problem* subsection that the values of the variable vector $\mathbf{x}$ in Table 3.3 represent the values of the CPs defining the chord and twist distributions. All blades are compared simultaneously in Figure 3.21. The similar results found in Figures 3.18 and 3.19 illustrates the effectiveness of the surrogate optimization technique. Although

the chord for both blades differ from the baseline fit towards the root (i.e. $x_1$), BEM predicts they have an almost identical performance in local $C_P$, see Figure 3.22. This is also true for the optimum blade found using MIRAS in the surrogate-optimization technique, see Figure 3.23. Figure 3.20 displays the chord and twist distributions of the optimum blade found using MIRAS, which differs slightly from the blade found using BEM. The small improvement in $C_P/C_{P,\text{fit}}$ in Table 3.3 from the surrogate optimization using BEM is reflected in the small increase in d$C_P$ compared to the baseline fit shown in Figure 3.22. This is not the case for MIRAS, however the optimum design gives almost identical performance compared to the baseline fit, see Figure 3.23.

**Table 3.3:** Blade shape results in terms of the objective function $-C_P(\mathbf{x})/C_{P,\text{fit}}$ and the variable vector $\mathbf{x}$.

| Model | Blade from: | $-C_P/C_{P,\text{fit}}$ | $x_1$ (m) | $x_2$ (m) | $x_3$ (deg.) | $x_4$ (deg.) |
|---|---|---|---|---|---|---|
| BEM/MIRAS | Fit | -1.0000 | 0.052 | 0.062 | 0.003 | 0.199 |
| BEM | Surr. | -1.0024 | 0.043 | 0.066 | 0.000 | 0.000 |
| BEM | Grid | -1.0049 | 0.027 | 0.073 | 0.000 | 0.000 |
| MIRAS | Surr. | -0.9996 | 0.055 | 0.064 | 0.000 | 0.000 |

### Design Space Shape

Two metrics were used to evaluate the accuracy of the surrogate model compared to the true function for the BEM case. Recall that quality testing of the surrogate for the MIRAS case cannot be done due to the large computational expense of MIRAS. The first is the correlation coefficient, $r^2$, that compares the shape of the design space and not the values. An $r^2 > 0.8$ indicates a surrogate with good predictive capabilities [92]. The second metric is the Normalized Root Mean Squared Error (NRMSE) that measures the error in values between the surrogate model and the true function. NRMSE should be as small as possible. A reasonably good model should have a NRMSE of less than 0.1. The $r^2$ and NRMSE are shown in Equations 3.9 and 3.10-3.11, respectively, where $\widehat{y} = \widehat{f}(\mathbf{x})$, $y = f(\mathbf{x})$, and $n_t = X^n$. The $r^2$ and NRMSE for the BEM case are 0.881 and 0.0679, respectively.

$$r^2 = \left( \frac{n_t \sum_{i=1}^{n_t} y^{(i)} \widehat{y}^{(i)} - \sum_{i=1}^{n_t} y^{(i)} \sum_{i=1}^{n_t} \widehat{y}^{(i)}}{\left[ n_t \sum_{i=1}^{n_t} (y^{(i)})^2 - \left( \sum_{i=1}^{n_t} y^{(i)} \right)^2 \right] \left[ n_t \sum_{i=1}^{n_t} (\widehat{y}^{(i)})^2 - \left( \sum_{i=1}^{n_t} \widehat{y}^{(i)} \right)^2 \right]} \right)^2 \tag{3.9}$$

$$\text{RMSE} = \sqrt{\frac{\sum_{i=1}^{n_t} (y^{(i)} - \widehat{y}^{(i)})^2}{n_t}} \tag{3.10}$$

$$\text{NRMSE} = \frac{\text{RMSE}}{y_{\max} - y_{\min}} \tag{3.11}$$

Figures 3.24, 3.25 and 3.26 depict the design space for the true function (BEM case), surrogate approximation (BEM case), and surrogate approximation for the MIRAS case, respectively. Note $x_1$, $x_2$, $x_3$ and $x_4$ in Figures 3.24, 3.25 and 3.26 represent normalized values using the upper and lower bounds shown in Table 3.2. Observe that the radial basis

function approximation in Figure 3.25 is similar to the true design space in Figure 3.24. The differences in both figures are quantified in the $r^2$ and NRMSE. The surrogate-design space for the MIRAS case (Figure 3.26) is almost identical to the BEM case (Figure 3.25). Using a surrogate model other than the ones tested in this work may improve the values of the $r^2$ and NRMSE metrics, and in turn the effectiveness of the surrogate-optimization technique for the model wind-turbine rotor design problem.

## 3.4 Conclusions

A surrogate-optimization framework has been developed to design a model wind-turbine rotor using both a computational cheap and costly objective function. The cheap model studied within the framework was the blade element momentum method (BEM), while a three-dimensional viscous-inviscid interaction code (MIRAS) was used as the costly model. A Latin hypercube sampling plan was used to create the initial set of blades, while a cubic radial basis function was used as the surrogate. An efficient search-and-exploit surrogate scheme was developed and applied to finally obtain well-designed rotor blades for the BEM and MIRAS cases. Results from the MIRAS case compared with the inverse-design technique show almost identical designs, which questions if there are any advantages in using advanced models for rotor design. Nevertheless, surrogate optimization provides an inspiring option for designing wind-turbine rotors using computational costly models.

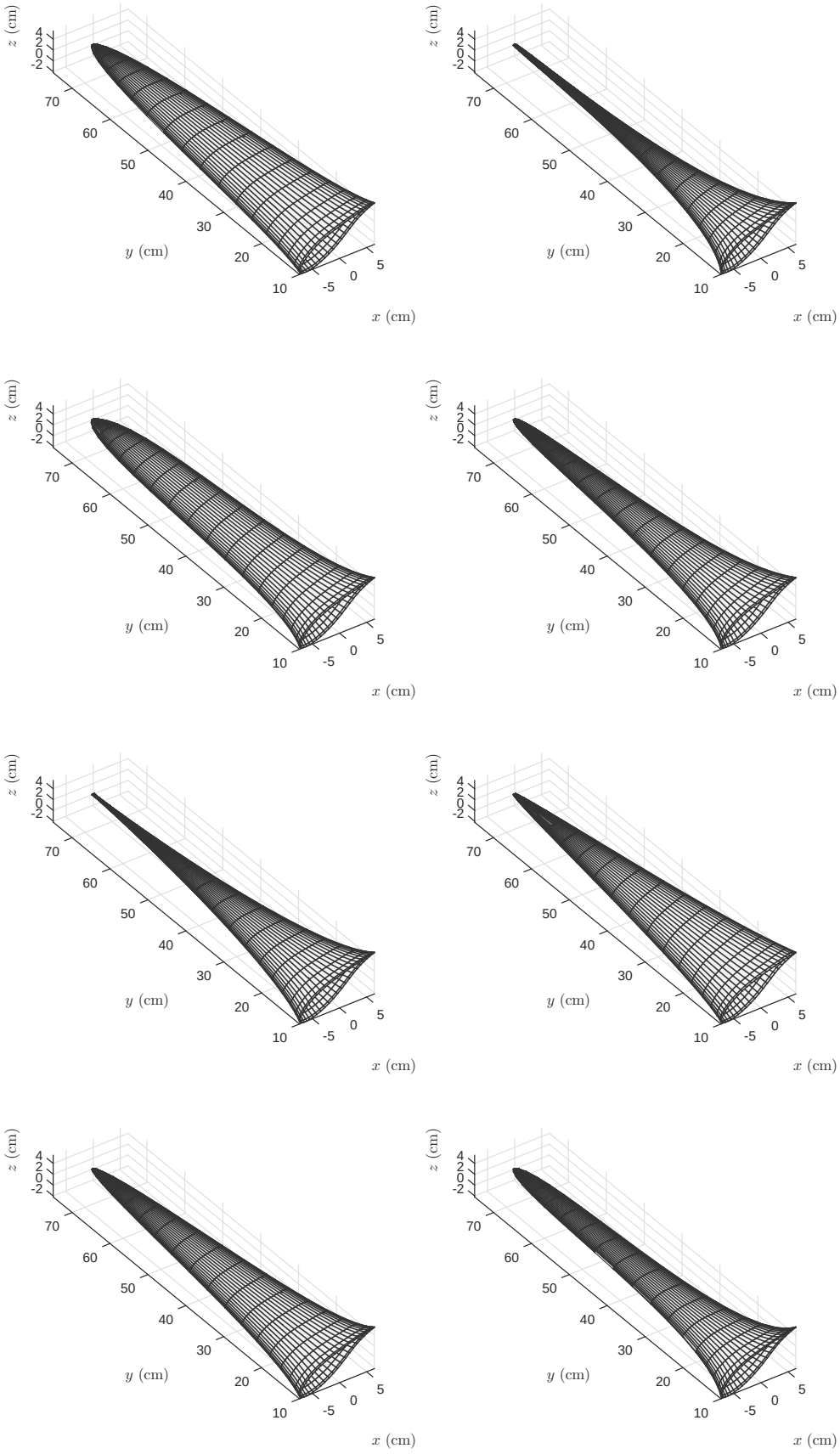


**Figure 3.16:** Eight blades generated from Latin hypercube sampling.

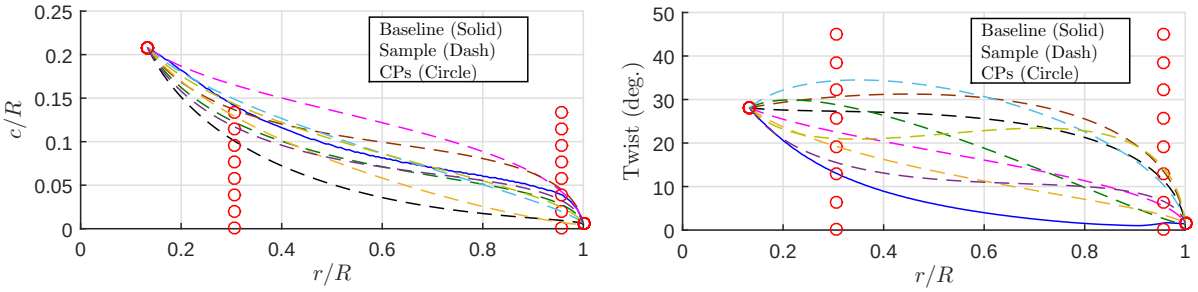


**Figure 3.17:** Eight blades generated from Latin hypercube sampling. The uniform distribution of the control points (CPs) illustrates the efficacy of the sampling technique.

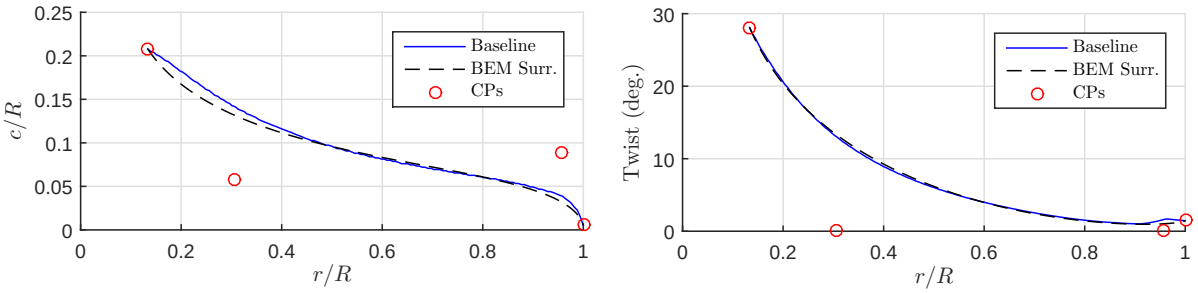


**Figure 3.18:** Optimum blade shape found from surrogate optimization using BEM.

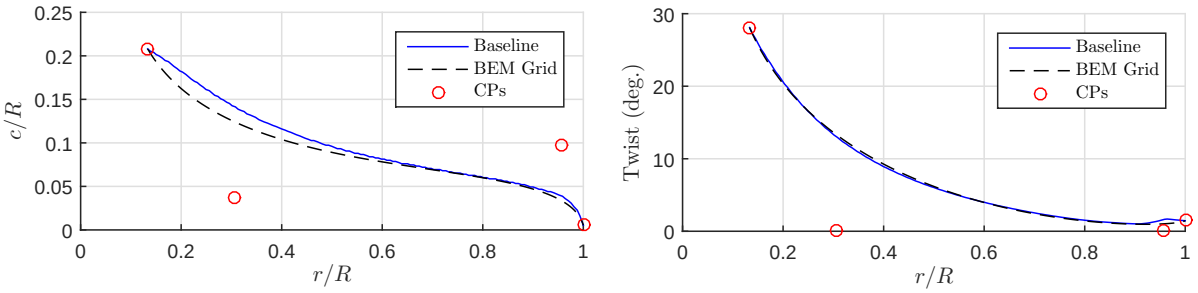


**Figure 3.19:** Optimum blade shape found from evaluating the true function on a $X^n$ (i.e. $12^4$) grid using BEM.

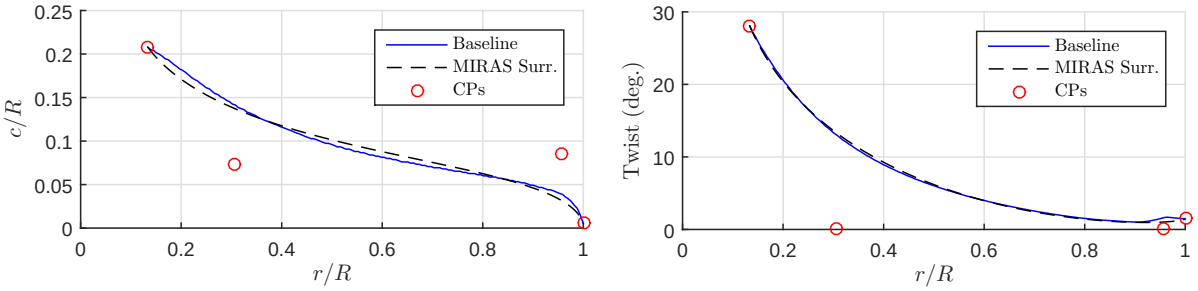


**Figure 3.20:** Optimum blade shape found from surrogate optimization using MIRAS.

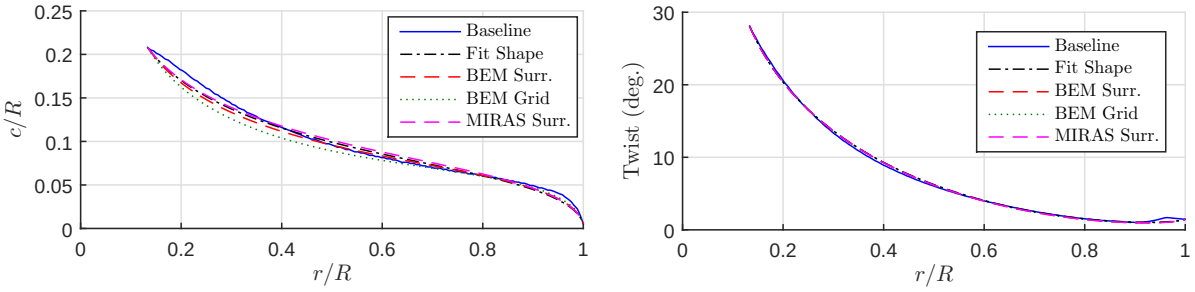


**Figure 3.21:** Optimum blade shapes found from the inverse design, surrogate-BEM, $X^n$-grid-BEM, and surrogate-MIRAS cases.

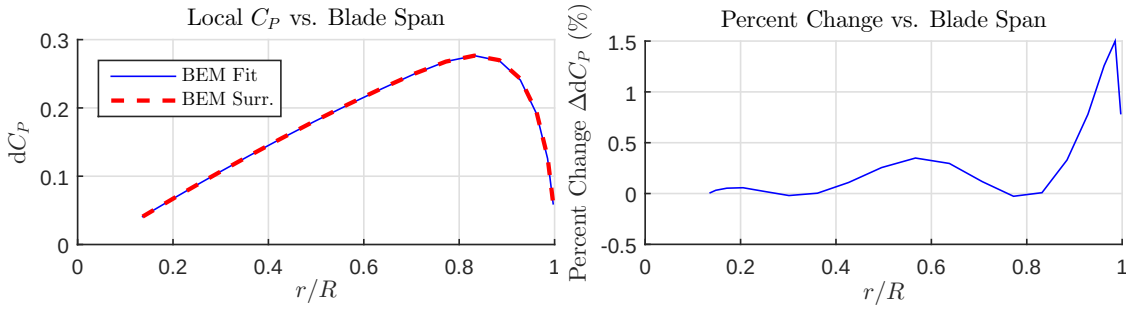


**Figure 3.22:** Comparison of local power coefficient, $dC_P$, vs. blade span from BEM (left). Solid line represents the fitted-baseline shape while the dashed line is the blade found from the surrogate optimization. Depiction of the percent increase (+) and decrease(-) in $dC_P$ of the optimum blade compared to the fit (right).

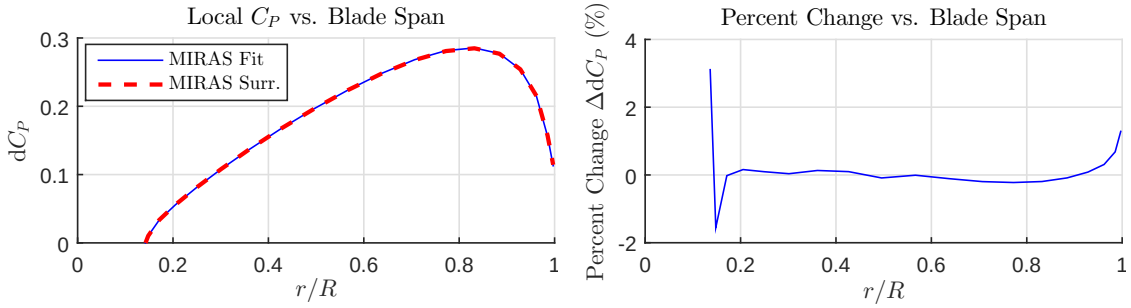


**Figure 3.23:** Comparison of local power coefficient, $dC_P$, vs. blade span from MIRAS (left). Solid line represents the fitted-baseline shape while the dashed line is the blade found from the surrogate optimization. Depiction of the percent increase (+) and decrease(-) in $dC_P$ of the optimum blade compared to the fit (right).

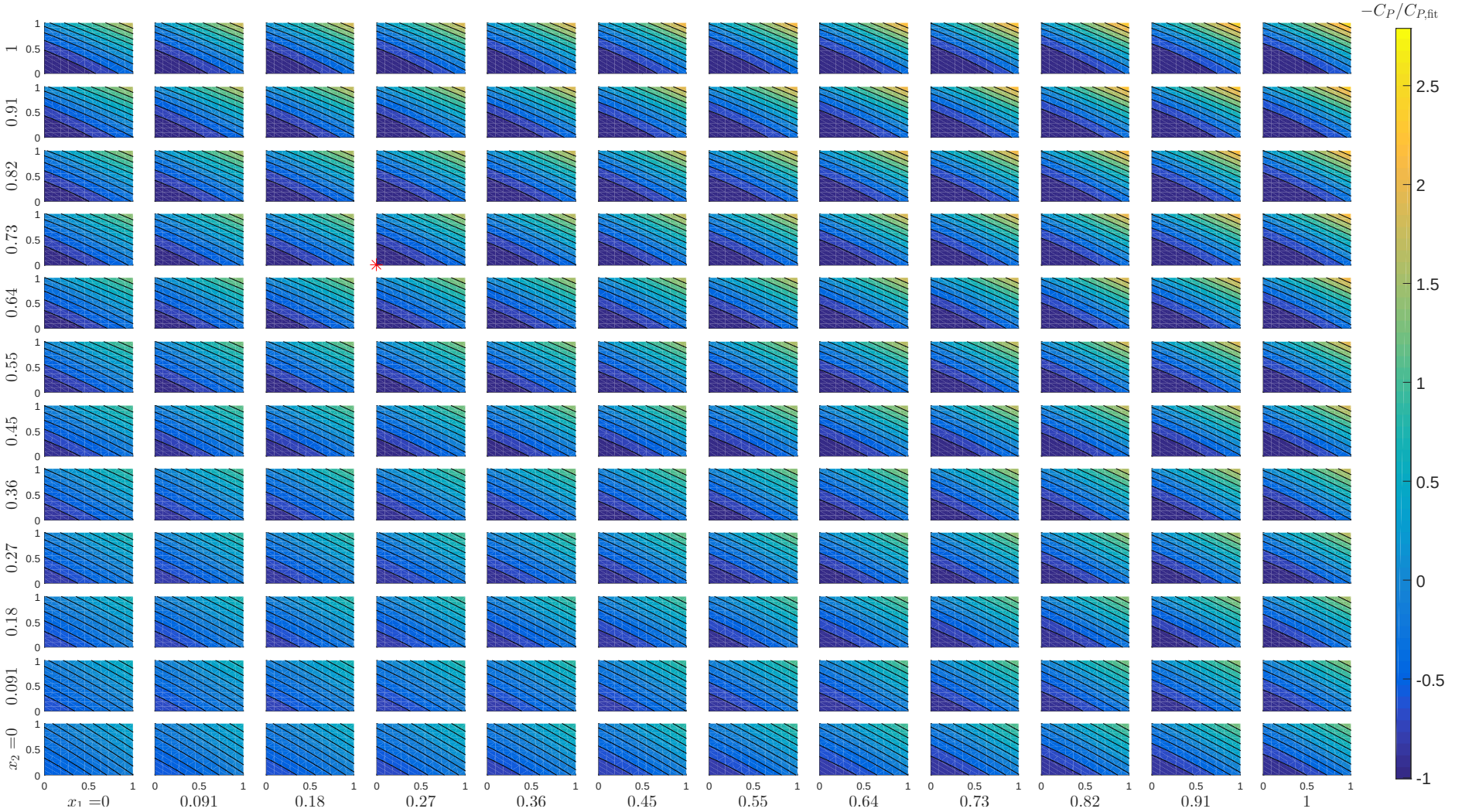


**Figure 3.24:** Design space found from evaluating the objective on a $X^n$ (i.e. $12^4$) grid for the BEM case. The values for design variable $x_3$ varies along the horizontal axis of each tile, $x_4$ along the vertical axes, while $x_1$ and $x_2$ can be read from the bottom of each column of tiles and the beginning of each row, respectively. Asterisk located at $[x_1, x_2, x_3, x_4] = [0.27, 0.73, 0, 0]$ is the minimum.

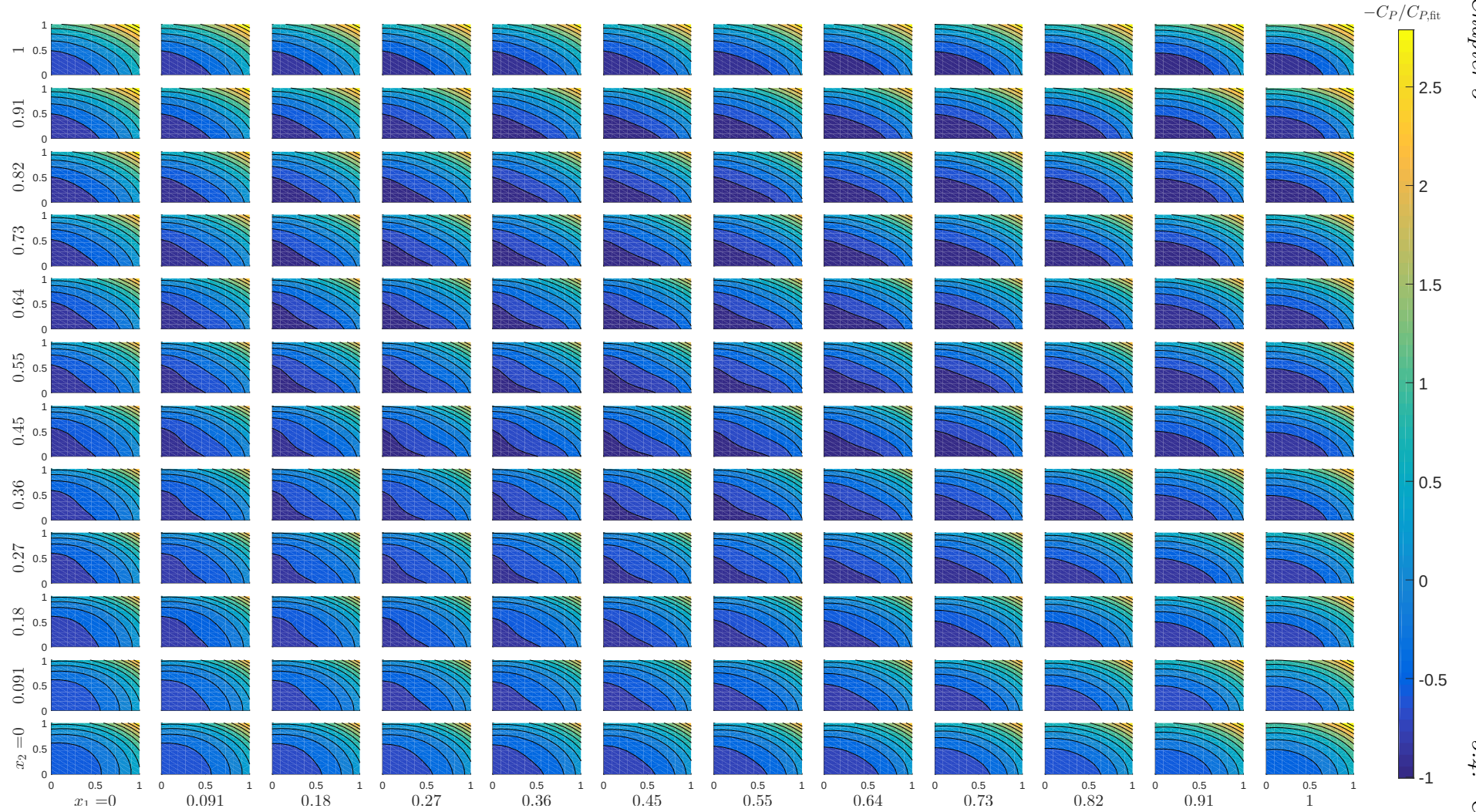


**Figure 3.25:** Design space found from evaluating the surrogate on a $X^n$ (i.e. $12^4$) grid for the BEM case. Max-min color scaling based on the true design space shown in Figure 3.24.

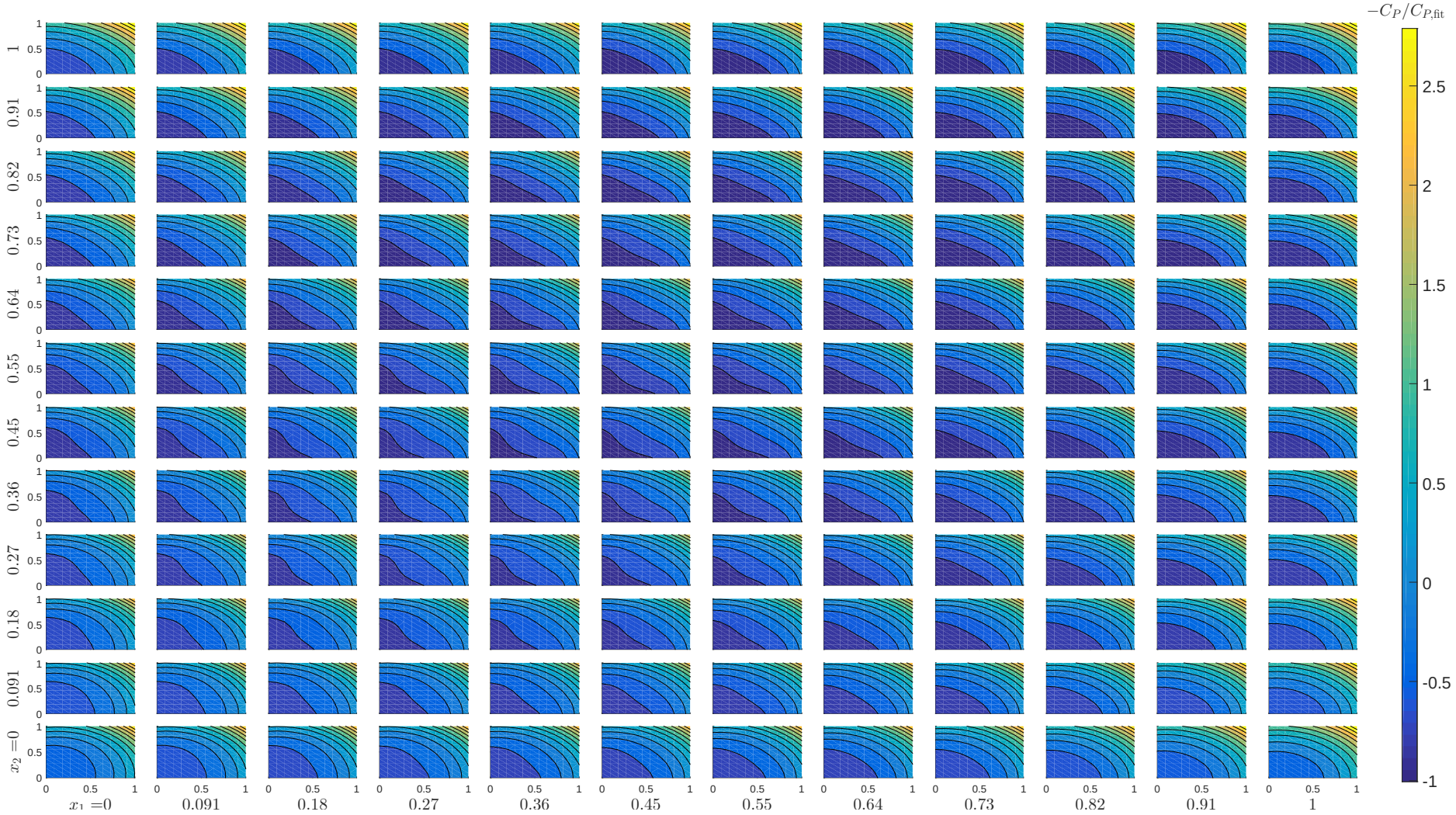


**Figure 3.26:** Design space found from evaluating the surrogate on a $X^n$ (i.e. $12^4$) grid for the MIRAS case. Max-min color scaling based on the true design space shown in Figure 3.24.

# Chapter 4

# Structural Design and Loads

## 4.1 Introduction

This chapter is based on the work: 'Development of a simple structural design method for large wind turbine blades' [4]. In Chapter 4, the stand-alone version of the structural design code will be presented. The structural design code combined with MIRAS-FLEX and FLEX5 for aero-structural optimization is presented in Chapter 5. The methods, results and conclusions are described in sections 4.2, 4.5, and 4.6, respectively.

## 4.2 Methodology

This section describes how the optimization is performed. First, the reference model used for the structural design will be presented. The objective, constraints and variables will be described next. Finally, the optimization procedure will be outlined.

### 4.2.1 NREL 5 MW Reference Model

The blade reference model for the NREL 5 MW from Resor [130] is implemented. The report from [130] documents the information used to create the NREL 5 MW structural design, which was based on basic design criteria by the IEC standards. The design documented in this report provides a good starting point for more detailed studies such as blade design optimization and blade design tool verification. As stated in [130], the blade only meets basic design criteria and has not been optimized in any way. The material properties were mostly taken from the Sandia 100 m blade design [131]. Table 4.1 lists the materials and their properties used in the design of [130]. A rough guideline for the placement of uni-directional (UD), tri-axial (Triax), and double biax (DB) materials in laminate data from [130] is depicted in Figure 4.1.

In Resor's report, the blade design was carried out using Sandia National Laboratories' *NuMAD* tool. The NREL 5 MW blade model is an input to NuMAD, see Figure 4.2. A built-in feature of NuMAD is then used to generate the laminate data as PreComp input files. PreComp is called automatically within NuMAD to output the structural properties ready for input in the aero-elastic code FAST, see Figures 4.3 and 4.4. In Figures 4.3 and 4.4, "NREL5MW Ref." is from reference [116], "SNL 61.5m" is the one obtained from Sandia using NuMAD [130], and "Validation" is from the author of this thesis using NuMAD.

'Blade Fraction' is the fractional distance along the blade-pitch axis from the root (Blade Fraction = 0.0) to the tip (Blade Fraction = 1.0). 'AeroCent' is the name of a FAST input parameter [116]. The FAST code assumes that the blade-pitch axis passes through each airfoil section at 25% chord. By definition, the quantity (AeroCent - 0.25) is the fractional distance to the aerodynamic center from the blade-pitch axis along the chord-line, positive toward the trailing edge. For example, at the tip (Blade Fraction

**Table 4.1:** Summary of material properties from [130] based on the Sandia 100-m blade [131]. Wind-turbine blades are primarily made of anisotropic or orthotropic (ortho) materials, rather than isotropic (iso).

| Material | | Gelcoat | E-LT-5500(UD) | SNL (Triax) | Saertex (DB) | FOAM | Carbon (UD) |
|---|---|---|---|---|---|---|---|
| Type | | iso | ortho | ortho | ortho | iso | ortho |
| Layer Thickness | [mm] | 0.05 | 0.47 | 0.94 | 1 | 1 | 0.47 |
| Ex | [MPa] | 3440 | 41800 | 27700 | 13600 | 256 | 114500 |
| Ey | [MPa] | 3440 | 14000 | 13650 | 13300 | 256 | 8390 |
| Gxy | [MPa] | 1380 | 2630 | 7200 | 11800 | | 5990 |
| prxy | [-] | 0.3 | 0.28 | 0.39 | 0.49 | 0.3 | 0.27 |
| Density | [kg/m$^3$] | 1235 | 1920 | 1850 | 1780 | 200 | 1220 |
| UTS | [MPa] | - | 972 | 600 | 144 | - | 1546 |
| UCS | [MPa] | - | 702 | - | 213 | - | 1047 |

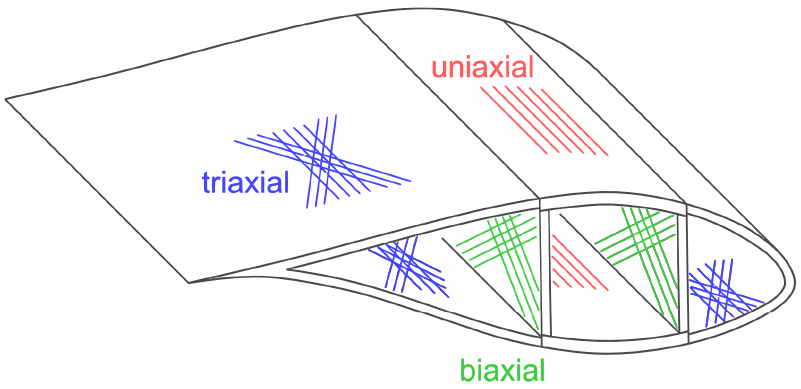


**Figure 4.1:** Rough guideline for the placement of uni-directional (UD), tri-axial (Triax), and double biax (DB) materials in laminate data from [130]. Figure taken from [132].

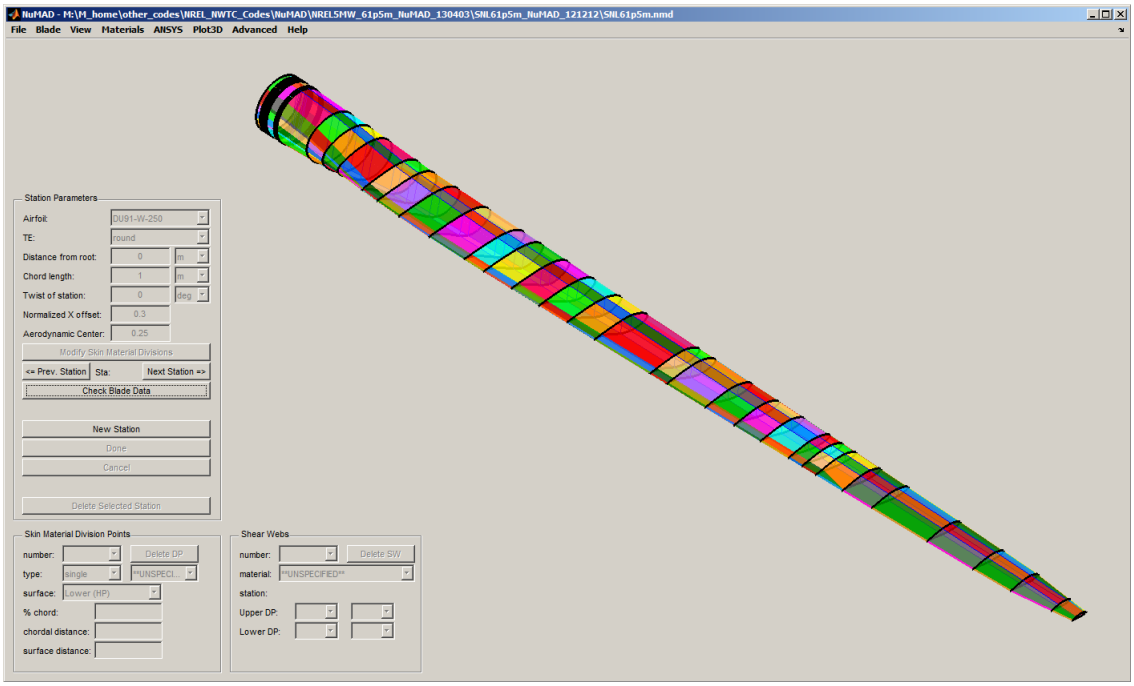


**Figure 4.2:** Structural design of the NREL 5 MW as described in [130] was done using Sandia National Laboratories' NuMAD tool.

= 1.0), AeroCent = 0.125 means that the aerodynamic center lies 0.125 chord-lengths toward the leading edge from the blade-pitch axis because (0.125 - 0.25) = -0.125.

The flap-wise and edge-wise section stiffness and inertia values, 'FlpStff,' 'EdgStff,' 'FlpIner,' and 'EdgIner' in Figures 4.3 and 4.4, are given about the principal structural axes of each cross section as oriented by the structural-twist angle, 'StrcTwst.' The values of the structural twist were assumed to be identical to the aerodynamic twist discussed in [116]. 'GJStff' represents the values of the blade torsion stiffness. 'EAStff' represents the values of the blade extensional stiffness. The edgewise center of mass (CM) offset values, 'EdgcgOf,' are the distances in meters along the chord-line from the blade-pitch axis to the CM of the blade section, positive toward the trailing edge. Reference [116] neglected the values of the flap-wise CM offsets, 'FlpcgOf,' and flap-wise and edge-wise elastic offsets, 'FlpEAOf' and 'EdgEAOf'. Instead, they were assumed zero as shown in Figure 4.4. 'BMassDen,' is the distributed blade section mass per unit length. 'PrecrvRef' and 'PreswpRef' are the pre-curve (or pre-bend) and pre-sweep in meters relative to the pitch-axis.

### 4.2.2 Objectives, Constraints and Variables

The objective is to minimize the COE subject to a number of non-linear in-equality and boundary constraints:

$$\begin{aligned} \underset{x}{\text{minimize}} \quad & \text{COE}(\mathbf{x}) \\ \text{subject to} \quad & \mathbf{x} \in \mathbb{R}^n, \\ & g_c(\mathbf{x}) \leq 0, c = 1, \ldots, N_c, \\ & x_k^L \leq x_k \leq x_k^U, k = 1, \ldots, n. \end{aligned} \tag{4.1}$$

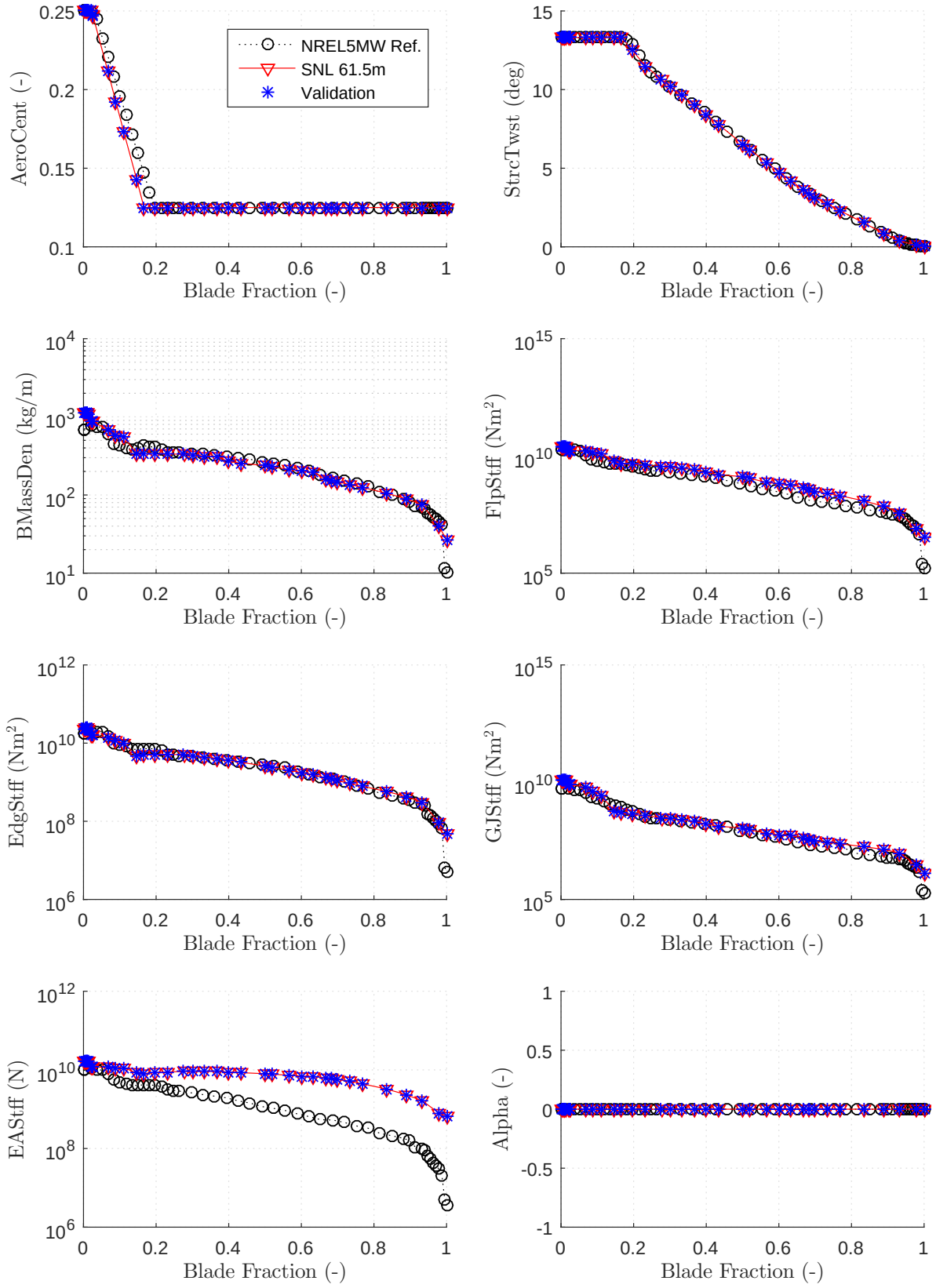


**Figure 4.3:** Structural properties of the NREL 5 MW from reference [116] (NREL5MW Ref.), from Sandia using NuMAD [130] (SNL 61.5m), and from the author using NuMAD (Validation).

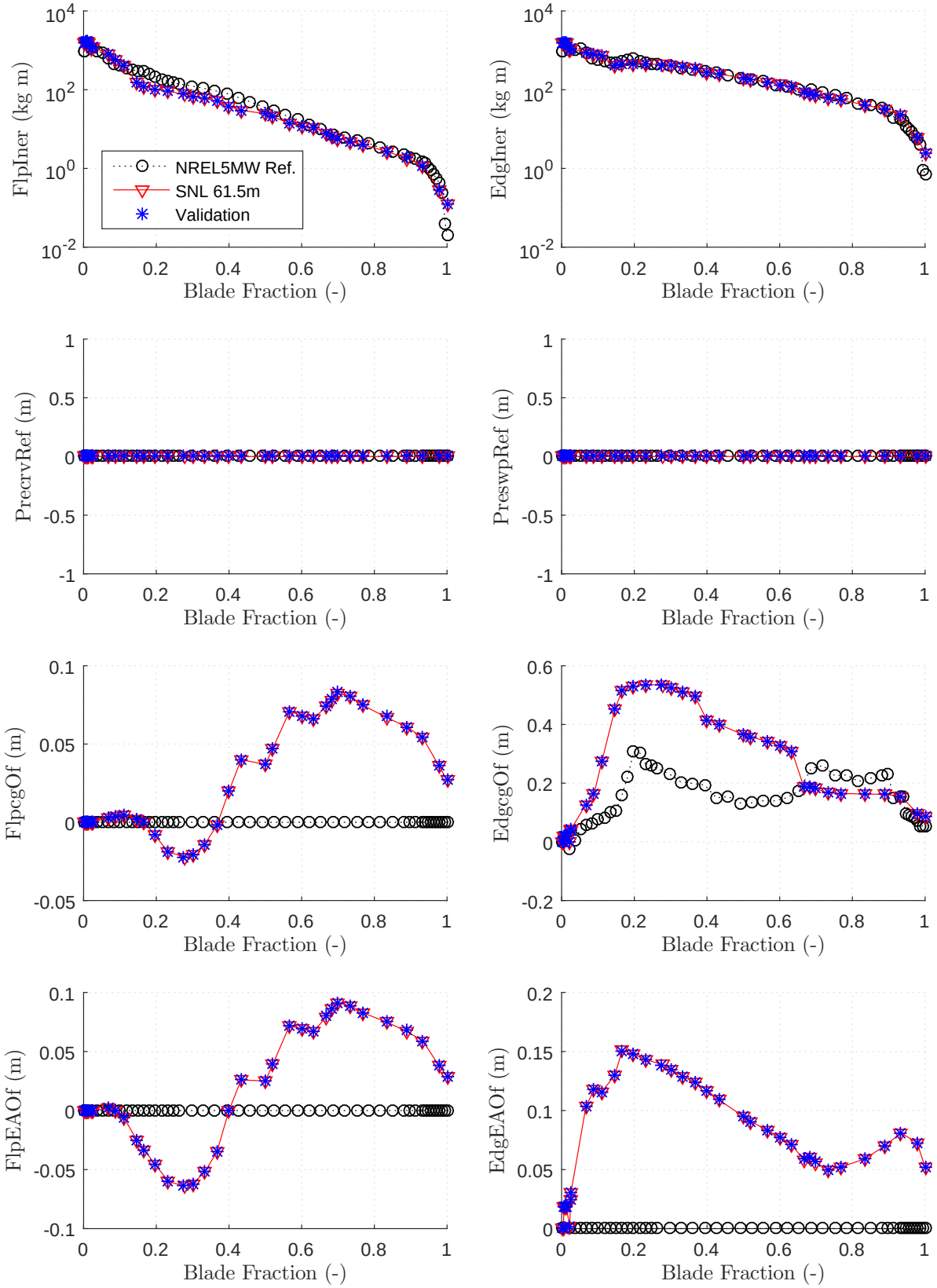


**Figure 4.4:** Structural properties of the NREL 5 MW from reference [116] (NREL5MW Ref.), from Sandia using NuMAD [130] (SNL 61.5m), and from the author using NuMAD (Validation).

where the objective is calculated from the NREL Wind Turbine Design Cost and Scaling Model [84]. The vector of design variables, $\mathbf{x}$, are the the spar-cap thickness and the chord-wise location of the webs (or spar width) along the blade span, see Figure 4.5. The vector $\mathbf{x}$ contains a total of $n$ variables that are real numbers, $\mathbb{R}$. Note a box-spar layup is assumed for the internal blade structure. The spar-cap thickness distribution is defined by eight control points (CPs), while the web layup is defined by the chord-wise locations of the two endpoints for each web (i.e. four CPs for a two-web layup), see Figure 4.6. Linear interpolation is performed to obtain values in-between the CPs. Each element of the vector of design variables ($x_k$) is bounded by upper ($x_k^U$) and lower ($x_k^L$) limits. Upper and lower bounds of the spar-cap thickness are used to prevent the caps on the upper and lower surface from merging into each other or becoming negative. Similarly, bounds on the webs are used to prevent the webs from merging into each other and also into different sectors of the cross-section. Variables have been normalized with the upper and lower bounds to prevent bias and improve optimizer performance.

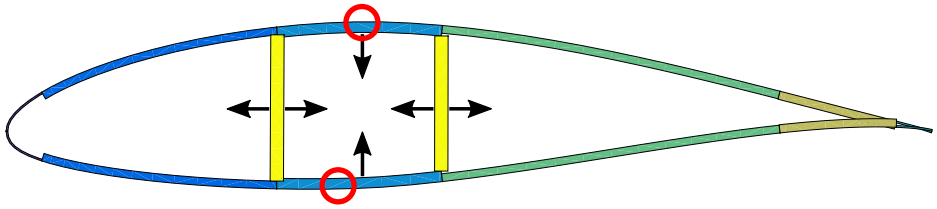

**Figure 4.5:** Depiction of the box-spar structural layup as defined in Resor [130]. Optimization variables are the spar-cap thickness and web layup shown as black arrows. Only the highest and lowest points on the airfoil contour (circles) are used to compute the strain constraint, see Equation (4.3).

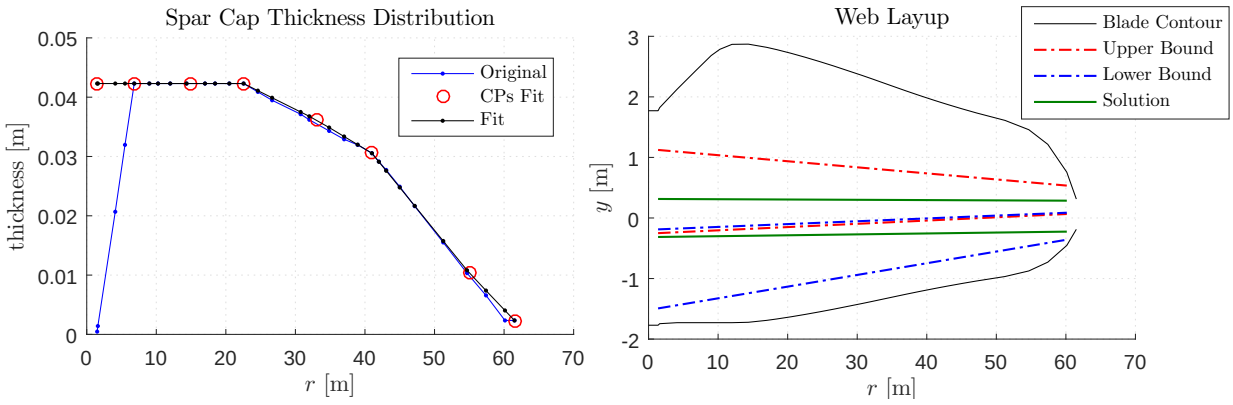


**Figure 4.6:** Optimization variables are the spar-cap thickness distribution (left) and web layup (right).

The non-linear in-equality constraints, $g_c(\mathbf{x}) \leq 0$, $c = 1, \ldots, N_c$, are:

$$\begin{aligned} &\text{blade natural frequency}(\mathbf{x}): && \omega_{\text{constraint}} \leq 0 \\ &\text{tip deflection}(\mathbf{x}): && \delta_{\text{constraint}} \leq 0 \\ &\text{tensile strain}(\mathbf{x}): && \epsilon_{\text{constraint},1} \leq 0 \\ &\text{compressive strain}(\mathbf{x}): && \epsilon_{\text{constraint},2} \leq 0 \\ &\text{spar-cap buckling}(\mathbf{x}): && \eta_{\text{constraint}} \leq 0 \end{aligned} \tag{4.2}$$

The COE objective, blade natural frequency, tip deflection, strain, and spar-cap buckling constraints are more specifically expressed as:

$$\begin{aligned}
\text{COE}_{\text{objective}} &= \text{Blade Cost/AEP} \\
\omega_{\text{constraint}} &= (3\omega_{\text{rotor}}\text{SF} - \omega)/\omega_{\text{rotor}} \\
\delta_{\text{constraint}} &= (\delta_{\text{tip}} - \delta_{\max})/\delta_{\max} \\
\epsilon_{\text{constraint,1}} &= (\epsilon_{\text{tension}}\text{SF} - \epsilon_{\text{ultimate,tension}})/\epsilon_{\text{ultimate,tension}} \\
\epsilon_{\text{constraint,2}} &= (\epsilon_{\text{compression}}\text{SF} - \epsilon_{\text{ultimate,compression}})/\epsilon_{\text{ultimate,compression}} \\
\eta_{\text{constraint}} &= (\eta - \eta_{\max})/\eta_{\max}
\end{aligned} \tag{4.3}$$

where AEP is the annual energy production and is assumed 1 (i.e. to be determined from the rotor optimization code in Chapter 5), $3\,\omega_{\text{rotor}}$ is the rotor blade passing frequency, SF is a safety factor, $\delta_{\max}$ is the maximum allowable tip deflection, $\epsilon_{\text{ultimate,tension}}$ and $\epsilon_{\text{ultimate,compression}}$ are the ultimate tensile and compressive strain, respectively, and $\eta_{\max}$ is the maximum allowable buckling coefficient set to 0.5. The buckling coefficient, $\eta$, is computed for the spar-caps only, and assumes that the spar-beam is modeled as a long orthotropic plate under uni-axial compression with all edges simply supported [133]. Skin and panel buckling are not considered. The tip deflection, $\delta_{\text{tip}}$, as well as the tensile ($\epsilon_{\text{tension}}$) and compressive ($\epsilon_{\text{compression}}$) strain are calculated from Euler-Bernoulli beam theory. The first and second blade natural frequencies, $\omega$, are obtained from BModes. Blade cost is obtained from a simple blade-mass vs. blade-cost relationship. More details on the natural frequency, tip deflection, and strain constraints are described next, and are also available in [130, 133, 134] and Sale [73].

**Strain and Deflection Analysis**

Strain in the location given by the coordinates $y$ and $z$ on the cross-section is estimated using the following [35]:

$$\epsilon(y,z) = \frac{M_1}{EI_1}z - \frac{M_2}{EI_2}y \tag{4.4}$$

where $M_1$ and $M_2$ are the bending moments about the principal axes calculated using:

$$M_1 = M_y\cos(\beta+v) - M_z\sin(\beta+v) \tag{4.5}$$

$$M_2 = M_y\sin(\beta+v) + M_z\cos(\beta+v) \tag{4.6}$$

where $\beta + v$ is the angle between the $y-$axis and the first principal axis. The $y-$axis is aligned with the tip chord. The bending stiffnesses about the principal axes, $EI_1$ and $EI_2$, are calculated using:

$$EI_1 = EI_y - EI_{yz}\tan(v) \tag{4.7}$$

$$EI_2 = EI_z - EI_{yz}\tan(v) \tag{4.8}$$

The bending stiffnesses $EI_y$, $EI_z$, and $EI_{yz}$ are referenced to the tension center. The stiffnesses are obtained from PreComp, which are defined at the shear center. The parallel-axis theorem is applied to obtain stiffnesses referenced to the tension center. The total safety factor for strain in Equation (4.3) is obtained from Table 4.2.

The tip displacement, $\delta$, of a beam or wind-turbine blade under a static load can be found by integrating the curvatures $\kappa_y$ and $\kappa_z$ from simple Euler-Bernoulli beam theory:

$$\kappa_1 = \frac{M_1}{EI_1} \tag{4.9}$$

**Table 4.2:** Safety factors used in evaluation of ultimate strength (IEC 7.6.2). Copied from Resor [130].

| | | |
|---|---|---|
| Partial safety factor for loads, $\gamma_f$ | 1.35 | |
| Partial safety factor for materials, $\gamma_m$ | 1.3 | Rupture from exceeding tensile or compression strength |
| Partial safety factor for consequences of failure, $\gamma_n$ | 1.0 | Component class 2 |
| Total safety factor | 1.755 | |

$$\kappa_2 = \frac{M_2}{EI_2} \tag{4.10}$$

$$\kappa_z = -\kappa_1 \sin(\beta + v) + \kappa_2 \cos(\beta + v) \tag{4.11}$$

$$\kappa_y = \kappa_1 \cos(\beta + v) + \kappa_2 \sin(\beta + v) \tag{4.12}$$

$$\frac{\mathrm{d}^2\delta_z}{\mathrm{d}x^2} = \kappa_y \tag{4.13}$$

$$\frac{\mathrm{d}^2\delta_y}{\mathrm{d}x^2} = \kappa_z \tag{4.14}$$

where $x$ is the span-wise beam location. The deflection normal ($\delta_n$) and tangential ($\delta_t$) to the rotor plane is obtained by rotating with the pitch angle, $\theta$:

$$\delta_{\text{tip}} = \delta_n = -\delta_y \sin(\theta) + \delta_z \cos(\theta); \tag{4.15}$$

$$\delta_t = \delta_y \cos(\theta) + \delta_z \sin(\theta); \tag{4.16}$$

The total safety factor for tip deflection is obtained from Table 4.3. The maximum

**Table 4.3:** Safety factors used in evaluation of tower clearance (IEC 7.6.5). Copied from Resor [130].

| | | |
|---|---|---|
| Partial safety factor for loads, $\gamma_f$ | 1.35 | |
| Partial safety factor for materials, $\gamma_m$ | 1.1 | |
| Partial safety factor for consequences of failure, $\gamma_n$ | 1.0 | Component class 2 |
| Total safety factor | 1.485 | |

allowable tip deflection, $\delta_{\max}$, is defined as the total tower clearance divided by the tower clearance safety factor. For example, the tower clearance for the NREL 5 MW reference turbine is 10.50 m, therefore:

$$\delta_{\max} = 10.50\,\text{m}/1.485 = 7.07\,\text{m} \tag{4.17}$$

### Buckling Analysis

For buckling analysis the spar-caps are modeled as a long orthotropic plate under uniaxial compression with all edges simply supported, see Figure 4.7 and references [133] and [134]. Referring to the coordinate system shown in Figure 4.7, the critical buckling load in terms

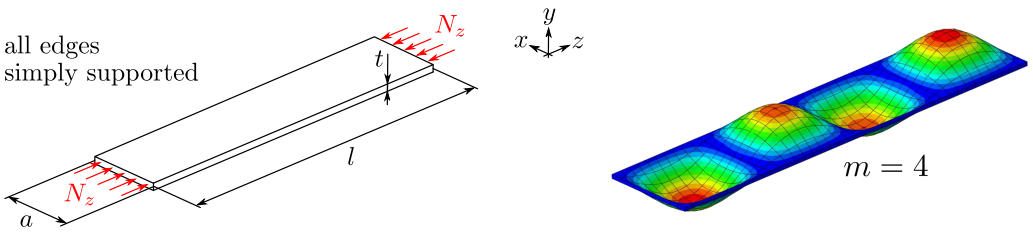


**Figure 4.7:** Spar-caps are modeled as a long orthotropic plate under uniaxial compression with all edges simply supported [133, 134].

of force per length $N_z^{\text{crit}}$ is:

$$N_z^{\text{crit}} = \pi^2 \left[ D_{11} \left(\frac{m}{l}\right)^2 + 2(D_{12} + 2D_{33}) \frac{1}{a^2} + D_{22} \frac{1}{a^4} \left(\frac{l}{m}\right)^2 \right] \tag{4.18}$$

where $l$ and $a$ are the length and width of the plate, respectively, $D_{ij}$ are the bending stiffnesses, and $m$ is the number of buckling waves in the longitudinal direction. Setting the aspect ratio $AR = a/l$:

$$N_z^{\text{crit}} = \frac{\pi^2}{a^2} \left[ D_{11} m^2 AR^2 + 2(D_{12} + 2D_{33}) + D_{22} \frac{1}{m^2} \frac{1}{AR^2} \right] \tag{4.19}$$

The minimum critical buckling load is:

$$\frac{\partial N_z^{\text{crit}}}{\partial AR} = \frac{\pi^2}{a^2} \left[ D_{11} m^2 2AR + D_{22} \frac{1}{m^2} \frac{-2}{AR^3} \right] = 0 \tag{4.20}$$

Solving for $AR$:

$$AR = \left(\frac{D_{22}}{D_{11}}\right)^{1/4} \frac{1}{m} \tag{4.21}$$

Combining Equations (4.19) and (4.21), the magnitude of the minimum critical buckling load is then:

$$N_z^{\text{crit}} = \frac{2\pi^2}{a^2} \left[ D_{12} + 2D_{33} + \sqrt{D_{11} D_{22}} \right] \tag{4.22}$$

The bending stiffness $D_{ij}$ is:

$$D_{ij} = \sum_{k=1}^{n} \frac{Q_{ij}}{3} (z_k^3 - z_{k-1}^3) \tag{4.23}$$

where $z$ refers to the local out-of-plane direction. All plies are assumed identical, thus the bending stiffness of a plate with total thickness $t$ is:

$$D_{ij} = \frac{Q_{ij} t^3}{12} \tag{4.24}$$

where $Q_{ij}$ are the reduced stiffnesses:

$$Q_{11} = \frac{E_1}{1 - v_{12} v_{21}} \tag{4.25}$$

$$Q_{22} = \frac{E_2}{1 - v_{12} v_{21}} \tag{4.26}$$

$$Q_{11} = \frac{v_{12}E_2}{1 - v_{12}v_{21}} \tag{4.27}$$

$$Q_{33} = G_{12} \tag{4.28}$$

where $v_{21} = E_2 \frac{v_{12}}{E_1}$. Inserting Equation (4.24) into Equation (4.22):

$$N_z^{\text{crit}} = \frac{\pi^2 t^3}{6a^2}[Q_{12} + 2Q_{33} + \sqrt{Q_{11}Q_{22}}] \tag{4.29}$$

The force per unit width, $N_z$, is obtained by interpreting the bending moment $M_x$ as a force couple with a distance $h$ between the forces:

$$N_z = \frac{M_x}{h}\frac{1}{a} \tag{4.30}$$

where $M_x$ is the flap-wise bending moment. The buckling coefficient, $\eta = N_z/N_z^{\text{crit}}$, is then

$$\eta_i = 6M_{x,i}a_i/[\pi^2(Q_{12} + 2Q_{33} + \sqrt{Q_{11}Q_{22}})h_i t_i^3] \tag{4.31}$$

where the buckling coefficient is evaluated at each station, $i$.

### 4.2.3 Optimization Procedure

The structural design code begins by tuning the generator and pitch controller as outlined in [135] and section 4.3. Then, a series of design load cases (DLCs) based on Resor [130] and the IEC 61400-1 standards [136] are computed, see Table 4.4. Both the control tuning as well as the DLC computations are performed using FLEX5 and assuming stiff blades. Recall that the present tool is to be integrated with a rotor optimization code, and therefore turbulent wind during normal and abnormal turbine operation was not considered. In the preliminary blade design stage, steady wind models were used in this work for simplicity and speed. DLC 6.1 and 6.3 are computed in 5 yaw error increments/decrements ranging from 30 and -30 (i.e. 13 load cases in total). The bending moments normal and tangential to the rotor plane from all DLCs are then transferred to the optimizer, which calls a structural module for a number of iterations to find the minimum COE.

Figure 4.8 depicts a flowchart of the structural module, which computes the objective and constraints. The inputs to the structural module are the DLC loads and $\mathbf{x}$. The vector $\mathbf{x}$ is used to create a structural layup and compute the objective, while the DLC loads together with the blade structural properties are used to compute the structural constraints. The SQP in the MATLAB optimizer, *fmincon* [137], modifies $\mathbf{x}$ to minimize the objective up to at least a local minimum and also satisfy all constraints. A cost module from NREL [84] is used to calculate the COE using blade mass as input. Only the blade component of the cost model is used in this chapter.

## 4.3 Control Tuning

The FLEX5 control system is designed for a variable-speed and variable-pitch wind turbine, and consists of two simple controllers. The first is a generator power versus rotor speed controller and the second is a proportional-integral (PI) pitch angle control of the rotor speed. The two controllers work independently in the below rated and above rated wind speed range, respectively. The generator power controller will be described first, then the pitch angle controller.

**Table 4.4:** Design load cases used in the structural design code based on [130] and [136].

| Design situation | DLC | Wind condition | Other conditions | Type of analysis |
|---|---|---|---|---|
| Normal Power Production (steady) | - | Steady Windspeed | 2 m/s increments from cut-in = 3 m/s to cut-out = 25 m/s | Ultimate strength |
| | 1.4 | Extreme Coherent gust with Direction change (ECD) | Rated wind ±2 m/s, 2 m/s spacing | Ultimate strength |
| Parked (standing still or idling) | 6.1 | Extreme Windspeed Model (EWM) 50-year recurrence period | Yaw error ±15°, 5° spacing | Ultimate strength |
| | 6.3 | EWM 1-year recurrence period | Extreme yaw misalignment, ±30° | Ultimate strength |

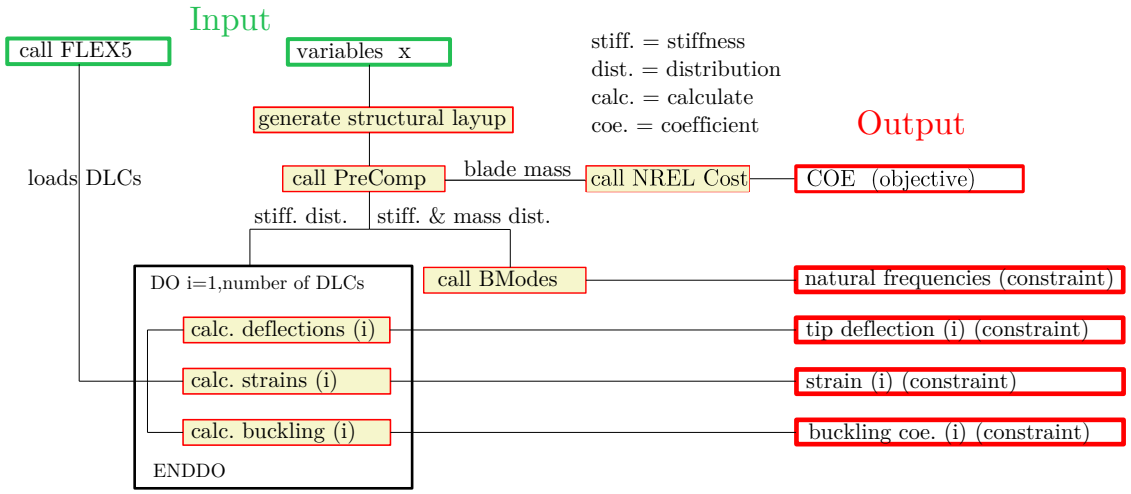


**Figure 4.8:** Flowchart for computing the objective and constraints using the vector of design variables, $\mathbf{x}$, and DLC loads from FLEX5 as input.

### 4.3.1 Generator Power Controller

According to [135], the generator power controller in FLEX5 specifies the power set-point for the generator as a tabulated function of generator speed. The input to the generator power controller is a low-pass-filtered RPM-signal from the generator model. In the generator model, the rotational speed is put through a low-pass filter to avoid instability of the free-free torsional mode of the rotor shaft when operating at constant power.

To set the power set-point, the user inputs to the FLEX5 generator control a table of wind-speed (`Wind`) versus minimum pitch angle (`minPitch`) and generator power (`pow(init)`), see Figure 4.9. In Figure 4.9, the minimum and maximum generator speeds are `N_min` and `N_max`, respectively. In-between `N_min` and `N_max` is the variable-speed operational region, where the generator torque controls the rotational speed to be proportional to the wind speed at a constant tip-speed ratio (TSR). The TSR that produces maximum $C_P$ or aerodynamic power is normally used, and can be determined by performing

```
*** Inputdata for Flex5 control system version 3.2 ***
NREL 5MW, variable speed
1067.8  3650.4       N1, Pow1  (rpm, kW) point on cubic part of P(rpm) curve
670.0  1173.7        N_min, N_max (rpm, rpm)
5000.0               Pmax (kW)
80  150              KI KP (Nm\s\rpm, Nm\rpm) const RPM control
0.30  0.7            F0 (Hz), Ksi (-)
0.034  0.08  0.0     KI KP KD (deg/s/rpm, deg/rpm, deg/rpm*s)
6.8                  KK (deg) (reduction of gain as function of pitch)
90.0  8.0            Teta_max Pitchrate_max  (deg,deg
10                   TauV (sec)  (wind-averaging)
16          No. of lines in table for Wind, minPitch, pow(init) (m/s,deg, kW)
 3.0    0.8     26.9
 5.0    0.8    409.5
 7.0    0.8   1151.5
 9.0    0.8   2447.6
11.0    0.8   4469.1
11.1    0.8   4576.0
11.4    0.8   4999.4
13.0    7.1   5000.0
15.0   11.0   5000.0
17.0   14.1   5000.0
19.0   16.8   5000.0
21.0   19.2   5000.0
23.0   21.5   5000.0
25.0   23.6   5000.0
27.0   25.6   5000.0
29.0   27.6   5000.0
```

**Figure 4.9:** Inputs to the FLEX5 control system.

a parametric study. The parametric study consists of computing the aerodynamic power for a range of rotational speeds or TSR at a wind speed that lies in the variable-speed operational region. The generator speed that produces maximum power is specified as `N1` and the power as `Pow1`. The `point on cubic part of P(rpm) curve` is `N1` and `Pow1`, since $\texttt{Pow}(\omega) = \frac{1}{2}\rho\omega^3 R^5 \pi C_{p,\max}/\mathrm{TSR}^3 = \text{const.} \cdot \omega^3$ in the variable-speed operational region, where $\omega = \texttt{N}(\pi/30)$. Figure 4.10 depicts a parametric study of the aerodynamic power versus TSR and pitch angle (left) using a simple BEM code to determine `N1` and `Pow1`.

The two gains for the PI controller of the generator are specified as `KI KP (Nm\s\rpm, Nm\rpm)`. The generator PI controller is used to maintain a constant speed below the rated wind speed and above `N_max`. The gains for the generator PI controller are not calculated in the present thesis, and thus the default values are used instead. Above the rated wind speed the generator power is kept constant at `Pmax`, in which case there is no longer any control of the RPM from the generator torque and the pitch control takes over. The `minPitch` is determined from the parametric study shown in Figure 4.10, which produces optimum power in the variable-speed region and constant power above the rated wind speed. Most parameters not discussed in Figure 4.9 are for the pitch angle controller discussed next.

### 4.3.2 Pitch Angle Controller

As reported in [135], a PI controller for the rotor-collective blade-pitch angle controller is used in FLEX5, where the input is the low-pas filtered generator speed and the pitch servo set-point as output. The error between the filtered generator speed and the rated

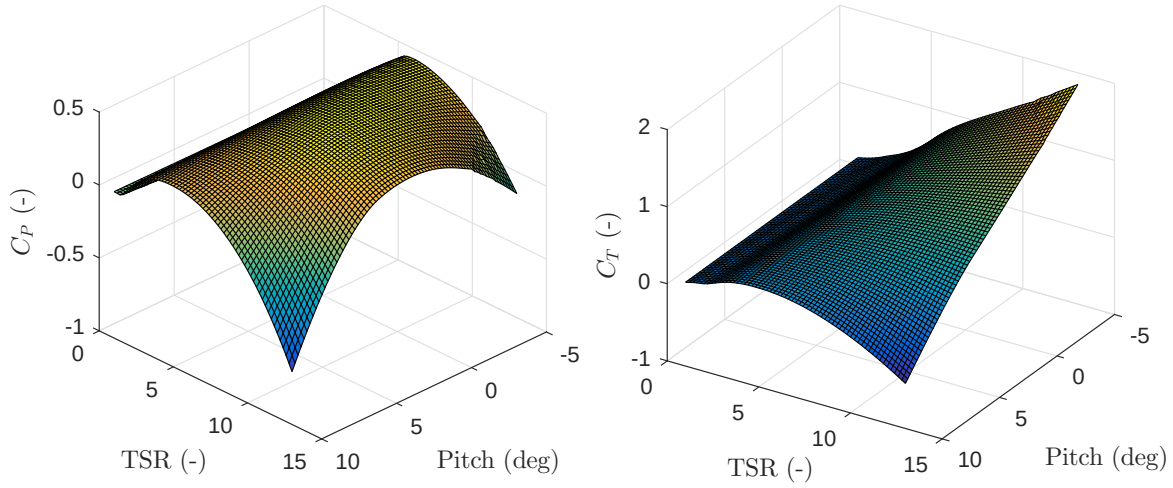


**Figure 4.10:** The optimal tip-speed ratio (TSR) and pitch angle for the variable-speed region is found by a parametric study of the aerodynamic power versus TSR and pitch angle (left). Right-side depicts the aerodynamic thrust versus TSR and pitch angle.

generator speed is measured to regulate the generator speed.

There are several techniques to select the tuning parameters for PI controllers, but the majority are based on simplified or linearized models and they do not consider factors such as turbulence [138]. For example, using a simplified model for tuning a real machine operating in turbulent conditions may not yield the desired behavior of the controller. Nevertheless, a simple approach, specifically the pole-placement technique, is used to tune the PI controller. The disadvantages of using the pole-placement approach is that it is based on a simple one degree of freedom model, and that the controller designer has to identify the optimal position of the pole.

The wind turbine is modeled as stiff with the shaft rotation as the only degree of freedom. The following second-order differential equation is then derived for the shaft rotation angle when the PI-control is active and the generator operates at constant power:

$$I_{\text{drivetrain}}\ddot{\phi} + D\dot{\phi} + K\phi \tag{4.32}$$

where $\phi$ is the error between the actual and reference (e.g. rated) rotor speed. The parameters $I_{\text{drivetrain}}$, $D$, and $K$ are given by:

$$I_{\text{drivetrain}} = I_{\text{rotor}} + N_{\text{gear}}^2 I_{\text{generator}} \tag{4.33}$$

$$D = \frac{1}{\Omega}\left(-\frac{dP}{d\theta}\right) K_P N_{\text{gear}} \frac{30}{\pi} - \frac{P_0}{\Omega_0^2} \tag{4.34}$$

$$K = \frac{1}{\Omega_0}\left(-\frac{dP}{d\theta}\right) K_I N_{\text{gear}} \frac{30}{\pi} \tag{4.35}$$

The PI-controlled rotor-speed error will respond as a second-order system with the natural frequency, $\omega_0$, and damping ratio, $\xi$:

$$\omega_0 = \sqrt{\frac{K}{I}} \tag{4.36}$$

$$\xi = \frac{D}{2\sqrt{KI}} \tag{4.37}$$

Reference [135] suggests a satisfactory response is obtained by aiming for the response characteristics given by $\omega_0 = 0.6\,\text{rad/s}$ and $\xi = 0.6$ to 0.7. Using Equations (4.33) to (4.37), the gains $K_P$ and $K_I$ are found:

$$K_P(\theta) = \frac{2I_{\text{drivetrain}}\Omega_0\xi\omega}{N_{\text{gear}}\left[-\frac{dP}{d\theta}(\theta=0)\right]}GK(\theta) \tag{4.38}$$

$$K_I(\theta) = \frac{I_{\text{drivetrain}}\Omega_0\omega^2}{N_{\text{gear}}\left[-\frac{dP}{d\theta}(\theta=0)\right]}GK(\theta) \tag{4.39}$$

where the gain corrector factor, $GK(\theta)$:

$$GK(\theta) = \frac{1}{1+\frac{\theta}{\theta_k}} \tag{4.40}$$

is multiplied with $K_P$ and $K_I$ to produce a constant gain over the range of relevant wind speeds. The gain corrector factor is needed to take into account the large variation of pitch sensitivity, $\frac{dP}{d\theta}$, with wind speed. Here, $\frac{dP}{d\theta}$ numerically increases with wind speed and therefore using the values of $K_P$ and $K_I$ without $GK(\theta)$ will not give the desired result. The expression in Equation (4.40) is due to the linear relation of pitch sensitivity as a function of the pitch angle ($\theta$).

The pitch sensitivity is found by computing $\frac{dP}{d\theta}$ in the rated power region based on the frozen-wake gradient as shown in Figure 4.11. A script using FLEX5 was written to automate the $\frac{dP}{d\theta}$ calculation procedure at each `minPitch` angle as described in section 4.3.1. An example of the procedure is applied on the NREL 5 MW as depicted in Figure 4.12. In Figure 4.12, a best-fit line is used to determine $\theta_k$ in Equation (4.40), which represents the blade-pitch angle at which the pitch sensitivity has doubled from its value at the rated operating point: $\frac{dP}{d\theta}(\theta=\theta_k) = 2\frac{dP}{d\theta}(\theta=0)$. Figures 4.13 and 4.14 depict the same procedure from reference [116] and using HAWCStab2 [89], respectively, used to compare the results obtained from the script.

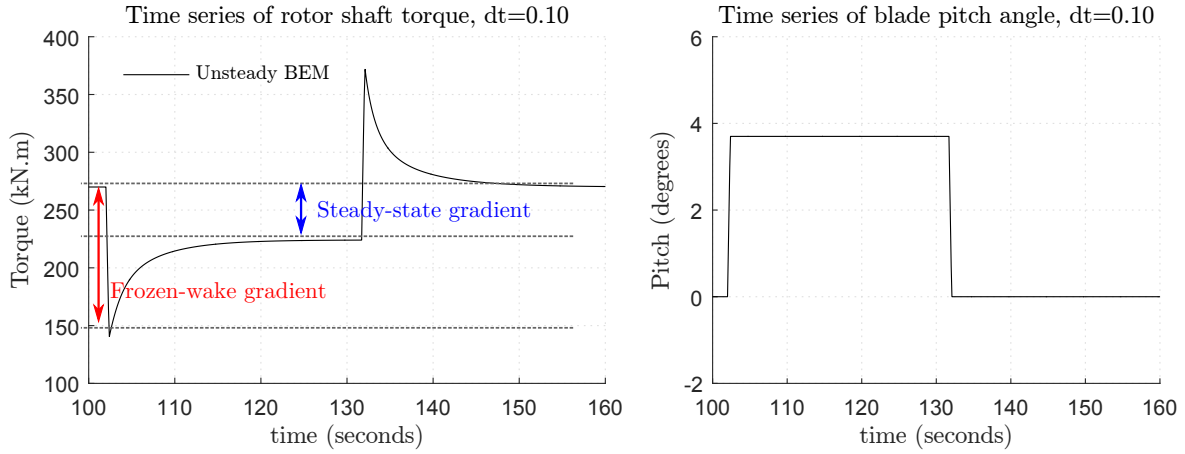


**Figure 4.11:** Rotor shaft torque for the Tjaereborg turbine (left) during a step input of the pitch (right) for a wind speed of 8.7 m/s.

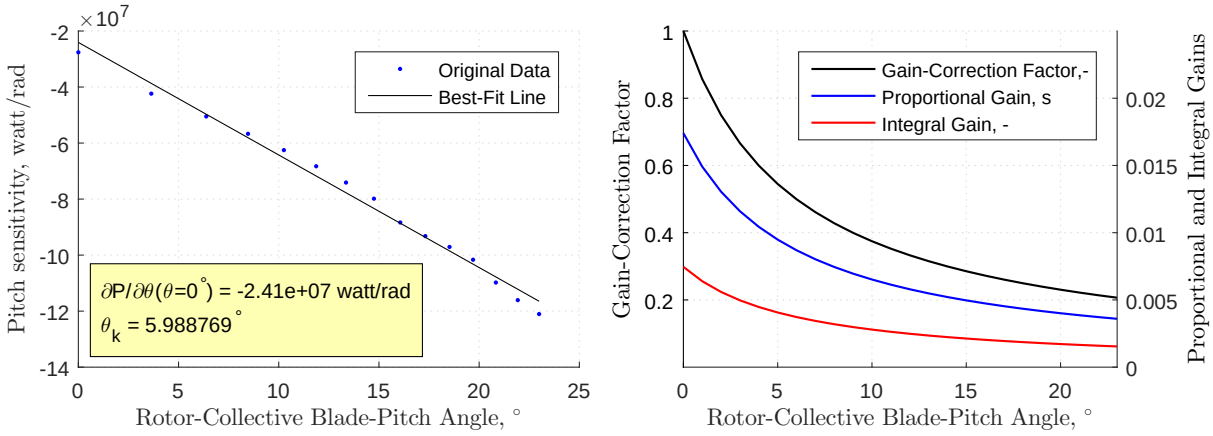


**Figure 4.12:** Best-fit line of pitch sensitivity (left) and baseline blade-pitch control system gain-scheduling law (right) using FLEX5.

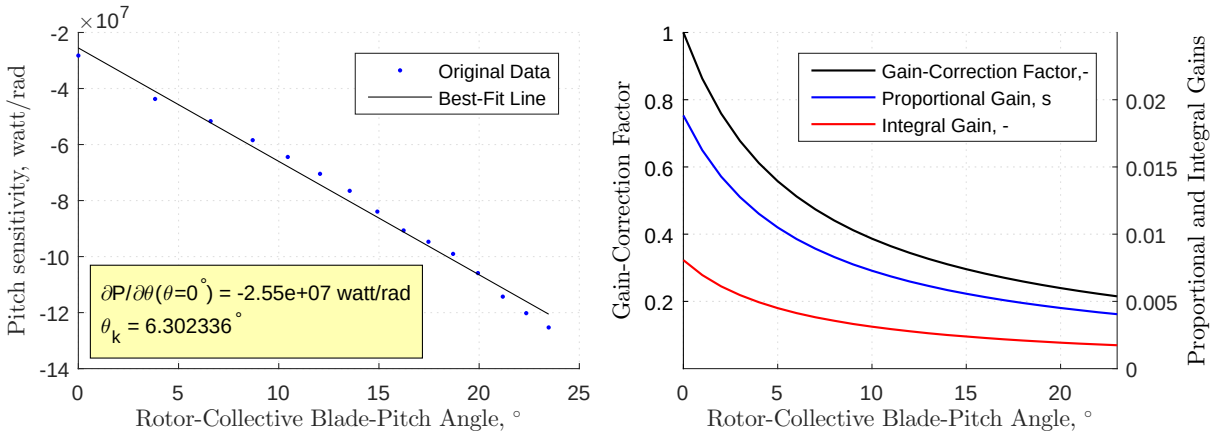


**Figure 4.13:** Best-fit line of pitch sensitivity (left) and baseline blade-pitch control system gain-scheduling law (right) from reference [116].

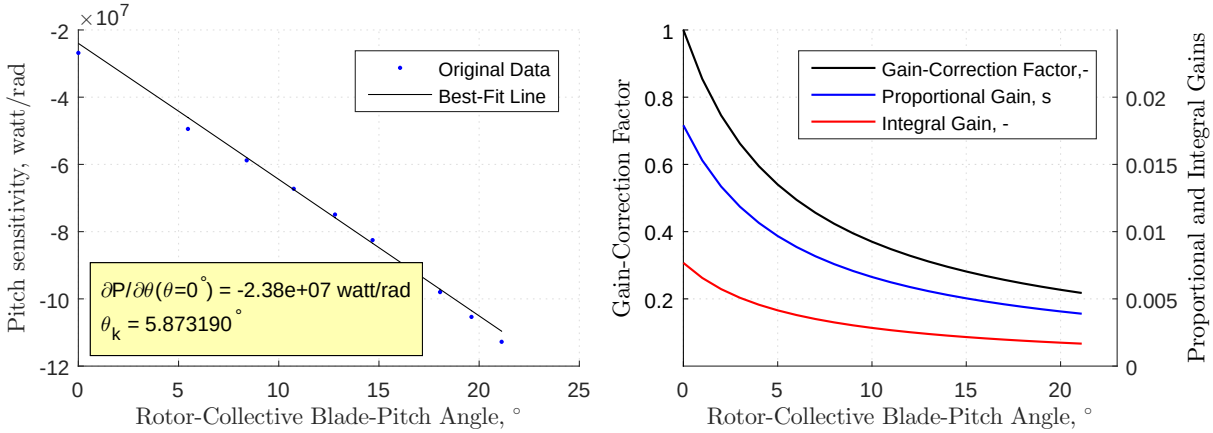


**Figure 4.14:** Best-fit line of pitch sensitivity (left) and baseline blade-pitch control system gain-scheduling law (right) using HAWCStab2.

## 4.4 Design Load Cases

The current section describes in more detail the load cases considered in the structural design code as well as in the rotor design framework (Chapter 5). All load cases have been included in the rotor design framework described in Chapter 5, but not in the stand-alone structural code described in section 4.2.3. All load cases are based on steady wind models. Load cases involving turbulent inflow and abnormal conditions have not been considered, since they are more likely to cause convergence issues for the optimization codes described in section 4.2.3 and Chapter 5. In other words, steady wind models are implemented to guarantee proper optimization functioning and robustness. Two types of load cases are considered in total and are outlined as follows:

- Power Production, see section 4.4.1;
- Parked (standstill or idling), see section 4.4.2.

Each type contains specific load cases, each of them is described in their respective sections. Section 4.4.3 describes the methodology used to group all load cases and to determine the most impactful loads.

### 4.4.1 Power Production

#### Steady wind speed

The steady wind speed load case during normal power production is intended to simulate DLC 1.3 in [136], but without the influence of extreme atmospheric turbulence or wind shear. Ultimate loads are collected at 2 m/s increments for wind speeds from cut-in to cut-out, e.g. 3 m/s and 25 m/s, respectively. Only 40 seconds of simulation time is used, since steady-state loads converge after the initial transient in the first 0 to 5 seconds. Figure 4.15 depicts the computed flap-wise and edge-wise blade root-bending moments from FLEX5 using a steady wind of 10.5 m/s as input. The oscillatory load arises from gravitational loads as well as the rotor tilt angle.

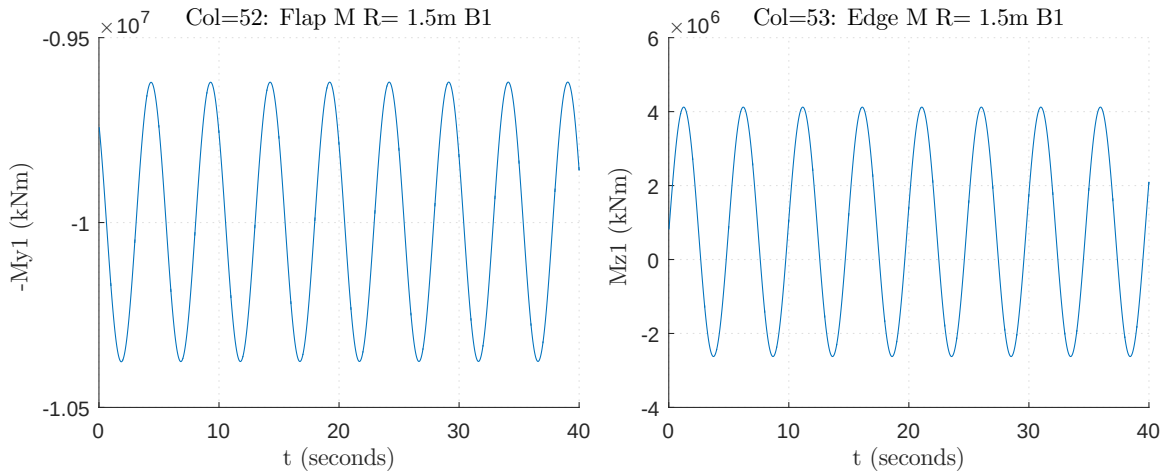


**Figure 4.15:** Flap-wise (left) and edge-wise (right) blade root bending moments resulting from a steady wind at 10.5 m/s.

**Extreme coherent gust with direction change (ECD)**

The extreme coherent gust with direction change has a magnitude of

$$V_{\text{cg}} = 15\,\text{m/s} \tag{4.41}$$

The wind speed is defined as:

$$V(z,t) = \begin{cases} V(z) & \text{for } t \leq 0 \\ V(z) + 0.5V_{\text{cg}}(1 - \cos(\pi t/T)) & \text{for } 0 \leq t \leq T \\ V(z) + V_{\text{cg}} & \text{for } t \geq T \end{cases} \tag{4.42}$$

where $T = 10\,\text{s}$ is the rise time and the wind speed $V(z)$ is given by the normal wind profile model. Figure 4.16 depicts the calculated rise in wind speed during the extreme coherent gust for $V_{\text{hub}} = 25\,\text{m/s}$.

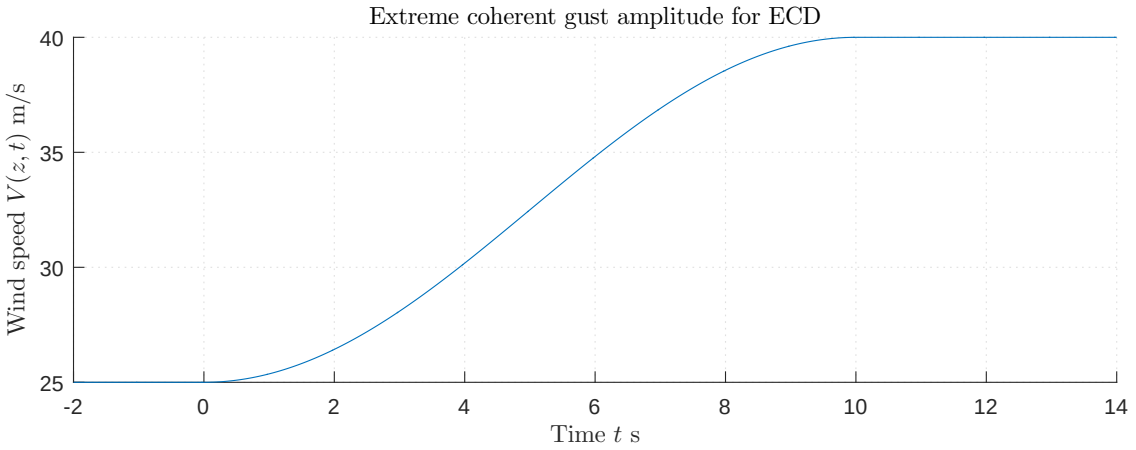


**Figure 4.16:** Extreme coherent gust for ECD using $V_{\text{hub}} = 25\,\text{m/s}$.

The rise in wind speed occurs simultaneously with the direction change $\theta$ from 0° up to and including $\theta_{\text{cg}}$, where the magnitude of $\theta_{\text{cg}}$ is:

$$\theta_{\text{cg}}(V_{\text{hub}}) \begin{cases} 180° & \text{for } V_{\text{hub}} < 4\,\text{m/s} \\ \frac{720°}{V_{\text{hub}}} & \text{for } 4\,\text{m/s} < V_{\text{hub}} < V_{\text{ref}} \end{cases} \tag{4.43}$$

The simultaneous direction change is:

$$\theta(t) = \begin{cases} 0° & \text{for } t < 0 \\ \pm 0.5\theta_{\text{cg}}(1 - \cos(\pi t/T)) & \text{for } 0 \leq t \leq T \\ \pm\theta_{\text{cg}} & \text{for } t > T \end{cases} \tag{4.44}$$

where $T = 10\,\text{s}$ is the rise time. Figure 4.17 depicts the direction change magnitude (left side), $\theta_{\text{cg}}$, and direction change (right side), $\theta(t)$, for $V_{\text{hub}} = 25\,\text{m/s}$. $\theta_{\text{cg}}$ and $\theta(t)$ are plotted as a function of $V_{\text{hub}}$ and time, respectively.

**Extreme operating gust (EOG)**

The extreme operating gust is simulated using the expression:

$$V(z,t) = \begin{cases} V(z) - 0.37V_{\text{gust}} \sin(3\pi t/T)(1 - \cos(2\pi t/T)) & \text{for } 0 \leq t \leq T \\ V(z) & \text{otherwise} \end{cases} \tag{4.45}$$

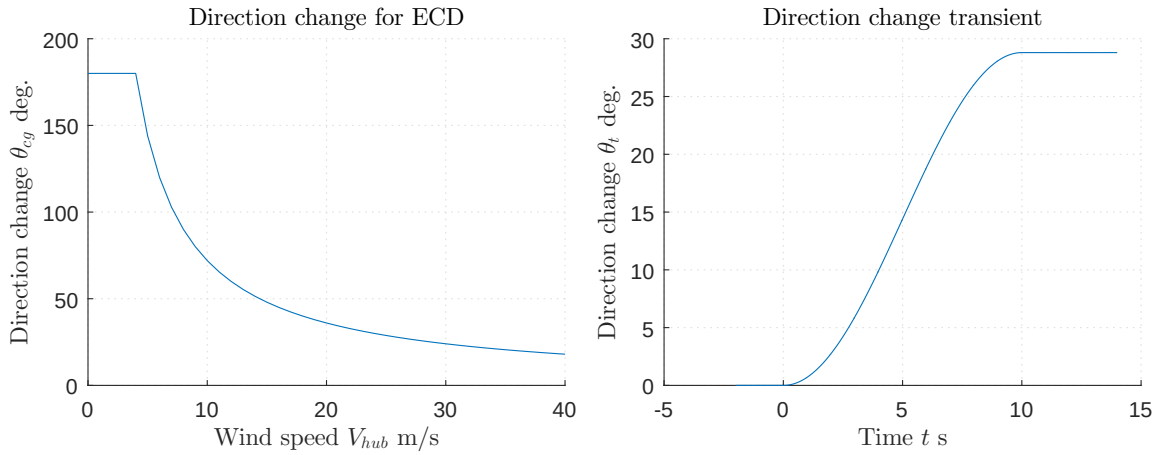


**Figure 4.17:** Direction change magnitude (left side), $\theta_{\text{cg}}$, and direction change (right side), $\theta(t)$, as a function of $V_{\text{hub}}$ and as a function of time for $V_{\text{hub}} = 25\,\text{m/s}$, respectively.

where $T = 10.5\,\text{s}$. The hub height gust magnitude $V_{\text{gust}}$ for a given wind turbine class is:

$$V_{\text{gust}} = \min\left\{1.35(V_{\text{e1}} - V_{\text{hub}}); 3.3\left(\frac{\sigma_1}{1 + 0.1(\frac{D}{\Lambda_1})}\right)\right\} \tag{4.46}$$

where $D$ is the rotor diameter, $\Lambda_1$ is the turbulence scale parameter, $sigma_1$ is the turbulence standard deviation, and $V_{\text{e1}}$ is the steady extreme wind speed with a 1-year recurrence period (see subsection 4.4.2). Figure 4.18 depicts an extreme operating gust for $V_{\text{hub}} = 25\,\text{m/s}$, Class $\text{I}_\text{A}$, $D = 42\,\text{m}$.

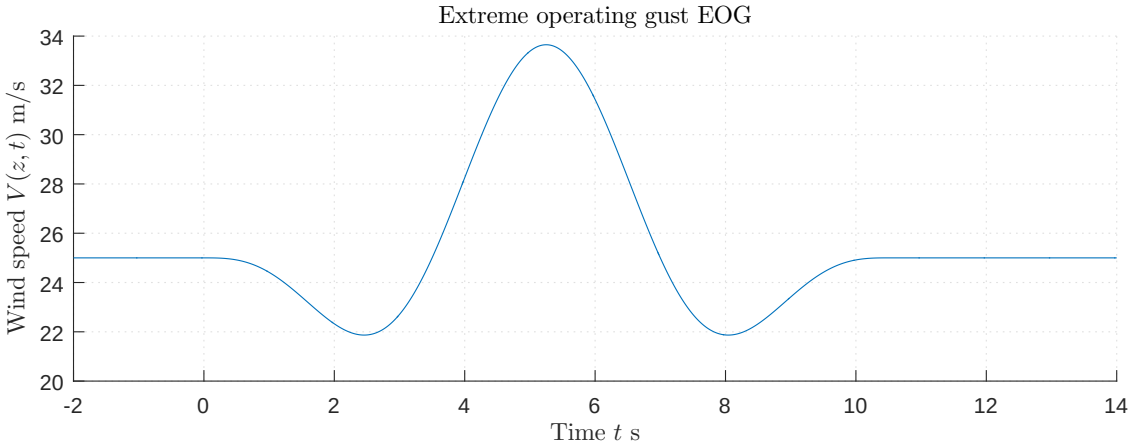


**Figure 4.18:** Extreme operating gust.

### 4.4.2 Parked (standstill or idling)

One of the IEC DLCs is to model a parked turbine in high winds. Following [130], the parked turbine in FLEX5 is modeled using the two assumptions below:

- The turbine uses full-span pitch so blades are feathered to a 90 degree pitch angle;

- The turbine's high-speed-shaft (HSS) brake is engaged, so rotor rotation is fixed at zero.

Since the rotor is stationary, the inflow factors in the BEM implementation of FLEX5 should be turned off. However, no on/off input parameter exists in the FLEX5 input file, so the induction factors are included in the simulations.

For DLC 6.1 and 6.3, the steady extreme wind speed models with a 50-year ($V_{e50}$) and 1-year ($V_{e1}$) recurrence period were used, respectively. The steady extreme wind speed model is given by:

$$V_{e50}(z) = 1.4V_{ref}\left(\frac{z}{z_{hub}}\right)^{0.11} \tag{4.47}$$

and

$$V_{e1}(z) = 0.8V_{e50}(z) \tag{4.48}$$

where $z$ is height and $z_{hub}$ is the turbine hub height. DLC 6.1 and 6.3 were performed with yaw angles of $\pm 15°$ and $\pm 30°$ in $5°$ intervals, respectively. $V_{ref}$ is the reference wind speed and is selected based on the turbine class. For example, a turbine class of IB gives $V_{ref} = 50\,\text{m/s}$.

### 4.4.3 Load Reduction

Structural design optimization codes normally require a series of load cases as input to compute strains, deflections, and buckling limits. Inputting all load cases into the structural design routine can overload the optimizer and make the optimizer run very slowly. Therefore, the least amount of load cases that are the design drivers should be used. However, extracting the most impactful loads from a large number of DLCs is a challenging task. Besides determining how to extract the most impactful loads, a dilemma also arises when the designer must determine which combination of flap-wise and edge-wise loads (also referred to as orthogonal loads) gives the worst-case scenario, see e.g. top-left and top-right of Figure 4.19.

A highly conservative approach is to take the maximum and minimum of the orthogonal loads experienced in the time series, and assume that the worst-case load is when each extreme load component occurs simultaneously. For a set of DLCs, the maximum/minimum is taken from the set of maximums/minimums of the DLCs. An alternative and more concise approach is to construct a "load envelope" instead. First, the flap-wise loads are plotted against the edge-wise loads as shown on the bottom-left of Figure 4.19. Then, a convex hull is fitted on the data set as shown in the bottom right of Figure 4.19 labeled 'Envelope'. The load envelope on the bottom right of Figure 4.19 consists of about 50% of the number of data points of the original time series, but still contains the worst-case combinations of flap-wise and edge-wise loads. The conservative maximum and minimum approach discussed previously is labeled as 'Max/Min' on the bottom right of Figure 4.19.

Figure 4.20 depicts the load envelope constructed once more to determine the worst-case combinations of flap-wise and edge-wise loads for an entire DLC. Figure 4.21 depicts the load envelope constructed based on the load envelopes from a set of DLCs. Figure 4.22 depicts the load envelope constructed based on the flap-wise and edge-wise loads from all load cases in all DLCs. The load envelope depicted in Figure 4.21 is the same as the one shown in Figure 4.22, but is computationally more efficient. Clearly, using load envelopes is an effective method to reduce a very large set of loads to the essential worst-case loads

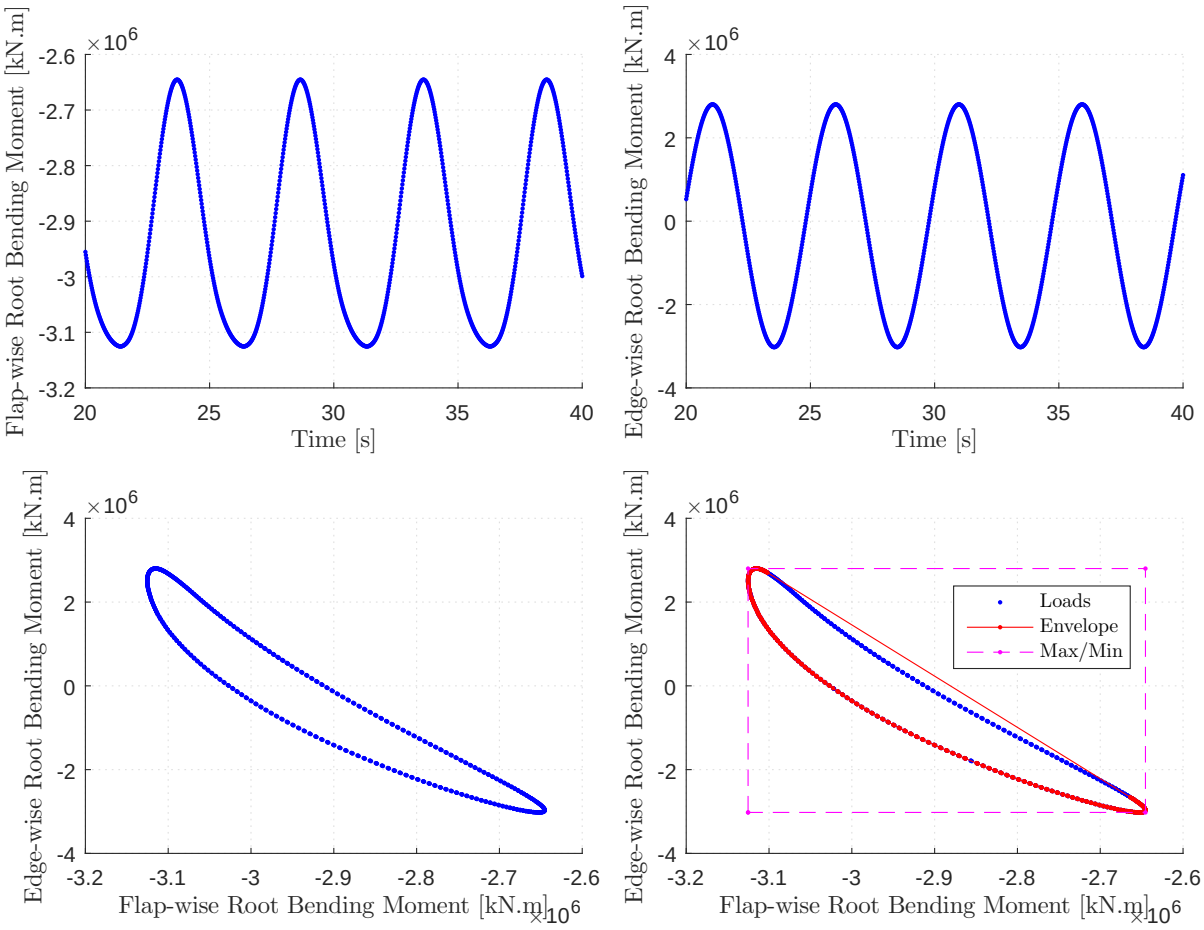


**Figure 4.19:** Time series of flap-wise (top-left) and edge-wise (top-right) root-bending moment for a steady wind of 29 m/s and 28 degree pitch. The flap-wise root-bending moment is plotted against the edge-wise root-bending moment (bottom-left), which is then used to construct a load envelope using a convex hull (bottom-right).

for input into a structural design code. Following the generation of the load envelope using a convex hull, there also exists an additional step where 'projected loads' are performed. Load projection is a method to create a more conservative load envelope, but is not implemented in this thesis. The blade bending moments from the load envelope or the max/min approach are sent to the structural solver directly ($M_y$ and $M_z$) and in-directly ($M_1$ and $M_2$) through Equations (4.4), (4.5), (4.6), (4.9), (4.10), and (4.31).

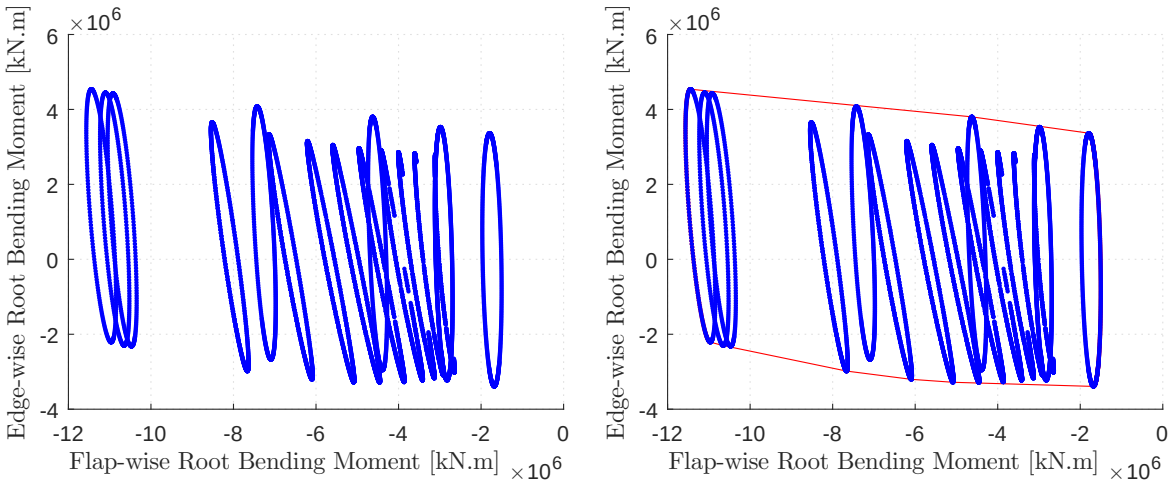


**Figure 4.20:** Load envelopes of flap-wise and edge-wise root-bending moments (left) for one DLC is used to construct an upper-level load envelope (right).

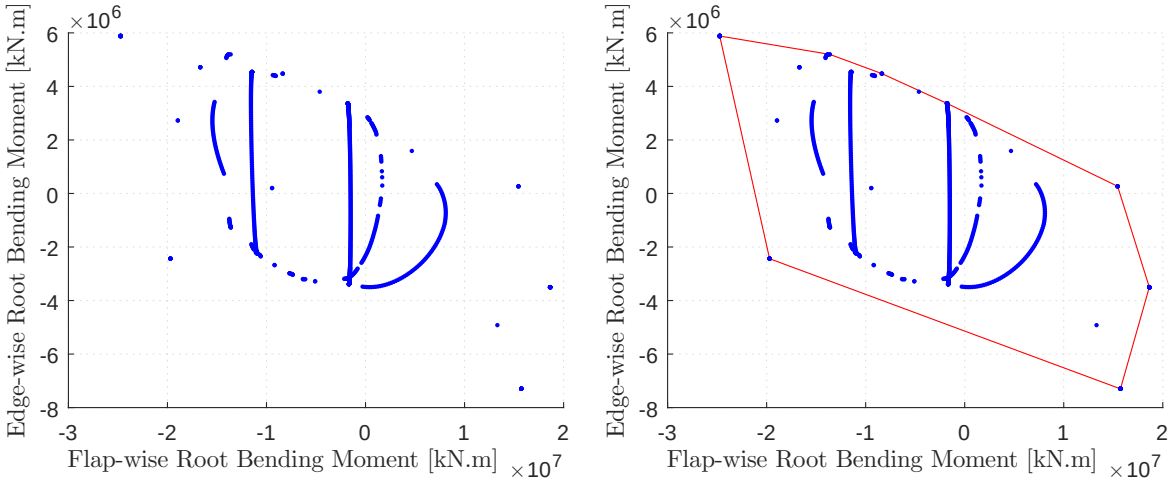


**Figure 4.21:** Load envelopes of flap-wise and edge-wise root-bending moments (left) of each DLC are used to construct a load envelope of the entire DLC set (right).

## 4.5 Results

The structural design code was applied on the NREL 5 MW wind-turbine blade as described in [116] and [130]. The structural layup for the NREL 5 MW was obtained from Resor [130] and was used as the initial starting point. Figures 4.5 and 4.23 depict the spar-cap thickness (left) and web layup (right) for the initial starting point and optimized blade, respectively. It is very important to note that only the minimum (Min-Min) values of the DLC loads were used in the current stand-alone study of the structural design code, see bottom right of Figure 4.19. A stricter structural design is performed in Chapter 5, where results using the load envelope methodology and all design load cases discussed in section 4.4 are used instead.

The initial and optimized blade mass are 16,489 kg and 16,133 kg, respectively, and all constraints are satisfied. A 2.16% reduction in COE was achieved. Figure 4.24 depicts the internal structure for the initial and optimized blades. Blade mass and COE were reduced by decreasing the spar-cap width. In the optimal blade, the increase in the fore

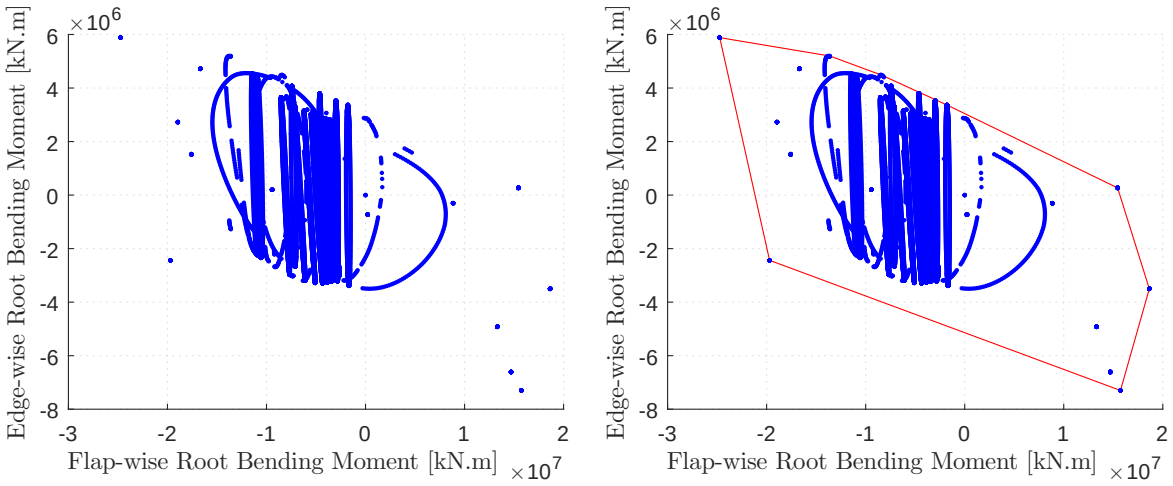


**Figure 4.22:** Flap-wise and edge-wise root-bending moments for all load cases in all DLCs (left). Load envelope of the entire DLC set (right).

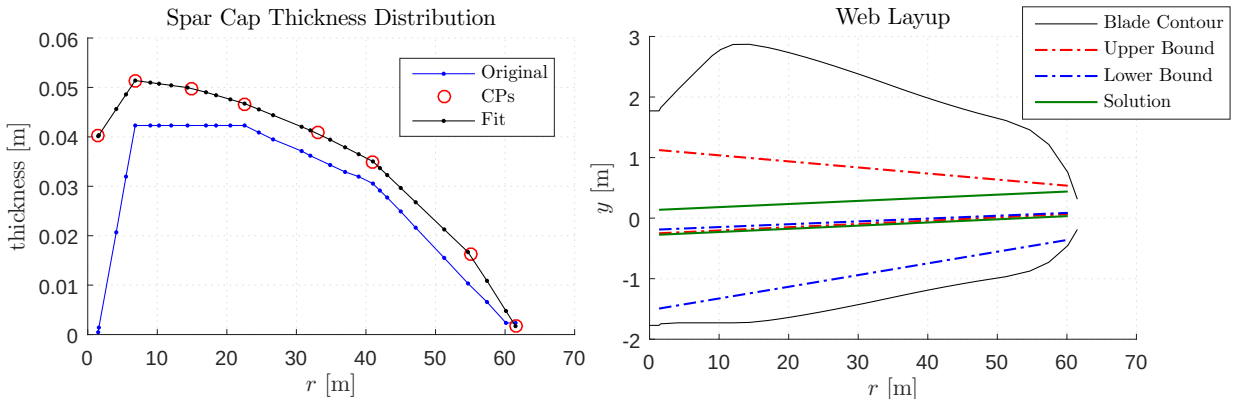


**Figure 4.23:** Optimal spar-cap thickness (left) and web layup (right) for the NREL 5 MW baseline wind turbine.

and aft panels to compensate the decrease in spar-width is taken into account in the blade mass calculation. The flap-wise, edge-wise, and axial stiffnesses, as well as the mass per length for the initial and optimized blades are shown in Figure 4.25.

Figures 4.26 and 4.27 depict the stress versus span-wise blade position for the initial and optimized blades. Note that stress, $\sigma$, is obtained from strain, $\epsilon$, through Hooke's law $\sigma = E\epsilon$ where $E$ is the modulus of elasticity of the material. Both designs satisfy the strain constraint, but the initial design violates the buckling constraint as shown in Figure 4.28. Table 4.5 shows the tip deflection and blade modal frequencies for the initial and optimized blades versus the constraint condition.

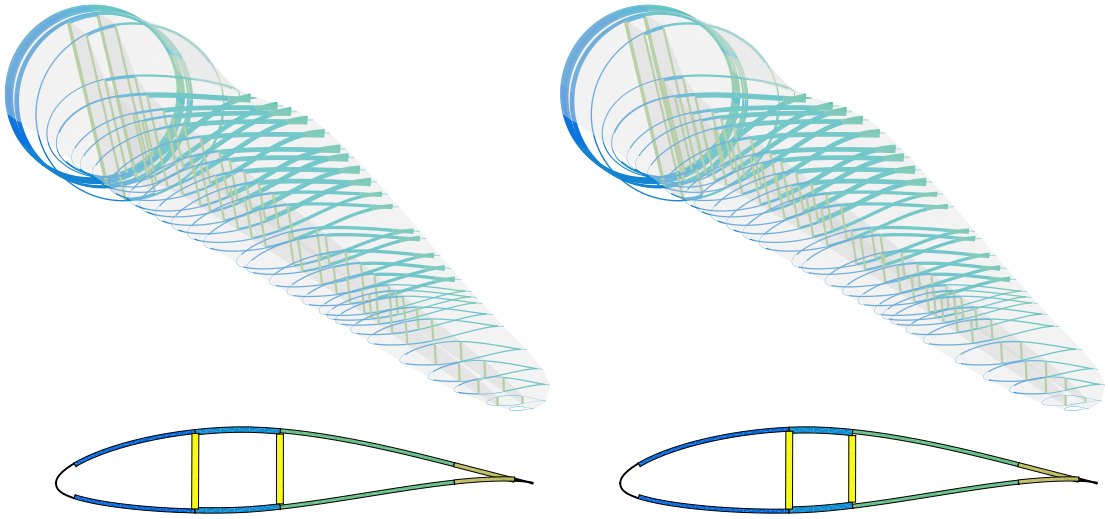

**Figure 4.24:** Initial (left) and optimal (right) internal blade structure found from structural design code.

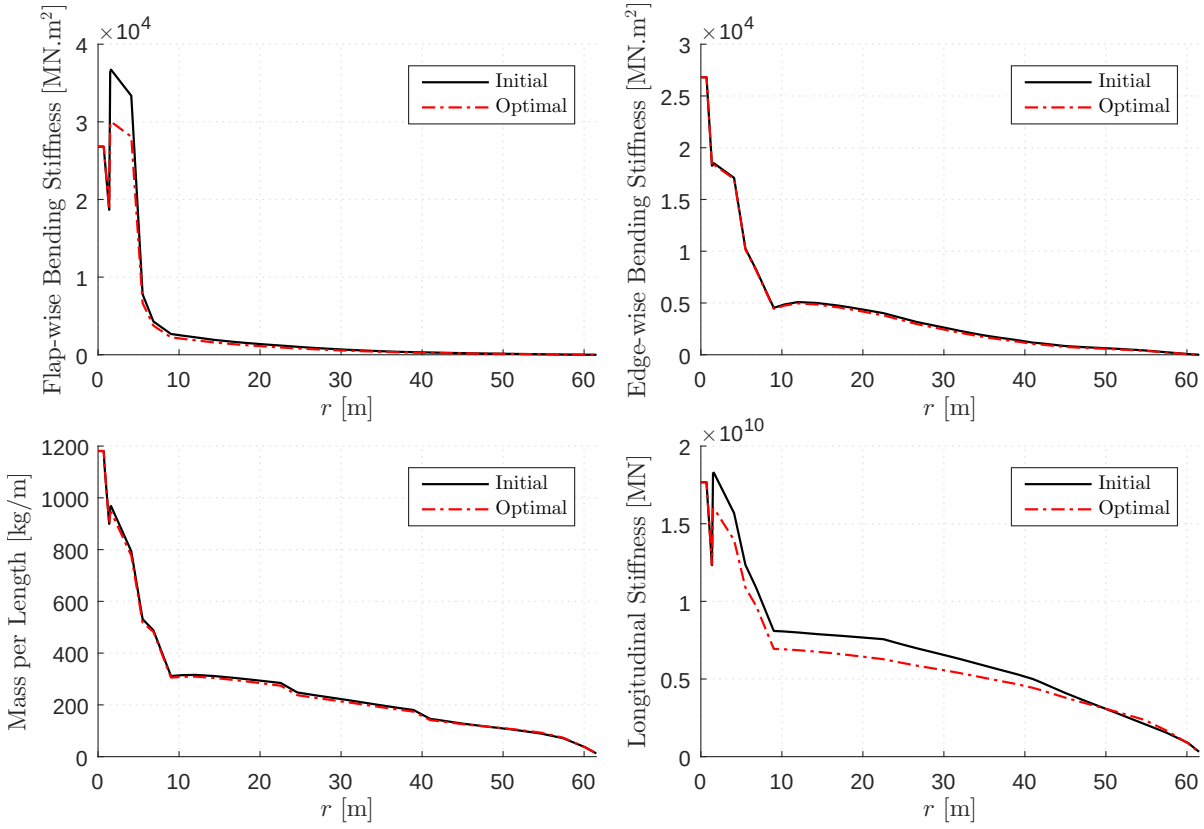


**Figure 4.25:** Flap-wise, edge-wise, and axial stiffnesses, as well as the mass per length for the initial (Initial) and optimized (Optimal) blades.

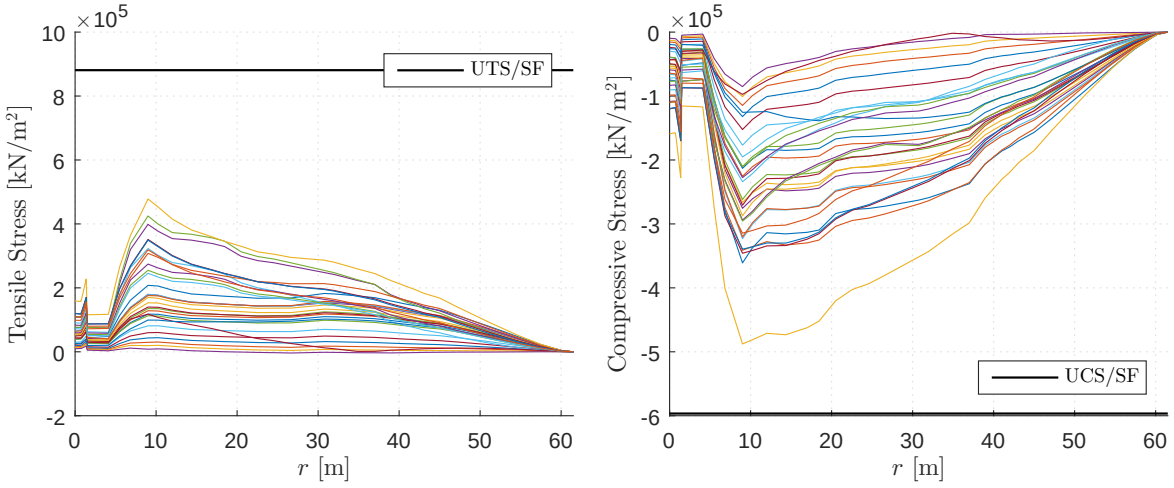


**Figure 4.26:** Tensile (left) and compressive (right) stress versus blade span-wise position computed from a series of DLCs for the initial blade. A constraint violation occurs when the magnitude of stress exceeds the magnitude of the ultimate tensile stress (UTS) or ultimate compressive stress (UCS) divided by the safety factor (SF).

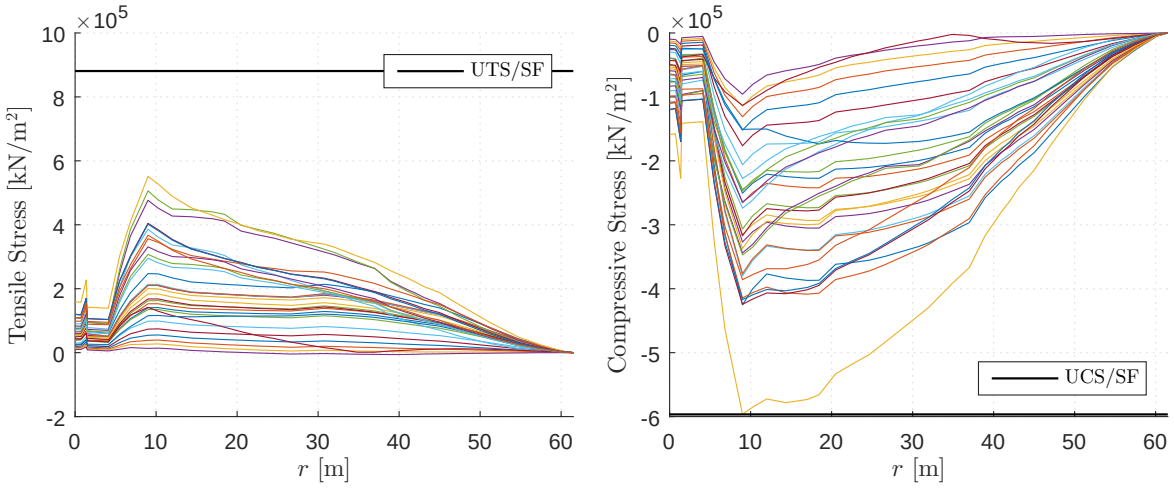


**Figure 4.27:** Tensile (left) and compressive (right) stress versus blade span-wise position computed from a series of DLCs for the optimized blade.

**Table 4.5:** Comparison of the maximum tip deflection normal to the rotor plane experienced in the DLCs, as well as the blade modal frequencies for the initial and optimized blades.

| | Max tip deflection (m) | Freq. blade mode 1 (Hz) | Freq. blade mode 2 (Hz) |
|---|---|---|---|
| Constraint Condition | $\leq 7.070$ | $\geq 0.635$ | $\geq 0.635$ |
| Initial | 5.898 | 0.733 | 1.122 |
| Optimal | 7.070 | 0.676 | 1.088 |

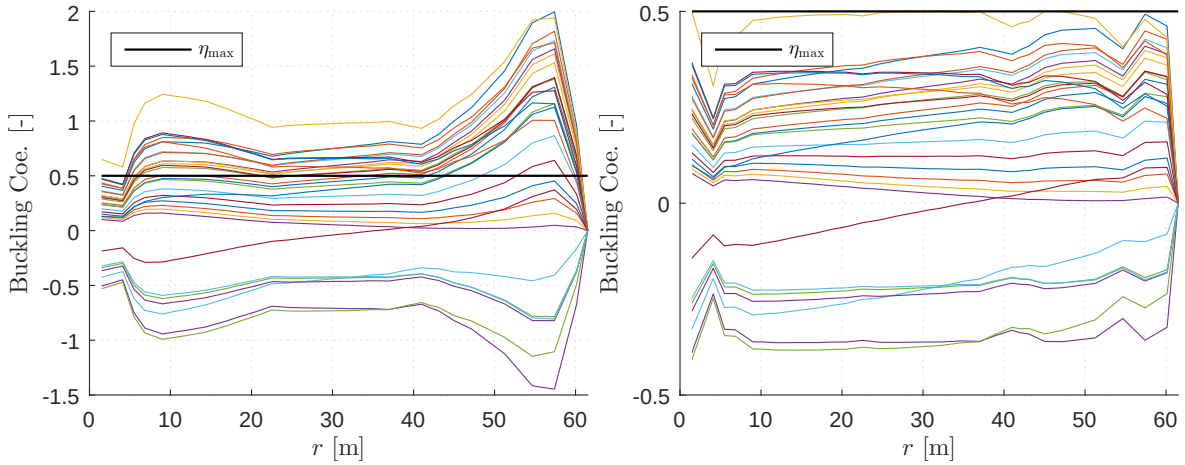


**Figure 4.28:** Computed buckling coefficient versus blade span-wise position for the initial (left) and optimized (right) blades. The buckling coefficient for the initial blade exceeds $\eta_{max}$, while the optimized blade does not.

## 4.6 Conclusions

A simple structural design code was developed to minimize the COE of the NREL 5 MW wind-turbine blade. Loads are calculated from the aero-elastic code FLEX5, while PreComp, BModes, as well as MATLAB code written by the author were used to compute the optimization objective and constraints. The initial and optimized blade mass are 16,488 kg and 16,133 kg, respectively. Further, a 2.16% reduction in COE was achieved for the NREL 5 MW blade in the four design load cases. In Chapter 5, the structural design tool is introduced into a rotor optimization code using a higher-fidelity aero-elastic model.

# Chapter 5

# Coupled Aerodynamic and Structural Design

## 5.1 Introduction

This chapter is based on the work: 'Large wind turbine rotor design using an aero-elastic / free-wake panel coupling code' [5] and 'Design of the OffWindChina 5-MW wind turbine rotor'. First, section 5.2 describes the methodology of the rotor design framework. The results and conclusions using MIRAS-FLEX is given in section 5.3. Using almost the same methodology but with FLEX5 instead MIRAS-FLEX, the design results for the offshore wind turbine in China (OffWindChina 5 MW) is described in section 5.4. Conclusions are given in section 5.5.

## 5.2 Methodology

This section describes the methodology used in the large wind-turbine rotor design framework. First, the optimization problem is shown, then the MIRAS-FLEX code, structural design code, and surrogate modeling components of the framework are described.

### 5.2.1 Optimization Problem

The design objective is to minimize the COE:

$$\begin{aligned} \underset{x}{\text{minimize}} \quad & \frac{\text{COE}}{\text{COE}_{\text{ref}}} \\ \text{subject to} \quad & \mathbf{x} \in \mathbb{R}^n, \\ & g_c(\mathbf{x}) \leq 0, \\ & x_k^L \leq x_k \leq x_k^U, k = 1, \ldots, n \end{aligned} \tag{5.1}$$

where the subscript, ref, denotes the reference (or baseline) blade. The vector $\mathbf{x}$ contains a total of $n$ variables that are real numbers, $\mathbb{R}$. The design variables, $\mathbf{x} = [x_1, x_2, \ldots, x_n]$, are control points (CPs) that define the chord, twist and relative thickness as a function of blade span, see Figure 5.1. B-splines [129] are used to parameterize the chord and twist distributions, while linear interpolation is used for the relative thickness distribution. Only two CPs each for the chord, twist, and relative thickness distributions at the outboard of the blade are optimized. The total number of CPs is then six. Anymore than six CPs would render the optimization too difficult to solve with the available computing resources. The upper ($U$) and lower ($L$) notations, $x_k^L \leq x_k \leq x_k^U$, are the upper and lower limits of the CPs, while the non-linear inequality constraint, $g_c \leq 0$, is to promote monotonically decreasing chord, twist, and relative thickness. The boundary and non-linear inequality constraints are required to ensure feasible blade designs.

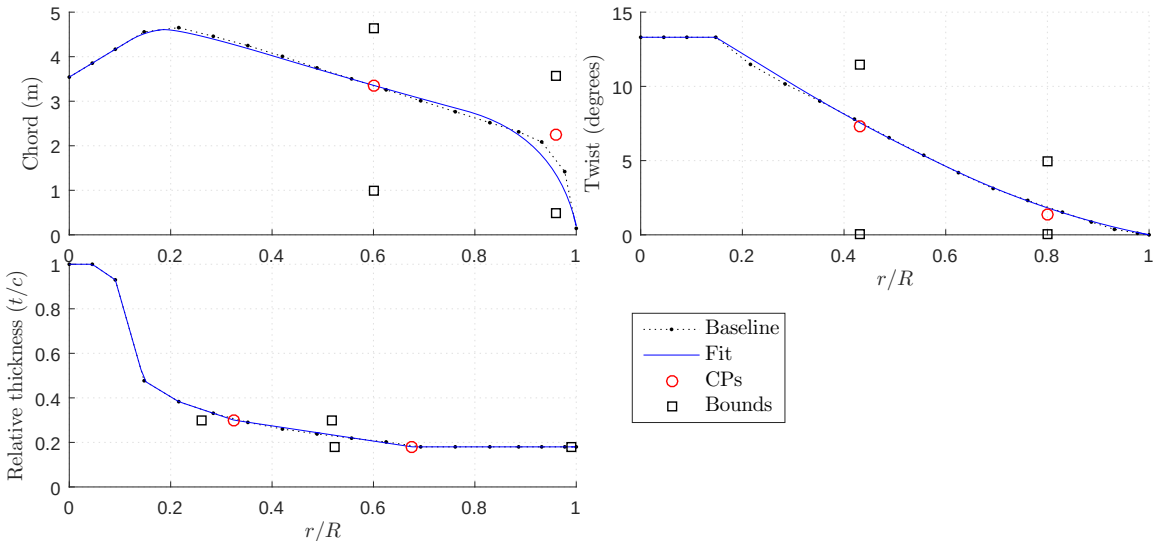


**Figure 5.1:** Blade geometry parameterization method fitted to the NREL 5 MW baseline wind turbine [116], where $r/R$ is the normalized blade radius.

Following [84], COE is calculated as:

$$\text{COE} = \frac{\text{FCR} \cdot (\text{TCC} + \text{BOS})}{\text{AEP}} + \text{AOE} \tag{5.2}$$

where FCR is fixed charge rate, TCC is turbine capital cost, BOS is balance of station, AOE is annual operating expenses, and AEP is annual energy production. FCR, TCC, and BOS are obtained from the NREL Wind Turbine Design Cost and Scaling Model [84]. Refer to section 1.3.7 of this thesis for more details. Note AOE was neglected because it gives an incentive to reduce AEP, see underlying equations in [84]. MIRAS-FLEX is used to compute AEP, see subsection 5.2.2, while a code based on classical laminate theory called PreComp [71] to compute the blade mass, see subsection 5.2.3. The rotor mass was computed from PreComp instead of the scaling law in [84] to estimate TCC.

### 5.2.2 Higher-Fidelity Aero-Elasic Code: MIRAS-FLEX

The aero-elastic code, MIRAS-FLEX [1], is composed of a free-wake panel code called MIRAS [97], and the elastic beam model of FLEX5 [25], see Figure 5.2. MIRAS is used to compute the aerodynamic flow solution while FLEX5 predicts the structural dynamics. MIRAS-FLEX uses a predictor-corrector and loosely-coupled approach to couple 22 DOFs from FLEX5 with MIRAS. Refer to sections 1.3.3 and 1.3.4 for a description of MIRAS and FLEX5, respectively. Chapter 2 describes the coupling methodology.

### 5.2.3 Structural Design Code

The simple optimization tool to design the internal structure of large wind-turbine blades from Chapter 4 has been modified for inclusion in the rotor design framework. The tool uses a combination of the classical laminate theory using a shear flow approach to compute blade structural properties, PreComp [71], a finite-element code to compute the blade coupled mode shapes, BModes [72], the Euler-Bernoulli beam theory to compute blade deflections and strains [35], and the BEM-based aero-elastic code FLEX5 to compute the

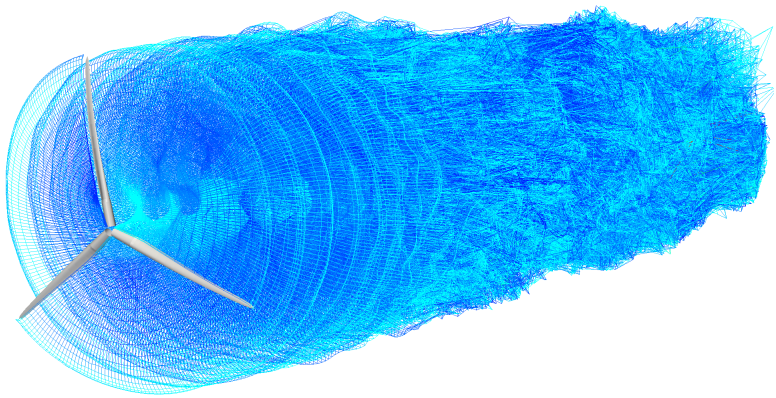

**Figure 5.2:** MIRAS-FLEX simulation with turbulent inflow.

DLCs. The objective is to minimize the blade mass subject to a number of boundary and non-linear inequality constraints:

$$
\begin{aligned}
\underset{y}{\text{minimize}} \quad & \text{Blade Mass} \\
\text{subject to} \quad & \mathbf{y} \in \mathbb{R}^n, \\
& (3\,\omega_{\text{rotor}}\,\text{SF} - \omega(\mathbf{y}))/\omega_{\text{rotor}} \leq 0, \\
& (\delta_{\text{tip}}(\mathbf{y}) - \delta_{\max})/\delta_{\max} \leq 0, \\
& (\epsilon_{\text{tension}}(\mathbf{y})\,\text{SF} - \epsilon_{\text{ultimate,tension}})/\epsilon_{\text{ultimate,tension}} \leq 0, \\
& (\epsilon_{\text{compression}}(\mathbf{y})\,\text{SF} - \epsilon_{\text{ultimate,compression}})/\epsilon_{\text{ultimate,compression}} \leq 0, \\
& (\eta(\mathbf{y}) - \eta_{\max})/\eta_{\max} \leq 0, \\
& y_k^L \leq y_k \leq y_k^U, k = 1, \ldots, n
\end{aligned}
\tag{5.3}
$$

where $3\,\omega_{\text{rotor}}$ is the rotor blade passing frequency, SF is a safety factor, $\delta_{\max}$ is the maximum allowable tip deflection, $\epsilon_{\text{ultimate,tension}}$ and $\epsilon_{\text{ultimate,compression}}$ are the ultimate tensile and compressive strain, respectively, and $\eta_{\max}$ is the maximum allowable buckling coefficient set to 0.5. The buckling coefficient, $\eta$, is computed for the spar-caps only, and assumes that the spar-beam is modeled as a long orthotropic plate under uni-axial compression with all edges simply supported [133]. Skin and panel buckling are not considered. The tip deflection, $\delta_{\text{tip}}$, as well as the tensile ($\epsilon_{\text{tension}}$) and compressive ($\epsilon_{\text{compression}}$) strain are calculated from Euler-Bernoulli beam theory. The natural frequencies for the first flap-wise and edge-wise blade modes, $\omega$, are obtained from BModes. All constraints are scaled to prevent bias and improve optimizer performance.

A box-spar layup is assumed for the internal blade structure, where the design variables, $\mathbf{y}$, are the spar-cap thickness and web layup (or spar width), refer to Chapter 4 for details. Figure 5.3 depicts the optimal spar-cap thickness (left) and web layup (right) for the NREL 5 MW baseline wind turbine [116, 130].

The structural design code begins by tuning the generator and pitch controller as outlined in [135]. Then, a series of DLCs based on Resor [130] and the IEC 61400-1 standards [136] are computed, see Table 5.1. Both the control tuning as well as the DLC computations are performed using FLEX5 and assuming stiff blades. MIRAS-FLEX is not used here because a significant portion of the cluster is needed to perform the task quickly in parallel (i.e. cluster needs to be shared with other users). Turbulent wind during normal and abnormal turbine operation was not considered. For the preliminary

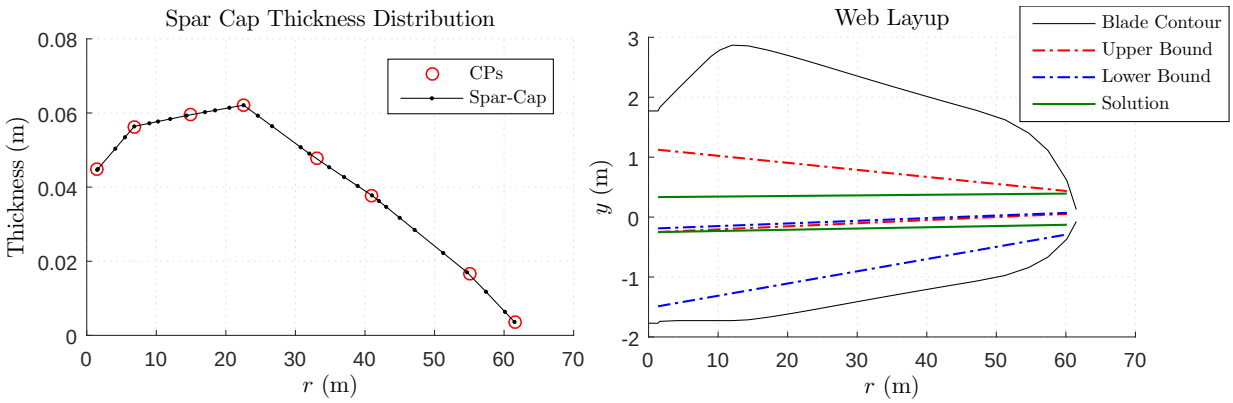


**Figure 5.3:** Optimal spar-cap thickness (left) and web layup (right) for the NREL 5 MW baseline wind turbine [116, 130].

blade design stage, steady wind models are used in this work for simplicity and speed. DLC 6.1 and 6.3 are computed in 5° yaw error increments/decrements ranging from 30° and -30° (i.e. 13 load cases in total for DLC 6.1 and 6.3). The bending moments normal and tangential to the rotor plane from all DLCs are collected to determine the most impactful load cases. The worst-case loads are then transferred to the optimizer, which calls a structural module for a number of iterations to find the minimum blade mass. The inputs to the structural module are the DLC loads and $\mathbf{y}$. The vector $\mathbf{y}$ is used to create a structural layup and compute the objective, while the DLC loads together with the blade structural properties are used to compute the structural constraints. The MATLAB optimizer, *fmincon* [137], modifies $\mathbf{y}$ to minimize the objective up to at least a local minimum and also satisfy all constraints.

Notice that the design of the controller as well as the inner structure are based on a rigid turbine, see Figure 5.4. In a fully aero-elastic design approach, Steps 2 to 4 should be repeated until convergence, where the blade stiffness distributions found from Step 4 are used to update the stiffness distributions used in Steps 2 and 3. Although not too difficult to implement, the fully aero-elastic design approach was omitted for simplicity, robustness, and faster code execution.

### 5.2.4 Surrogate Modeling

MIRAS-FLEX requires much more computational time than BEM-based aero-elastic codes. Therefore, the number of calls to MIRAS-FLEX in a numerical optimization problem must be kept to a minimum. The surrogate-based optimization code developed by the authors [3] and as described in Chapter 3 is used in the present blade design framework. In general, surrogate-based optimization consists of three steps to find the minimum of a function:

1. creating a sampling plan;
2. constructing a surrogate, and;
3. searching and exploiting the surrogate.

The sampling plan is created using the Latin hypercube sampling technique [3, 92], the surrogate is constructed using a radial basis function, and prediction-based exploitation [3, 92] is used to search and exploit the surrogate. For details, refer to [3] or Chap-

**Table 5.1:** Design load cases used in the structural design code based on [130] and [136].

| Design situation | DLC | Wind condition | Other conditions | Type of analysis |
|---|---|---|---|---|
| Normal Power Production (steady) | - | Steady Windspeed | 2 m/s increments from cut-in = 3 m/s to cut-out = 25 m/s | Ultimate strength |
| | 1.4 | Extreme Coherent gust with Direction change (ECD) | Rated wind ±2 m/s, 2 m/s spacing | Ultimate strength |
| | 2.3[1] | Extreme Operating Gust (EOG) | Rated wind ±2 m/s, 2 m/s spacing | Ultimate strength |
| Parked (standing still or idling) | 6.1 | Extreme Windspeed Model (EWM) 50-year recurrence period | Yaw error ±15°, 5° spacing | Ultimate strength |
| | 6.3 | EWM 1-year recurrence period | Extreme yaw misalignment, ±30° | Ultimate strength |

[1] Without external or internal electrical fault including loss of electrical network.

ter 3. Each candidate blade design in steps i) and iii) above goes through six stages to determine the COE, see Figure 5.4.

## 5.3 Rotor Design using MIRAS-FLEX

### 5.3.1 Blade Design Results

Table 5.2 and Figure 5.5 (top) depict the results from the optimization of Problem (5.1) using the NREL 5 MW baseline wind turbine [116, 130] as the reference and MIRAS-FLEX to compute the AEP. Table 5.3 and Figure 5.5 (bottom) depict the results when a simple BEM code [35] is used instead of MIRAS-FLEX. Airfoils are comprised of a cylinder, DU airfoils, and a NACA airfoil as described in [116]. The reference structural layup is obtained from [130]. Rotor radius and tip speed are kept the same throughout the optimization. A Weibull probability distribution with shape and scale parameters of $k = 2.48$ and $A = 7.68$ m/s, respectively, was used to calculate the AEP. The total computational time for the MIRAS-FLEX and BEM based optimizations are approximately 56 and 7 hours, respectively. Note the framework has not been optimized for speed, therefore the computational times given should be interpreted as maximum values.

Table 5.2 and Table 5.3 show the results of COE, AEP, maximum flap-wise root-bending moment experienced in the DLCs ($M_{\text{flap}}$), thrust at rated wind speed ($T_{\text{rated}}$), and blade mass in tonnes ($m_{\text{blade}}$). Table 5.2 shows +1.89%, +1.87%, +5.47%, +0.19%, and +0.75% improvements for COE, AEP, $M_{\text{flap}}$, $T_{\text{rated}}$, and $m_{\text{blade}}$, respectively, for the MIRAS-FLEX case. When using simple BEM, Table 5.3 shows +0.85%, +0.72%, +2.71%, +2.35%, and +1.95%, respectively. Figure 5.6 depicts the exterior shape and interior structure of the blade for the baseline, MIRAS-FLEX solution, and BEM solution. The spar-cap thickness and web layup are plotted in Figure 5.7 for the MIRAS-

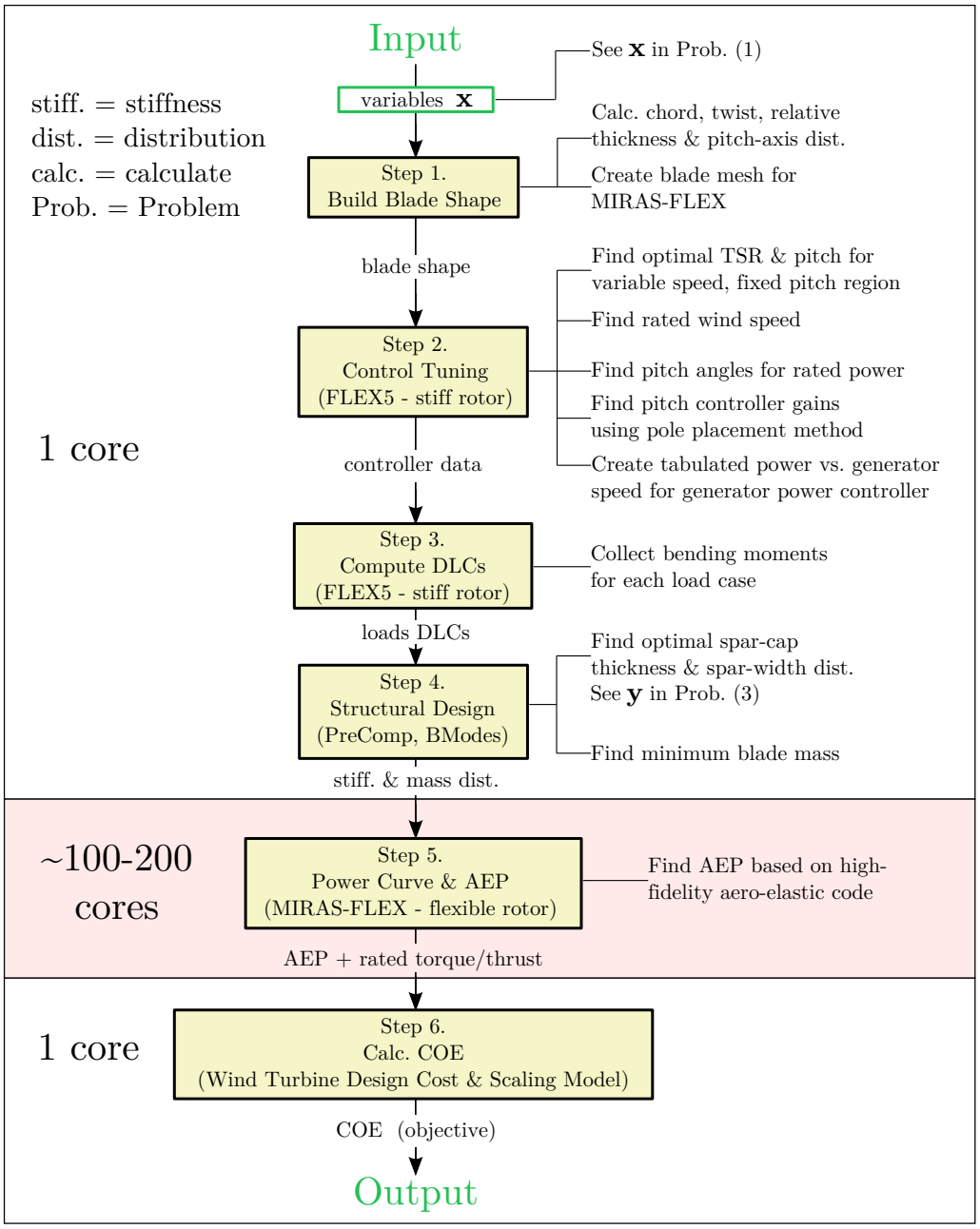


**Figure 5.4:** Flowchart for evaluating a candidate blade design comprised of six steps: 1) Build blade shape, 2) control tuning, 3) compute DLCs, 4) structural design, 5) compute AEP, and 6) calculate COE.

FLEX (top) and BEM (bottom) solutions, respectively. Comparing the two designs in Figure 5.5, differences are mainly seen at the blade tip for the chord distribution. The MIRAS-FLEX solution has a sharp blade tip, while the BEM solution does not. Detailed investigation of the local blade aerodynamics during power production and the DLCs is needed to determine the cause for the sharp blade tip. It is worth noting that very different approaches are used to model the flow near the tip in MIRAS and BEM.

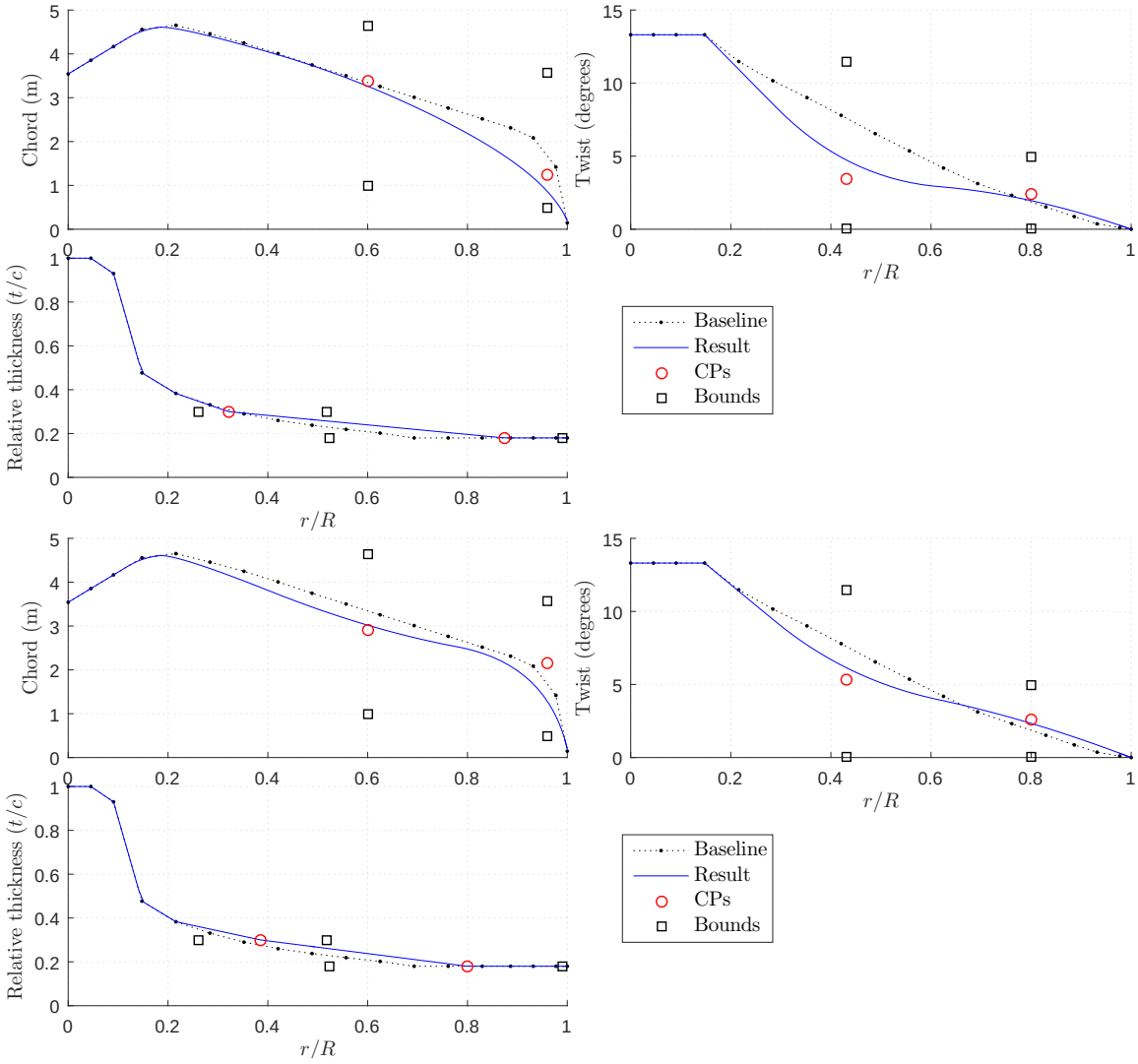


**Figure 5.5:** Blade geometry results where $r/R$ is the normalized blade radius using MIRAS-FLEX (top) and simple BEM (bottom).

**Table 5.2:** Results from the optimization of Problem (5.1) for the MIRAS-FLEX case.

| Quantity | COE ($/kWh) | AEP (GWh/year) | $M_{\text{flap}}$ (MN.m) | $T_{\text{rated}}$ (MN) | $m_{\text{blade}}$ (tonnes) |
|---|---|---|---|---|---|
| Reference Fit | 0.08401 | 18.5982[2] | 21.235 | 0.64811 | 16.98735 |
| Optimized | 0.08242 | 18.94690[2] | 20.074 | 0.64691 | 16.85920 |
| % Improvement | +1.89% | +1.87% | +5.47% | +0.19% | +0.75% |

[2] The wake was cut short to reduce computing time, therefore AEP for MIRAS-FLEX is larger than BEM. Consequently, COE for MIRAS-FLEX will be less than BEM as well, see Equation (5.2).

**Table 5.3:** Results from the optimization of Problem (5.1) for the BEM case.

| Quantity | COE ($/kWh) | AEP (GWh/year) | $M_{\text{flap}}$ (MN.m) | $T_{\text{rated}}$ (MN) | $m_{\text{blade}}$ (tonnes) |
|---|---|---|---|---|---|
| Reference Fit | 0.08781 | 17.79432 | 21.235 | 0.67325 | 16.98735 |
| Optimized | 0.08706 | 17.92297 | 20.660 | 0.65744 | 16.65589 |
| % Improvement | +0.85% | +0.72% | +2.71% | +2.35% | +1.95% |

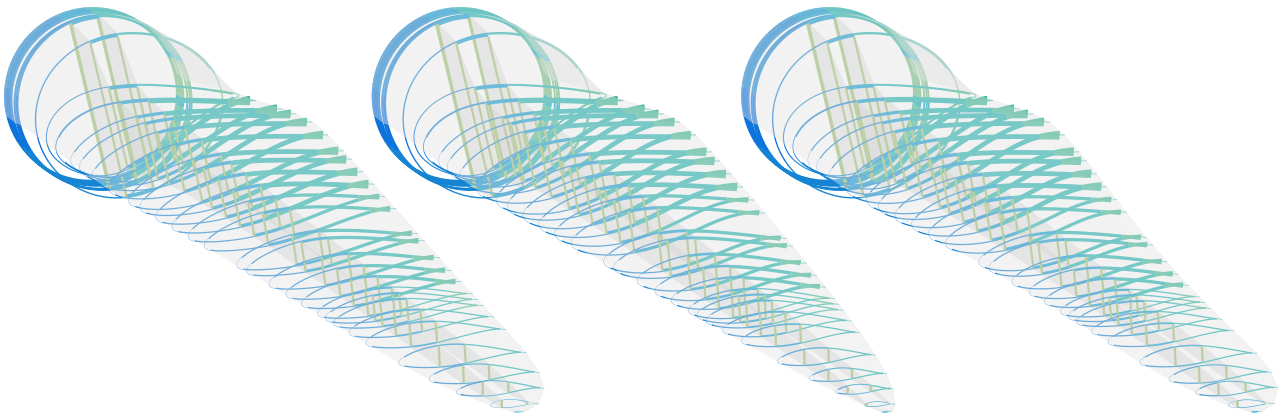

**Figure 5.6:** Blade shape and internal structure for the baseline (left), MIRAS-FLEX solution (middle) and BEM solution (right).

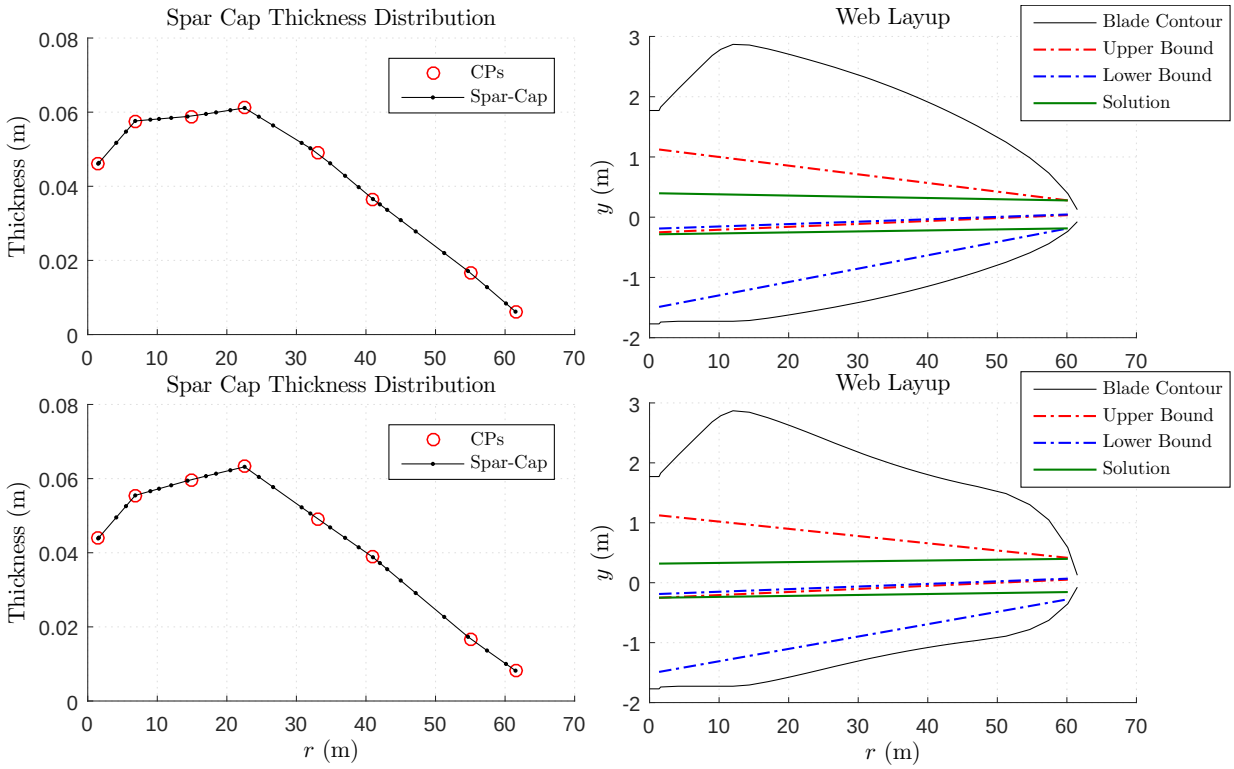


**Figure 5.7:** Spar-cap thickness (left) and web layup (right) for the MIRAS-FLEX (top) and BEM (bottom) solutions.

## 5.4 Rotor Design using FLEX5 for OffWindChina 5 MW

FLEX5 was used instead of MIRAS-FLEX for the design of a 5 MW wind turbine in the OffWindChina project to allow a higher number of design variables in the rotor design framework. Variables were added to design the root section of the blade and to determine the optimal rotor radius. Adding further variables than those mentioned in section 5.2.1 and using MIRAS-FLEX would have made the optimization computationally infeasible. The computational cost to run such an optimization would have impeded a significant amount of other users from using the cluster.

The present section on the OffWindChina 5 MW design consists of three subsections: 1) Wind site data, 2) Reference Data for Blade Design, and 3) Blade design results.

### 5.4.1 Wind Site Data

The wind turbine rotor is to be designed for an offshore site on the southeastern coast of China near the city of Shanghai and Jiangsu. Reference [139] contains normal and extreme wind conditions data at 12 coastal locations along China's coastline: Changhai, Xingcheng, Changdao, Chengshantou, Qingdao, Lvshi, Shengshi, Dachendao, Pingtan, Nanao, Shangchuandao, and Xisha. Figure 5.8 depicts the 12 locations (left) alongside a geographical map of China's coastline (right).

The data contained in the reference are based on daily meteorological data measured at 10 m height above ground for periods of 40-62 years. The reference also contains statistical analysis on the data. For example, Weibull and lognormal probability distributions were applied to fit the yearly wind speeds. Figure 5.9 is a table from [139] with Weibull parameters for the 12 coastal locations. The coastal location of Shengshi was chosen for the wind turbine rotor design study, since it lies the closest to Shanghai and does not suffer from typhoons as much as the other coastal locations in China.

The probability density function (pdf) of wind speed is a function that describes the relative likelihood for wind speed to take on a given value. The probability density function, $f(v)$, of the Weibull distribution is:

$$f(v) = \frac{k}{c}\left(\frac{v}{c}\right)^{k-1} \exp\left[-\left(\frac{v}{c}\right)^{k}\right] \tag{5.4}$$

where $v$ is the wind speed in meters per second, $k$ ($> 0$) is the dimensionless Weibull shape parameter, and $c$ ($> 0$) is the scale parameter in meters per second. The Weibull distribution for Shengshi is shown in Figure 5.10. The cumulative distribution function of the Weibull distribution is:

$$F(v) = 1 - \exp\left[-\left(\frac{v}{c}\right)^{k}\right] \tag{5.5}$$

Since the Weibull parameters from [139] are based on measurements from 10 m above ground, extrapolation is required to estimate the Weibull parameters for a turbine hub height of approximately 90 m. Inverse transform sampling with Equation (5.5) is used to extract the wind speeds. Next, the wind speeds are extrapolated to 90 m using the logarithmic law:

$$v_2 = v_1 \frac{\ln\left(h_2/z_0\right)}{\ln(h_1/z_0)} \tag{5.6}$$

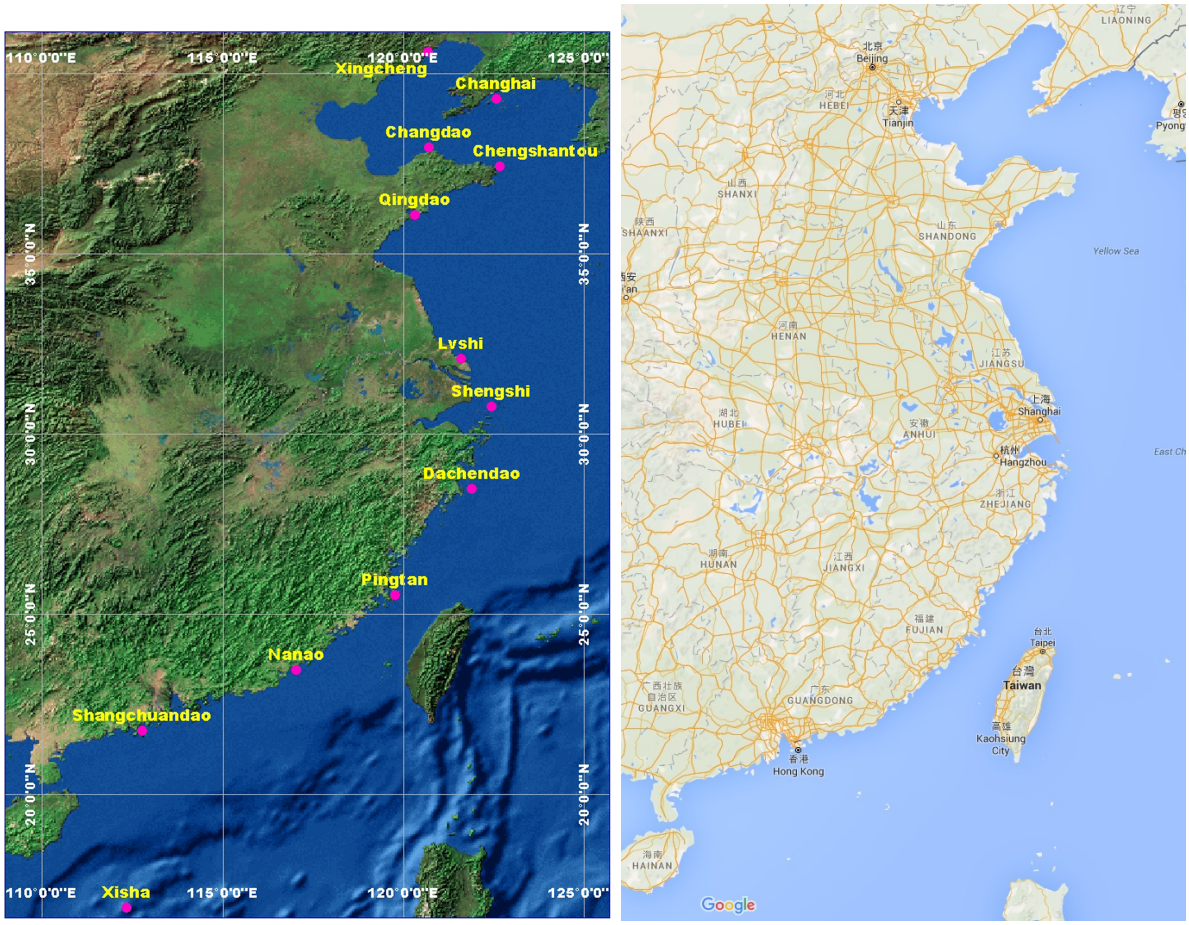


**Figure 5.8:** Geographic locations of 12 coastal meteorological stations (left) retrieved from [139]. A geographical map of China's coastline shown on the right side (Map data ©Google).

| Station | Weibull model | | | | Lognormal model | | | |
|---|---|---|---|---|---|---|---|---|
| | *c* | *k* | KS | AE | *μ* | *σ* | KS | AE |
| Changhai | 5.4163 | 2.1197 | 0.0814 | 0.3418 | 1.4516 | 0.4816 | **0.0360** | **0.079** |
| Xingcheng | 3.1332 | 1.9079 | **0.0637** | **0.1311** | 0.8601 | 0.592 | 0.0695 | 0.166 |
| Changdao | 6.2164 | 2.1208 | 0.0642 | 0.3085 | 1.5815 | 0.5061 | **0.0422** | **0.1598** |
| Chengshantou | 7.1395 | 2.064 | 0.067 | 0.3949 | 1.7138 | 0.5169 | **0.0390** | **0.1582** |
| Qingdao | 5.4875 | 2.333 | 0.0783 | 0.313 | 1.4836 | 0.4454 | **0.0378** | **0.089** |
| Lvshi | 4.2805 | 2.4144 | 0.0774 | 0.1957 | 1.237 | 0.4501 | **0.0591** | **0.1221** |
| Shengshi | 7.6818 | 2.4751 | **0.0434** | **0.1953** | 1.8203 | 0.4604 | 0.0524 | 0.3125 |
| Dachendao | 8.2196 | 2.1925 | **0.0412** | **0.1687** | 1.8522 | 0.5371 | 0.0726 | 0.5703 |
| Pingtan | 6.2933 | 2.0223 | 0.0528 | 0.2452 | 1.5743 | 0.5506 | **0.0473** | **0.2417** |
| Nanao | 4.2659 | 1.8345 | 0.0679 | 0.1912 | 1.158 | 0.607 | **0.0444** | **0.1828** |
| Shangchuandao | 5.2826 | 1.8599 | 0.0699 | 0.3086 | 1.3841 | 0.5772 | **0.0497** | **0.1583** |
| Xisha | 5.2425 | 2.1065 | **0.0439** | **0.1527** | 1.4023 | 0.5394 | 0.063 | 0.2912 |

doi:10.1371/journal.pone.0136876.t002

**Figure 5.9:** Estimate of parameters in Weibull and lognormal distributions by fitting yearly mean wind speeds for all 12 coastal stations. Also shown are the results of the Kolmogorov-Smirnov (KS) test and absolute error (AE) criterion. A smaller KS or AE indicates a better fitting. Retrieved from [139].

where $v_2$ is the estimated wind speed at hub height $h_2$. The wind speed $v_1$ is obtained from inverse transform sampling and $h_1$ is the reference height of 10 m. A roughness length of $z_0 = 0.001$ is selected, which corresponds to the roughness length scale at sea [140]. The

wind speeds $v_2$ are placed into bins of width 0.5 from 0 to 25 m/s. A Weibull probability distribution is then fitted to obtain the Weibull parameters $k = 2.4694$ and $c = 9.4925$ at $h_2$, see Figure 5.10.

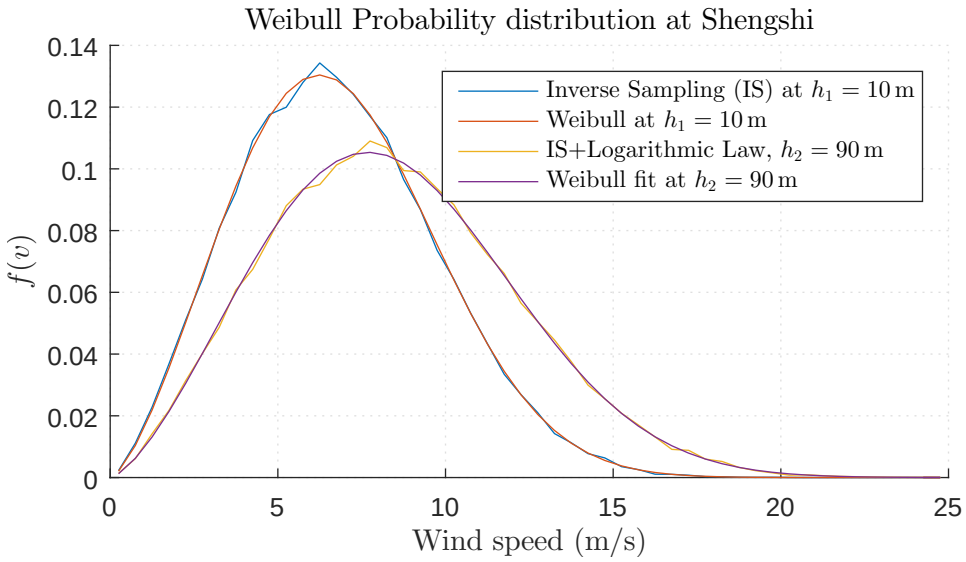


**Figure 5.10:** Measured and estimated Weibull probability distributions at Shengshi for heights of 10 m and 90 m, respectively.

The average wind speed of the site, $V_{\text{avg}}$, is computed as:

$$V_{\text{avg}} = \int f(v) v \, \mathrm{d}v \tag{5.7}$$

which results in an average wind speed of 8.4194 m/s for the Weibull probability distribution at Shengshi. Based on $V_{\text{avg}} = 8.4194$ m/s, and because the site is offshore and the turbulence intensity is low compared to the onshore case, a Class IIC turbine from IEC 61400-1 is selected for the rotor design.

### 5.4.2 Reference Data for Blade Design

The airfoils used for the blade design is comprised of DTU low noise airfoils (DTU-LN), the DU-W-405LM airfoil [116], and a cylinder for the root section. Figure 5.11 depicts the airfoil profile coordinates used in the blade design. The lift and drag coefficients for the profiles were computed using Q$^3$UIC, see Figure 5.12. A smoothing spline was applied on the lift and drag coefficients, see Figure 5.13, to remove the jagged results in the stall region from the Q$^3$UIC computations. As shown in Figure 5.14, Viterna extrapolation was performed to obtain the lift and drag coefficients for -180° to 180° angles of attack.

A reference blade is required for the blade design and the one from the NREL 5 MW [116] is chosen for this purpose. Only the blade span-wise chord, twist, and relative thickness distributions from the NREL 5 MW are used as reference values. Figure 5.15 depicts the chord, twist and relative thickness distributions for the NREL 5 MW as well as best-fit curves using B-splines denoted as “Baseline” and “Fit”, respectively.

Although the pre-bend and sweep can be parameterized and set as design variables in the optimization, they were set to zero. An optimization including the pre-bend and sweep as design variables did not result in good blade designs. Analysis of the

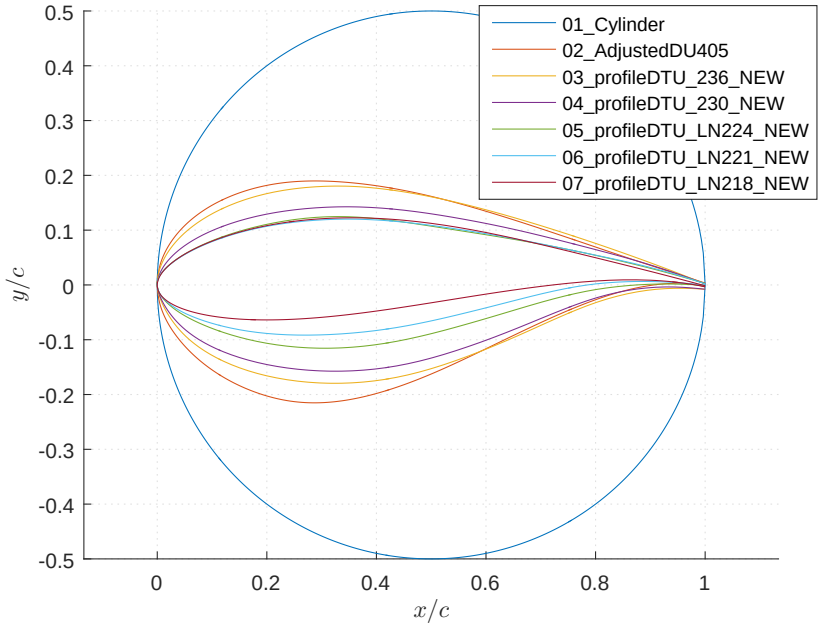


**Figure 5.11:** Airfoil profiles used for the blade design consists of DTU-LN, DU-W-405LM, and a cylinder.

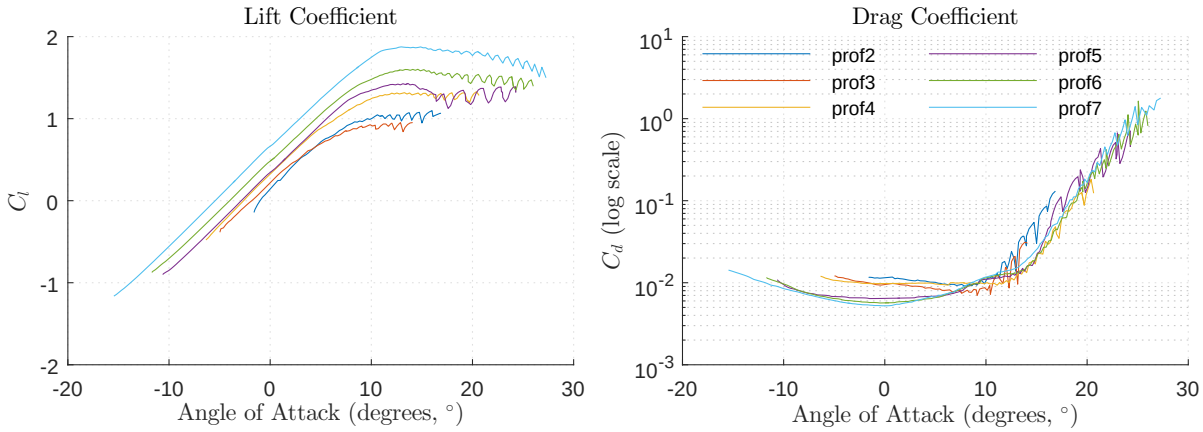


**Figure 5.12:** Airfoil lift (left) and drag (right) data computed from Q$^3$UIC.

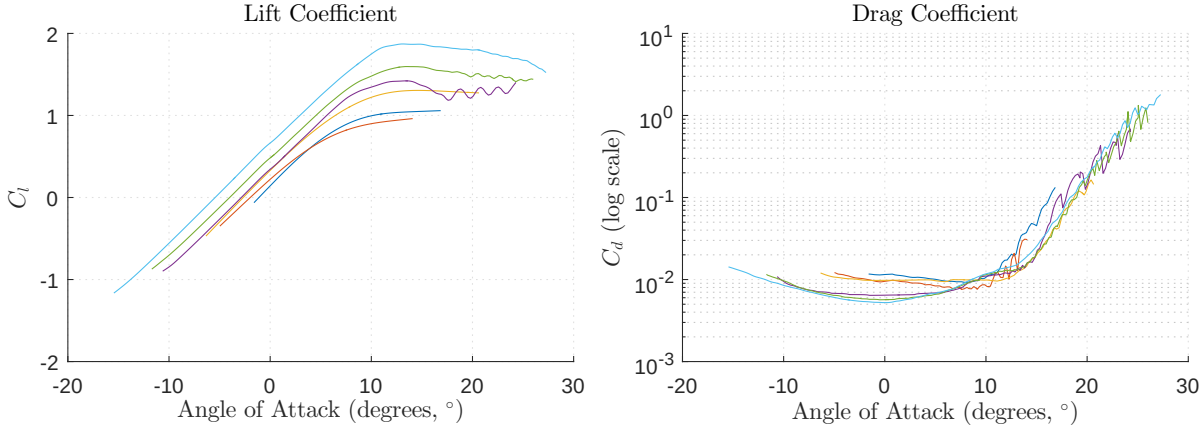


**Figure 5.13:** Application of a smoothing spline on the airfoil lift (left) and drag (right) data computed from Q$^3$UIC.

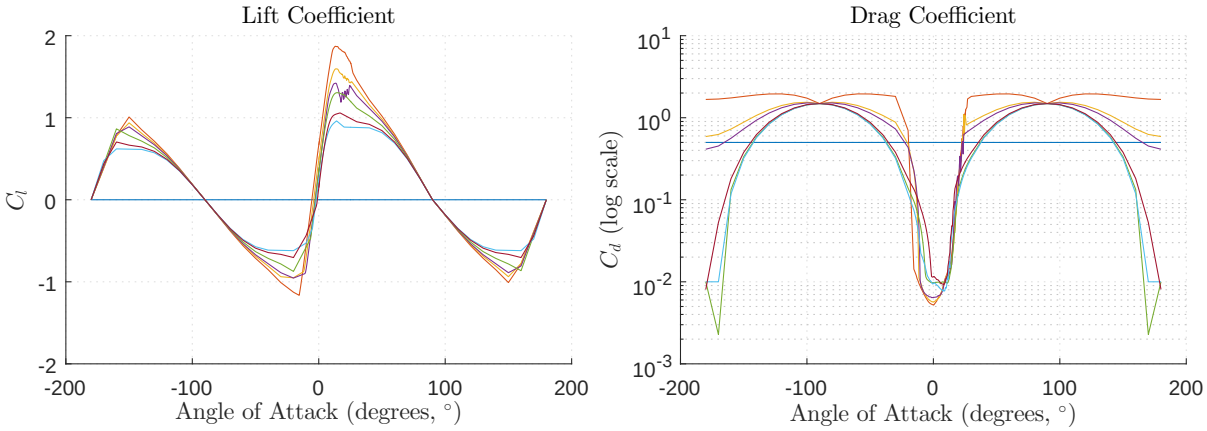


**Figure 5.14:** Application of Viterna extrapolation on the airfoil lift (left) and drag (right) data from smoothing splines.

optimization results showed that FLEX5 produces more AEP for blades with very large sweep, and the optimization focused on increasing the sweep as much as possible rather than optimizing the other parameters: chord, twist and relative thickness. A remedy would be to first carry out an optimization of chord, twist, and relative thickness, and subsequently optimize the pre-bend and sweep using a multi-body FEM code such as HAWC2. It is not clear how sweep is handled in FLEX5, which is based on mode shapes of straight blades.

### 5.4.3 Blade Design Results

The blade design for the 5 MW OffWindChina rotor was performed using seven different values of rotor radius. One meter increments/decrements were used relative to the reference value of 63 m from the NREL 5 MW: 60 m, 61 m, 62 m, 63 m, 64 m, 65 m, and 66 m. The effect on the COE by increasing and decreasing the rotor radius is shown in Figure 5.16. Evidently, COE decreases when the rotor radius increases. The reduction in COE for the optimized blade design (Optimum) relative the baseline (Baseline) is nearly the same for each rotor radius, however this trend is not seen for the AEP, maximum flap-wise root-bending moment experienced in the DLCs, and blade mass in Figure 5.16. Based on the results shown in Figure 5.16, a rotor radius of 65 m was selected. The optimum rotor with the 65 m radius produces the lowest COE and does not produce a flap-wise root-bending moment greater than the baseline design. The blade mass is also lower than rotor radius = 63 m, 64 m, and 66 m. Figure 5.17 depicts the optimized blade design for the 130 m diameter rotor.

### 5.4.4 Rotor Performance

#### Performance in Steady Conditions

Figure 5.18 depicts the performance metrics of the OffWindChina 5 MW against the reference (or baseline) for a wind sweep between 4 and 24 m/s. Figure 5.18 shows that the optimized design produces more electrical power (top-right) and less thrust (bottom-right) than the baseline design. However, the horizontal distance between the blade tip pointing closest towards the ground and the tower center (Tip dist to Twr center) is greater for the optimized design than the baseline between 10 and 12 m/s wind speeds.

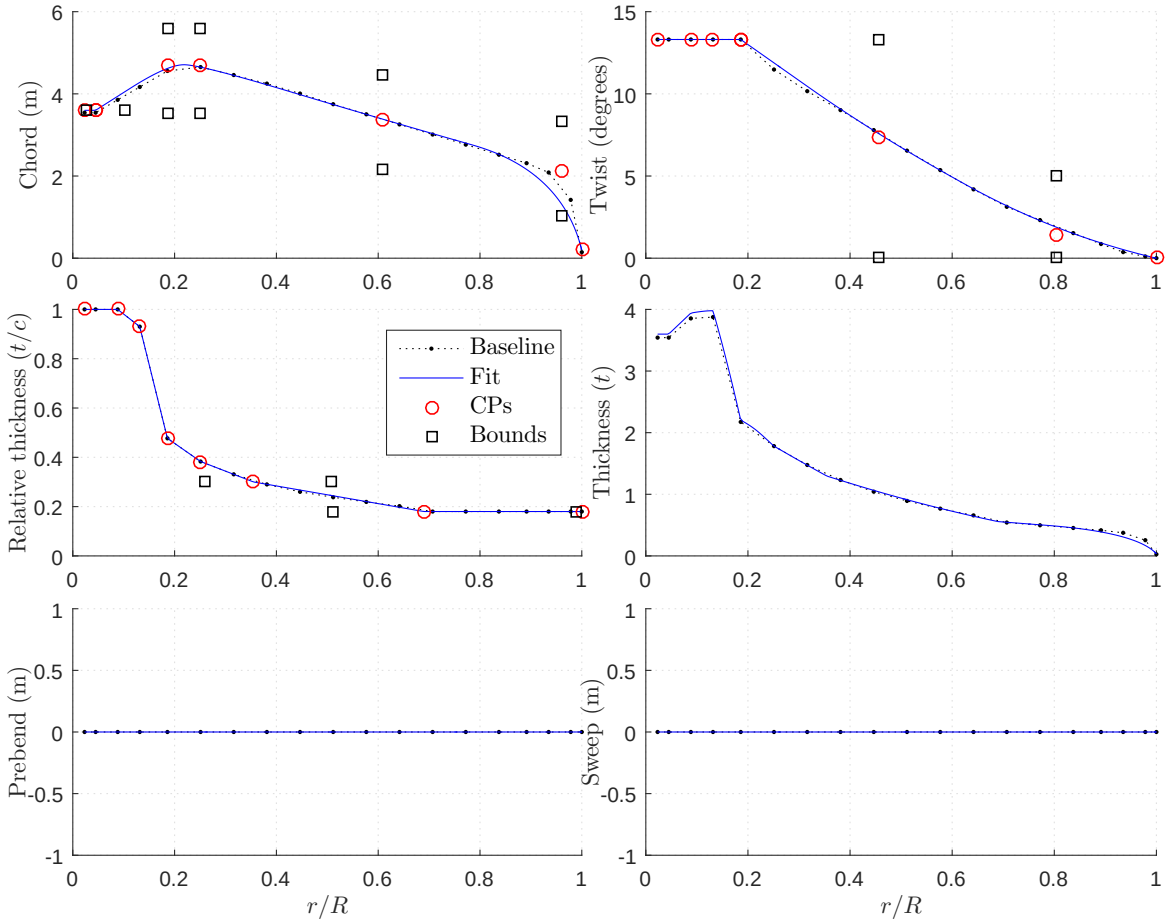


**Figure 5.15:** Parameterization method fitted to the reference blade based on the NREL 5 MW.

Given that the tower radius is approximately 2.6 m, the blade tips are at least 5.4 m away from tower strike.

### Performance in Turbulent Conditions

The performance of the baseline and optimum designs were also checked by running DLC1.2 [136] using the normal turbulence model (NTM). The turbulence intensity versus wind speed is depicted in Figure 5.19. Recall that the design is based on Class IIC. Seven seeds were used for each wind speed from 3 m/s up to 25 m/s in 2 m/s steps. The time of each simulation is 700 seconds, but the first 70 seconds are removed to avoid initial transients from affecting the fatigue calculations, see later. In total, there are 84 turbulent simulations carried out. Figures 5.20, 5.21, 5.22, and 5.23 are sample outputs of tip deflections and blade root-bending moments from the 84 simulations performed.

Tables 5.4 and 5.5 contain the lifetime damage-equivalent-loads (DEL) based on an equivalent load frequency of 1 Hz for the baseline (B) and optimum (O) designs. DELs are computed using MLife [141]. The total number of equivalent cycles from the 84 simulations is 595,079,722 per 20 years. Sensors are labeled according to span-wise blade position in meters, where 0ST is the rotor center and 65ST is the blade tip. For example, 2ST is located 2 m from the rotor center and represents the blade root. Note $L_{\text{Ult}}$ is the highest load (in absolute value) that the cross-section can withstand before failure based on its ultimate strength, see [142]. $L_{\text{Ult}}$ should be based on a finite-element analysis of the cross-section of the component (e.g. blade), but is roughly estimated here using simple

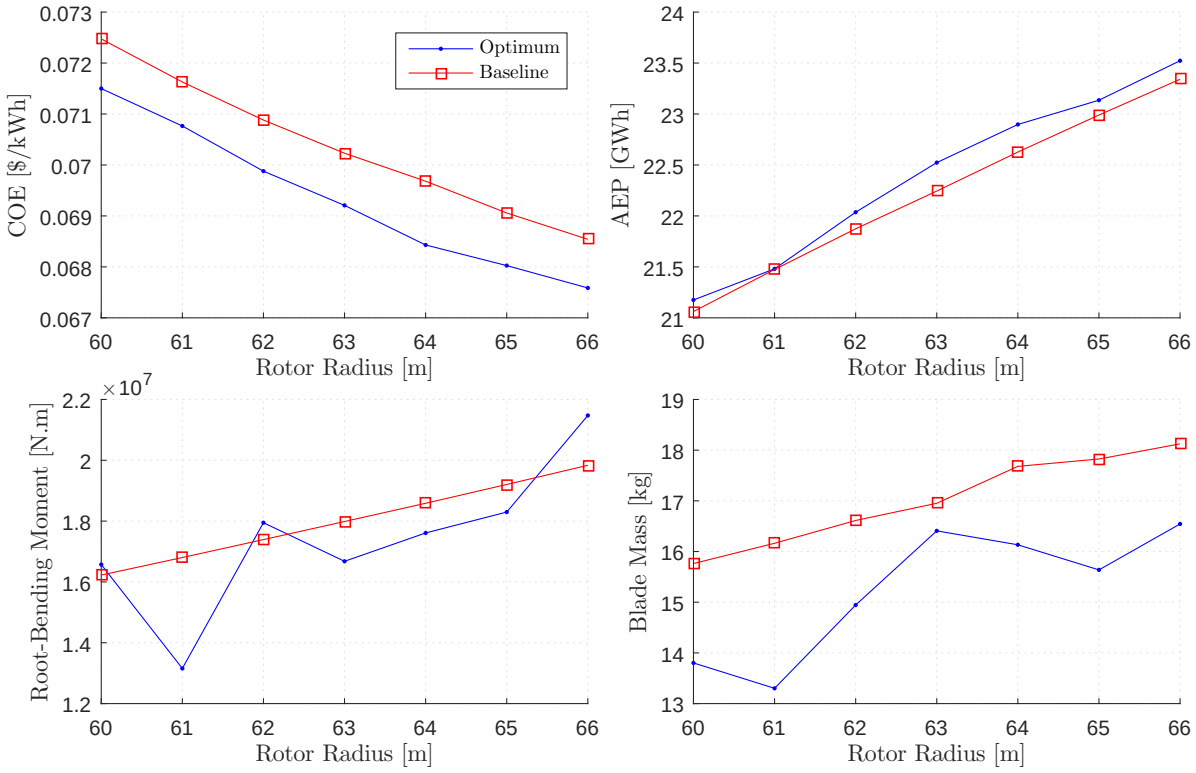


**Figure 5.16:** COE (top-left), AEP, flap-wise root-bending moment, and blade mass versus rotor radius.

bending from Euler-Bernoulli beam theory:

$$L_{\text{Ult}} = \frac{\sigma_{\text{Ult}} EI}{yE} \frac{1}{\text{SF}} \tag{5.8}$$

where $\sigma_{Ult}$ is the effective single cycle strength of the material, $EI$ is the bending stiffness of the cross-section, $E$ is the modulus of elasticity of the material, and $y$ is the distance between the tension center of the cross-section and the point in the cross-section of maximum stress. For the fatigue analysis based on flap-wise bending moments, $y$ is assumed equal to the maximum cross-sectional thickness divided by two. Likewise, for the edge-wise bending moments, $y$ is assumed equal to the chord length divided by two. The assumed values of $y$ are rough estimates for the points of maximum stress in the cross-section.

A safety factor of SF = 1.955 is selected assuming adequate SN curve data, see Table 25 in [130]. For the fatigue damage calculation, the material of the spar caps as well as the leading-edge and trailing-edge reinforcements are assumed to be uni-axial glass fiber - epoxy composite. Therefore, the assumed single cycle stress of the material is $\sigma_{\text{Ult}} = 1000 \times 10^6$ Pa and the assumed modulus of elasticity is $E = 29.38 \times 10^9$ Pa. The material values were obtained from [131]. Tables 5.4 and 5.5 show that the DELs for the optimum design are lower than the baseline for both flap-wise and edge-wise bending moments in DLC1.2.

**Table 5.4:** Lifetime DELs based on flap-wise bending moment for the optimum (O) and baseline (B) designs. $L_{\text{Ult}}$ is the ultimate load and the lower DEL is in bold.

| Sensor | Units | $L_{\text{Ult,B}}$ | $L_{\text{Ult,O}}$ | DEL,B | DEL,O |
|---|---|---|---|---|---|
| 2ST | (kN.m) | 272,243.96 | 164,026.24 | 6,653.92 | **6,154.13** |
| 3ST | (kN.m) | 193,660.02 | 118,854.50 | 6,408.46 | **5,925.14** |
| 6ST | (kN.m) | 249,281.61 | 213,427.75 | 5,927.19 | **5,476.98** |
| 9ST | (kN.m) | 188,741.54 | 182,507.36 | 5,448.58 | **5,031.65** |
| 12ST | (kN.m) | 68,828.05 | 79,071.45 | 4,863.64 | **4,486.53** |
| 16ST | (kN.m) | 62,865.00 | 73,176.47 | 4,179.38 | **3,846.53** |
| 21ST | (kN.m) | 54,596.28 | 73,944.82 | 3,525.40 | **3,236.40** |
| 25ST | (kN.m) | 45,777.41 | 61,005.54 | 2,911.10 | **2,661.22** |
| 29ST | (kN.m) | 37,843.83 | 53,207.87 | 2,347.25 | **2,132.21** |
| 33ST | (kN.m) | 30,693.06 | 45,708.70 | 1,837.95 | **1,659.47** |
| 37ST | (kN.m) | 24,454.46 | 31,741.62 | 1,389.55 | **1,245.74** |
| 42ST | (kN.m) | 18,505.78 | 19,460.54 | 998.38 | **885.98** |
| 46ST | (kN.m) | 13,815.70 | 12,065.80 | 669.57 | **583.83** |
| 50ST | (kN.m) | 10,900.18 | 8,939.04 | 402.88 | **342.80** |
| 54ST | (kN.m) | 8,017.80 | 6,077.83 | 200.49 | **165.00** |
| 58ST | (kN.m) | 5,394.57 | 3,795.59 | 83.31 | **66.34** |
| 61ST | (kN.m) | 3,510.41 | 2,076.86 | 25.20 | **19.74** |
| 64ST | (kN.m) | 1,308.77 | 537.73 | 1.53 | **1.18** |
| 65ST | (kN.m) | 23.29 | 22.56 | 0.00 | 0.00 |

**Table 5.5:** Lifetime DELs based on edge-wise bending moment for the optimum (O) and baseline (B) designs. $L_{\text{Ult}}$ is the ultimate load and the lower DEL is in bold.

| Sensor | Units | $L_{\text{Ult,B}}$ | $L_{\text{Ult,O}}$ | DEL,B | DEL,O |
|---|---|---|---|---|---|
| 2ST | (kN.m) | 272,214.94 | 164,013.83 | 6,782.98 | **5,506.60** |
| 3ST | (kN.m) | 186,009.71 | 112,011.81 | 6,466.80 | **5,143.18** |
| 6ST | (kN.m) | 168,003.19 | 98,446.95 | 5,923.01 | **4,493.91** |
| 9ST | (kN.m) | 121,235.00 | 77,156.57 | 5,447.34 | **3,922.90** |
| 12ST | (kN.m) | 41,513.71 | 28,773.64 | 4,910.29 | **3,306.76** |
| 16ST | (kN.m) | 39,722.59 | 27,214.47 | 4,303.18 | **2,657.98** |
| 21ST | (kN.m) | 36,327.44 | 25,817.98 | 3,722.84 | **2,098.68** |
| 25ST | (kN.m) | 32,655.91 | 23,818.26 | 3,155.00 | **1,621.72** |
| 29ST | (kN.m) | 26,916.88 | 20,279.32 | 2,599.95 | **1,220.39** |
| 33ST | (kN.m) | 22,706.63 | 17,541.01 | 2,068.50 | **888.41** |
| 37ST | (kN.m) | 18,563.95 | 14,505.42 | 1,571.53 | **619.78** |
| 42ST | (kN.m) | 15,337.02 | 11,883.89 | 1,123.57 | **409.32** |
| 46ST | (kN.m) | 11,735.96 | 8,950.97 | 741.00 | **251.54** |
| 50ST | (kN.m) | 9,330.82 | 6,855.33 | 429.50 | **136.79** |
| 54ST | (kN.m) | 7,595.56 | 5,254.13 | 198.81 | **59.79** |
| 58ST | (kN.m) | 5,615.74 | 3,724.81 | 75.41 | **21.76** |
| 61ST | (kN.m) | 3,695.39 | 2,389.03 | 21.00 | **5.89** |
| 64ST | (kN.m) | 1,676.51 | 1,161.96 | 1.30 | **0.35** |
| 65ST | (kN.m) | 89.24 | 81.35 | 0.00 | 0.00 |

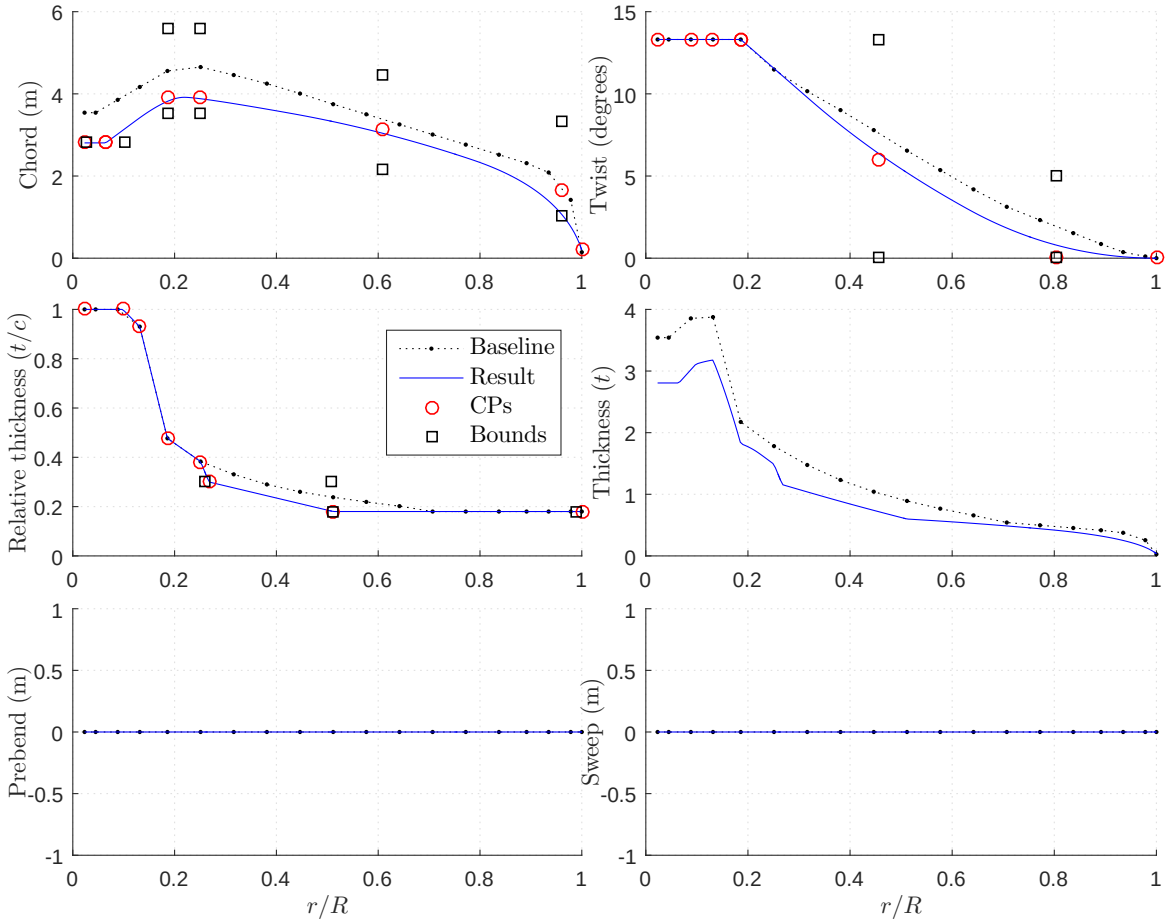


**Figure 5.17:** Final blade design results for the OffWindChina 5 MW with a rotor radius of 65 m.

### Extreme-Event Tables

Extreme-event tables were created based on the design load cases described in section 4.4. The extreme blade tip-to-tower-center clearance (Atip) and blade tip deflections (Uy1, Uz1, Uy2, Uz2, etc.) for the optimum and baseline blades are given in Tables 5.7 and 5.9, respectively. Similarly, the extreme blade root-bending moments (Mx1, My1, Mz1, Mx2, My2, Mz2, etc.) for the optimum and baseline blades are given in Tables 5.6 and 5.8, respectively. Note that the number in, e.g. Uy1, Uz1, Uy2, Uz2, etc., indicates the blade number. Tables 5.6 and 5.8 show that the optimum blade in general experiences smaller blade root-bending moment loads compared to the baseline blade. Tables 5.7 and 5.9 show that the optimum and baseline blades experience similar extreme tip-to-tower-center clearance and blade tip deflection values. The smallest values for the tip-to-tower-center clearance for the optimum and baseline blades are 7.86 and 7.90 m, respectively. Given that the tower radius is approximately 2.6 m, the blade tips are at least 5.2 m away from tower strike.

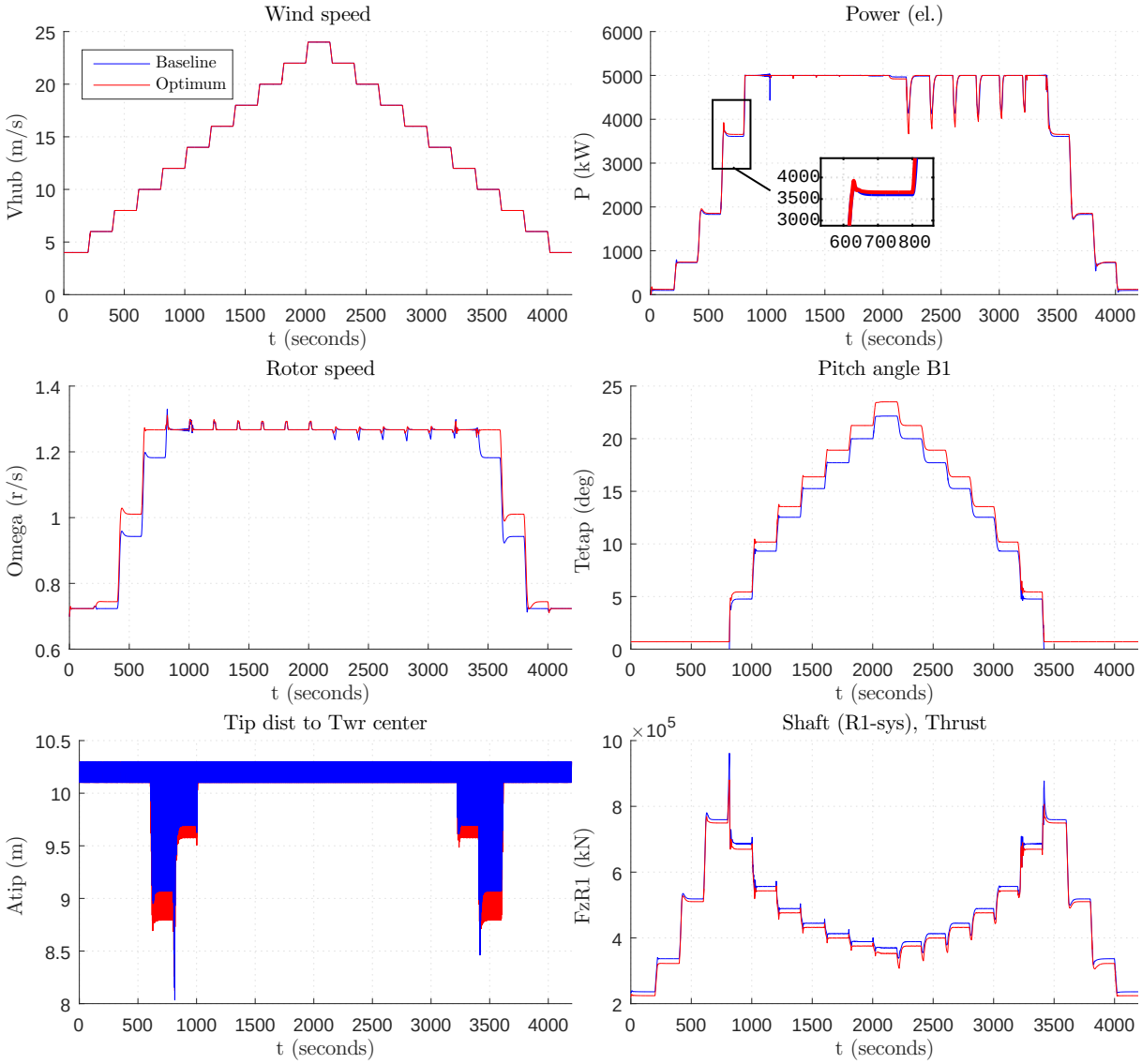


**Figure 5.18:** Increasing and decreasing wind speed simulation for the OffWindChina 5 MW.

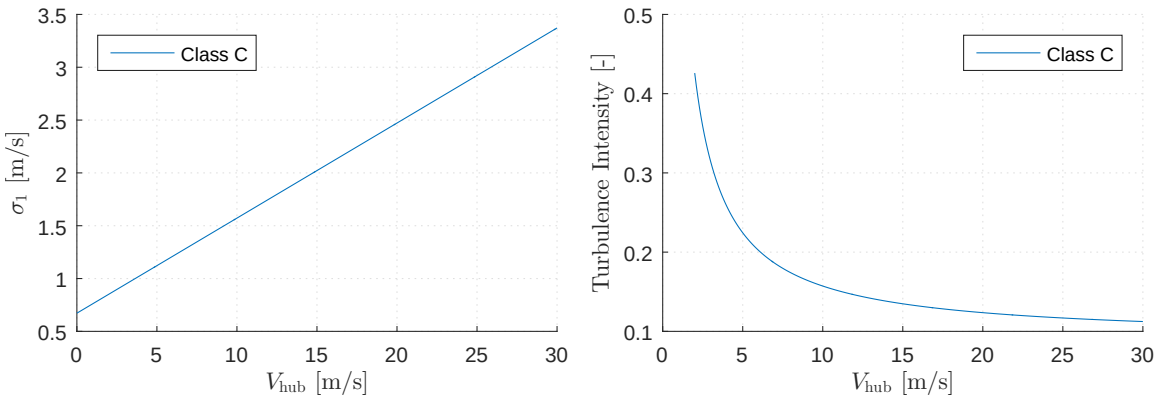


**Figure 5.19:** Class C turbulence standard deviation (left) and intensity (right) versus wind speed for the normal turbulence model (NTM).

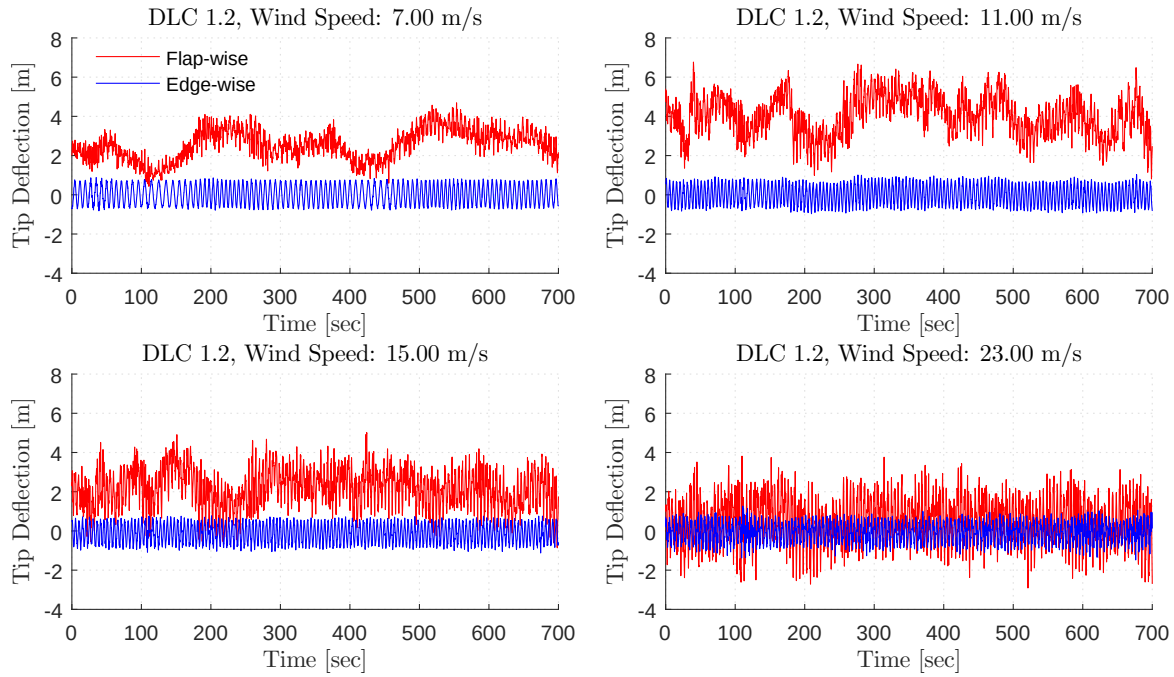


**Figure 5.20:** Flap-wise and edge-wise tip deflections for the optimum blade for DLC 1.2 with 7 (top-left), 11 (top-right), 15 (bottom-left), and 23 m/s (bottom-right) wind speeds.

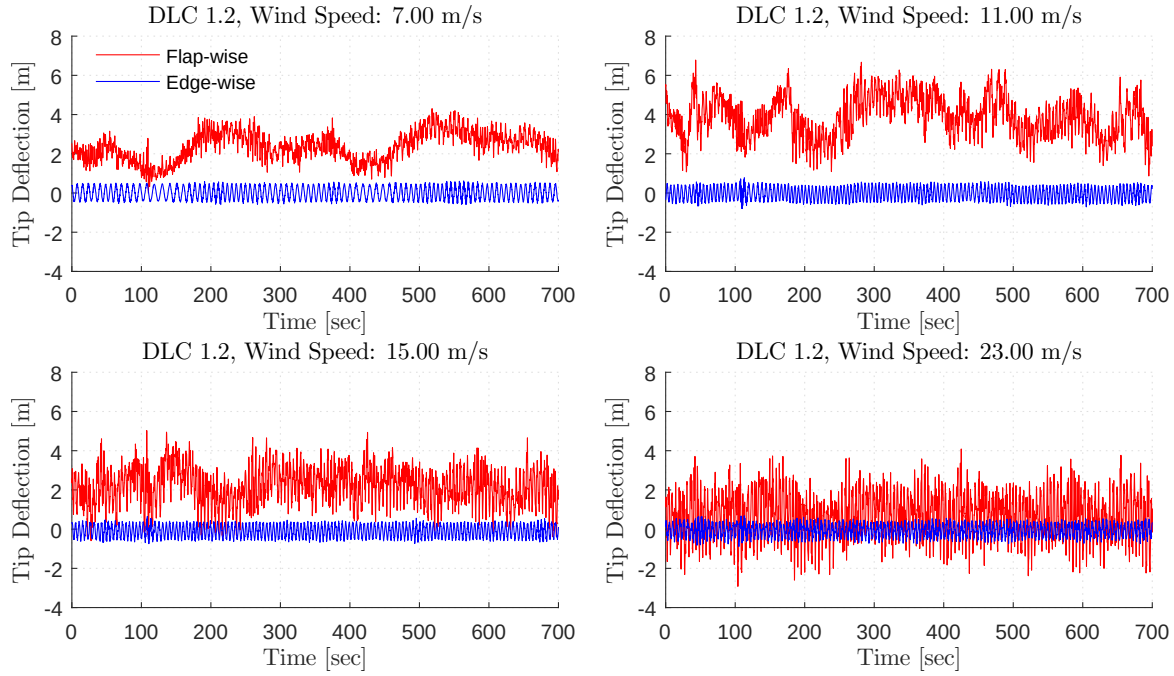


**Figure 5.21:** Flap-wise and edge-wise tip deflections for the baseline blade for DLC 1.2 with 7 (top-left), 11 (top-right), 15 (bottom-left), and 23 m/s (bottom-right) wind speeds.

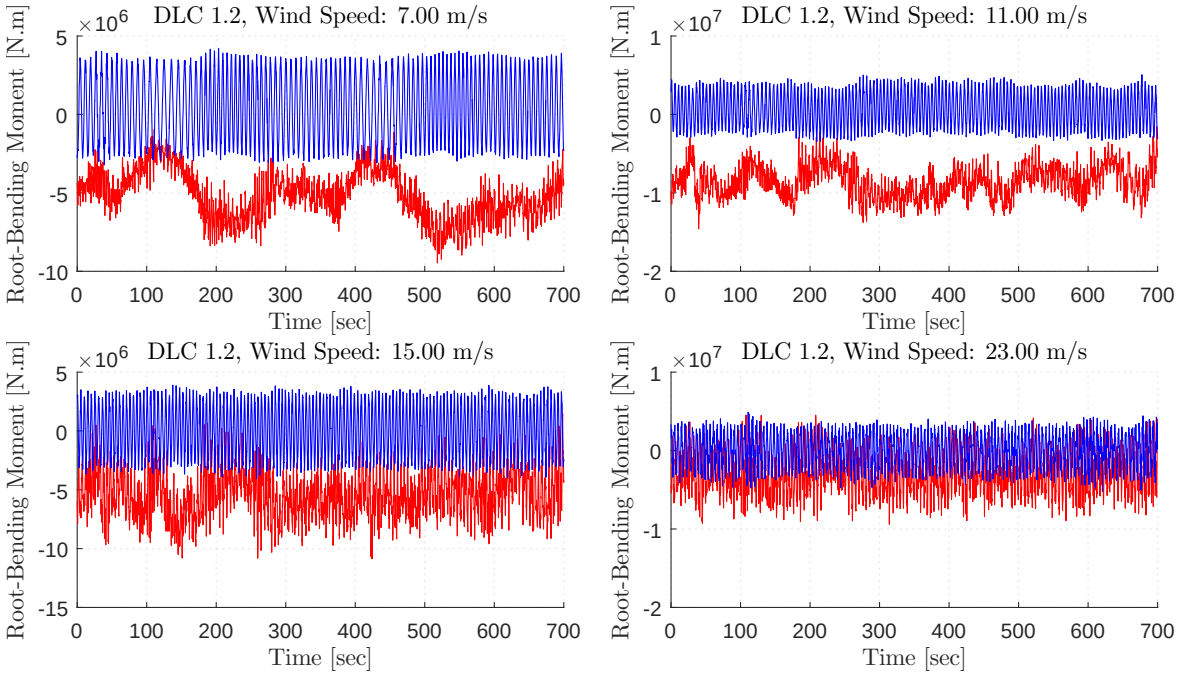


**Figure 5.22:** Flap-wise and edge-wise blade root-bending moments for the optimum blade for DLC 1.2 with 7 (top-left), 11 (top-right), 15 (bottom-left), and 23 m/s (bottom-right) wind speeds.

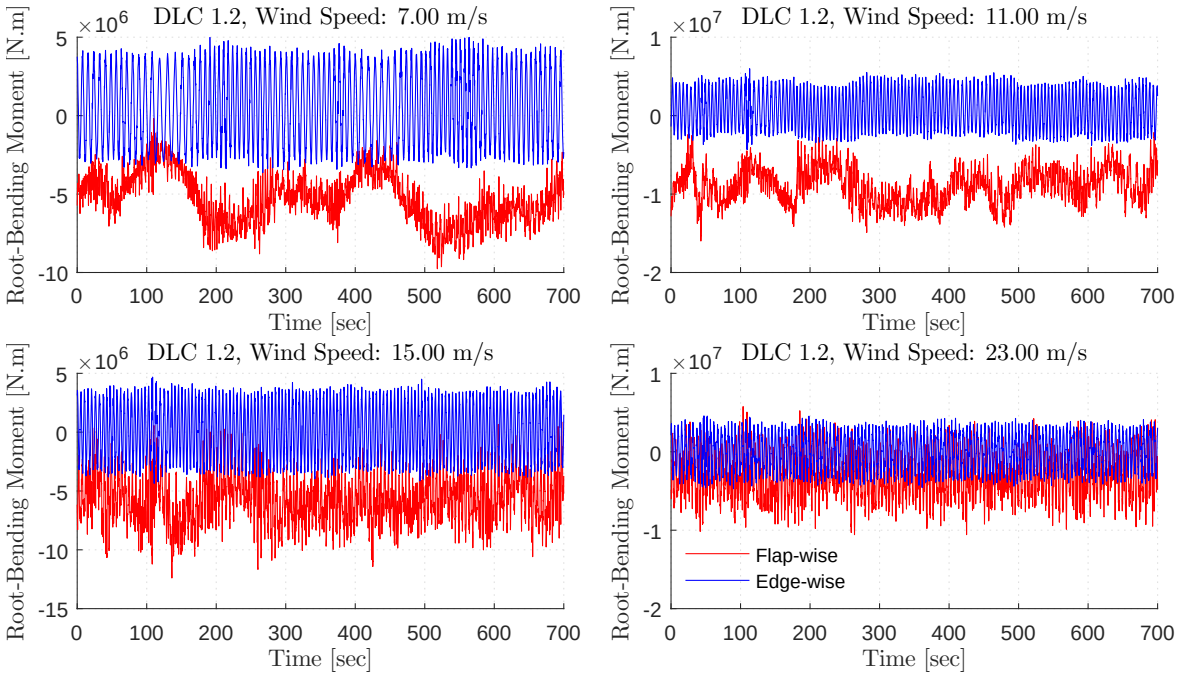


**Figure 5.23:** Flap-wise and edge-wise blade root-bending moments for the baseline blade for DLC 1.2 with 7 (top-left), 11 (top-right), 15 (bottom-left), and 23 m/s (bottom-right) wind speeds.

**Table 5.6:** Extreme-event table for blade root-bending moments of the optimum blade generated using MExtremes [143].

| Parameter | Type | File Name | DLC | Extr. Val | Mx1 (kNm) | -My1 (kNm) | Mz1 (kNm) | Mx2 (kNm) | -My2 (kNm) | Mz2 (kNm) | Mx3 (kNm) | -My3 (kNm) | Mz3 (kNm) | Time (sec) | Vhub (m/s) |
|---|---|---|---|---|---|---|---|---|---|---|---|---|---|---|---|
| Mx1 | Min | 03_yaw_p05 | DLC6.1 | -2.18E+05 | **-2.18E+05** | 6.17E+06 | -3.23E+05 | -7.22E+04 | -1.00E+07 | 8.45E+05 | -1.70E+05 | -1.84E+06 | -7.52E+05 | 2.56 | 70.00 |
| Mx1 | Max | 05_yaw_n25 | DLC6.3 | 1.98E+05 | **1.98E+05** | -1.62E+07 | -7.46E+06 | -9.99E+04 | 9.46E+06 | 3.25E+05 | -4.50E+04 | 6.66E+06 | -1.36E+06 | 5.00 | 56.00 |
| -My1 | Min | 07_yaw_n15 | DLC6.1 | -2.53E+07 | 2.41E+04 | **-2.53E+07** | 5.87E+06 | -1.75E+05 | 6.46E+06 | -5.88E+05 | -1.65E+05 | 1.01E+07 | 2.45E+05 | 0.78 | 70.00 |
| -My1 | Max | 01_yaw_p15 | DLC6.1 | 1.80E+07 | -8.76E+04 | **1.80E+07** | -6.94E+05 | -1.75E+04 | -1.52E+07 | 2.59E+06 | -9.39E+04 | -1.15E+07 | 2.78E+05 | 4.20 | 70.00 |
| Mz1 | Min | 01_yaw_p30 | DLC6.3 | -9.45E+06 | 3.27E+03 | 1.64E+07 | **-9.45E+06** | 6.45E+04 | -1.02E+07 | 3.40E+06 | 7.08E+03 | -1.23E+07 | 2.06E+06 | 1.20 | 56.00 |
| Mz1 | Max | 05_yaw_n25 | DLC6.3 | 9.19E+06 | 2.81E+04 | -1.82E+07 | **9.19E+06** | -9.74E+04 | 9.45E+06 | -2.56E+04 | -3.78E+04 | 6.83E+06 | -1.72E+06 | 4.50 | 56.00 |
| Mx2 | Min | 06_Vhub_p2n | DLC1.4 | -1.76E+05 | -1.28E+03 | -6.55E+06 | 2.81E+06 | **-1.76E+05** | -9.39E+05 | -7.43E+04 | -1.78E+04 | -4.10E+06 | -2.73E+06 | 26.56 | 27.51 |
| Mx2 | Max | 01_yaw_p30 | DLC6.3 | 6.45E+04 | 3.47E+03 | 1.65E+07 | -9.43E+06 | **6.45E+04** | -1.02E+07 | 3.39E+06 | 7.10E+03 | -1.23E+07 | 2.06E+06 | 3.12 | 56.00 |
| -My2 | Min | 04_Vhub_n2n | DLC1.4 | -1.55E+07 | 7.26E+03 | -7.25E+06 | 3.28E+06 | -2.43E+04 | **-1.55E+07** | 2.79E+06 | 5.14E+03 | -7.56E+06 | -2.37E+06 | 24.40 | 19.97 |
| -My2 | Max | 06_yaw_n30 | DLC6.3 | 1.03E+07 | 1.38E+05 | -1.95E+07 | -3.41E+06 | -5.77E+04 | **1.03E+07** | -4.31E+05 | -1.03E+04 | 6.83E+06 | -2.96E+06 | 4.28 | 56.00 |
| Mz2 | Min | 03_Vhub_p2p | DLC1.4 | -3.23E+06 | -2.71E+04 | -7.75E+06 | 1.62E+06 | -2.26E+04 | -5.77E+06 | **-3.23E+06** | -3.66E+04 | -6.12E+06 | 1.68E+06 | 5.28 | 13.30 |
| Mz2 | Max | 05_Vhub_r0n | DLC1.4 | 5.41E+06 | 1.23E+04 | -8.76E+06 | -4.66E+05 | 1.83E+03 | -1.47E+07 | **5.41E+06** | 1.83E+03 | -1.29E+07 | -3.23E+05 | 22.72 | 18.12 |
| Mx3 | Min | 05_yaw_n05 | DLC6.1 | -1.95E+05 | -1.09E+05 | -1.07E+07 | 3.14E+05 | -1.28E+05 | -2.68E+06 | -4.68E+05 | **-1.95E+05** | 5.62E+06 | -2.65E+05 | 1.22 | 70.00 |
| Mx3 | Max | 02_Vhub_r0p | DLC1.4 | 2.96E+04 | -7.50E+03 | -1.15E+07 | 1.29E+06 | 5.32E+03 | -1.18E+07 | 4.29E+06 | **2.96E+04** | -1.29E+07 | -5.39E+05 | 22.24 | 16.99 |
| -My3 | Min | 02_Vhub_r0 | DLC2.3 | -1.47E+07 | 2.57E+04 | -1.27E+07 | -1.02E+06 | 5.98E+03 | -1.35E+07 | 4.42E+06 | 1.60E+04 | **-1.47E+07** | 3.13E+06 | 23.28 | 14.98 |
| -My3 | Max | 07_yaw_n15 | DLC6.1 | 1.01E+07 | 2.41E+04 | -2.53E+07 | 5.87E+06 | -1.75E+05 | 6.46E+06 | -5.88E+05 | -1.65E+05 | **1.01E+07** | 2.45E+05 | 0.62 | 70.00 |
| Mz3 | Min | 03_Vhub_p2p | DLC1.4 | -3.25E+06 | -1.54E+05 | -2.53E+05 | 1.31E+06 | 3.69E+03 | -6.31E+06 | 1.92E+06 | -6.06E+04 | -1.11E+06 | **-3.25E+06** | 26.80 | 27.78 |
| Mz3 | Max | 04_Vhub_n2n | DLC1.4 | 5.31E+06 | 1.58E+04 | -1.23E+07 | 4.67E+05 | 1.64E+04 | -8.64E+06 | -5.40E+05 | 6.26E+03 | -1.22E+07 | **5.31E+06** | 21.82 | 14.07 |

**Table 5.7:** Extreme-event table for blade tip deflections of the optimum blade generated using MExtremes [143].

| Parameter | Type | File Name | DLC | Extr. Val | Atip (m) | Uz1 (m) | Uy1 (m) | Uz2 (m) | Uy2 (m) | Uz3 (m) | Uy3 (m) | Time (sec) | Vhub (m/s) |
|---|---|---|---|---|---|---|---|---|---|---|---|---|---|
| Atip | Min | 01_Vhub_n2p | DLC1.4 | 7.86 | **7.86** | 4.72 | 0.88 | 5.89 | 0.05 | 5.72 | 0.15 | 23.10 | 17.06 |
| Atip | Max | c01 | DLC Steady | 10.30 | **10.30** | 0.89 | 0.01 | 0.92 | -0.67 | 1.06 | 0.53 | 8.70 | 3.00 |
| Uz1 | Min | 01_yaw_p30 | DLC6.3 | -7.33 | 10.30 | **-7.33** | -2.47 | 4.50 | 0.77 | 5.22 | 0.45 | 0.68 | 56.00 |
| Uz1 | Max | 07_yaw_n15 | DLC6.1 | 11.33 | 10.20 | **11.33** | 1.27 | -1.43 | -0.01 | -3.75 | 0.45 | 0.84 | 70.00 |
| Uy1 | Min | 05_yaw_n25 | DLC6.3 | -3.06 | 10.20 | 6.55 | **-3.06** | -3.37 | 0.32 | -2.81 | -0.09 | 5.00 | 56.00 |
| Uy1 | Max | 05_yaw_n25 | DLC6.3 | 2.31 | 10.20 | 8.11 | **2.31** | -3.39 | 0.28 | -2.89 | -0.13 | 4.48 | 56.00 |
| Uz2 | Min | 06_yaw_n30 | DLC6.3 | -3.88 | 10.20 | 8.33 | -1.74 | **-3.88** | 0.15 | -2.95 | -0.57 | 4.40 | 56.00 |
| Uz2 | Max | 04_Vhub_n2n | DLC1.4 | 7.87 | 10.10 | 3.38 | 0.55 | **7.87** | 0.53 | 3.65 | -0.68 | 24.50 | 20.17 |
| Uy2 | Min | 03_Vhub_p2p | DLC1.4 | -0.87 | 10.30 | 3.64 | 0.22 | 2.60 | **-0.87** | 2.76 | 0.23 | 5.28 | 13.30 |
| Uy2 | Max | 05_Vhub_r0n | DLC1.4 | 1.07 | 10.10 | 4.07 | -0.27 | 7.06 | **1.07** | 6.10 | -0.25 | 22.76 | 18.21 |
| Uz3 | Min | 07_yaw_n15 | DLC6.1 | -3.75 | 10.20 | 11.33 | 1.27 | -1.43 | -0.01 | **-3.75** | 0.45 | 0.74 | 70.00 |
| Uz3 | Max | 02_Vhub_r0 | DLC2.3 | 7.22 | 10.20 | 6.08 | -0.38 | 6.44 | 0.80 | **7.22** | 0.62 | 23.34 | 14.95 |
| Uy3 | Min | 03_Vhub_p2 | DLC2.3 | -0.83 | 10.10 | 2.03 | 0.26 | 2.87 | 0.15 | 1.85 | **-0.83** | 26.78 | 12.30 |
| Uy3 | Max | 04_Vhub_n2n | DLC1.4 | 1.10 | 10.20 | 6.03 | -0.01 | 4.16 | -0.24 | 6.06 | **1.10** | 21.86 | 14.16 |

**Table 5.8:** Extreme-event table for blade root-bending moments of the baseline blade generated using MExtremes [143].

| Parameter | Type | File Name | DLC | Extr. Val | Mx1 (kNm) | -My1 (kNm) | Mz1 (kNm) | Mx2 (kNm) | -My2 (kNm) | Mz2 (kNm) | Mx3 (kNm) | -My3 (kNm) | Mz3 (kNm) | Time (sec) | Vhub (m/s) |
|---|---|---|---|---|---|---|---|---|---|---|---|---|---|---|---|
| Mx1 | Min | 03_yaw_p05 | DLC6.1 | -2.46E+05 | **-2.46E+05** | 9.00E+06 | -3.52E+05 | -1.03E+05 | -8.82E+06 | 6.30E+05 | -2.12E+05 | 5.82E+05 | -8.87E+05 | 0.86 | 70.00 |
| Mx1 | Max | 06_yaw_n30 | DLC6.3 | 2.94E+05 | **2.94E+05** | -2.06E+07 | -2.21E+06 | -4.27E+04 | 1.12E+07 | -1.06E+06 | -1.57E+04 | 7.20E+06 | -2.79E+06 | 2.96 | 56.00 |
| -My1 | Min | 07_yaw_n15 | DLC6.1 | -2.65E+07 | -8.04E+04 | **-2.65E+07** | 6.09E+06 | -2.06E+05 | 9.62E+06 | -5.85E+05 | -1.22E+05 | 1.16E+07 | -7.96E+04 | 0.82 | 70.00 |
| -My1 | Max | 01_yaw_p15 | DLC6.1 | 1.96E+07 | -3.37E+04 | **1.96E+07** | -9.16E+05 | -5.53E+04 | -1.50E+07 | 2.53E+06 | -1.20E+05 | -9.79E+06 | -7.55E+04 | 4.42 | 70.00 |
| Mz1 | Min | 01_yaw_p30 | DLC6.3 | -8.41E+06 | -1.24E+05 | 1.69E+07 | **-8.41E+06** | 5.09E+04 | -1.07E+07 | 3.60E+06 | -1.27E+04 | -1.30E+07 | 2.18E+06 | 0.94 | 56.00 |
| Mz1 | Max | 04_Vhub_n2n | DLC1.4 | 7.20E+06 | -7.76E+04 | -1.59E+07 | **7.20E+06** | 2.76E+04 | -1.40E+07 | 2.78E+04 | 2.31E+04 | -7.99E+06 | -2.32E+05 | 23.56 | 18.14 |
| Mx2 | Min | 03_Vhub_p2p | DLC1.4 | -2.48E+05 | -7.30E+04 | 1.67E+06 | -3.18E+06 | **-2.48E+05** | 7.09E+06 | 7.27E+05 | -1.73E+04 | -6.06E+06 | 2.60E+06 | 28.72 | 28.30 |
| Mx2 | Max | 01_Vhub_n2p | DLC1.4 | 6.17E+04 | -8.02E+03 | -1.03E+07 | 3.51E+06 | **6.17E+04** | -1.38E+07 | -6.47E+05 | -2.28E+04 | -1.24E+07 | 3.78E+06 | 22.50 | 15.65 |
| -My2 | Min | 04_Vhub_n2n | DLC1.4 | -1.68E+07 | -1.12E+04 | -8.17E+06 | 3.72E+06 | -4.72E+04 | **-1.68E+07** | 3.22E+06 | 2.90E+04 | -8.26E+06 | -2.48E+06 | 24.40 | 19.97 |
| -My2 | Max | 06_yaw_n30 | DLC6.3 | 1.13E+07 | 2.93E+05 | -2.06E+07 | -2.18E+06 | -4.06E+04 | **1.13E+07** | -9.56E+05 | -1.48E+04 | 7.20E+06 | -2.73E+06 | 4.26 | 56.00 |
| Mz2 | Min | c11 | DLC Steady | -3.38E+06 | -6.53E+04 | -4.20E+06 | 1.35E+06 | -3.51E+04 | -3.70E+06 | **-3.38E+06** | -6.47E+04 | -4.60E+06 | 1.64E+06 | 5.26 | 19.00 |
| Mz2 | Max | 05_Vhub_r0n | DLC1.4 | 5.96E+06 | 2.53E+04 | -9.50E+06 | -3.32E+05 | -5.29E+04 | -1.59E+07 | **5.96E+06** | 2.43E+04 | -1.35E+07 | -3.27E+05 | 22.70 | 18.07 |
| Mx3 | Min | 06_Vhub_p2n | DLC1.4 | -2.71E+05 | -1.86E+04 | -3.19E+06 | -2.83E+06 | -3.78E+04 | -3.36E+06 | 2.74E+06 | **-2.71E+05** | 5.38E+06 | -2.69E+05 | 28.12 | 28.30 |
| Mx3 | Max | 02_Vhub_r0p | DLC1.4 | 6.41E+04 | -2.00E+04 | -1.25E+07 | 2.66E+06 | -1.77E+04 | -1.29E+07 | 4.20E+06 | **6.41E+04** | -1.39E+07 | -1.05E+06 | 21.98 | 16.42 |
| -My3 | Min | 02_Vhub_r0 | DLC2.3 | -1.59E+07 | 6.04E+04 | -1.38E+07 | -9.37E+05 | -3.21E+04 | -1.47E+07 | 4.94E+06 | -3.31E+03 | **-1.59E+07** | 3.53E+06 | 23.28 | 14.98 |
| -My3 | Max | 07_yaw_n15 | DLC6.1 | 1.16E+07 | -8.03E+04 | -2.65E+07 | 6.09E+06 | -2.06E+05 | 9.62E+06 | -5.85E+05 | -1.22E+05 | **1.16E+07** | -7.95E+04 | 0.64 | 70.00 |
| Mz3 | Min | 02_Vhub_r0p | DLC1.4 | -3.58E+06 | -2.07E+05 | 2.14E+06 | 1.51E+06 | -8.45E+03 | -4.78E+06 | 1.85E+06 | -1.07E+05 | 1.34E+06 | **-3.58E+06** | 26.80 | 25.72 |
| Mz3 | Max | 04_Vhub_n2n | DLC1.4 | 5.94E+06 | 3.10E+04 | -1.33E+07 | 6.71E+05 | 3.28E+04 | -9.50E+06 | -4.43E+05 | -4.22E+04 | -1.34E+07 | **5.94E+06** | 21.82 | 14.07 |

**Table 5.9:** Extreme-event table for blade tip deflections of the baseline blade generated using MExtremes [143].

| Parameter | Type | File Name | DLC | Extr. Val | Atip (m) | Uz1 (m) | Uy1 (m) | Uz2 (m) | Uy2 (m) | Uz3 (m) | Uy3 (m) | Time (sec) | Vhub (m/s) |
|---|---|---|---|---|---|---|---|---|---|---|---|---|---|
| Atip | Min | 01_Vhub_n2p | DLC1.4 | 7.90 | **7.90** | 4.68 | 0.52 | 5.92 | 0.01 | 5.68 | 0.05 | 23.10 | 17.06 |
| Atip | Max | c01 | DLC Steady | 10.30 | **10.30** | 0.76 | -0.02 | 0.79 | -0.42 | 0.96 | 0.34 | 8.70 | 3.00 |
| Uz1 | Min | 01_yaw_p15 | DLC6.1 | -7.26 | 10.30 | **-7.26** | 0.32 | 6.79 | 0.24 | 4.93 | -0.10 | 4.62 | 70.00 |
| Uz1 | Max | 07_yaw_n15 | DLC6.1 | 11.01 | 10.20 | **11.01** | 0.67 | -2.30 | 0.08 | -3.99 | 0.31 | 0.90 | 70.00 |
| Uy1 | Min | 01_yaw_p30 | DLC6.3 | -1.31 | 10.30 | -7.08 | **-1.31** | 4.45 | 0.44 | 5.09 | 0.24 | 0.96 | 56.00 |
| Uy1 | Max | 04_Vhub_n2n | DLC1.4 | 0.87 | 10.30 | 7.12 | **0.87** | 6.36 | -0.14 | 3.53 | -0.16 | 23.66 | 18.37 |
| Uz2 | Min | 06_yaw_n30 | DLC6.3 | -3.86 | 10.20 | 8.01 | -1.04 | **-3.86** | 0.06 | -2.94 | -0.31 | 0.82 | 56.00 |
| Uz2 | Max | 04_Vhub_n2n | DLC1.4 | 7.82 | 10.10 | 3.43 | 0.32 | **7.82** | 0.30 | 3.60 | -0.46 | 24.52 | 20.22 |
| Uy2 | Min | 03_Vhub_p2p | DLC1.4 | -0.56 | 10.30 | 3.44 | 0.08 | 2.35 | **-0.56** | 2.66 | 0.14 | 5.22 | 13.30 |
| Uy2 | Max | 05_Vhub_r0n | DLC1.4 | 0.61 | 10.10 | 3.97 | -0.21 | 6.96 | **0.61** | 5.87 | -0.22 | 22.76 | 18.21 |
| Uz3 | Min | 07_yaw_n15 | DLC6.1 | -3.99 | 10.20 | 11.01 | 0.67 | -2.30 | 0.08 | **-3.99** | 0.31 | 0.76 | 70.00 |
| Uz3 | Max | 02_Vhub_r0 | DLC2.3 | 7.13 | 10.20 | 6.01 | -0.29 | 6.38 | 0.44 | **7.13** | 0.35 | 23.36 | 14.94 |
| Uy3 | Min | 03_Vhub_p2p | DLC1.4 | -0.57 | 10.10 | 2.67 | 0.16 | 3.54 | 0.07 | 2.53 | **-0.57** | 6.96 | 13.30 |
| Uy3 | Max | 04_Vhub_n2n | DLC1.4 | 0.66 | 10.20 | 5.97 | -0.04 | 4.13 | -0.19 | 6.07 | **0.66** | 21.88 | 14.21 |

## 5.5 Conclusions

The majority of blade design problems rely on aero-elastic codes that use BEM approaches to model the rotor aerodynamics. The present work describes an approach to wind-turbine rotor design by incorporating a higher-fidelity free-wake panel aero-elastic code called MIRAS-FLEX. A framework comprised of MIRAS-FLEX, a structural design code, and a surrogate-based numerical optimization technique has been developed and applied to optimize the NREL 5 MW baseline wind-turbine rotor. Comparisons were made by using MIRAS-FLEX and a simple BEM code to compute the annual energy production. Reductions in cost of energy were obtained for both cases. The framework using FLEX5 instead of MIRAS-FLEX was then applied to design a 5 MW offshore wind turbine rotor in China.

# Chapter 6

# Conclusions

## 6.1 Summary

The thesis project can be summarized by the development of four codes: 1) MIRAS-FLEX, 2) surrogate-based rotor design framework, 3) structural design code, and 4) coupled aero-structural rotor design framework. Each code from 1 to 4 is described in a separate chapter in Chapters 2 to 5. The following is a very brief summary of each code:

The first is the novel aero-elastic tool, MIRAS-FLEX, that combines a 3D viscous-inviscid interactive method, MIRAS, with the dynamics model used in the aero-elastic code FLEX5. MIRAS-FLEX is advantageous to standard aero-elastic codes because it uses a more advanced aerodynamic model than BEM and is still computationally efficient.

Second is the rotor design framework based on a surrogate optimization methodology using MIRAS as the aerodynamic model. The framework presents a unique approach because most aerodynamic wind-turbine rotor design codes use the more common and inexpensive BEM technique. Designing a rotor using a computationally expensive MIRAS instead of an inexpensive BEM code is a challenge, which is resolved by using the proposed surrogate-based approach.

The third code is the simple structural design tool. The structural design code was developed to perform more realistic large wind-turbine rotor designs in a coupled surrogate-optimization and aero-structural framework. A stand-alone structural design code was developed to minimize the cost of energy of the NREL 5MW wind-turbine blade.

Lastly, codes 1 to 3 listed above were combined to create a unique framework to design large wind-turbine rotors. The framework contains MIRAS-FLEX, the surrogate-optimization code, and structural design code. The optimization framework was used to design large wind-turbine blades using both FLEX5 and MIRAS-FLEX with good results obtained.

## 6.2 Areas for Improvement

The codes described in the present thesis can always be improved in one form or another. The first is MIRAS-FLEX and the second is the rotor-design framework.

The primary concern by one reviewer regarding the development of MIRAS-FLEX was the following:

> "The development of the advanced aeroelastic code, MIRAS-FLEX, is based on a more detailed aerodynamic model, but for the structural dynamics part the lowest possible order model was used. A linear, modal dynamics code that suppresses torsion of the blades. In OC3 comparison the results are grouped into mainly two types of codes. One with all modal codes (e.g. FAST, FLEX) and another with non-linear multi-body codes (HAWC2 and ADAMS). The differences between the two sets are only related to the way the different codes model structural dynamics (non-linear geometric couplings

> due to large deflections, torsion dynamics suppressed by most modal codes). Some explanation of the above choice should be provided in the revised text given that HAWC2 code is also available at DTU."

At the beginning of the PhD project three codes were considered to couple with MIRAS: 1) FLEX5, 2) HAWC2, and 3) FAST modal/BeamDyn. FAST was ruled out because a 100% DTU code was desirable, which leaves options 1) and 2). Option 1) is a simpler and a much faster code than 2), and was developed at the Fluid Mechanics section at DTU by Stig Øye, which is also the same section where the MIRAS code was developed. Option 2) is a more complicated and slower code than option 1) due to the large number of DOFs, and is developed at Risø.

Based on the above discussion, FLEX5 was chosen because of simplicity, speed, and proximity of the main developer for guidance. Once the coupling of MIRAS with FLEX5 is fully understood and optimized, future work would then entail the coupling of MIRAS with HAWC2. Strong-coupling methods should be implemented in MIRAS-FLEX and comparisons with loose-coupling approaches should be carried out first. Strong coupling might resolve the discrepancies seen in the higher frequency range for turbulent inflow conditions.

For the rotor-design framework, there are many areas of improvement. In the author's opinion, one of the most comprehensive and detailed rotor design frameworks to date is the one developed by Bottasso [60, 75, 144]. The design framework, called Cp-Max (Code for Performance Maximization), was further developed by Bortolotti [145] and Sartori [146]. Therefore, the goal of the rotor design framework described in this thesis would be to incorporate at least all the high-fidelity tools (or equivalents) from Cp-Max. There are two groups of codes used in the multidisciplinary design of wind-turbines outlined in this thesis and [60, 75, 144]: 1) aero-servo-elastic codes and 2) structural design tools.

In terms of the aero-servo-elastic tools to compute, e.g. AEP and the DLCs, reference [60] uses Cp-Lambda (Code for Performance, Loads and Aeroelasticity by Multi-Body Dynamic Analysis). Cp-Lambda consists of BEM and geometrically exact beam theory for the aerodynamic and structural-dynamic modeling. Since MIRAS is more advanced than BEM, perhaps MIRAS coupled with HAWC2 will be preferred over Cp-Lambda for the rotor design framework in this thesis.

The PreComp and BModes tools described in Chapter 4 should be replaced by the finite-element based BECAS [76] and FRANS from DTU, or the publicly available VABS [77] and SwiftComp [147]. In [60], the finite element cross-sectional model ANBA (Anisotropic Beam Analysis) is used. In addition to the cross-sectional model, a fully resolved 3D FEM package such as Abaqus/CAE [148] should be included in the framework to make the structural design as realistic as possible. The FEM package, MSC Nastran, is used in the structural design framework in [75].

Other improvements to the rotor design framework would include the addition of more variables for the aerodynamic shape and structural sizing. For example, variables defining the airfoil shapes, sweep and pre-bend can be included for the aerodynamic design. For the structural sizing, the blade span-wise thicknesses of the outer shell and webs can be added as variables. The complete set of DLCs and fatigue damage calculations can be included to ensure the feasibility of the blade design. Sub-level optimizations to maximize the performance of the controller should be added as well.

# Bibliography


[1] Sessarego M, Ramos-García N, Shen W. Development of a fast fluid-structure coupling technique for wind turbine computations. *Journal of Power and Energy Engineering* 2015; **3**:1–6, doi:10.4236/jpee.2015.37001.

[2] Sessarego M, Ramos-García N, Sørensen JN, Shen WZ. Development of an aeroelastic code based on three-dimensional viscous-inviscid method for wind turbine computations. *Wind Energy* 2017; doi:10.1002/we.2085. URL `http://dx.doi.org/10.1002/we.2085`, we.2085.

[3] Sessarego M, Ramos-García N, Yang H, Shen WZ. Aerodynamic wind-turbine rotor design using surrogate modeling and three-dimensional viscous-inviscid interaction technique. *Renewable Energy* 2016; **93**:620 – 635, doi:http://dx.doi.org/10.1016/j.renene.2016.03.027. URL `http://www.sciencedirect.com/science/article/pii/S0960148116302117`.

[4] Sessarego M, Shen WZ. Development of a simple structural design method for large wind turbine blades. 12th EAWE PhD Seminar on Wind Energy in Europe, 25-27 May 2016: DTU Lyngby, Denmark, 2015.

[5] Sessarego M, Ramos-García N, Shen WZ, Sørensen JN. Large wind turbine rotor design using an aero-elastic / free-wake panel coupling code. *Journal of Physics: Conference Series* 2016; **753**(4):042 017. URL `http://stacks.iop.org/1742-6596/753/i=4/a=042017`.

[6] International Energy Agency. *World Energy Outlook* 2015.

[7] International Energy Agency. *Key World Energy Statistics* 2015.

[8] Shafiee S, Topal E. When will fossil fuel reserves be diminished? *Energy Policy* 2009; **37**(1):181 – 189, doi:http://dx.doi.org/10.1016/j.enpol.2008.08.016. URL `http://www.sciencedirect.com/science/article/pii/S0301421508004126`.

[9] Kyoto Protocol. URL `http://unfccc.int/kyoto_protocol/items/2830.php`, retrieved August, 2016.

[10] COP21: United Nations conference on climate change. URL `http://www.cop21.gouv.fr/en/`, retrieved August, 2016.

[11] Global Wind Energy Council. *Wind & Climate Change* 2012.

[12] Global Wind Energy Council. *Global Wind Report: Annual Market Update* 2015.

[13] Technology roadmap: Wind energy 2013. URL `https://www.iea.org/publications/freepublications/publication/Wind_2013_Roadmap.pdf`.

[14] Bungartz HJ, Mehl M, Schäfer M. *Fluid Structure Interaction II: Modelling, Simulation, Optimization*, *1439-7358*, vol. 73. Springer Berlin Heidelberg, 2010, doi:10.1007/978-3-642-14206-2.

[15] Ross MR, Sprague MA, Felippa CA, Park K. Treatment of acoustic fluid-structure interaction by localized lagrange multipliers and comparison to alternative interface-coupling methods. *Computer Methods in Applied Mechanics and Engineering* 2009; **198**(912):986 – 1005, doi:http://dx.doi.org/10.1016/j.cma.2008.11.006. URL `http://www.sciencedirect.com/science/article/pii/S0045782508004076`.

[16] Takizawa K, Fritze M, Montes D, Spielman T, Tezduyar T. Fluid-structure interaction modeling of ringsail parachutes with disreefing and modified geometric porosity. *Computational Mechanics* 2012; **50**(6):835–854, doi:10.1007/s00466-012-0761-3. URL `http://dx.doi.org/10.1007/s00466-012-0761-3`.

[17] Dumont K, Vierendeels J, Kaminsky R, van Nooten G, Verdonck P, Bluestein D. Comparison of the hemodynamic and thrombogenic performance of two bileaflet mechanical heart valves using a CFD/FSI model. *Journal of Biomechanical Engineering* Jan 2007; **129**(4):558–565, doi:10.1115/1.2746378. URL `http://dx.doi.org/10.1115/1.2746378`.

[18] Wang C, Tay Z. Hydroelastic analysis and response of pontoon-type very large floating structures. *Fluid Structure Interaction II*, *Lecture Notes in Computational Science and Engineering*, vol. 73, Bungartz HJ, Mehl M, Schäfer M (eds.). Springer Berlin Heidelberg, 2010; 103–130, doi:10.1007/978-3-642-14206-2_5. URL `http://dx.doi.org/10.1007/978-3-642-14206-2_5`.

[19] Bazilevs Y, Hsu MC, Kiendl J, Wüchner R, Bletzinger KU. 3D simulation of wind turbine rotors at full scale. Part II: Fluid-structure interaction modeling with composite blades. *International Journal for Numerical Methods in Fluids* 2011; **65**(1-3):236–253, doi:10.1002/fld.2454. URL `http://dx.doi.org/10.1002/fld.2454`.

[20] Hsu MC, Bazilevs Y. Fluid-structure interaction modeling of wind turbines: simulating the full machine. *Computational Mechanics* 2012; **50**(6):821–833, doi:10.1007/s00466-012-0772-0. URL `http://dx.doi.org/10.1007/s00466-012-0772-0`.

[21] Kim H, Lee S, Son E, Lee S, Lee S. Aerodynamic noise analysis of large horizontal axis wind turbines considering fluid-structure interaction. *Renewable Energy* 2012; **42**(0):46 – 53, doi:http://dx.doi.org/10.1016/j.renene.2011.09.019. URL `http://www.sciencedirect.com/science/article/pii/S0960148111005374`, International Symposium on Low Carbon and Renewable Energy Technology 2010 (ISLCT 2010).

[22] Yu DO, Kwon OJ. Time-accurate aeroelastic simulations of a wind turbine in yaw and shear using a coupled CFD-CSD method. *Journal of Physics: Conference Series* 2014; **524**(1):012 046. URL `http://stacks.iop.org/1742-6596/524/i=1/a=012046`.

[23] Yu DO, Kwon OJ. A coupled CFD-CSD method for predicting HAWT rotor blade performance. *Aerospace Sciences Meetings*. American Institute of Aeronautics and Astronautics, 2013; –, doi:10.2514/6.2013-911. URL `http://dx.doi.org/10.2514/6.2013-911`.

[24] Joachim Christian Heinz. Partitioned Fluid-Structure Interaction for Full Rotor Simulations Using CFD. PhD Thesis, Technical University of Denmark 2013.

[25] Øye S. FLEX4 simulation of wind turbine dynamics. *Proceedings of 28th IEA Meeting of Experts Concerning State of the Art of Aeroelastic Codes for Wind Turbine Calculations*, International Energy Agency: Lyngby, 1996; 71–76.

[26] Jonkman JM, Buhl ML. *FAST User's Guide*. National Renewable Energy Laboratory, Golden, Colorado. August 2005. NREL/EL-500-29798.

[27] Kim T, Hansen AM, Branner K. Development of an anisotropic beam finite element for composite wind turbine blades in multibody system. *Renewable Energy* 2013; **59**:172 – 183, doi:http://dx.doi.org/10.1016/j.renene.2013.03.033. URL `http://www.sciencedirect.com/science/article/pii/S0960148113001894`.

[28] Rubak R, Petersen JT. Monopile as part of aeroelastic wind turbine simulation code. *Proceedings of Copenhagen Offshore Wind 2005, October 26-28, 2005*, 2005.

[29] Bossanyi E. *GH Bladed Theory Manual*. Garrad Hassan and Partners Ltd., Bristol, England 2003.

[30] Zhu WJ, Shen WZ, Sørensen JN. Integrated airfoil and blade design method for large wind turbines. *Renewable Energy* 2014; **70**(0):172 – 183, doi:http://dx.doi.org/10.1016/j.renene.2014.02.057. URL `http://www.sciencedirect.com/science/article/pii/S0960148114001827`, Special issue on aerodynamics of offshore wind energy systems and wakes.

[31] Riziotis VA, Manolas DI, Voutsinas SG. Advanced aeroelastic modeling of swept rotor blades. European Wind Energy Conference and Exhibition 2011: Brussels, Belgium, 2011.

[32] Gebhardt C, Roccia B. Non-linear aeroelasticity: An approach to compute the response of three-blade large-scale horizontal-axis wind turbines. *Renewable Energy* 2014; **66**:495 – 514, doi:http://dx.doi.org/10.1016/j.renene.2013.12.040. URL `http://www.sciencedirect.com/science/article/pii/S0960148114000111`.

[33] Branlard E, Papadakis G, Gaunaa M, Winckelmans G, Larsen TJ. Aeroelastic large eddy simulations using vortex methods: unfrozen turbulent and sheared inflow. *Journal of Physics: Conference Series* 2015; **625**(1):012 019. URL `http://stacks.iop.org/1742-6596/625/i=1/a=012019`.

[34] Schepers G. Advanced aerodynamic tools for large rotors. Retrieved August, 2016. URL `http://www.eera-avatar.eu/`.

[35] Hansen MOL. *Aerodynamics of wind turbines*. 2 edn., Earthscan: London, 2008.

[36] van Garrel A. Development of a wind turbine aerodynamics simulation module. *Technical Report ECN-C–03-079*, Energy research Centre of the Netherlands, August 2003.

[37] Hansen M, Sørensen J, Voutsinas S, Sørensen N, Madsen H. State of the art in wind turbine aerodynamics and aeroelasticity. *Progress in Aerospace Sciences* 2006; **42**(4):285 – 330, doi:http://dx.doi.org/10.1016/j.paerosci.2006.10.002. URL `http://www.sciencedirect.com/science/article/pii/S0376042106000649`.

[38] Bauchau OA, Craig JI. *Structural Analysis: With Applications to Aerospace Structures*, *Solid Mechanics and Its Applications*, vol. 163. Springer Netherlands, 2009, doi:10.1007/978-90-481-2516-6.

[39] Modelling techniques (finite element method) part 1. Retrieved October, 2016. URL `http://what-when-how.com/the-finite-element-method/modelling-techniques-finite-element-method-part-1/`.

[40] Bennett J. The effect of mass and web spacing on the loads and structural response of increasing wind turbine blade size. Master's Thesis, KTH Industrial Engineering and Management, September 2012.

[41] Degroote J, Bathe KJ, Vierendeels J. Performance of a new partitioned procedure versus a monolithic procedure in fluid-structure interaction. *Computers & Structures* 2009; **87**(11-12):793 – 801, doi:http://dx.doi.org/10.1016/j.compstruc.2008.11.013. URL `http://www.sciencedirect.com/science/article/pii/S0045794908002605`, Fifth MIT Conference on Computational Fluid and Solid Mechanics.

[42] Krenk S. *Non-linear Modeling and Analysis of Solids and Structures*. Cambridge University Press, 2009.

[43] Idelsohn SR, Del Pin F, Rossi R, Oñate E. Fluid-structure interaction problems with strong added-mass effect. *International Journal for Numerical Methods in Engineering* 2009; **80**(10):1261–1294, doi:10.1002/nme.2659. URL `http://dx.doi.org/10.1002/nme.2659`.

[44] Farhat C, van der Zee KG, Geuzaine P. Provably second-order time-accurate loosely-coupled solution algorithms for transient nonlinear computational aeroelasticity. *Computer Methods in Applied Mechanics and Engineering* 2006; **195**:1973 – 2001, doi:http://dx.doi.org/10.1016/j.cma.2004.11.031. URL `http://www.sciencedirect.com/science/article/pii/S0045782505001945`.

[45] Gear C, Wells D. Multirate linear multistep methods. *BIT Numerical Mathematics* 1984; **24**(4):484–502, doi:10.1007/BF01934907. URL `http://dx.doi.org/10.1007/BF01934907`.

[46] Boorsma K, Hartvelt M, Orsi L. Application of the lifting line vortex wake method to dynamic load case simulations. *Journal of Physics: Conference Series* 2016; **753**(2):022 030. URL `http://stacks.iop.org/1742-6596/753/i=2/a=022030`.

[47] Bazilevs Y, Hsu MC, Akkerman I, Wright S, Takizawa K, Henicke B, Spielman T, Tezduyar TE. 3D simulation of wind turbine rotors at full scale. Part I: Geometry modeling and aerodynamics. *International Journal for Numerical Methods in Fluids* 2011; **65**(1-3):207–235, doi:10.1002/fld.2400. URL `http://dx.doi.org/10.1002/fld.2400`.

[48] Branlard E, Machefaux E, Gaunaa M, Sørensen H, Troldborg N. *Validation of vortex code viscous models using lidar wake measurements and CFD*. European Wind Energy Association (EWEA), 2014.

[49] The Knowledge Centre Wind turbine Materials and Constructions (WMC). FOCUS6. Retrieved October, 2016. URL `http://www.wmc.eu/focus6.php`.

[50] Sørensen JN, Mikkelsen RF, Henningson DS, Ivanell S, Sarmast S, Andersen SJ. Simulation of wind turbine wakes using the actuator line technique. *Philosophical Transactions of the Royal Society of London A: Mathematical, Physical and Engineering Sciences* Jan 2015; **373**(2035):–. URL `http://rsta.royalsocietypublishing.org/content/373/2035/20140071.abstract`.

[51] Saverin J, Peukert J, Marten D, Pechlivanoglou G, Paschereit CO, Greenblatt D. Aeroelastic simulation of multi-MW wind turbines using a free vortex model coupled to a geometrically exact beam model. *Journal of Physics: Conference Series* 2016; **753**(8):082 015. URL `http://stacks.iop.org/1742-6596/753/i=8/a=082015`.

[52] Hodges DH, Yu W. A rigorous, engineer-friendly approach for modelling realistic, composite rotor blades. *Wind Energy* 2007; **10**(2):179–193, doi:10.1002/we.215. URL `http://dx.doi.org/10.1002/we.215`.

[53] Yu D, Kwon H, Kwon OJ. Performance enhancement of HAWT rotor blades by aerodynamic shape optimization. *Aerospace Sciences Meetings*. American Institute of Aeronautics and Astronautics, 2012; –, doi:10.2514/6.2012-1292. URL `http://dx.doi.org/10.2514/6.2012-1292`.

[54] Andersen S, Sørensen J, Shen W, Mikkelsen R. Simulation and prediction of wakes and wake interaction in wind farms. PhD Thesis 2014.

[55] Wang Q, Johnson N, Sprague MA, Jonkman JM. BeamDyn: A high-fidelity wind turbine blade solver in the FAST modular framework. *AIAA SciTech*. American Institute of Aeronautics and Astronautics, 2015; –, doi:10.2514/6.2015-1465. URL `http://dx.doi.org/10.2514/6.2015-1465`.

[56] Bak C, Zahle F, Bitsche R, Kim T, Yde A, Henriksen LC, Natarajan A, Hansen MH. Description of the DTU 10 MW reference wind turbine. *Technical Report I-0092*, DTU Wind Energy, July 2013.

[57] Braaten ME, Gopinath A. Aero-structural analysis of wind turbine blades with sweep and winglets: Coupling a vortex line method to ADAMS/AeroDyn. GT2011-45904, Proceedings of ASME Turbo Expo 2011, 2011.

[58] Wilson RE, Lissaman PBS. *Applied aerodynamics of wind power machines*. Oregon State University: Corvallis, 1974.

[59] Burton T, Jenkins N, Sharpe D, Bossanyi E. *Wind Energy Handbook*. 2nd edn., Wiley, 2011.

[60] Bottasso C, Campagnolo F, Croce A. Multi-disciplinary constrained optimization of wind turbines. *Multibody System Dynamics* 2012; **27**(1):21–53, doi:10.1007/s11044-011-9271-x. URL `http://dx.doi.org/10.1007/s11044-011-9271-x`.

[61] Ashuri T, Zaaijer M, Martins J, van Bussel G, van Kuik G. Multidisciplinary design optimization of offshore wind turbines for minimum levelized cost of energy. *Renewable Energy* March 2014; **68**:893–905, doi:10.1016/j.renene.2014.02.045. URL `http://linkinghub.elsevier.com/retrieve/pii/S0960148114001360`.

[62] Chattot JJ. Optimization of wind turbines using helicoidal vortex model. *Journal of Solar Energy Engineering* Nov 2003; **125**(4):418–424, doi:10.1115/1.1621675. URL `http://dx.doi.org/10.1115/1.1621675`.

[63] Wijnen M, Chattot JJ. Multi-point optimization of wind turbine blades using helicoidal vortex model. *Computational Fluid Dynamics 2010*, Kuzmin A (ed.). Springer Berlin Heidelberg, 2011; 235–240, doi:10.1007/978-3-642-17884-9_28. URL `http://dx.doi.org/10.1007/978-3-642-17884-9_28`.

[64] Johansen J, Sørensen NN. Aerodynamic investigation of winglets on wind turbine blades using CFD. *Technical Report Risø-R-1543(EN)*, Risø National Laboratory, Roskilde, Denmark, February 2006.

[65] Lee KH, Kim KH, Lee DH, Lee KT, Park JP. Two-step optimization for wind turbine blade with probability approach. *Journal of Solar Energy Engineering* June 2010; **132**(3):034 503–034 503, doi:10.1115/1.4001671. URL `http://dx.doi.org/10.1115/1.4001671`.

[66] Bourguet R, Martinat G, Harran G, Braza M. Aerodynamic multi-criteria shape optimization of VAWT blade profile by viscous approach. *Wind Energy*, Peinke J, Schaumann P, Barth S (eds.). Springer Berlin Heidelberg, 2007; 215–219, doi:10.1007/978-3-540-33866-6_39. URL `http://dx.doi.org/10.1007/978-3-540-33866-6_39`.

[67] Sun H. Wind turbine airfoil design using response surface method. *Journal of Mechanical Science and Technology* 2011; **25**(5):1335–1340, doi:10.1007/s12206-011-0310-6. URL `http://dx.doi.org/10.1007/s12206-011-0310-6`.

[68] Han Z, Zhang K, Song W, Liu J. Surrogate-based aerodynamic shape optimization with application to wind turbine airfoils. *Aerospace Sciences Meetings*. American Institute of Aeronautics and Astronautics, 2013; –, doi:10.2514/6.2013-1108. URL `http://dx.doi.org/10.2514/6.2013-1108`.

[69] Ribeiro A, Awruch A, Gomes H. An airfoil optimization technique for wind turbines. *Applied Mathematical Modelling* 2012; **36**(10):4898 – 4907, doi:http://dx.doi.org/10.1016/j.apm.2011.12.026. URL `http://www.sciencedirect.com/science/article/pii/S0307904X11008146`.

[70] Ning A, Damiani R, Moriarty PJ. Objectives and constraints for wind turbine optimization. *Journal of Solar Energy Engineering* June 2014; **136**(4):041 010–041 010, doi:10.1115/1.4027693. URL `http://dx.doi.org/10.1115/1.4027693`.

[71] Bir GS. *User's Guide to PreComp: Pre-Processor for Computing Composite Blade Properties*. National Renewable Energy Laboratory, 1617 Cole Blvd, Golden, CO 80401, September 2005. URL `https://nwtc.nrel.gov/PreComp`.

[72] Bir GS. *User's Guide to BModes: Software for Computing Rotating Beam Coupled Modes*. National Renewable Energy Laboratory, 1617 Cole Blvd, Golden, CO 80401, September 2007. URL `https://nwtc.nrel.gov/BModes`.

[73] Sale DC. *User's Guide to Co-Blade: Software for Structural Analysis of Composite Blades*. Northwest National Marine Renewable Energy Center, Department of Mechanical Engineering, University of Washington, Seattle, WA, September 2012.

[74] Hu W, Park D, Choi D. Structural optimization procedure of a composite wind turbine blade for reducing both material cost and blade weight. *Engineering Optimization* 2013; **45**(12):1469–1487, doi:10.1080/0305215X.2012.743533. URL `http://dx.doi.org/10.1080/0305215X.2012.743533`.

[75] Bottasso CL, Campagnolo F, Croce A, Dilli S, Gualdoni F, Nielsen MB. Structural optimization of wind turbine rotor blades by multilevel sectional/multibody/3D-FEM analysis. *Multibody System Dynamics* 2014; **32**(1):87–116, doi:10.1007/s11044-013-9394-3. URL `http://dx.doi.org/10.1007/s11044-013-9394-3`.

[76] Blasques JP, Stolpe M. Multi-material topology optimization of laminated composite beam cross sections. *Composite Structures* 2012; **94**(11):3278 – 3289, doi:http://dx.doi.org/10.1016/j.compstruct.2012.05.002. URL `http://www.sciencedirect.com/science/article/pii/S0263822312002085`.

[77] Yu W, Hodges DH, Ho JC. Variational asymptotic beam sectional analysis - an updated version. *International Journal of Engineering Science* 2012; **59**:40 – 64, doi:http://dx.doi.org/10.1016/j.ijengsci.2012.03.006. URL `http://www.sciencedirect.com/science/article/pii/S0020722512000493`, the Special Issue in honor of Victor L. Berdichevsky.

[78] Chehouri A, Younes R, Ilinca A, Perron J. Review of performance optimization techniques applied to wind turbines. *Applied Energy* 2015; **142**(0):361 – 388, doi:http://dx.doi.org/10.1016/j.apenergy.2014.12.043. URL `http://www.sciencedirect.com/science/article/pii/S0306261914013002`.

[79] Xudong W, Shen WZ, Zhu WJ, Sørensen JN, Jin C. Shape optimization of wind turbine blades. *Wind Energy* 2009; **12**(8):781–803.

[80] Schepers JG, Snel H. Model experiment in controlled conditions. *Technical Report ECN Final Report ECN-E-07-042*, Energy research Centre of the Netherlands February 2007.

[81] Fuglsang P, Madsen H. Optimization method for wind turbine rotors. *Journal of Wind Engineering and Industrial Aerodynamics* 1999; **80**(12):191 – 206, doi:http://dx.doi.org/10.1016/S0167-6105(98)00191-3. URL `http://www.sciencedirect.com/science/article/pii/S0167610598001913`.

[82] Maki K, Sbragio R, Vlahopoulos N. System design of a wind turbine using a multi-level optimization approach. *Renewable Energy* 2012; **43**(0):101 – 110, doi:http://dx.doi.org/10.1016/j.renene.2011.11.027. URL `http://www.sciencedirect.com/science/article/pii/S096014811100629X`.

[83] Ning A, Damiani R, Moriarty P. Objectives and constraints for wind turbine optimization. *Aerospace Sciences Meetings*. American Institute of Aeronautics and Astronautics, 2013; –, doi:10.2514/6.2013-201. URL `http://dx.doi.org/10.2514/6.2013-201`.

[84] Fingerish L, Hand M, Laxson A. Wind turbine design cost and scaling model. *Technical Report NREL/TP-500-40566*, National Renewable Energy Laboratory, 1617 Cole Blvd, Golden, CO 80401, December 2006, doi:10.2172/947422.

[85] Bottasso CL, Croce A, Sartori L, Grasso F. Free-form design of rotor blades. *Journal of Physics: Conference Series* 2014; **524**(1):012 041. URL `http://stacks.iop.org/1742-6596/524/i=1/a=012041`.

[86] Sessarego M, Dixon K, Rival D, Wood D. A hybrid multi-objective evolutionary algorithm for wind-turbine blade optimization. *Engineering Optimization* August 2014; :1–20doi:10.1080/0305215X.2014.941532. URL `http://dx.doi.org/10.1080/0305215X.2014.941532`.

[87] Sessarego M, Wood D. Multi-dimensional optimization of small wind turbine blades. *Renewables: Wind, Water, and Solar* 2015; **2**(1):9, doi:10.1186/s40807-015-0009-x. URL `http://dx.doi.org/10.1186/s40807-015-0009-x`.

[88] Zahle F, Tibaldi C, Pavese C, McWilliam MK, Blasques JPAA, Hansen MH. Design of an aeroelastically tailored 10 MW wind turbine rotor. *Journal of Physics: Conference Series* 2016; **753**(6):062 008. URL `http://stacks.iop.org/1742-6596/753/i=6/a=062008`.

[89] Lars Christian Henriksen CT, Bergami L. *HAWCStab2 User Manual*. DTU Wind Energy, Technical University of Denmark, Frederiksborgvej 399 4000 Roskilde, Denmark, September 2015.

[90] OpenMDAO. Retrieved October, 2016. URL `http://openmdao.org`.

[91] Wächter A, Biegler TL. On the implementation of an interior-point filter line-search algorithm for large-scale nonlinear programming. *Mathematical Programming* 2006; **106**(1):25–57, doi:10.1007/s10107-004-0559-y. URL `http://dx.doi.org/10.1007/s10107-004-0559-y`.

[92] Forrester AIJ, Sóbester A, Keane AJ. *Engineering Design via Surrogate Modelling: A Practical Guide*. John Wiley & Sons, Ltd, 2008, doi:10.1002/9780470770801. URL `http://dx.doi.org/10.1002/9780470770801`.

[93] Ramos-García N, Sørensen JN, Shen WZ. A strong viscous-inviscid interaction model for rotating airfoils. *Wind Energy* 2014; **17**(12):1957–1984, doi:10.1002/we.1677. URL `http://dx.doi.org/10.1002/we.1677`.

[94] Drela M. XFOIL: An analysis and design system for low reynolds number airfoils. *Low Reynolds Number Aerodynamics. Springer-Verlag Lec. Notes in Eng. 54*. 1989; .

[95] Timmer WA, van Rooij RPJOM. Summary of the Delft University wind turbine dedicated airfoils. *Journal of Solar Energy Engineering* November 2003; **125**(4):488–496, doi:10.1115/1.1626129. URL `http://dx.doi.org/10.1115/1.1626129`.

[96] Lighthill MJ. On displacement thickness. *Journal of Fluid Mechanics* 1958; **4**, doi:10.1017/S0022112058000525.

[97] Ramos-García N, Sørensen JN, Shen WZ. Three-dimensional viscous-inviscid coupling method for wind turbine computations. *Wind Energy* 2016; **19**(1):67–93, doi:10.1002/we.1821. URL `http://dx.doi.org/10.1002/we.1821`.

[98] Ramos-García N, Sørensen JN, Shen WZ. Simulations of the yawed MEXICO rotor using a viscous-inviscid panel method. *Journal of Physics: Conference Series* 2014; **524**(1):012 026. URL http://stacks.iop.org/1742-6596/524/i=1/a=012026.

[99] Ramos-García N, Sørensen JN, Shen WZ. Validation of a three-dimensional viscous-inviscid interactive solver for wind turbine rotors. *Renewable Energy* 2014; **70**(0):78 – 92, doi:http://dx.doi.org/10.1016/j.renene.2014.04.001. URL http://www.sciencedirect.com/science/article/pii/S096014811400247X, Special issue on aerodynamics of offshore wind energy systems and wakes.

[100] Katz J, Plotkin A. *Low-Speed Aerodynamics*. Second edn., Cambridge University Press, 2001. URL http://dx.doi.org/10.1017/CBO9780511810329, Cambridge Books Online.

[101] Leishman JG, Bhagwat MJ, Bagai A. Free-vortex filament methods for the analysis of helicopter rotor wakes. *Journal of Aircraft* Sep 2002; **39**(5):759–775, doi:10.2514/2.3022. URL http://arc.aiaa.org/doi/abs/10.2514/2.3022.

[102] Scully M. Computation of helicopter rotor wake geometry and its influence on rotor harmonic airloads. PhD Thesis, Massachusetts Institute of Technology. Dept. of Aeronautics and Astronautics. February 1975.

[103] Squire H. The growth of a vortex in turbulent flow. *Aeronautical Quarterly* 1965; **16**:302–306.

[104] Bhagwat MJ, Leishman JG. Technical note: Accuracy of straight-line segmentation applied to curvilinear vortex filaments. *Journal of the American Helicopter Society* 2001-04-01T00:00:00; **46**(2):166–169, doi:doi:10.4050/JAHS.46.166. URL http://www.ingentaconnect.com/content/ahs/jahs/2001/00000046/00000002/art00008.

[105] Ramos-García N, Sørensen JN, Shen WZ. Hybrid wake model for free vortex viscous-inviscid simulations. *Proceedings of the World Renewable Energy Congress XIII* 2014; .

[106] Ramos-García N, Mølholm Hejlesen M, Sørensen JN, Walther JH. Hybrid vortex simulations of wind turbines using a three-dimensional viscous-inviscid panel method. *Submitted to Wind Energy* 2016; .

[107] Hejlesen MM, Rasmussen JT, Chatelain P, Walther JH. A high order solver for the unbounded poisson equation. *Journal of Computational Physics* 2013; **252**:458 – 467, doi:http://dx.doi.org/10.1016/j.jcp.2013.05.050. URL http://www.sciencedirect.com/science/article/pii/S0021999113004324.

[108] Walther JH, Hejlesen MM, Rasmussen JT, Chatelain P, Walther JH. IUTAM symposium on particle methods in fluid dynamics: High order poisson solver for unbounded flows. *Procedia IUTAM* 2015; **18**:56 – 65, doi:http://dx.doi.org/10.1016/j.piutam.2015.11.006. URL http://www.sciencedirect.com/science/article/pii/S2210983815002758.

[109] Schepers JG, Snel H. Dynamic inflow: Yawed conditions and partial span pitch control. *Technical Report*, ECN-C- -95-056, Petten, The Netherlands 1995.

[110] Snel H, Schepers JG. Joint investigation of dynamic inflow effects and implementation of an engineering method. *Technical Report*, ECN-C- -94-107, Petten, The Netherlands 1995.

[111] Øye S. Dynamic stall, simulated as a time lag of separation. *Proceedings of the 4th IEA Symposium on the Aerodynamics of Wind Turbines*, McAnulty KF (ed.), ETSU-N-118: Harwell Laboratory, Harwell, UK, 1991.

[112] Hau E, Von Renouard H. *Wind Turbines: Fundamentals, Technologies, Application, Economics*. 2 edn., Springer, 2006.

[113] Jonkman J. Modeling of the UAE wind turbine for refinement of FAST_AD. *Technical Report NREL/TP-500-34755*, National Renewable Energy Laboratory, Golden, Colorado 80401-3393, December 2003.

[114] Wilson R, Walker S, Heh P. *Technical and User's Manual for the FAST_AD Advanced Dynamics Code*. Oregon State University, Corvallis, Oregon 97331-6001, OSU/NREL report 99-01 edn. May 1999.

[115] Sessarego M. A hybrid multi-objective evolutionary algorithm for wind-turbine blade optimization. Master's Thesis, University of Calgary, April 2013.

[116] Jonkman J, Butterfield S, Musial W, Scott G. Definition of a 5-MW reference wind turbine for offshore system development. *Technical Report NREL/TP-500-38060*, National Renewable Energy Laboratory, 1617 Cole Blvd, Golden, CO 80401 February 2009, doi:10.2172/947422.

[117] Heinz J, Sørensen N, Zahle F. Partitioned fluid-structure interaction for full rotor computations using CFD. PhD Thesis 2013.

[118] Laino DJ, Hansen AC. *User's Guide to the Computer Software Routines AeroDyn Interface for ADAMS*. Windward Engineering, LC, Salt Lake City, UT 84117. September 2001.

[119] Wang Q, Sprague MA, Jonkman JM. Partitioned nonlinear structural analysis of wind turbines using BeamDyn. *AIAA SciTech*. American Institute of Aeronautics and Astronautics, 2016; –, doi:10.2514/6.2016-0753. URL `http://dx.doi.org/10.2514/6.2016-0753`.

[120] Buhl ML. NWTC Information Portal (Modes). URL `https://nwtc.nrel.gov/Modes`, last modified 28-September-2014 ; Accessed 24-November-2015.

[121] Du Z, Selig M. A 3-D stall-delay model for horizontal axis wind turbine performance prediction. *Aerospace Sciences Meetings*. American Institute of Aeronautics and Astronautics, 1998; –, doi:10.2514/6.1998-21. URL `http://dx.doi.org/10.2514/6.1998-21`.

[122] Jonkman J, Musial W. Offshore code comparison collaboration (OC3) for IEA task 23 offshore wind technology and deployment. *Technical Report NREL/TP-5000-48191*, National Renewable Energy Laboratory, 1617 Cole Boulevard, Golden, Colorado 80401 December 2010.

[123] *Wine HQ*. URL `https://www.winehq.org`.

[124] The MathWorks Inc., Natick, MA. *MATLAB 2014b*.

[125] Selig MS, Tangler JL. Development and application of a multipoint inverse design method for horizontal axis wind turbines. *Wind Engineering* 1995; **19**(2).

[126] Bak C. Aerodynamic design of wind turbine rotors. *Technical Report I-3202(EN)*, Risø DTU: National Laboratory for Sustainable Energy, September 2011.

[127] Lee S. Inverse design of horizontal axis wind turbine blades using a vortex line method. *Wind Energy* 2015; **18**(2):253–266, doi:10.1002/we.1695. URL `http://dx.doi.org/10.1002/we.1695`.

[128] Tangler J, Kocurek JD. Wind turbine post-stall airfoil performance characteristics guidelines for blade-element momentum methods. *43rd AIAA Aerospace Sciences Meeting and Exhibit* 10-13 January 2005; .

[129] Piegl L, Tiller W. *The NURBS Book (2nd Ed.)*. Springer-Verlag New York, Inc.: New York, NY, USA, 1997.

[130] Resor BR. Definition of a 5MW / 61.5m wind turbine blade reference model. *Technical Report SAND2013-2569*, Sandia National Laboratories, Albuquerque, New Mexico 87185 and Livermore, California 94550, April 2013.

[131] Griffith DT, Ashwill TD. The Sandia 100-meter all-glass baseline wind turbine blade: SNL100-00. *Technical Report SAND2011-3779*, Sandia National Laboratories, Albuquerque, New Mexico 87185 and Livermore, California 94550, June 2011.

[132] Bitsche RD. Structural design and analysis of wind turbine rotor blades. *Lecture Notes*. DTU Wind Energy, 2014.

[133] Kassapoglou C. *Buckling of Composite Plates*. John Wiley & Sons, Ltd, 2010; 119–144, doi:10.1002/9780470972700.ch6. URL `http://dx.doi.org/10.1002/9780470972700.ch6`.

[134] Robert D Bitsche JPB, Stolpe M. *Notes from Course 46415: Structural Analysis and Design Optimization of Wind Turbine Blades*. Department of Wind Energy, Technical University of Denmark,, Lyngby, Denmark June 2015.

[135] Hansen M, Hansen AD, Larsen TJ, Øye S, Sørensen P, Fuglsang P. Control design for a pitch-regulated, variable speed wind turbine. *Technical Report Ris-R-1500(EN)*, Risø National Laboratory, P.O.Box 49, DK-4000 Roskilde, Denmark, January 2005. URL `http://www.ieawind.org/task_23/Subtask_2S_docs/Meeting%2004_Roskilde%20II/ris-r-1500.pdf`.

[136] *International Standard IEC 61400-1: Wind turbine - Part 1: Design requirements*. Third edn., IEC 61400-1:2005(E), International Electrotechnical Commission, 2005. URL `https://webstore.iec.ch/publication/5426`.

[137] The MathWorks Inc., Natick, MA. *MATLAB 2015b*.

[138] Tibaldi C, Hansen MH, Henriksen LC. Optimal tuning for a classical wind turbine controller. *Journal of Physics: Conference Series* 2014; **555**(1):012 099. URL `http://stacks.iop.org/1742-6596/555/i=1/a=012099`.

[139] Meng Gao JN, Wu X. Normal and extreme wind conditions for power at coastal locations in China. *PLoS ONE* August 2015; **10**(8), doi:10.1371/journal.pone.0136876.

[140] Silva J, Ribeiro C, Guedes R. Roughness length classification of corine land cover classes. *European Wind Energy Conference & Exhibition (EWEC) 2007*, MEGAJOULE Consultants: Rua Eng. Frederico Ulrich, 2650, 4470-605 Maia, Portugal, 2007. URL `http://www.megajoule.pt/img_upload/Publications/545_Ewec2007fullpaper1.pdf`.

[141] Hayman GJ, M Buhl J. *MLife User's Guide for Version 1.00*. National Renewable Energy Laboratory, 1617 Cole Blvd, Golden, CO 80401 October 2012. URL `https://nwtc.nrel.gov/MLife`.

[142] Hayman GJ. *MLife Theory Manual for Version 1.00*. National Renewable Energy Laboratory, 1617 Cole Blvd, Golden, CO 80401 October 2012. URL `https://nwtc.nrel.gov/MLife`.

[143] Hayman GJ. *MExtremes Manual Version 1.00*. National Renewable Energy Laboratory, 1617 Cole Blvd, Golden, CO 80401 September 2015. URL `https://nwtc.nrel.gov/MExtremes`.

[144] Bottasso CL, Bortolotti P, Croce A, Gualdoni F. Integrated aero-structural optimization of wind turbines. *Multibody System Dynamics* 2015; :1–28doi:10.1007/s11044-015-9488-1. URL `http://dx.doi.org/10.1007/s11044-015-9488-1`.

[145] Bortolotti P, Bottasso CL, Croce A. Combined preliminary–detailed design of wind turbines. *Wind Energy Science* 2016; **1**(1):71–88, doi:10.5194/wes-1-71-2016. URL `http://www.wind-energ-sci.net/1/71/2016/`.

[146] Sartori L, Bortolotti P, Croce A, Bottasso CL. Integration of prebend optimization in a holistic wind turbine design tool. *Journal of Physics: Conference Series* 2016; **753**(6):062 006. URL `http://stacks.iop.org/1742-6596/753/i=6/a=062006`.

[147] AnalySwift. URL `http://analyswift.com/`.

[148] Dassault Systèmes Simulia Corp. *Abaqus/CAE User's Guide*. Providence, RI, USA.

[149] Gustafson G. *Differential Equations and Linear Algebra*. unpublished, Retrieved September, 2016. URL `http://www.math.utah.edu/~gustafso/`.

# Appendix A

# Multi-rate Approach Example

Multi-rate methods [45] are designed to solve systems of ordinary differential equations (ODEs) consisting of subsystems with different timescales. The purpose of multi-rate methods are to reduce the integration time by using larger step-sizes for the variables in a system that behave slowly compared to the system with fast variables. Multi-rate methods could be classified in the partitioned approach category, since each of the systems can have their own distinct solver. However, the coupling approach differs to loose- and strong-coupling in that an interpolation step is required to transfer information from the system with the larger time-step to the system with the smaller and faster time-step. When the time-step in a multi-rate approach is set to be the same for all systems, then the multi-rate solver will behave similarly to loose-coupling since the interpolation step is no longer needed. An example will be used to illustrate the methodology. Figure A.1

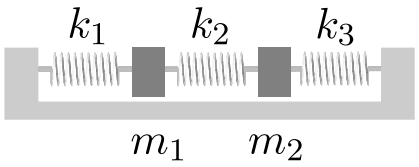


**Figure A.1:** Coupled mass-spring system. Image modified from [149].

depicts a coupled mass-spring system with two degrees of freedom. The two DOFs are the horizontal displacements $x_1(t)$ and $x_2(t)$ of each of the two masses $m_1$ and $m_2$. Both masses are connected by springs $k_1$, $k_2$ and $k_3$ and slide along a frictionless horizontal surface. Further assumptions are as follows:

1. The masses are assumed to be point masses concentrated at their center of gravity.
2. The displacements of the masses $x_1(t)$ and $x_2(t)$ are measured from their equilibrium positions where positive is towards the right and negative is towards the left.
3. The mass of each spring is negligible.
4. Each spring operates according to Hooke's law where the Hooke's constants are given by $k_1$, $k_2$ and $k_3$.
5. The first ($k_1$) and last ($k_3$) spring are attached to fixed walls.

Using Newton's Second Law, the equations of motion are given as follows:

$$m_1\ddot{x}_1(t) = -k_1x_1(t) + k_2[x_2(t) - x_1(t)] \tag{A.1}$$

$$m_2\ddot{x}_2(t) = -k_2[x_2(t) - x_1(t)] - k_3x_2(t) \tag{A.2}$$

This coupled mass-spring system will contain one fast and one slow varying component when the mass and stiffness coefficients are set, for example, as follows:

$m_1 = 1\,\text{kg}$
$m_2 = 1\,\text{kg}$
$k_1 = 0.01\,\text{kg/m}$
$k_2 = 1\,\text{kg/m}$
$k_3 = 100\,\text{kg/m}$

The analytical solutions to Equations (A.1) and (A.2) using the above coefficients are:

$$x_1(t) = -(101\cos((\sqrt{10101}t)/10))/10001 - (9900\cos(t))/10001 \tag{A.3}$$

$$x_2(t) = (10100\cos((\sqrt{10101}t)/10))/10001 - (99\cos(t))/10001 \tag{A.4}$$

which is approximately equal to:

$$x_1(t) = -0.01\cos(10.05t) - 0.99\cos(t) \tag{A.5}$$

$$x_2(t) = 1.01\cos(10.05t) - 0.01\cos(t) \tag{A.6}$$

Figure A.2 depicts the analytical solution to Equations (A.3) and (A.4). The motion of the first mass, $x_1(t)$, becomes the slow varying component because the second term with the larger amplitude (0.99) and smaller frequency (1) in Equation (A.5) dominates the first term. Similarily, the motion of the second mass, $x_2(t)$, becomes the fast varying component because the first term with the larger amplitude (1.01) and higher frequency (10.05) in Equation (A.6) dominates the second term.

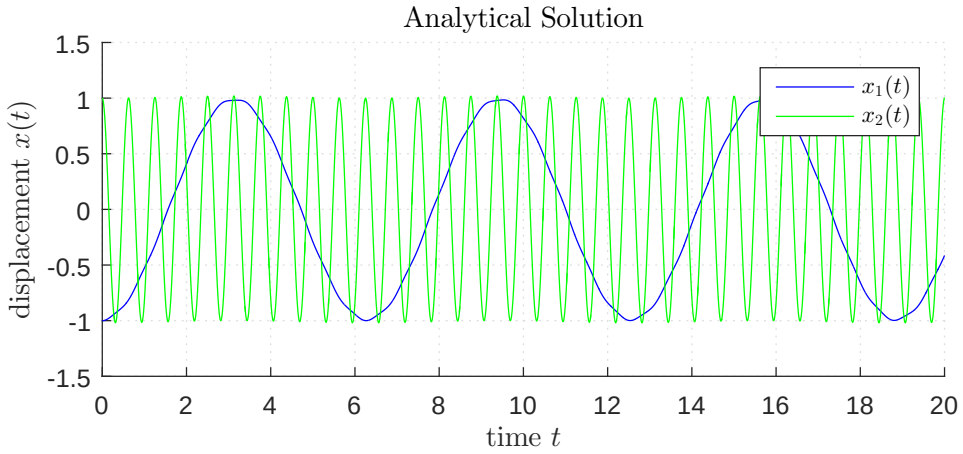


**Figure A.2:** Analytical solution to the coupled mass-spring system problem, where $x_1(t)$ and $x_2(t)$ are the slow and fast varying components, respectively.

The coupled mass spring system in Equations (A.3) and (A.4) can be solved numerically using a second order Adams-Bashforth method using a step size of $h = 0.01\,\text{s}$ for both components. The left side of Figure A.3 depicts the result from using the method. However, in the case when the slow varying component is computationally intensive compared to the fast varying component, using a step size of $h = 0.01\,\text{s}$ for the slow varying component is undesirable. By using a multi-rate method where the step-size for the fast-varying component is $h = 0.01\,\text{s}$ while the step-size for the slow-varying component is set to $h = 10 \times 0.01 = 0.1\,\text{s}$, one can achieve almost the same result in a more computationally efficient manner, see right-side of Figure A.3.

Using the larger step size of $h = 0.1\,\text{s}$ for both the fast and slow varying components is not possible. Figure A.4 depicts the erroneous result from using $h = 0.1\,\text{s}$ for both components. The fast varying component requires a much smaller step size compared to the slow varying component.

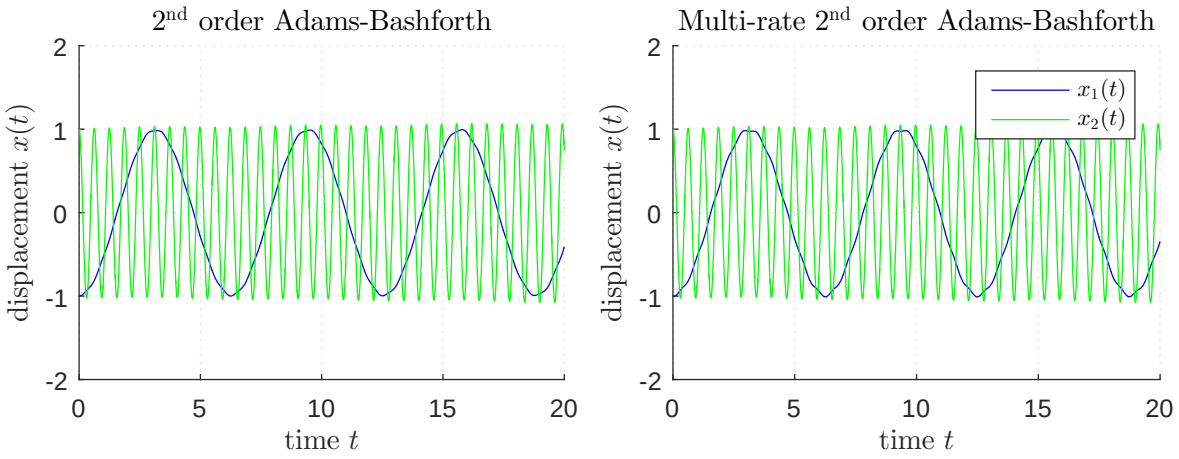


**Figure A.3:** Comparison of the 2nd order Adams-Bashforth (left) and the multi-rate approach (right) for solving the coupled mass-spring system problem. The multi-rate approach produces the same results using a larger time-step size for the slow varying component.

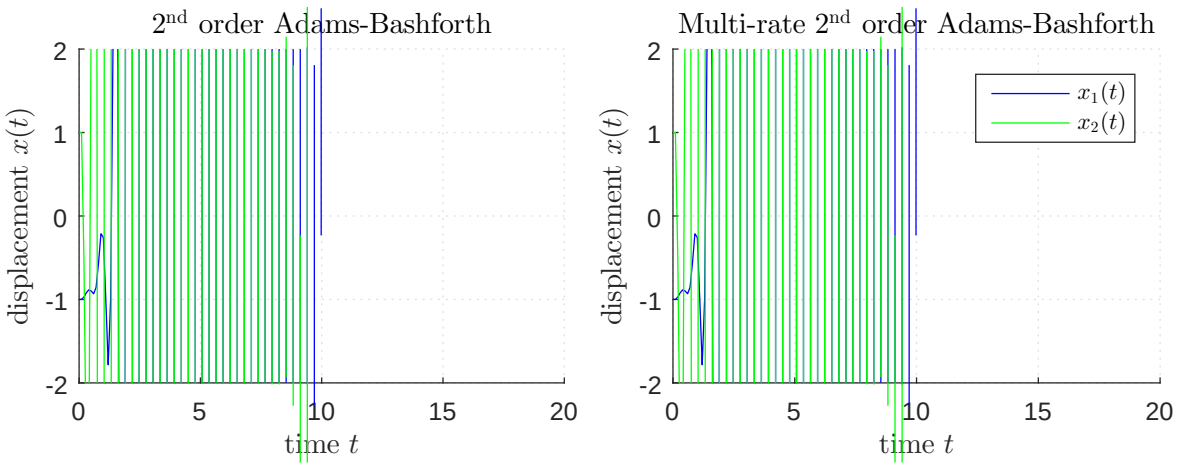


**Figure A.4:** The coupled mass-spring system problem cannot be solved when using the larger time-step size of $h = 0.1\,\mathrm{s}$ for both the slow and fast varying components.

# Appendix B

# Simple Test Problem using Surrogate Modeling

A simple analytical test problem is the Branin function:

$$f(\mathbf{x}) = \left(x_2 - \frac{5.1}{4\pi^2}x_2 + \frac{5}{\pi}x_1 - 6\right)^2 + 10\left[\left(1 - \frac{1}{8\pi}\right)\cos x_1 + 1\right] + 5x_1, \quad x_1 \in [-5, 10], x_2 \in [0, 15] \tag{B.1}$$

with one inequality constraint:

$$g(\mathbf{x}) = 0.2 - x_1 x_2 \leq 0, \quad x_1, x_2 \in [0, 1]. \tag{B.2}$$

The variables $x_1$ and $x_2$ are between 0 and 1. Before entering Equation (B.1), $x_1$ and $x_2$ are un-normalized using the bounds $x_1 \in [-5, 10]$ and $x_2 \in [0, 15]$. The global constrained optimum lies at $x_1 = 0.9677$ and $x_2 = 0.2067$ with a value of $f(\mathbf{x}) = 5.5757$.

Figure B.1 depicts the exact (left) and predicted (right) objective-function space. The exact objective values were obtained by evaluating Equation (B.1) on a fine grid, while the predicted values were obtained by evaluating the surrogate model on the same grid. Similarly, Figure B.2 depicts the exact (left) and predicted (right) constraint-function space. The exact and predicted constraint values were obtained in the same manner using Equation (B.2) instead of Equation (B.1). The optimal constrained value obtained from the surrogate-based optimization using a cubic radial basis function, 16 sample points, and 10 infill points is $f(\mathbf{x}) = 5.5757$ at $x_1 = 0.9676$ and $x_2 = 0.2067$.

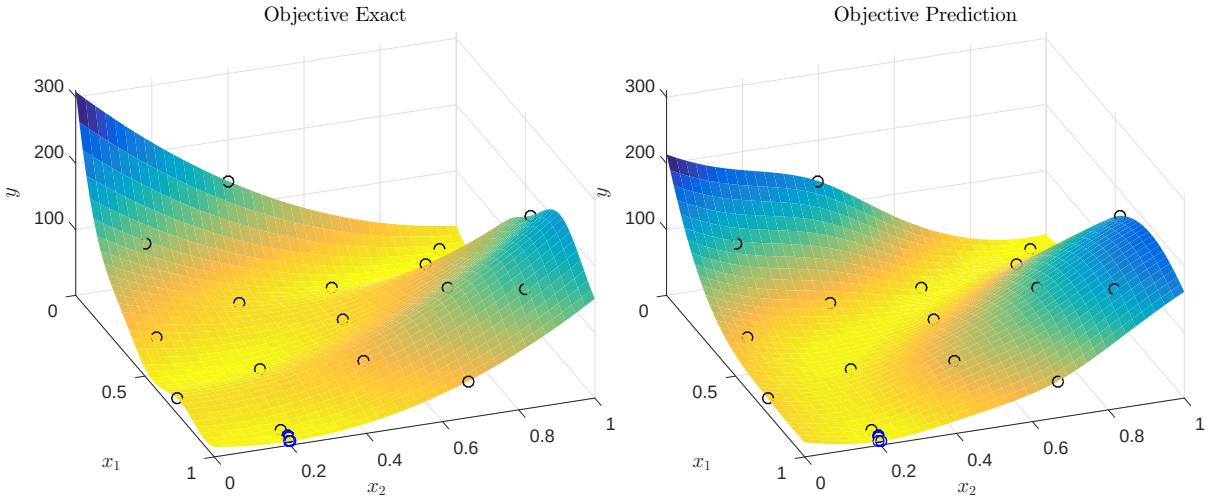


**Figure B.1:** Actual (left) and (predicted) objective function space for the two-variable Branin test problem. Black and blue circles represent sampled and infill points, respectively. The infill points are clustered near the global minimum at $x_1 = 0.974$ and $x_2 = 0.231$.

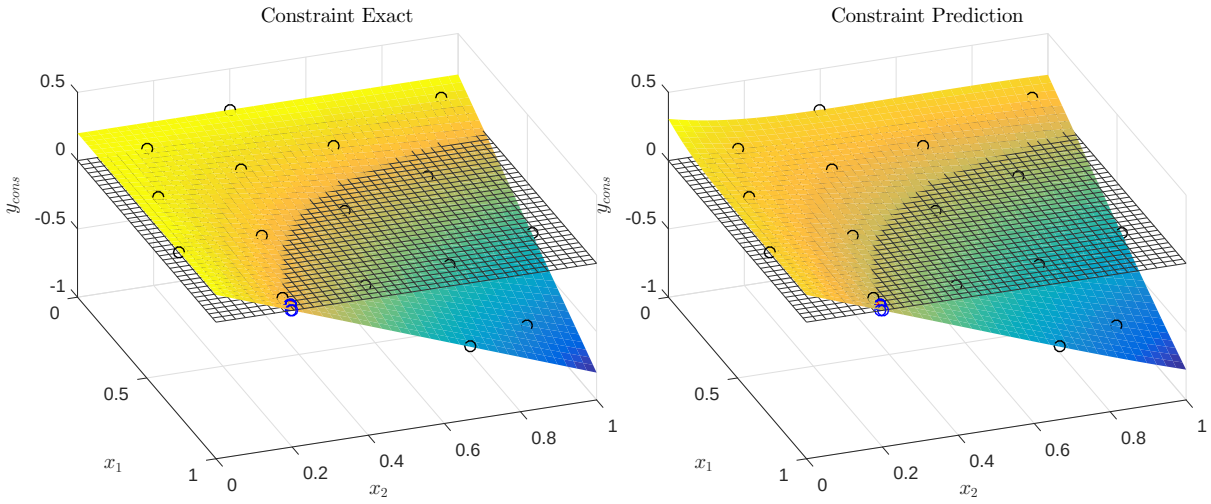


**Figure B.2:** Actual (left) and (predicted) constraint function space for the two-variable Branin test problem. Black and blue circles represent sampled and infill points, respectively. The infeasible region is above the black mesh, i.e. $y_{\text{cons}} > 0$. The global minimum lies on the border between the infeasible and feasible regions.

# Appendix C

# Non-Uniform Rational B-Splines

## C.1 Introduction

Two common methods of representing curves and surfaces in geometric modeling are implicit equations and parametric functions [129]. An implicit equation describes a relationship between the coordinates of the point lying on the curve. For example,

$$f(x, y) = x^2 + y^2 - 1 = 0 \tag{C.1}$$

is an implicit equation representing a circle centered at $(x, y) = (0, 0)$ in a two-dimensional Cartesian coordinate system. In a parametric equation, the coordinates of a point on the curve is represented separately as an explicit function of an independent parameter:

$$\mathbf{C}(u) = (x(u), y(u)) \quad a \leq u \leq b \tag{C.2}$$

where $\mathbf{C}(u)$ is a vector-valued function of the independent variable, $u$. The interval $[a, b]$ is arbitrary but is usually normalized to $[0, 1]$. The parametric functions:

$$\begin{aligned} x(u) &= \cos(u) \\ y(u) &= \sin(u) \quad 0 \leq u \leq \frac{\pi}{2} \end{aligned} \tag{C.3}$$

can be used to draw the first quadrant of the circle given by Equation (C.1).

## C.2 Bézier Curves

An $n$th degree Bézier curve is a parametric function and is expressed as:

$$\mathbf{C}(u) = \sum_{i=0}^{n} B_{i,n}(u)\mathbf{P}_i \quad 0 \leq u \leq 1 \tag{C.4}$$

where geometric coefficients, $\mathbf{P}_i$, are called *control points*, and the basis functions, $B_{i,n}(u)$, are the $n$th-degree Bernstein polynomials:

$$B_{i,n}(u) = \frac{n!}{i!(n-i)!} u^i (1-u)^{n-i} \tag{C.5}$$

The Bernstein polynomials for $n = 1$ are:

$$\begin{aligned} B_{0,1}(u) &= \frac{1!}{0!(1-0)!} u^0 (1-u)^{1-0} = 1 - u \\ B_{1,1}(u) &= \frac{1!}{1!(1-1)!} u^1 (1-u)^{1-1} = u \end{aligned} \tag{C.6}$$

Similar results are computed for $n = 2, 3, \ldots$ using Equation (C.5) for higher degree Bézier curves as needed. The first, second and third degree Bézier curves are given by Equations (C.7), (C.8) and (C.9), respectively:

$$\mathbf{C}(u) = (1-u)\mathbf{P}_0 + u\mathbf{P}_1 \quad 0 \leq u \leq 1 \tag{C.7}$$

$$\mathbf{C}(u) = (1-u)^2\mathbf{P}_0 + 2u(1-u)\mathbf{P}_1 + u^2\mathbf{P}_2 \quad 0 \leq u \leq 1 \tag{C.8}$$

$$\mathbf{C}(u) = (1-u)^3\mathbf{P}_0 + 3u(1-u)^2\mathbf{P}_1 + 3u^2(1-u)\mathbf{P}_2 + u^3\mathbf{P}_3 \quad 0 \leq u \leq 1 \tag{C.9}$$

Figures C.1, C.2, and C.3 depict the Bézier curves and Bernstein polynomials for $n = 1$, 2 and 3, respectively, for arbitrary values of $\mathbf{P}_0$, $\mathbf{P}_1$, $\mathbf{P}_2$, and $\mathbf{P}_3$.

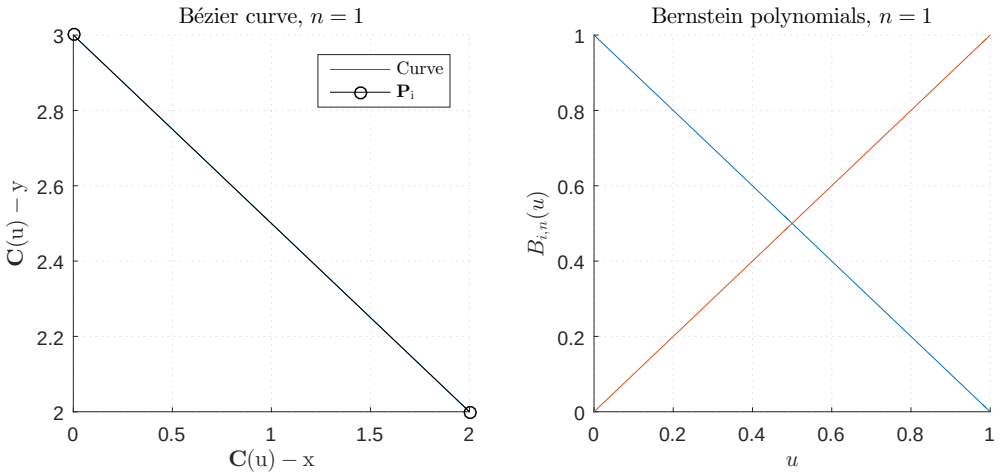


**Figure C.1:** Bézier curve and Bernstein polynomials for $n = 1$.

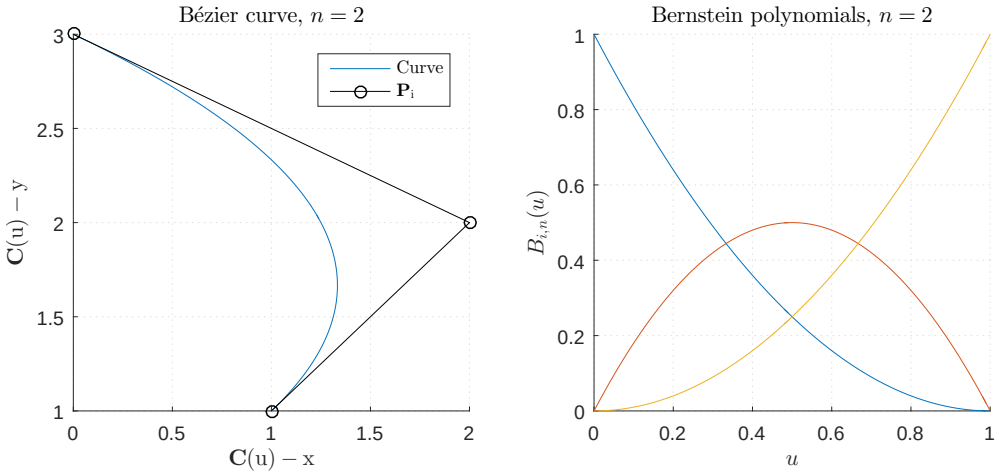


**Figure C.2:** Bézier curve and Bernstein polynomials for $n = 2$.

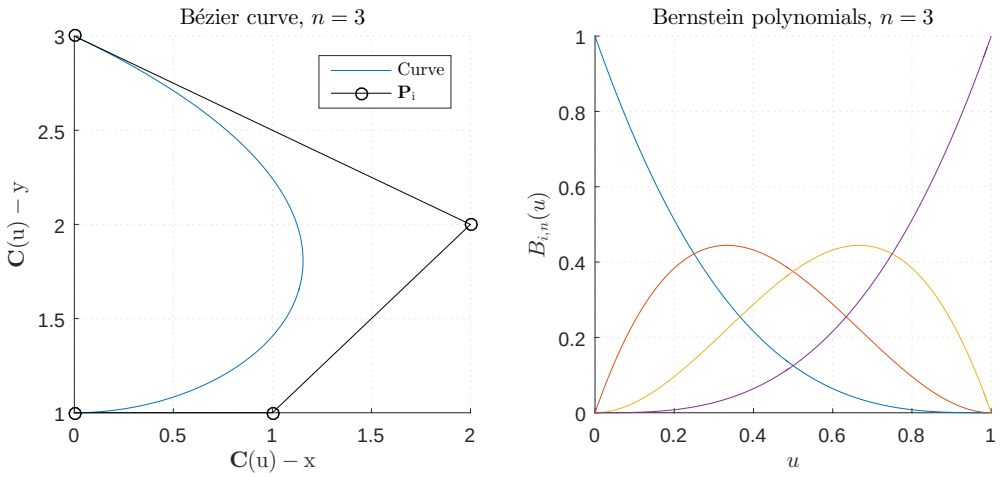


**Figure C.3:** Bézier curve and Bernstein polynomials for $n = 3$.

## C.3 B-Spline Curves

An $p$th degree B-spline curve is also a parametric function and is expressed as:

$$\mathbf{C}(u) = \sum_{i=0}^{n} N_{i,p}(u)\mathbf{P}_i \quad 0 \leq u \leq 1 \tag{C.10}$$

where the geometric coefficients, $\mathbf{P}_i$ $(i = 0, 1, 2, \ldots, n)$, are the control points, and $N_{i,p}(u)$ are the $p$th degree B-spline basis functions:

$$\begin{aligned} N_i, 0(u) &= \begin{cases} 1 & \text{if } u_i \leq u \leq u_{i+1} \\ 0 & \text{otherwise} \end{cases} \\ N_{i,p}(u) &= \frac{u - u_i}{u_{i+p} - u_i} N_{i,p-1}(u) + \frac{u_{i+p+1} - u}{u_{i+p+1} - u_{i+1}} N_{i+1,p-1}(u) \end{aligned} \tag{C.11}$$

defined on:

$$U = \{u_0, \ldots, u_m\} \tag{C.12}$$

with $m + 1$ knots. The knot vector $U$ is an increasing sequence of real numbers, i.e., $u_i \leq u_{i+1}, i = 0, \ldots, m - 1$, and the $u_i$ are called *knots*. Only non-periodic knot vectors are considered here and also in [129], which have the form:

$$U = \{\underbrace{0, \ldots, 0}_{p+1}, u_{p+1}, \ldots, u_{m-p-1}, \underbrace{1, \ldots, 1}_{p+1}\} \tag{C.13}$$

Non-periodic knot vectors have a multiplicity of $p + 1$ for the first and last knots, see Equation (C.13). A knot vector is said to be *uniform* if all interior knots are equally spaced, otherwise it is non-uniform. A non-periodic knot vector of the form:

$$U = \{\underbrace{0, \ldots, 0}_{p+1}, \underbrace{1, \ldots, 1}_{p+1}\} \tag{C.14}$$

where $n = p$ yields the Bernstein polynomials of degree $p$, see Equation (C.5). Therefore, Equation (C.10) is a generalization of the Bézier curve representation in Equation (C.4). Figures C.4, C.5, and C.6 depict examples of B-spline curves.

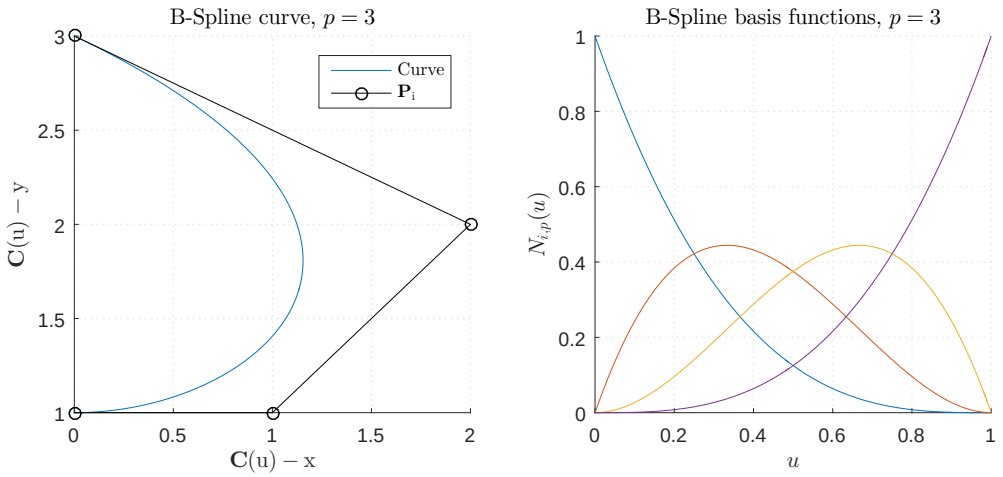


**Figure C.4:** A cubic B-spline curve on $U = \{0, 0, 0, 0, 1, 1, 1, 1\}$, i.e. a cubic Bézier curve.

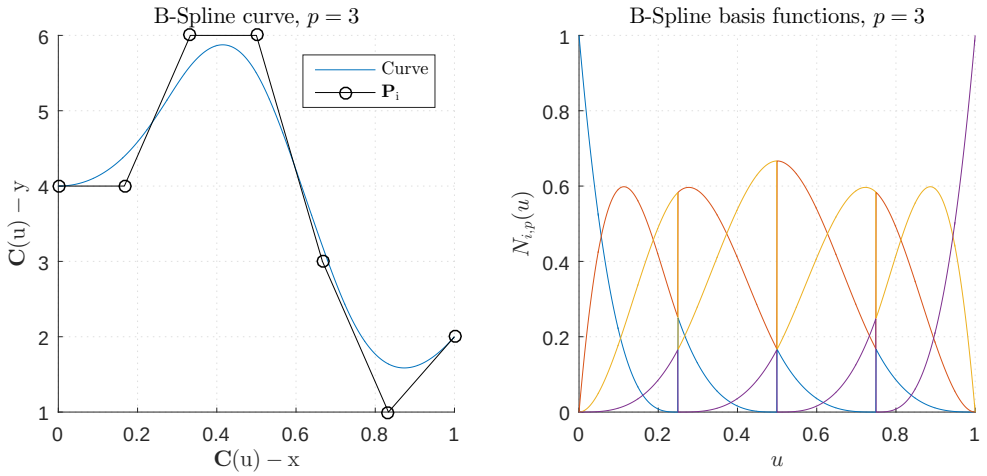


**Figure C.5:** Cubic B-spline curve on $U = \{0, 0, 0, 0, \frac{1}{4}, \frac{1}{2}, \frac{3}{4}, 1, 1, 1, 1\}$ (left) and cubic basis functions (right).

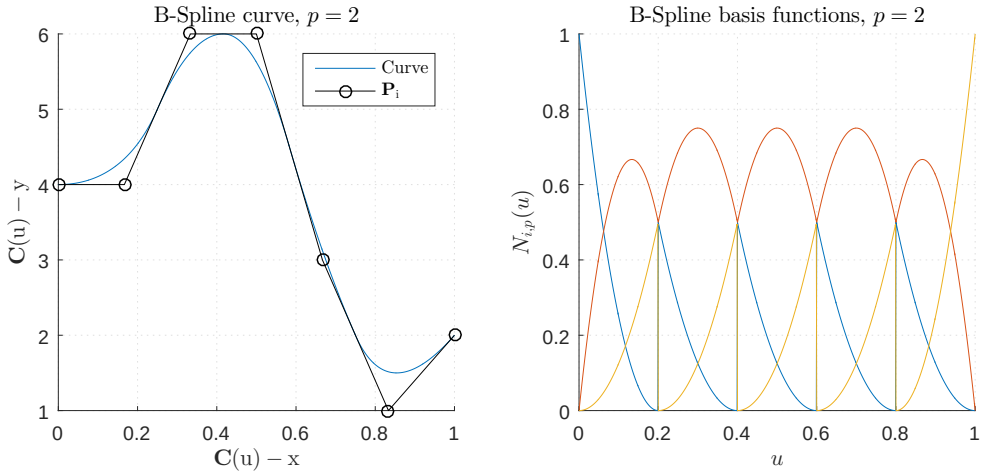


**Figure C.6:** Quadratic B-spline curve on $U = \{0, 0, 0, \frac{1}{5}, \frac{2}{5}, \frac{3}{5}, \frac{4}{5}, 1, 1, 1\}$ (left) and quadratic basis functions (right).

## C.4 NURBS Curves

A $p$th-degree Non-Uniform Rational B-Spline (NURBS) is defined by:

$$\mathbf{C}(u) = \frac{\sum_{i=0}^{n} N_{i,p}(u) w_i \mathbf{P}_i}{\sum_{i=0}^{n} N_{i,p}(u) w_i} \quad 0 \leq u \leq 1 \tag{C.15}$$

where $\mathbf{P}_i$ $(i = 0, 1, 2, \ldots, n)$, are the control points, $w_i$ are the *weights*, and $N_{i,p}(u)$ are the $p$th degree B-spline basis functions defined on the non-periodic and non-uniform knot vector:

$$U = \{\underbrace{0, \ldots, 0}_{p+1}, u_{p+1}, \ldots, u_{m-p-1}, \underbrace{1, \ldots, 1}_{p+1}\} \tag{C.16}$$

Unless otherwise stated, $w_i > 0$ for all $i$. Equation (C.15) can be rewritten in the form:

$$\mathbf{C}(u) = \sum_{i=0}^{n} R_{i,p}(u) \mathbf{P}_i \quad 0 \leq u \leq 1 \tag{C.17}$$

where

$$R_{i,p}(u) = \frac{N_{i,p}(u) w_i}{\sum_{j=0}^{n} N_{j,p}(u) w_j} \tag{C.18}$$

The $R_{i,p}(u)$ are called *rational basis functions*; they are piecewise rational functions on $u \in$[0,1]. The weights allows further modification to attain local shape control. When $w_i = 1$ for all $i$, then $R_{i,p}(u) = N_{i,p}(u)$ for all $i$. A NURBS curve with no interior knots, i.e. Equation (C.14), is a rational Bézier curve, since $N_{i,p}(u)$ reduce to $B_{i,n}(u)$. Therefore, NURBS curves contain non-rational B-Spline and rational and non-rational Bézier curves as special cases. NURBS will not be discussed further, since they have not been used in the present thesis.

# Appendix D

# Interactive PDFs

This appendix chapter contains interactive three-dimensional portable document format (3D PDF) files and a flash video. The most recent version of Adobe Acrobat Reader is required to view the 3D PDFs. Adobe flash player plugin is required to view the flash video.

**Figure D.1:** MIRAS-FLEX simulation with turbulent inflow from Chapter 2.

**Figure D.2:** Animation of MIRAS-FLEX simulation from Chapter 2.

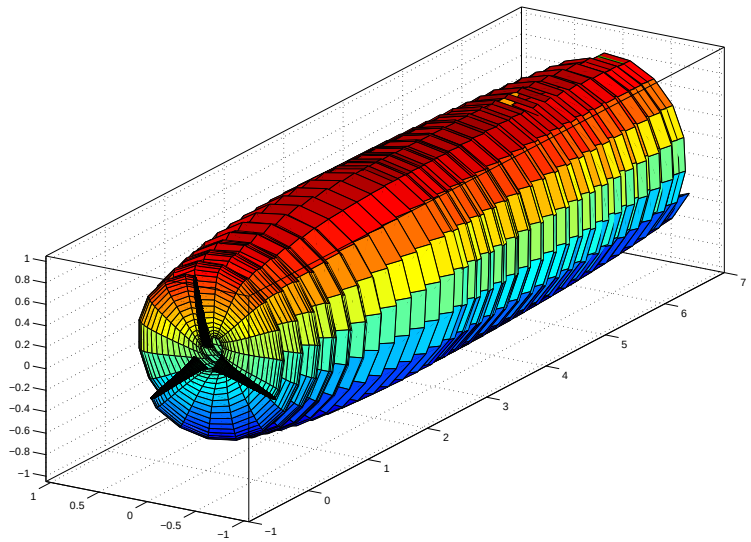


**Figure D.3:** Free wake behind the wind-turbine rotor model from a MIRAS simulation in Chapter 3.

# Appendix E

# Conference Posters

# Development of a fast fluid-structure coupling technique for wind turbine computations

Sessarego M., Shen W.Z., Ramos-García N., Sørensen J.N.

**OffWindChina**
R&D of optimal wind turbine rotors under offshore wind conditions in China

## 1. Introduction

1. Fluid-structure interaction simulations are used to model the aero-elastic response of horizontal-axis wind turbines (HAWTs). We use the fast code *MIRAS* for the fluid solver and *FLEX5* for the structure.
2. *MIRAS* [1] is a 3D viscous-inviscid solver for aerodynamic HAWT simulations developed by Ramos-García. Inviscid part solved using 3D panel method; viscous part using boundary layer solver in *Q³UIC*.
3. *FLEX5* [2] is an aero-elastic code for HAWTs developed by Øye. Aerodynamics are modeled using the BEM method, while the dynamics are modeled using carefully selected degrees of freedom.
4. Structural behaviour in MIRAS is included by coupling MIRAS with the structural model in FLEX5. This code is referred to as *MIRAS-FLEX*.

## 2. MIRAS and FLEX5 Coordinate Systems

Coupling MIRAS with FLEX5 requires careful consideration of the distinct coordinate systems (CSs). The MIRAS CS is shown in Figure 1. The CS is centered at the hub where the x-axis is aligned with the rotor shaft. The geometrical description of FLEX5 is shown in Figure 2. Unlike MIRAS, which models the rotor only, FLEX5 models the complete turbine and foundation.

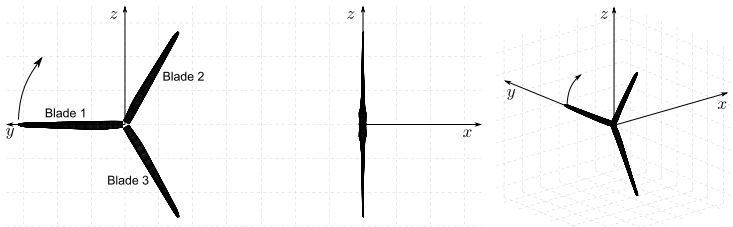


**Figure 1.** MIRAS coordinate system in the front (left), side (middle), and isometric (right) views.

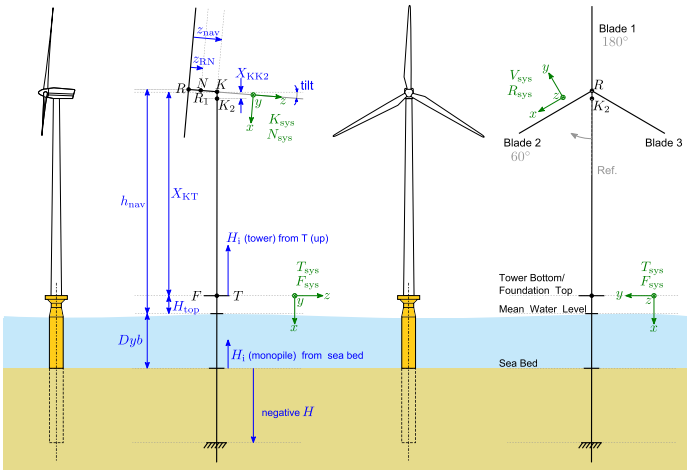


**Figure 2.** FLEX5 parameters and coordinate systems.

## 3. Mesh Update

FLEX5 uses Euler-Bernoulli beam theory to predict the elastic deformation of the turbine blades. Thus, the displacement field of various cross-sections of the blade in MIRAS are based solely on rigid body translations and rotations, see Figure 3 and Eqs. 1-3. Figure 4 displays the updated blade mesh in MIRAS.

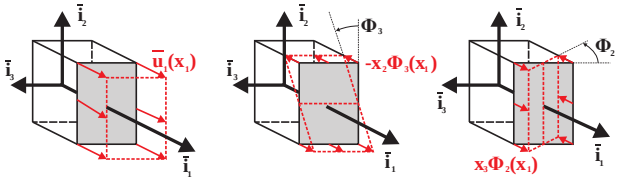

*Bauchau et al.* [3]

**Figure 3.** Axial displacement field in Euler-Bernoulli beam theory as described in *Bauchau et al.* [3], see Eq. 1.

$$u_1(x_1,x_2,x_3) = \bar{u}_1(x_1) - x_3\frac{d\bar{u}_3(x_1)}{dx_1} - x_2\frac{d\bar{u}_2(x_1)}{dx_1}, \quad (1)$$

$$u_2(x_1,x_2,x_3) = \bar{u}_2(x_1), \quad (2)$$

$$u_3(x_1,x_2,x_3) = \bar{u}_3(x_1). \quad (3)$$

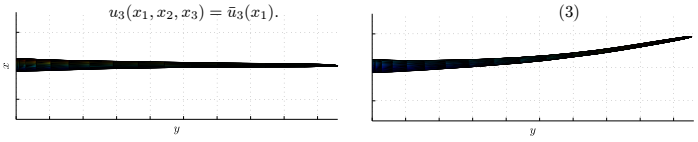

**Figure 4.** Un-deformed (left) and deflected (right) blade in MIRAS. Flapwise deflection shown.

## 4. Coupling Methodology

A loosely-coupled methodology is used based on the work of Farhat [4]. The loosely-coupled approach was selected to minimize the number of calls to the computationally intensive MIRAS in the MIRAS-FLEX code. The loose-coupling is displayed in Figure 5.

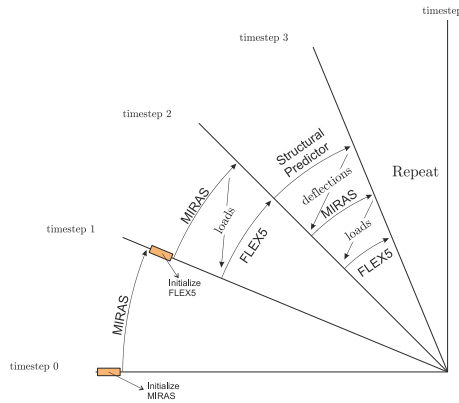


**Figure 5.** Loose-coupling methodology in MIRAS-FLEX. Black lines represent a rotating blade.

## 5. Results

A 5-MW HAWT was simulated with the newly developed MIRAS-FLEX code. Figure 6 displays the wake for a turbine with fixed (MIRAS) and flexible (MIRAS-FLEX) blades. Due to blade bending, the rotor power and thrust in MIRAS-FLEX is lower than in MIRAS only, see Figure 7. Similarly, the tangential and normal loads in MIRAS-FLEX are also lower, particularly near the tip, as shown in Figure 8.

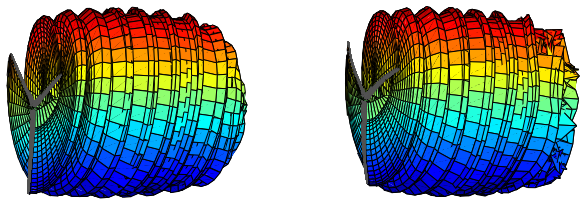

**Figure 6.** Visualization of the wake from MIRAS (left) and MIRAS-FLEX (right).

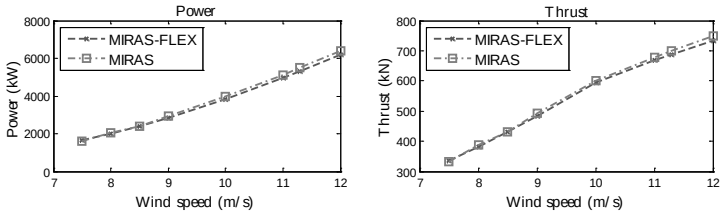


**Figure 7.** Rotor power (left) and thrust (right) comparison between MIRAS and MIRAS-FLEX.

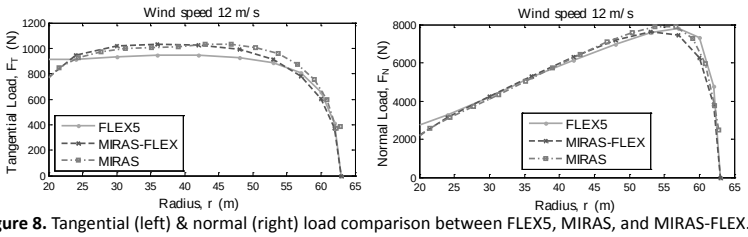


**Figure 8.** Tangential (left) & normal (right) load comparison between FLEX5, MIRAS, and MIRAS-FLEX.

## 6. Conclusions

- MIRAS has been coupled with FLEX5 to predict the aero-elastic response of wind turbines;
- MIRAS-FLEX gives lower predictions of rotor power and thrust in comparison with MIRAS, particularly at higher wind speeds;
- MIRAS-FLEX also gives lower prediction of loads in comparison with MIRAS, especially near the tip where deflections are the highest;
- Fast fluid-structure-interaction simulations can now be performed with MIRAS-FLEX, which was not possible with MIRAS alone.

**REFERENCES:**

[1] Ramos-García N, Sørensen JN, Shen WZ. Three-dimensional viscous-inviscid coupling method for wind turbine computations. Accepted for publication in *Wind Energy* 2014.
[2] Øye S. FLEX4 simulation of wind turbine dynamics. *Proceedings of 28th IEA Meeting of Experts Concerning State of the Art of Aeroelastic Codes for Wind Turbine Calculations*, International Energy Agency: Lyngby, 1996.
[3] Bauchau OA, Craig JI (eds.). *Structural Analysis: With Applications to Aerospace Structures, Solid Mechanics and Its Applications*, vol. 163. Springer Netherlands, 2009.
[4] Farhat C, van der Zee KG, Geuzaine P. Provably second-order time-accurate loosely-coupled solution algorithms for transient nonlinear computational aeroelasticity. *Computer Methods in Applied Mechanics and Engineering* 2006; **195**:1973-2001.

DTU Wind Energy
Department of Wind Energy

**ENERGY AND ENVIRONMENT FOR THE FUTURE**
Monday 24 - Tuesday 25 November 2014,
Eigtveds Pakhus, Copenhagen

Innovationsfonden
FORSKNING, TEKNOLOGI & VÆKST I DANMARK

# Development of a fast fluid-structure coupling technique for wind turbine computations

Sessarego M., Shen W.Z., Ramos-García N., Sørensen J.N.
Department of Wind Energy, Fluid Mechanics Section, Technical University of Denmark, DK-2800

**OffWindChina**
R&D of optimal wind turbine rotors under offshore wind conditions in China

## 1. Introduction

- Fluid-structure interaction simulations are used to model the aero-elastic response of horizontal-axis wind turbines (HAWTs). We use the fast code *MIRAS* for the flow solver and *FLEX5* for the structure.
- *MIRAS* [1] is a 3D viscous-inviscid solver for aerodynamic HAWT simulations developed by DTU Wind Energy. Inviscid part is solved using 3D panel method; viscous part is solved using boundary layer solver in *Q³UIC* [1].
- *FLEX5* [2] is an aero-elastic code for HAWTs developed by Øye. Aerodynamics are modeled using the blade element momentum (BEM) method, while the dynamics are modeled using carefully selected degrees of freedom (DOFs).
- Structural behavior in MIRAS is included by coupling MIRAS with the structural model in FLEX5. This code is referred to as *MIRAS-FLEX*. Up to 21 DOFs in MIRAS-FLEX describe the motions of the wind turbine structure under unsteady or steady wind inflow conditions.

## 2. MIRAS and FLEX5 Coordinate Systems

Coupling MIRAS with FLEX5 requires careful consideration of the distinct coordinate systems (CSs). The MIRAS CS is shown in Figure 1, while the CSs in FLEX5 are shown in Figure 2.

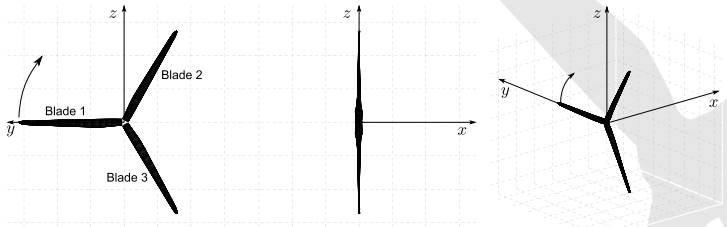


**Figure 1.** MIRAS coordinate system in the front (left), side (middle), and isometric (right) views.

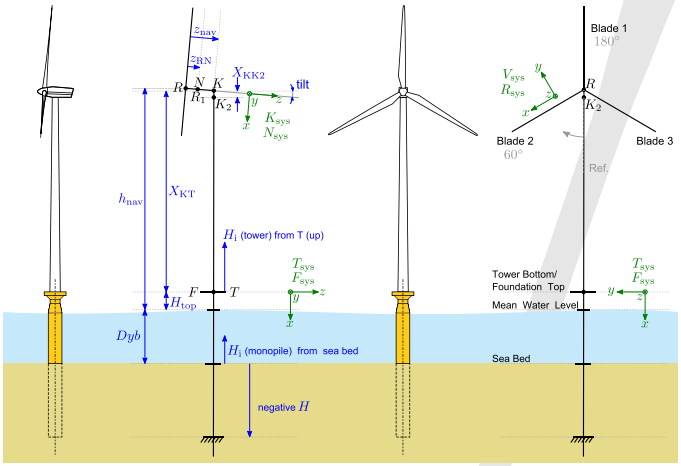


**Figure 2.** FLEX5 parameters and coordinate systems.

## 3. Deformation and Aerodynamic Load Transfer

FLEX5 uses Euler-Bernoulli beam theory to predict the elastic deformation of the turbine blades. Thus, blade deformations in MIRAS are based solely on rigid body translations and rotations, see Figure 3. Figure 4 displays the updated blade mesh in MIRAS under flapwise loading. Aerodynamic load transfer from MIRAS to FLEX5 is performed through interpolation between the 3D mesh of MIRAS and the 1D beam of FLEX5. Figure 5 illustrates the concept.

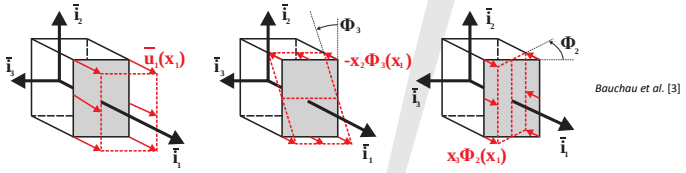


**Figure 3.** Axial displacement field in Euler-Bernoulli beam theory as described in *Bauchau et al.* [3].

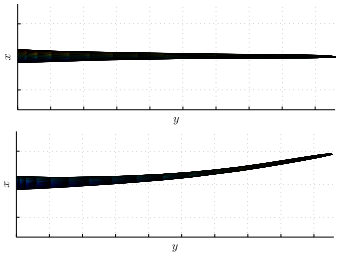

**Figure 4.** Un-deformed (top) and flapwise deflected (bottom) blade in MIRAS.

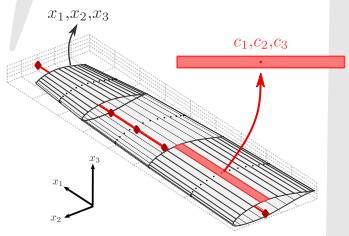

**Figure 5.** Aerodynamic load transfer from 3D mesh of MIRAS to 1D beam of FLEX5.

## 4. Coupling Methodology

A loosely-coupled, multi-rate methodology [4] was selected to minimize the number of calls to the computationally intensive MIRAS in the MIRAS-FLEX code. The loosely-coupled, multi-rate approach is depicted in Figure 6.

**Figure 6.**
Loosely-coupled/multi-rate methodology in MIRAS-FLEX. Black lines represent a clockwise rotating blade starting from an azimuthal position of 180° and ending at 90°.

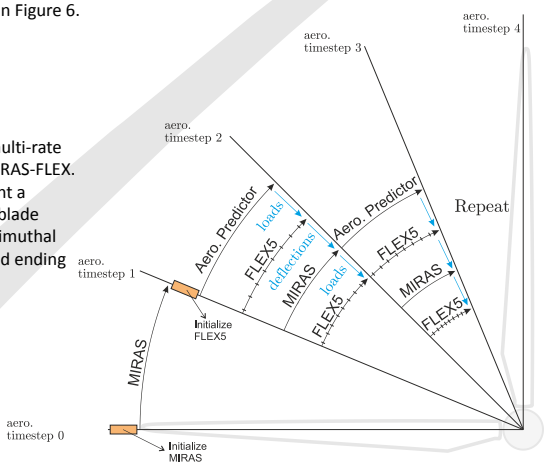


## 5. Validation and Results

MIRAS-FLEX was compared against BEM-based aero-elastic codes FLEX5 and FASTv8, as well as the actuator line (AL-FLEX) code EllipSys3D-FLEX5 (work in progress). Figure 9 displays the values of two DOFs for a steady wind input of 10 m/s to a 2.75-MW wind turbine.

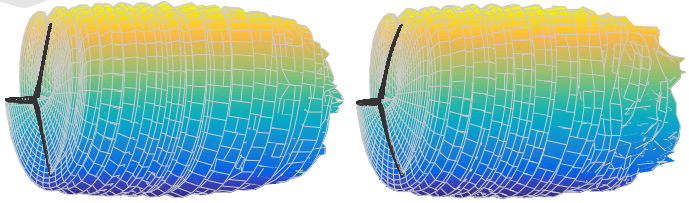

**Figure 7.** Visualization of the wake from MIRAS (left) and MIRAS-FLEX (right).

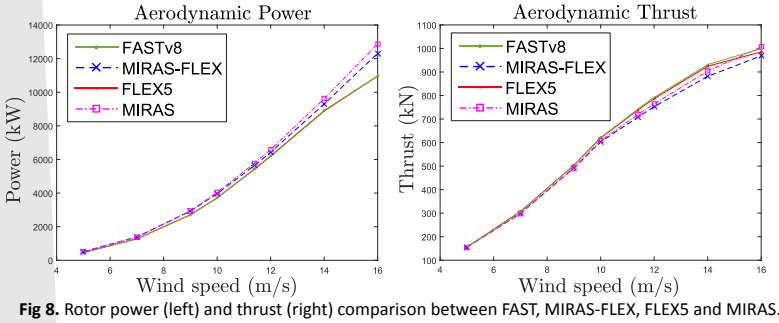


**Fig 8.** Rotor power (left) and thrust (right) comparison between FAST, MIRAS-FLEX, FLEX5 and MIRAS.

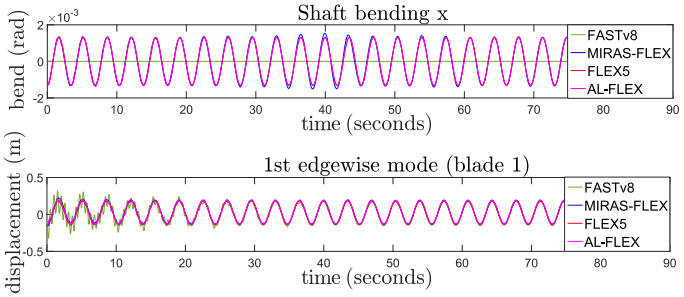


**Figure 9.** Shaft bending (top) and 1st edgewise blade mode (bottom) degrees of freedom for FAST, MIRAS-FLEX, FLEX5 and AL-FLEX.

## 6. Conclusions

- A 3D viscous-inviscid solver, MIRAS, has been coupled with FLEX5 to predict the aero-elastic response of wind turbines. MIRAS-FLEX is unique since it does not rely on BEM theory, which is typically used in standard aero-elastic codes such as FLEX5, FAST, and HAWC2.
- MIRAS-FLEX allows up to 21 degrees of freedom to model the motions of the wind turbine structure under steady and unsteady wind inflow conditions.
- Fast fluid-structure-interaction simulations can now be performed with MIRAS-FLEX, which was not possible with MIRAS alone.

**REFERENCES:**

[1] Ramos-García N, Sørensen JN, Shen WZ. Three-dimensional viscous-inviscid coupling method for wind turbine computations. *Wind Energy* 2014.
[2] Øye S. FLEX4 simulation of wind turbine dynamics. *Proceedings of 28th IEA Meeting of Experts Concerning State of the Art of Aeroelastic Codes for Wind Turbine Calculations*, International Energy Agency: Lyngby, 1996.
[3] Bauchau OA, Craig JI (eds.). *Structural Analysis: With Applications to Aerospace Structures, Solid Mechanics and Its Applications*, vol. 163. Springer Netherlands, 2009.
[4] Gear C, Wells D. Multi-rate linear multistep methods. *BIT Numerical Mathematics, Kluwer Academic Publishers* 1984; **24**:484-502.

# Development of a simple structural design method for large wind turbine blades

Sessarego M., Shen W. Z.
Fluid Mechanics Section, Department of Wind Energy, Technical University of Denmark, DK-2800

OffWindChina
R&D of optimal wind turbine rotors under offshore wind conditions in China

## 1. Introduction

A simple optimization tool to design the internal structure of large wind turbine blades has been developed. The tool uses a combination of classical laminate theory using a shear flow approach to compute blade structural properties, PreComp [1], a finite-element code to compute the blade coupled mode shapes, BModes [2], Euler-Bernoulli beam theory to compute blade deflections and strains, and the aero-elastic code FLEX5 [3] to compute the design load cases (DLCs). Although several structural optimization tools for wind-turbine blades have already been developed in the past, e.g. [4], [5] and [6], the motivation for its development is to integrate the tool with a rotor optimization code from [7] using a higher-fidelity aero-elastic model [8], see Fig. 1. The methods, results and conclusions are described next.

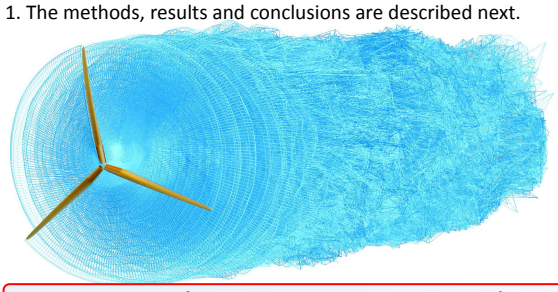

**Figure 1.** Higher-fidelity aero-elastic model used in rotor optimization code.

## 2. Objective, Constraints and Variables

The objective is to minimize the cost of energy (COE) subject to a number of non-linear inequality constraints:

$$\begin{aligned} &\text{minimize} && \text{COE}(\mathbf{x}) \\ &\text{subject to} && \text{blade natural frequency } (\mathbf{x}): && \omega_{\text{constraint}} \leq 0 \\ &&& \text{tip deflection } (\mathbf{x}): && \delta_{\text{constraint}} \leq 0 \\ &&& \text{ultimate strain } (\mathbf{x}): && \varepsilon_{\text{constraint},1} \leq 0, \quad \varepsilon_{\text{constraint},2} \leq 0 \\ &&& \text{spar-cap buckling } (\mathbf{x}): && \eta_{\text{constraint}} \leq 0 \end{aligned} \tag{1}$$

$$\text{COE}_{\text{objective}} = \text{Blade Cost} / \text{AEP} \tag{2}$$

$$\omega_{\text{constraint}} = \frac{3\omega_{\text{rotor}} - \omega \text{ SF}}{\omega_{rotor}} \tag{3}$$

$$\delta_{\text{constraint}} = \frac{\delta_{\text{tip}} - \delta_{\max}}{\delta_{\max}} \tag{4}$$

$$\varepsilon_{\text{constraint},1} = \frac{\varepsilon_{\text{tension}} \text{ SF} - \varepsilon_{\text{ultimate,tension}}}{\varepsilon_{\text{ultimate,tension}}} \tag{5}$$

$$\varepsilon_{\text{constraint},2} = \frac{\varepsilon_{\text{compression}} \text{ SF} - \varepsilon_{\text{ultimate,compression}}}{\varepsilon_{\text{ultimate,compression}}} \tag{6}$$

$$\eta_{\text{constraint}} = \frac{\eta - \eta_{\max}}{\eta_{\max}} \tag{7}$$

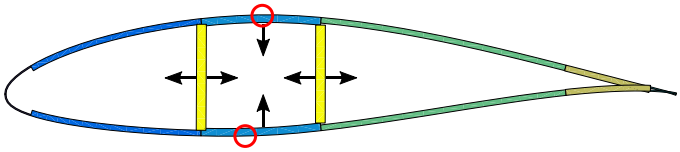

**Figure 2.** Depiction of the box-spar structural layup as defined in Resor [9]. Optimization variables are the spar-cap thickness and web layup shown as black arrows. Only the highest and lowest points on the airfoil contour (circles) are used to compute the strain constraint.

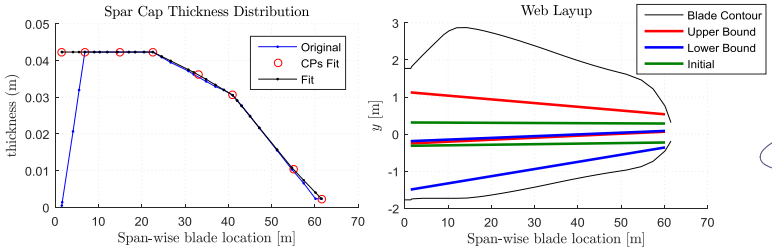


**Figure 3.** Optimization variables are the spar-cap thickness distribution (left) and web layup (right). The spar-cap distribution is defined by eight control points (CPs), while the web layup is defined by the chord-wise locations of the two endpoints for each web. The upper and lower bounds of the webs are used to prevent the webs from merging into each other and also into different sectors of the cross-section.

## 3. Optimization Procedure

The structural design code begins with computing a series of DLCs as described in Resor [9] and the IEC 61400-1 standards [10] using FLEX5 and assuming stiff blades, see Table 1.

**Table 1.** Design load cases used in the structural design code based on [9] and [10].

| Design situation | DLC | Wind condition | Other conditions | Type of analysis |
|---|---|---|---|---|
| Power Production | - | Steady wind | 2 m/s increments from cut-in = 3 m/s to cut-out = 25 m/s | Ultimate strength |
| | 1.4 | Extreme Coherent gust with Direction change (ECD) | Rated wind ± 2 m/s, 2 m/s spacing | Ultimate strength |
| Parked (standing still or idling) | 6.1 | Extreme Windspeed Model (EWM) 50-year recurrence period | Yaw error ± $15^0$, $5^0$ spacing | Ultimate strength |
| | 6.3 | EWM 1-year recurrence period | Extreme yaw misalignment, ± $30^0$ | Ultimate strength |

The bending moments normal and tangential to the rotor plane from all DLCs are then transferred to the optimizer, which calls a structural module for a number of iterations to find the minimum COE. Fig. 4 depicts a flowchart of the structural module, which computes the objective and constraints. The inputs to the structural module are the DLC loads and **x**. The vector **x** is used to create a structural layup and compute the objective, while the DLC loads together with the blade structural properties are used to compute the structural constraints. The MATLAB optimizer, *fmincon* [11], modifies **x** to minimize the objective up to at least a local minimum and also satisfy all constraints. A cost module from National Renewable Energy Laboratory (NREL) [12] is used to calculate the COE using blade mass as input.

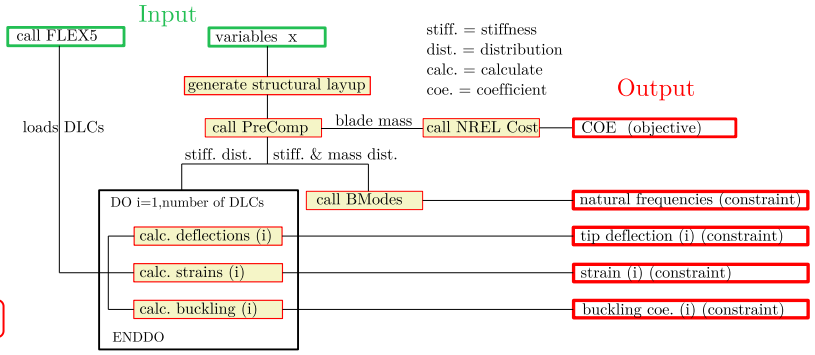


**Figure 4.** Flowchart for computing the objective and constraints using vector of design variables, **x**, and DLC loads from FLEX5 as input.

## 4. Results

The structural design code was applied on the NREL 5MW wind-turbine blade as described in [9] and [13]. The structural layup for the NREL 5MW was obtained from Resor [9] and was used as the initial starting point. The initial and optimized blade mass are 16,489 kg and 16,139 kg, respectively, and all constraints are satisfied. A 2.1% reduction in COE was achieved. Blade mass and COE were reduced mostly by decreasing the spar-cap width. In the optimal blade, the increase in the fore and aft panels to compensate the decrease in spar-width is taken into account in the blade mass calculation. Fig. 5 depicts the internal structure for the initial (left) and optimal (right) blades.

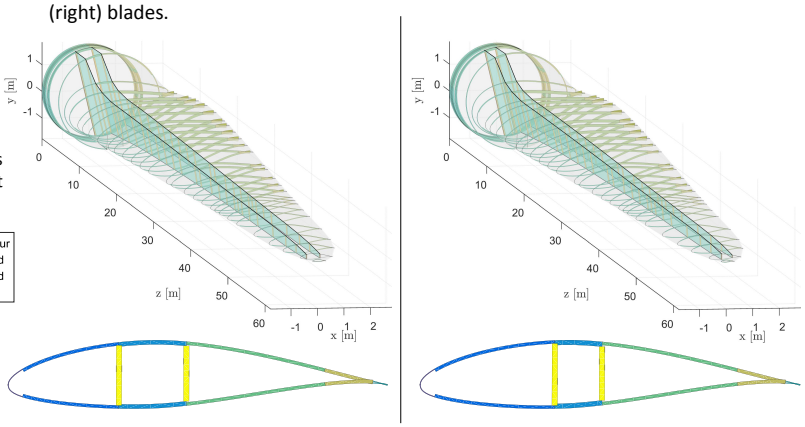


**Figure 5.** Initial (left) and optimal (right) internal blade structure found from structural design code.

## 5. Conclusions

A simple structural design code was developed to minimize the cost of energy (COE) of the NREL 5MW wind-turbine blade. Loads are calculated from the aero-elastic code FLEX5, while PreComp, BModes, as well as MATLAB code written by the authors were used to compute the optimization objective and constraints. The initial and optimized blade mass are 16,489 kg and 16,139 kg, respectively. Further, a 2.1% reduction in COE was achieved for the NREL 5MW blade in the four design load cases. In the future, the structural design tool will be coupled with a rotor optimization code using a higher-fidelity aero-elastic model.

## 6. References

[1] Bir, G. S., "User's Guide to PreComp," 2005.
[2] Bir, G. S., "User's Guide to BModes," 2007.
[3] Øye, S., "FLEX4 simulation of wind turbine dynamics," 1996.
[4] Sale, D., "User's Guide to Co-Blade," 2012.
[5] Bottasso, C. L., Campagnolo, F., Croce, A., Dilli, S., Gualdoni, F., Nielsen, M.B., "Structural optimization of wind turbine rotor blades by multilevel sectional/multibody/3D-FEM analysis," 2014.
[6] Hu, W., Park, D., Choi, D., "Structural optimization procedure of a composite wind turbine blade for reducing both material cost and blade weight," 2013.
[7] Sessarego, M., Ramos-García, N., Yang, H., Shen, W. Z., "Aerodynamic wind-turbine rotor design using surrogate modeling and three-dimensional viscous–inviscid interaction technique," 2016.
[8] Sessarego, M., Ramos-García, N., Shen, W. Z., "Development of a Fast Fluid-Structure Coupling Technique for Wind Turbine Computations," 2015.
[9] Resor, B., "Definition of a 61.5-Meter Wind Turbine Blade Reference Model," 2013.
[10] Internatinal Energy Agency "IEC 61400-1", 3rd Edition, 2005-08.
[11] The MathWorks Inc., Natick, MA, MATLAB 2015b.
[12] Fingersh, L., Hand, M., and Laxson, A., "Wind Turbine Design Cost and Scaling Model," 2006.
[13] Jonkman J., Butterfield S., Musial W., Scott G. 2009, "Definition of a 5-MW reference wind turbine for offshore system development," 2009.

# Large Wind Turbine Rotor Design using an Aero-Elastic / Free-Wake Panel Coupling Code

**Matias Sessarego, Néstor Ramos-García, Wen Zhong Shen, Jens Nørkær Sørensen**

Technical University of Denmark, Department of Wind Energy, Kgs. Lyngby, Denmark

## 1 Introduction

Wind-turbine blade design is a complex iterative process, which requires knowledge in several areas of engineering. In the past, blade plan-form design was performed using simple analytical expressions based on wind-turbine rotor aerodynamics only, see e.g. [1]. Today, the advances in computing resources have permitted solution of sophisticated numerical optimization problems involving two or more disciplines in the design process [2]. Despite the advances in computing techniques in the recent years, the majority of blade design problems still rely on aero-elastic codes that use blade element momentum (BEM) approaches to model the rotor aerodynamics. The present work describes an approach to wind-turbine rotor design by incorporating a higher-fidelity free-wake panel aero-elastic coupling code called MIRAS-FLEX [3], see Fig. 1.

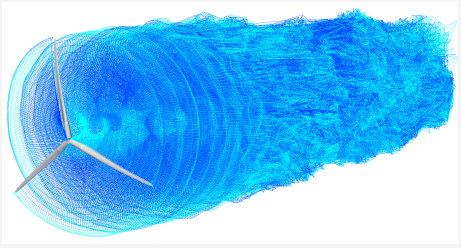

**Fig. 1:** MIRAS-FLEX simulation with turbulent inflow.

## 2 Methodology

The design objective is to minimize the cost of energy (COE):

$$\begin{aligned} \underset{x}{\text{minimize}} \quad & \frac{\text{COE}}{\text{COE}_{\text{ref}}} \\ \text{subject to } & \mathbf{x} \in \mathbb{R}^n, \\ & g_c(\mathbf{x}) \leq 0, \\ & x_k^L \leq x_k \leq x_k^U,\ k = 1, \ldots, n \end{aligned} \tag{1}$$

where the subscript, ref, denotes the reference blade. The design variables, $\mathbf{x} = [x_1, x_2, \ldots, x_n]$, are control points (CPs) that define the chord, twist and relative thickness as a function of blade span, see Fig. 2.

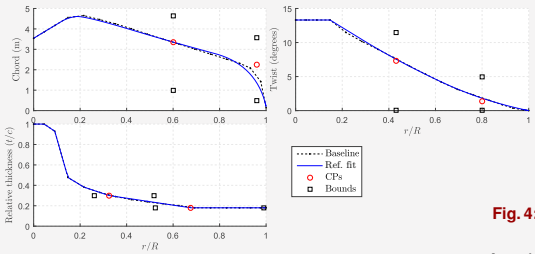


**Fig. 2:** Blade geometry parameterization method fitted to the NREL 5MW baseline wind turbine (Ref. fit), where $r/R$ is the normalized blade radius.

Problem 1 is solved using a surrogate-based optimization scheme developed by the authors [4]. Following [5], COE is calculated as:

$$\text{COE} = \frac{\text{FCR} \cdot (\text{TCC} + \text{BOS})}{\text{AEP}} + \text{AOE} \tag{2}$$

where MIRAS-FLEX is used to compute the annual energy production (AEP), while a code based on classical laminate theory called PreComp [6] to compute the blade mass ($m_{\text{blade}}$). $m_{\text{blade}}$ is used as input for TCC.

The structural objective is to minimize the blade mass subject to boundary and non-linear inequality constraints:

$$\begin{aligned} \underset{y}{\text{minimize}} \quad & \text{Blade Mass} \\ \text{subject to } & \mathbf{y} \in \mathbb{R}^n, \\ & \omega_{\text{constraint}}(\mathbf{y}) \leq 0 \\ & \delta_{\text{constraint}}(\mathbf{y}) \leq 0 \\ & \epsilon_{\text{constraint},1}(\mathbf{y}) \leq 0 \\ & \epsilon_{\text{constraint},2}(\mathbf{y}) \leq 0 \\ & \eta_{\text{constraint}}(\mathbf{y}) \leq 0 \\ & y_k^L \leq y_k \leq y_k^U,\ k = 1, \ldots, n \end{aligned} \tag{3}$$

where $\omega_{\text{constraint}}$, $\delta_{\text{constraint}}$, $\epsilon_{\text{constraint},1}$, $\epsilon_{\text{constraint},2}$, and $\eta_{\text{constraint}}$ are the blade eigen-frequency, tip deflection, tensile and compressive strain, and buckling constraints, respectively.

A box-spar layup is assumed for the internal blade structure, where the design variables, $\mathbf{y}$, are the spar-cap thickness and web layup (or spar width), see Figs. 3 and 4. The spar-cap thickness distribution is defined by eight CPs, while the web layup is defined by the chord-wise locations of the two span-wise endpoints for each web. A reduced set of DLCs computed using FLEX5 in accordance with the IEC standards [7] is used as input to the structural optimization code.

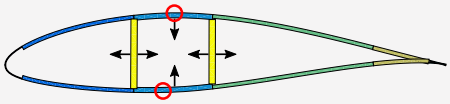

**Fig. 3:** A cross-section where the variables are the spar-cap thickness and the chord-wise location of the webs (arrows). Only the highest and lowest points on the airfoil contour (circles) are used to compute the strain constraint, see Problem (3).

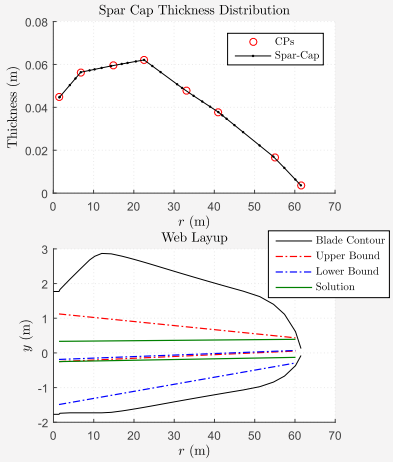


**Fig. 4:** Optimal spar-cap thickness (top) and web layup (bottom) for the NREL 5MW baseline wind turbine.

As shown in Fig. 5, each candidate blade design in the optimization goes through six stages to estimate the COE: 1) Build blade shape, 2) control tunning, 3) compute DLCs, 4) structural design, 5) compute AEP, and 6) calculate COE.

## 3 Results

Table 1 and Fig. 6 depict the results from the optimization of Problem (1) using the NREL 5MW baseline wind turbine as the reference. Table 1 shows the improvements obtained for COE, AEP, maximum flapwise root-bending moment experienced in the DLCs ($M_{\text{flap}}$), and blade mass in tonnes ($m_{\text{blade}}$).

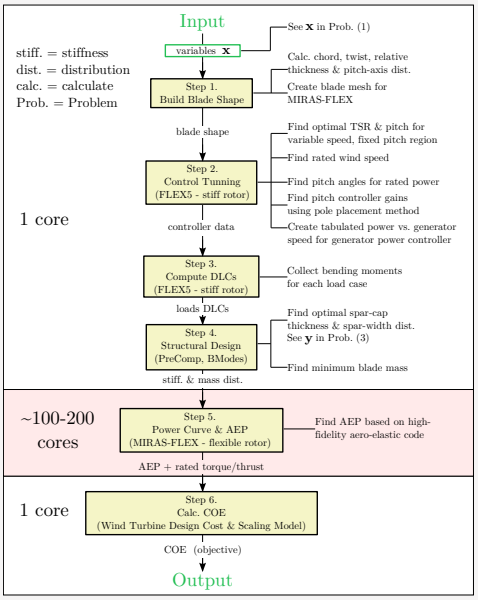


**Fig. 5:** Flowchart for evaluating a candidate blade design comprised of six steps: 1) Build blade shape, 2) control tunning, 3) compute DLCs, 4) structural design, 5) compute AEP, and 6) calculate COE.

**Table 1:** Results from the optimization of Problem (1).

| Quantity | COE ($/kWh) | AEP (GWh/yr) | $M_{\text{flap}}$ (MN.m) | $m_{\text{blade}}$ (tons) |
|---|---|---|---|---|
| Ref. fit | 0.084 | 18.6 | 21.2 | 17.0 |
| Optimum | 0.082 | 18.9 | 20.1 | 16.9 |
| % Improv. | +1.9% | +1.9% | +5.5% | +0.8% |

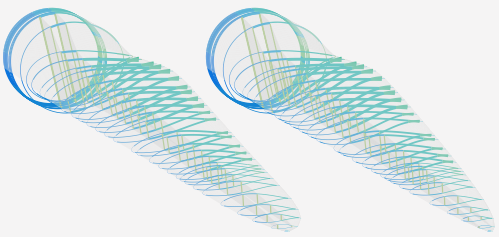

**Fig. 6:** Blade shape and internal structure for the baseline 'Ref. fit' (left), and 'Optimum' solution (right).

## 4 Conclusions

The majority of blade design problems rely on aero-elastic codes that use BEM approaches to model the rotor aerodynamics. The present work describes an approach to wind-turbine rotor design by incorporating a higher-fidelity free-wake panel aero-elastic code called MIRAS-FLEX. Reduction in cost of energy was obtained using the proposed methodology.

## References

[1] Wilson R E and Lissaman P B S 1974 *Applied aerodynamics of wind power machines* (Corvallis: Oregon State University)

[2] Ashuri T, Zaaijer M, Martins J, van Bussel G and van Kuik G 2014 *Renewable Energy* **68** 893–905 ISSN 09601481

[3] Sessarego M, Ramos-García N and Shen W 2015 *Journal of Power and Energy Engineering* **3** 1–6 ISSN 2327-588X

[4] Sessarego M, Ramos-García N, Yang H and Shen W Z 2016 *Renewable Energy* **93** 620 – 635 ISSN 0960-1481

[5] Fingersh L, Hand M and Laxson A 2006 Wind turbine design cost and scaling model Tech. rep. National Renewable Energy Laboratory 1617, Cole Blvd, Golden, CO 80401

[6] Bir G S 2005 *User's Guide to PreComp: Pre-Processor for Computing Composite Blade Properties* National Renewable Energy Laboratory 1617, Cole Blvd, Golden, CO 80401

[7] 2005 *International Standard IEC 61400-1* (IEC)

DTU Wind Energy is a department of the Technical University of Denmark with a unique integration of research, education, innovation and public/private sector consulting in the field of wind energy. Our activities develop new opportunities and technology for the global and Danish exploitation of wind energy. Research focuses on key technical-scientific fields, which are central for the development, innovation and use of wind energy and provides the basis for advanced education at the education.

We have more than 240 staff members of which approximately 60 are PhD students. Research is conducted within nine research programmes organized into three main topics: Wind energy systems, Wind turbine technology and Basics for wind energy.

**Technical University of Denmark**
Department of Wind Energy
Nils Koppels Allé
Building 403
2800 Kgs. Lyngby
Denmark
Telephone  46 77 50 85

info@vindenergi.dtu.dk
www.vindenergi.dtu.dk